Tectonostratigraphic evolution of a salt giant during passive margin development: Santos Basin, offshore Brazil

by

Clara Rosa Rodriguez Rondon

A thesis submitted in partial fulfilment for the

degree of Doctor of Philosophy at

Imperial College London

Department of Earth Science and Engineering

August 2017

Abstract

The stratigraphy of ancient salt giants provides constraints on syndepositional basin tectonics and physiography, and/or variations in climate or sea level. Moreover, subsequent deformation and dissolution of salt directly controls the distribution and architecture of the sedimentary overburden. Hence, salt directly influence the overall tectono-stratigraphic evolution and hydrocarbon potential of salt-dominated passive margins. This study focuses on the Santos Basin, a salt-dominated basin offshore eastern Brazil. To date, few studies have attempted to characterise the architecture of this stratified salt giant (i.e., Ariri Fm.) deposited during Late Aptian opening of the South Atlantic Ocean. In addition, no studies have characterised the deep-water salt tectonic structural style or salt dissolution and its control on deep-water sedimentation. In this study, 3D seismic reflection and borehole data are integrated to constrain the regional tectono-stratigraphic evolution of the Ariri Fm., from its deposition, to its subsequent deformation and partial dissolution. The integration of 3D seismic and borehole data shows that an up 2.5 km thick Ariri Fm. comprises four key evaporite-dominated intervals of distinct composition recording at least 12 cycles of basin filling and dessication in < ca. 530 ka. Moreover, this study reveals that rifting-inherited basin physiography controlled salt thickness and composition leading to stratigraphic variations across structural domains. Overall, thinner salt and higher anhydrite net thickness occur towards structurally high domains, compared to, structurally lower domains where the salt is thicker and anhydrite net thickness is less. In addition, results of this work suggest that more anhydrite was deposited closer to the entrance of fresh seawater, whereas more bittern salts were deposited in more hydrologically restricted locations. Seismic stratigraphy and seismic attribute analysis illustrate how subsequent gravity-driven downdip salt flow directly controlled the Santos Basin deep-water slope morphology, influencing sediment dispersal and architecture. During the Turonian-middle Campanian, sand-rich channels and lobes were confined within proximal minibasins and to the hangingwalls of landward-dipping, salt-detached listric faults. During the middle Campanian-to-Paleocene, sand-rich channels and lobes eventually filled and bypassed proximal minibasins, with deposition then occurring further downslope. The work presented here illustrates how syn-depositional seabed deformation, driven by passive and active diapirism, and salt-detached thrusting and folding downslope directly controlled sediment distribution

and architecture. During the Paleocene-to-middle Oligocene, continued rise of salt walls dissected previously deposited deep-water systems, with increased deposition of MTCs. In addition, during the Palaeocene, dissolution of the crest of salt walls led to the truncation of intrasalt stratigraphy and formation of a salt karst seascape, with subterranean dissolution driving overburden deformation. Widespread salt dissolution likely occurred due to downward migration of NaCl-undersaturated seawater through the thin unlithified roofs of salt walls. Dissolution of the crests led to local caprock formation and the subsequent disruption, collapse and rotation of the overburden. An alternative hypothesis is that salt dissolution occurred due to the updip lateral migration of formation fluids from deep-water channels and lobes deposited along the flanks of the crests of salt walls. This thesis helps to improve our understanding of ancient salt giants, and the control salt tectonics and salt dissolution has on deep-water reservoir deposition and architecture. In addition, findings of this work have direct implications for assessing the Santos Basin post-salt hydrocarbon potential of this previously underexplored interval.

Declaration

This work is my own, except where other authors are cited. The results presented in this thesis has not been submitted for a degree at the Imperial College London or in any other institution.



Clara Rodriguez

The copyright of this thesis rests with the author and is made available under a Creative Commons Attribution Non-Commercial No Derivatives licence. Researchers are free to copy, distribute or transmit the thesis on the condition that they attribute it, that they do not use it for commercial purposes and that they do not alter, transform or build upon it. For any reuse or redistribution, researchers must make clear to others the licence terms of this work.

Acknowledgments

First and foremost, I want to thank my supervisor Christopher Jackson. I deeply appreciate all his advices, his time, patience and support during my PhD. Having Chris as my supervisor has been an honour for me. My supervisors, Rebecca Bell and Atle Rotetvan are also thanked for their always significant and ideal contributions during this research. Having Chris, Becky and Atle as my supervisors made my time during the PhD an enjoyable experience.

The continuous support, patience and love from my family was fundamental during the PhD experience. I gratefully thank my husband, Alejandro, and my daughters, Claire, Amelie, and Audrey. They were my inspiration during the creative times and 'my rock' during the tough times. I also thank my mother, Clara, my mother-in-law, Margot, and my father, Adolfo, for their time and help during my PhD studies. This PhD thesis would not have been possible without their support. My brothers, Justo and Adolfo, and my sisters-in-law, Claudia and Mariolys, are also thanked for their valuable support.

I thank Mike Hudec and Martin Jackson (RIP) for inviting me to present my PhD research at the AGL annual meetings in 2014 and 2015. Mike and Martin have always inspired me to love and study salt tectonics.

CGG is also thanked for providing the 3D seismic reflection dataset that was used during this PhD research. I also thank Statoil for proving the very fundamental borehole data to be able to accomplish my thesis objectives. I would also like to acknowledge my sponsor and 2D seismic data provider, WesternGeco, Schlumberger. In particular, I am grateful for all the valuable discussions with my former manager at WesternGeco, Malcolm Francis. His teachings and advices, before, and during my PhD, were key to accomplish the objectives of this research. Thank you to Montserrat Portet and Sugandha Tewari for their valuable support during the PhD. I also thank all the members of the Basins Research Group that helped me and inspired me to always try harder and do better during the time of this research; Aruna Mannie, Antje Lenhart, Johan Claringbould, Thilo Wrona, Oliver Duffy, Donatella Astratti, Matt Lewis, Adam Suleiman, Matt Reeve, Tom Phillips and Alexander Coleman, thank you all. Ian Davison and Webster Mohriak are also thanked for all the suggestions and critique of Chapter 5 manuscript, which has been submitted for publication.

Table of contents

Page No.

Chapter 1 Introduction **1**

1.1. Rationale **1**
1.2. Research aims **4**
1.3. Thesis outline **5**
1.4. Publication status **6**
1.5. Contributions to other articles **7**

Chapter 2: Research context **10**

2.1. Salt deposition and stratigraphy **10**

2.1.1. What is salt? **10**

2.1.2. Evaporite crystallization sequence **11**

2.1.3. Ancient Salt giants: Key controls on its deposition and stratigraphic variability **12**

2.2. Salt tectonics in passive margins **21**

2.2.1. Salt and sediment interactions: Key concepts **21**

2.2.2. Salt-related structural styles along passive margins **24**

2.2.3. Intraslope salt-sediment interactions **27**

2.2.4. Salt-related trapping along passive margins **30**

2.3. Salt dissolution **32**

2.3.1. Significance of salt dissolution **32**

2.3.2. Solubility of salt **33**

2.3.3. Mechanisms of salt dissolution **34**

2.3.4. Crestal caprock and solution breccias **35**

2.3.5. Salt dissolution-related local morphologies **36**

2.3.6. Submarine salt dissolution: previous studies **38**

Chapter 3: Study area: Santos Basin, offshore eastern Brazil **40**

3.1 Regional context **40**

3.2 South Atlantic salt deposition: Key controversies **43**

3.3 Stratigraphy of the Ariri Formation: Previous studies and unanswered questions **49**

3.4 Post-salt sequence in the Santos Basin: is there any overlooked hydrocarbon exploration potential? **50**

3.5 Salt dissolution in the Santos Basin **54**

Chapter 4: Data and methods **56**

4.1. Data **56**

4.2. Data preparation and integration **58**

4.3. Vertical seismic resolution estimations **60**

4.4. Seismic-well tie **61**

4.5. Intrasalt lithology interpretation and stratigraphic correlation **62**

4.6. Horizon interpretation and mapping **65**

4.7. Thickness maps **66**

4.8. Velocity model and depth conversion **66**

4.9. Seismic attribute analysis for the geological interpretation **68**

Chapter 5: Stratigraphy of salt giants: New insights from the Santos Basin, offshore Brazil **72**

5.1 Abstract **72**

5.2 Introduction **73**

5.2.1 Early Cretaceous salt of the South Atlantic: Previous studies and controversies **77**

5.2.2 Stratigraphy of the Ariri Formation: Previous studies **79**

5.3 Tectono-stratigraphic framework **82**

5.4 Data and methods **85**

5.5 Structural framework **88**

5.6 The Ariri Formation: Composition and seismic expression **96**

5.6.1 Composition **96**

5.6.2 Seismic expression of intrasalt units **96**

5.7 The Ariri Formation: Key stratigraphic intervals **98**

5.8 The Ariri Formation: Key controls on the composition and stratigraphic architecture and their significance **107**

5.8.1 Climate, water depth and duration of deposition **108**

5.8.2 Syn-depositional basin physiography **113**

5.8.3 Basin hydrology **115**

5.9 Conclusions **119**

5.10 Acknowledgments **121**

Chapter 6: Minibasin development and reservoir deposition on a salt-influenced deep-water slope **123**

6.1 Abstract **123**

6.2 Introduction **125**

6.3 Geological Setting **128**

6.4 Data and methods **133**

6.5 Minibasin structure and stratigraphy **137**

6.5.1 Proximal thick minibasins **137**

6.5.2 Medial shallow minibasins **140**

6.5.3 Distal minibasins **141**

6.6 Minibasins deep-water depositional elements **144**

6.7 Tectono-stratigraphic development of intraslope minibasins **149**

6.7.1 Unit 1: Albian - Cenomanian **152**

6.7.2 Unit 2: Turonian to Mid-Campanian **152**

6.7.3 Unit 3: Mid-Campanian to Palaeocene **158**

6.7.4 Unit 4: Palaeocene to Mid-Oligocene **182**

6.7.5 Unit 5: Mid-Oligocene to Pleistocene **186**

6.8 Discussion **188**

6.8.1 Regional controls on minibasin tectono-stratigraphic architecture **188**

6.8.2 Local controls on paleo-seafloor relief and sediment architecture **190**

6.8.3 Exploration significance **193**

6.8.4 Conclusions 195

Chapter 7: Evidence for and significance of submarine dissolution 198

7.1 Abstract **198**

7.2 Introduction **199**

7.3 Geological setting **203**

7.4 Dataset **208**

7.5 Methods **209**

7.6 Salt-related structural domains **212**

7.7 Top Salt and intrasalt stratigraphy **216**

7.8 Post-salt sedimentary overburden **218**

7.9 Seismic expression of salt karst **222**

7.9.1 Salt dissolution-related sinkholes or dolines **222**

7.9.2 Residual mounds **225**

7.9.3 Breccia pipes or chimneys and associated sinkholes **230**

7.10 Subaerial or submarine salt dissolution? **237**

7.11 Discusion **241**

7.11.1 Mechanism of salt dissolution **241**

7.11.2 Salt dissolution implications **244**

7.12 Conclusions **247**

Chapter 8: Discussion and conclusions 249

8.1 How rapidly was the Santos Basin salt giant deposited and what are the implications of this rapid deposition? **249**

8.2 Can thickness and stratigraphic variability within a salt giant provide clues to temporal and spatial variations in syndepositional basin physiography? **251**

8.3 What can salt giants stratigraphic architecture tell us about syn-depositional basin hydrology? **253**

8.4 How does salt movement control instraslope deep-water sediment architecture along the Santos Basin slope? **255**

8.5 Could previously underexplored post-salt intervals have hydrocarbon exploration significance? **256**

8.6 What are the implications of these findings for the overall understanding of salt and sediment interactions along salt-influenced slopes? **258**

8.7 What is the role of the intrasalt stratigraphic heterogeneity on the development of local dissolution-related morphologies, and the overall external morphology of salt structures? **260**

8.8 What was the impact of salt dissolution in the post-salt sedimentary overburden? **262**

8.9 What was the mechanism leading to salt dissolution? **264**

8.10 Future work **266**

Bibliography **267**

Appendix (CD enclosed)

List of Figures

Chapter 1: Introduction

1.1. World map highlighting some examples of ancient salt giants and its tectonic setting. After Warren, 2010. **2**

Chapter 2: Research context

2.1. End-member models for the deposition of ancient salt giants. Modified after Prothero and Schwab (2003) and Warren (2006). **14**

2.2. Carbonate-evaporite basin subjected to complete drawdown. After Tucker (1991). See text for description. **16**

2.3. Carbonate-evaporite Patterns of evaporite distribution in desiccating deep basins. Modified from Hsü (1972). **17**

2.4. Example of ancient salt giant: Pennsylvanian Paradox Formation (a) Regional map of the Paradox Basin illustraiting salt distribution. Modified from Trudgill (2011). (b) General cross section through the Paradox Basin, modified from Peterson and Hite (1969), Hite and Buckner (1981), Williams-Stroud (1994); (c) typical evaporite cycle, after Eoff et al., 2012. **19**

2.5. Example of ancient salt giants, Late Permian Zechstein Supergroup: (a) Location of the Permian salt Basin. (b) Depositional salt thickness distribution of the Zechstein Supergroup. After Glennie et al. (2003). (c)Depositional model of the Zechstein Supergroup, after Clark et al., 1998. (d) Typical evaporite cycle after Taylor (1990); (e) Conceptual model illustrating the Permian tectonostratigraphic evolution of the Stavanger Fault System, after Jackson and Lewis (2013). **20**

2.6. Overburden strata thickness variations and age relations to underlying salt flow. Modified from Jackson and Hudec (2017). **22**

2.7. Simplified block diagrams illustrating salt and sediment interactions and trapping styles along passive margins. Constructed based on information gathered by several previous studies (e.g.; Rowan and Weimer, 1998; Pettinghill and Weimer, 2002; Weimer and Pettinghill, 2007; Hudec et al., 2009; Mayall et al., 2010; Albertão et al., 2011; Liu and Li, 2011; Jackson and Hudec, 2017). **23**

2.8. Salt-related structural styles along the Angolan passive margins, offshore West Africa. Modified from Brun and Fort (2004). **26**

2.9. Examples of trapping along salt-influenced slopes. (a) Onlap trapping within minibasins, Auger and Macaroni fields, Gulf of Mexico. Modified from (b) Merluza field in the Santos Basin, offshore eastern Brazil, producing from Upper Cretaceous-age sandstone-rich turbidites on a salt-cored high. Modified from Riddle et al. (1995). (c) Examples of post-salt deep-water reservoirs in the Campos Basin, offshore east Brazil. Modified from Bruhn, 2003. **31**

2.10. (a) Crestal caprock. After Jackson et al., 2013; Hallager et al. 1990. (b) Crestal aprock zonation after Jackson and Hudec, 2017; Jackson et al 2013, Warren, 2006, Posey and Kyle, 1988. **35**

2.11. Collapse sinkhole above a salt dome in the Zagros Mountains, Iran, after Gutierrez and Lizaga (2016). **37**

2.12. Simplified sketch of surface and near-surface karst in gypsum and carbonate settings. Modified from Gutierrez et al. (2014). **37**

2.13. Modern submarine brine lake in the Orca Basin, Gulf of Mexico. After Pilcher and Blumstein (2006). **38**

Chapter 3: Study area

3.1. Early Cretaceous paleogeography illustrating the South Atlantic salt giant and the location of the Santos Basin (after Lentini et al., 2012). **42**

3.2. (a) Location of the Santos Basin; (b) Santos Basin bathymetry and location of the study area; (c) Santos Basin gravity anomalies (Sandwell and Smith v. 18.1). **44**

3.3. (a) Stratigraphic column for the Santos Basin, after Modica and Brush (2004), Duarte and Viana (2007), Moreira et al. (2007), and Jackson (2012). 3.3. (b) Cross-section the Santos Basin, after Modica and Brush (2004), and Jackson (2012). Location is shown in Figure 3.2. **47**

3.4. Gravity anomalies by Sandwell and Smith v. 18.1 scaled to depth of basement showing the limits of the Santos Basin. Basinwide geoseismic sections illustrating salt thickness variations are after Davison et al., 2012 (see Figure 3.5 for vertical scale). **51**

3.5. Basinwide geoseismic sections. After Davison et al. (2012). **52**

Chapter 4: Data and methods

4.1. (a) Study area and dataset. See location of 3D survey relative to key structural elements like Outer High, and the Albian Gap. (b) Seabed depth-structural map gighlighting the present-day bathymetry in the study area. **57**

4.2. Example of integration of previous studies: Regional salt structure map by Guerra and Underhill (2012) overlapped by the new Top salt time-structure map interpreted using the data available in the study area. **59**

4.3. Examples of frecuency spectrums calculated for the postsalt (a) and the intrasalt (b). **60**

4.4. (a) Example of seismic-well tie for the salt sequence (b) Relative acoustic impedance volume is filtered to highlight and compare the high acoustic

impedance anhydrite from the low-acoustic impedance bittern salts and medial acoustic impedance halite. **62**

4.5. Crossplot analysis used to interpret lithology at the well locations (a) Sonic vs. Density coloured with GR values; (b) Sonic vs. density coloured with the evaporates interpreted. **63**

4.6. Integrated approach used for the regional well correlation: (a) laterally extensive carnallite layer identified at the wells and interpreted using the seismic; (b) anhydrite layers pinching and thinning towards the North and Tupi sub-high. **64**

4.7. Depth conversion of the base salt structure map to minimise or eliminate velocity pull ups effects caused by salt structures. **67**

4.8. Examples of seismic attributes used for this study. **70**

Chapter 5: Stratigraphy of salt giants: New insights from the Santos Basin, offshore Brazil

5.1. Conceptual model for the stratigraphic architecture of a carbonate-evaporite basin subjected to complete drawdown (after Tucker, 1991). (A) Carbonate deposition during highstands; (B) Gypsum deposition during slow sea level fall; (C) Halite and bittern salts are deposited during lowstands and basin desiccation; (D) Gypsum is deposited during refill of the basin. **76**

5.2. (A) Early Cretaceous paleogeography illustrating the South Atlantic salt giant (after Lentini et al., 2012); (B) Geographic setting of the Santos Basin (C) Geoseismic section illustrating the passive margin structural domains and illustrating the salt thickness variations the Santos Basin. 2D seismic line courtesy of WesternGeco. **80**

5.3. Regional intra-salt well correlation between two boreholes 270 km apart from each other (after De Freitas, 2006). **82**

5.4. Santos Basin seismic stratigraphic framework including mapped horizons. Key stratigraphic intervals are specified for this and previous studies. B1, B2 and B3 refer to competent layers or 'beams' defined by high amplitude continuous reflections and D1, D2 and D3 refer to ductile detachment zones defined by acoustically transparent, poorly continuous reflections (Fiduk and Rowan, 2012). **84**

5.5. Seismic and geoseismic sections 2 boreholes in the study area illustrating the mapped horizons and defined key stratigraphic intervals. Seismic data courtesy of CGG. See Figure 2B for location. **87**

5.6. Present-day structural framework of the study area including (A) Base of salt depth-structure map illustrating the sub-salt basin physiography and the presence of the Sugar Loaf and Tupi sub-highs; (B) Top of salt depth-structure map illustrating the salt-related structural domains and (C) Salt thickness depth map, seabed to top salt isochore map. **91**

5.7. (A) NW-SE seismic and geoseismic cross-sections and mapped horizons illustrating the salt thickness variations and the seismic expression of the intrasalt key stratigraphic intervals the Thick Salt and Sugar Loaf domains; (B) NNE-SSW seismic and geoseismic cross-sections with the mapped horizons illustrating the salt thickness variations and intrasalt seismic expression from the minibasin domain towards the Sugar Loaf domain; (C) NNW-SSE seismic and geoseismic cross-section illustrating the salt thickness variations and intrasalt seismic expression the Tupi domain. See Figure 5C for locations. 3D seismic data courtesy of CGG. **93**

5.8. Seismic-well tie for the intra-salt key stratigraphic intervals. **97**

5.9. (A) A1 thickness map in depth (isochore); (B) A2 thickness map in depth (isochore); (C) A3 thickness map in depth (isochore); (D) A4 thickness map in depth (isochore). The isochores illustrate intra-salt diapirism by A1 (in pink) **99**

5.10. (A) Well correlation the Thick Salt and Sugar Loaf domains illustrating variations in intra-salt thickness and lithology proportions; (B) well

correlation the Minibasin and Sugar Loaf domains illustrating variations in intra-salt thickness and lithology proportions **109**

5.11. SW-NE detailed intrasalt well correlation the Outer High. The detailed correlation was done using the relative acoustic impedance to identify evaporite layers between the boreholes. **111**

5.12. Proposed model for A1, A2 and A3 intrasalt key stratigraphic intervals illustrating the influences of the syn-depositional basin physiography in the resulting stratigraphic architecture. **117**

5.13. Duration of deposition estimated based on the thickness of each evaporite cycle and depositional rates from ancient and modern salt basins **118**

Chapter 6: Minibasin development and reservoir deposition on a salt-influenced deep-water slope: Santos Basin, offshore Brazil

6.1. (a) Passive margin salt-related domains. 1b) Block diagrams illustrating examples of depositional elements interacting with salt and related potential trapping styles along the passive margin. **126**

6.2. (a) Brazilian sedimentary basins; (b) Study area and dataset; (c) Geoseismic profile across the study area, after Modica and Brush, 2004; Jackson, 2012. **129**

6.3. Chrosnostratigraphic table. After Moreira, 2007 and Jackson, 2012. **130**

6.4. Deepwater Santos Basin paleogeography. Modified after Modica and Brush, 2004. 4a) Albian paleogeography; 4b) Late Campanian paleogeography; 4c) Middle Eocene paleogeography; 4d) Late Eocene paleogeography. **132**

6.5. Seismic-well correlation, attributes and vertical seismic resolution. **136**

6.6. (a) Postsalt isophach (Seabed to top salt depth thickness map); (b) Minibasin types . **138**

6.7. Minibasins (a) Proximal thick minibasins; (b) Medial shallow minibasins; (c) Distal elongated Minibasins. **139**

6.8. Seismic-well tie. (a) Borehole 369a penetrating a shallow minibasin. See Figure 6.7b for location. (b) Borehole 723C penetrating the flank of a distal minibasins. See Figure 6.7c for location. **143**

6.9. Regional isochrones illustrating deposition and salt-related deformation in the post-salt of central deep-water Santos Basin. (a) Albian-Cenomanian unit 1 twt thickness map; (b) Turonian to Mid-Campanian Unit 2 twt thickness map; (c) Mid-Campanian to Paleocene Unit 3 twt thickness map; (d) Paleocene to Mid Oligocene Unit 4 twt thickness map; (e) Mid-Oligocene to present-day Unit 5 twt thickness map. **149**

6.10. Detailed thickness maps of the proximal minibasins (A-C) illustrating local intra-minibasins depocenters and shifting of depocenters during minibasin development. **154**

6.11. (a) Seismic profile minibasin C illustrating the key horizons and units interpreted. See Figure 10 for location. (b) Seismic profile along minibasin B with key horizons and units interpreted. See Figure 10 for location. (c) Geoseismic profile along minibasin B illustrating the main depositional elements with the defined units. d: Sweetness attribute in the proximal part of minibasin B illustrating ponded lobes, channels, MTCs and background deposits. (e): Sweetness attribute south of minibasin B illustrating the main depositional elements identified. **157**

6.12. (a) Sweetness and variance attribute blending for Unit 2a and Top Salt attribute interval shown on Figure 6.11a (b) Sweetness and variance attribute blending for Unit 2b and Top Salt attribute interval shown on Figure 6.11a. (c) Sweetness and variance attribute blending for Unit 3a and Top Salt attribute interval shown on Figure 6.11b (d) Sweetness and variance attribute blending for Unit 3b and Top Salt Lower attribute interval shown on Figure 6.11b (e) Sweetness and variance attribute blending for Top Unit 3b - 250 ms (TWT) (f) Sweetness and variance attribute blending for Top Unit 3b - 100 ms (TWT) (g) Sweetness and variance attribute blending for Top Unit 3b - 50 ms (TWT). **163**

6.13. Sweetness and variance attribute blending illustrating dissected channels by present-day salt walls. **167**

6.14. (a) Seismic sections deep minibasins D and shallow minibasin E. (b) Seismic section minibasin E. See locations on Figure 6.13 (b) Sweetness and variance attribute blending for Unit 2b and Top Salt. **168**

6.15. Unit 3 deep-water depositional systems part of the Inner Sao Paulo Fold Belt and the distal minibasins on the Sao Paulo Plateau. Based on seismic attribute analysis and thicknessmaps. Detailed isochrons, attribute maps and seismic sections are shown on Figures 6.16-6.22. **170**

6.16. (a) Unit 3- Detailed isochron map highlighting increase in thickness above synclines and salt-cored faults. See location on Figure 6.15. (b) sweetness and variance visual blending illustrating the spill of channels from proximal overfilled minibasins towards distal minibasins. (c) channel deflection and development of lateral accretion packages. See location on 6.16 b and 6.15. **171**

6.17. (a),(b) and (c) Seismic sections showing deposition of deep-water Clastic systems in the Inner Sao Paulo Fold Belt. Increase in thickness are observed above synclines and salt-cored faults. See Figure 6.16 a and b for locations. (d,e) Seismic sections illustrating high-amplitude lateral accretion packages. See Figure 6.16 c for locations. **172**

6.18. (a) Detailed isochron map for Unit 3 minibasins I, J and K. Increase in thickness occurs around salt-cored folds and associated to lobes deposition where frontally confined. (b) Sweetness and variance blending illustrating deep-water clastic deposition within minibasins I, J and K. See interpretation and location in Figure 6.15. Channel deflection next to a salt cored fold can be observed within Minibasin K. See also Figure 6.19 c. **174**

6.19. (a) and (b): Seismic sections the distal part of minibasin I, illustrating lobes deposition and confinement. For locations, see Figures 6.18 a and b (c) Amplitude contrast showing channel deflection around salt-cored fold. (d) and (e) Seismic sections minibasin J. For locations, see Figures 6.18 a and b e, f, g: Seismic sections minibasin K For locations, see Figures 6.18 a and b. **175**

6.20. (a) Unit 3 detailed isochron thickness variations for minibasins L and M. (b) Sweetness and variance attribute blending for minibasins L and M.

See interpretation and location on Figure 6.15. (c) Amplitude contrast attribute highlighting an intra-minibasin MTC. **177**

6.21. (a), (b) and (c): Seismic sections minibasin L. See locations on Figure 6.20. (d), (e) and (f): Seismic sections minibasin M. See locations on figure 6.20. **178**

6.22. Channel and Levee geometry, thickness and amplitudes variations in minibasin M. Rotation of infra-levee seismic reflections towards the channel axis indicate salt growth during deposition. **181**

6.23. (a) Unit 4 seismic expression of mass transport complexes within minibasin B. See Figure 6.11 b and c for location. (b) Sweetness and variance attribute blending for Unit 4a. (c) Sweetness and variance attribute blending for Unit 4b. **183**

6.24. Seismic expression of regional-scale linear MTCs marking the end of deep- water deposition the inner Sao Paulo Fold Belt and the Sao Paulo plateau. **185**

6.25. Seismic expression of MTCs within Unit 5. (a) Amplitude contrast attribute of intra-Unit 5 horizon highlighting blocks and chaotic matrix. (b) seismic secion the minibasin; (c) seismic secion along the minibasin. **187**

Chapter 7: Evidence for and significance of submarine dissolution

7.1. Worldwide evidence of dissolution: (a) Collapse sinkhole above a salt dome in the Zagros Mountains, Iran, after Gutierrez and Lizaga (2016); (b) Deeply-buried, Ordovician-age carbonate karst morphologies in the Tarim Basin, China, after Zeng et al. (2011); (c) near-seabed flat-topped salt diaper in the Barents Sea, after Koyi et al. (1995); (d) Salt wall caprock in Netherlands, after Duin (2001); (e) present-day submarine brine lake in the Gulf of Mexico, after Pilcher and Blumstein (2006). **201**

7.2. (a) Eastern Brazil salt-dominated sedimentary basins highlighting the location of the Santos Basin, offshore Brazil; (b) Study area in the central

deep-water Santos Basin. Location of 2D seismic profile used for basin modelling and 3D seismic reflection and borehole data. **205**

7.3. (a) Seismic stratigraphic framework; Intrasalt key stratigraphic intervals are specified for this and previous studies. B1, B2 and B3 refer to competent layersor 'beams' defined by high amplitude continuous reflections. D1, D2 and D3 refer to ductile detachment zones defined by acoustically transparent, poorly continous reflections (Fiduk and Rowan, 2012). (b) 2D depth seismic profile illustrating salt-related structural domains in the Santos Basin. (c) Geoseismic profile with units interpreted. **206**

7.4. a: Top salt structural map with locations of salt walls of interest b: Seismic section salt diapirs with flat crests c: Seismic section salt diapirs with rounded and rugose crests. **214**

7.5. (a) Top Salt lithology in a structurally-low and reltively undeformed area (borehole 532A) b: Intrasalt seismic expression and stratigraphy for borehole 709. **216**

7.6. Overburden seismic expression and stratigraphy. Post-salt seismic-borehole tie. **219**

7.7. Seismic expression of sinkholes: (a) R-west top salt structural map. See Figure 7.14 a for location; (b) Amplitude contrast attribute map for R-west; (c) Seismic section long the crest of R-west illustrating the geometry of sinkholes (indicated by white arrows) and their relationship to A3 intrasalt stratigraphy. Loction shown on Fig. 7.7 a and b; (d) Sweetness attribute of section on Figure 7.7c illustrating amplitude variations along the Top Salt. **223**

7.8. Seismic expression of sinkholes: (a) Seismic section along the crest of R-east illustrating the geometry of sinkholes (indicated by white arrows) and their relationship to dipping-A2 intrasalt stratigraphy. Location is shown on Fig. 7.8 d; (b) Sweetness arttribute of section on Figure 7.8a illustrating amplitude variations along the Top Salt; (c) Chaos attribute of section on Figure 7.8a illustrating sinkholes along the Top Salt; (d)

Amplitude contrast attribute map of R-east. See Figure 7. 14c for location. **224**

7.9. Seismic expression of residual mounds: (a) Seismic section along the crest of F-east illustrating residual mounds above the main top salt level (mounds are indicated by white arrows), See Figure 7.9 c and d for location; (b) Sweetness attribute for section on Figure 7.9 a illustrating facies variations along the Top Salt; (c) Top Salt structure map for F-east. See Figure 7.14 f for location; (d) Amplitude contrast attribute map for F-east Top Salt highlighting residual mounds above the nearly-horizontal Top Salt. **227**

7.10. Seismic expression of residual salt karst-related mounds. (a) Seismic section along the crest of F-west illustrating residual mounds defined by highly-reflective packages along the Top Salt (mounds are indicated by white arrows). See location on (d); (b) Chaos attribute for seismic section on (a) highlighting the discontinuities along the Top Salt and within the overburden; (c) Sweetness attribute for section on (a) illustrating the facies variations within the mounds; (d) Top Salt structural map for F-west. See Fig. 14.d for Location. **228**

7.11. Seismic expression of residual salt karst-related mounds. (a) Seismic section mounds on R-Central salt diapir illustrating remnant mounds after A3 dissolution. See (b) and (c) for location; (b) Top Salt structural map for R-Central. See Fig. 14b for location; (c). Amplitude contrast attribute map highlighting the location of residual mounds. **229**

7.12. Seismic expression of collapse breccia pipes indicated by the white arrows. (a) Seismic seccion F-central illustrating local collapse within the overburden. (b) Chaos attribute of seismic section on (a) highlighting breccia pipes (c) Sweetness attribute of seismic setion on (a) highlighting discontinuities along the Top Salt/caprock. (d) Map of intra-Unit 3 horizon illustrating the pipes in plan-form. (e) Variance attribute map of intra-Unit 3 horizon on (d). **231**

7.13. (a) Map of intra-Unit 3 horizon showing deformation within the overburden/roof above F-central. (b) Map of Top Salt for F-central

illustrating dissolution of the crest (c) and (d): Seismic sections F-central showing flanking minibasin and channel. **232**

7.14. (a) R-west Top Salt (b) R-central Top Salt (c) R-east Top Salt (d): F-west Top Salt (e): F-central Top Salt f: F-east Top Salt. **234**

7.15. (a) Model used for basin restoration based on interpretation of 2D seismic profile. See Key on Figure 7.3. Basin restorations to Mid-Oligocene on (b) and (c): using minimum and maximum Beta stretching factor, respectively. Basin restorations to Paleocene on (c) and (e) using minimum and maximum Beta stretching factors, respectively. **239**

7.16. Styles of dissolution **246**

List of Tables

Chapter 2: Research context

2.1. Evaporite crystallisation sequence in increasingly concentrated hypersaline solutions. After Warren (2006) and Warren (2012). **12**

Chapter 5: Stratigraphy of salt giants: New insights from the Santos Basin, offshore Brazil

5.1. Evaporites typical borehole log response expected from wireline logs. Information gathered from literature review (After Mohriak et al. 2009; Schlumberger, 1991; Halliburton, 1994). **90**

5.2. Structural domains. **92**

5.3. Key stratigraphic intervals. Thickness ranges estimated from isochores and borehole data in areas where less post-depositional salt flow has occurred. Evaporite proportions domains are also included. **100**

Chapter 6: Minibasin development and reservoir deposition on a salt-influenced deep-water slope: Santos Basin, offshore Brazil

6.1 Vertical seismic resolution of intervals of interest and structural domains. **134**

6.2 Seismic facies and depositional elements identified with the post-salt in central deep-water Santos Basin. Depositional elements are defined based on the integration of seismic stratigraphy and seismic geomorphology. **146**

Chapter 7: Evidence for and significance of submarine dissolution

7.1 Post-salt sediment key input parameters based on seismic interpretation and well reports available. **211**

7.2 Overburden seismic expression and thickness variations above dissolved flat crests. **220**

7.3 Overburden seismic expression and thickness variations above dissolved rugose crests. **221**

Chapter 1

Introduction

1.1. Rationale

Salt giants consist of hundreds to more than several thousand meters-thick evaporite-dominated successions deposited in isolated sedimentary basins (Fig. 1; e.g.; the Jurassic Louann salt in the Gulf of Mexico, e.g., Bird et al., 2005; the Messinian salt in the Mediterranean sea, e.g., Cartwright et al., 2012; the Permian Zechstein Supergroup in Europe, e.g., Stewart and Clark, 1999; the Pennsylvanian Paradox Formation, e.g., Trudgill, 2011 and the circum-South Atlantic salt basins offshore west Africa and offshore east Brazil, e.g., Jackson et al. 2000, Davison, 2007). Where thickly developed and mobile, salt directly controlled the evolution of ancient sedimentary basins. However, the study of salt giants and their impact on basin development is extremely challenging due to several reasons. First, due to the absence of modern analogues of comparable scale and thickness to ancient salt giants, and which occur in similar tectonic and hydrological settings. Second, due to its low density and negligible yield strength salt is mechanically unstable, thus salt flows like a viscous fluid due to differential flow under gravitational forces, distorting the original stratigraphy as large salt structures develop (e.g., Hudec and Jackson, 2007). Third, salt is soluble; hence when it becomes in contact with subaerial or NaCl-undersaturated submarine fluids, salt is dissolved and/or altered (e.g., Warren, 1997). Forth, seismic reflection imaging of salt-related deformation can be challenging due to issues related to

steeply dipping flanks of large salt structures, and the lithological and hence acoustic heterogeneity imparted onto salt bodies due to dissolution-related diagenetic processes (e.g., Jackson and Lewis, 2012; Davison, 2013; Jones and Davison, 2014). Fifth, hydrocarbon exploration and production boreholes avoid drilling through salt due to engineering difficulties. There is thus an overall lack of information regarding the lithology and stratigraphy within the salt giants, even if in-situ. Consequently, many uncertainties and controversies remain regarding salt deposition and stratigraphy, its effects on sediment distribution, and the kinematics and effects related to its eventual dissolution. Reducing these uncertainties and resolving these controversies is critical for several reasons. For example, from a fundamental point-of-view, understanding the composition and stratigraphic architecture of salt giants can provide insights into the syndepositional

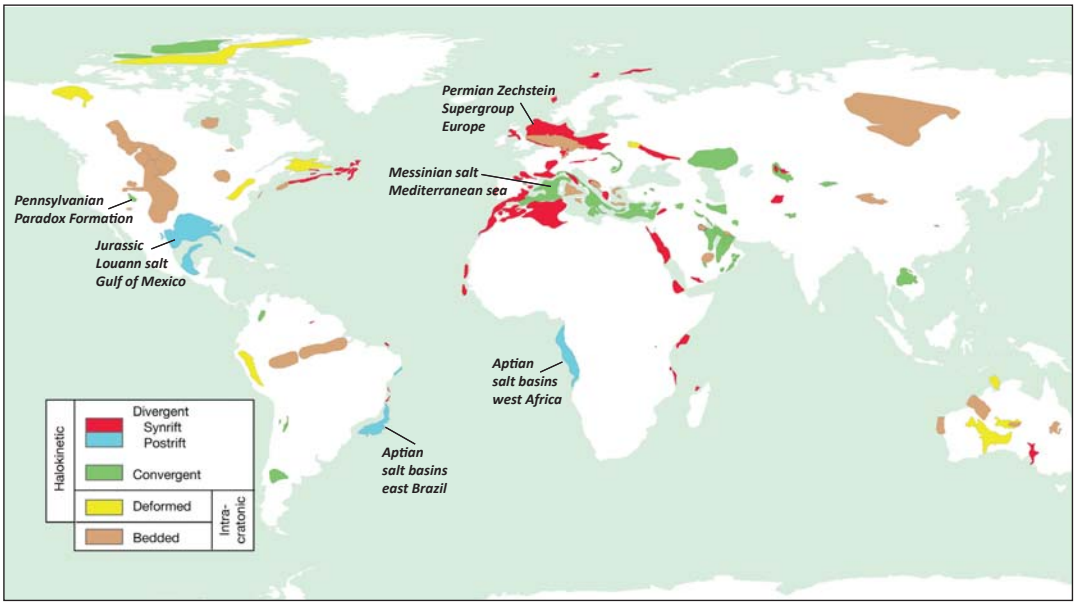


Figure 1: World map highlighting some examples of ancient salt giants and its tectonic setting. After Warren, 2010

basin physiography, climate, eustatic variations, and tectonics during salt deposition. In terms of its applied significance, it is important to understand salt composition and related tectonics because the growth of salt structures can directly influence all the elements of the petroleum systems, including sediment dispersal, reservoir trapping styles, and migration fairways,

thereby impacting hydrocarbon exploration and production in sedimentary basins (e.g., Hudec and Jackson, 2007; Archer et al., 2012). Moreover, a salt layer may form a perfect seal for hydrocarbons due to its low permeability; and the low conductivity of salt means that it can also impact the thermal evolution of sedimentary basins (e.g.; Jackson and Hudec, 2017). Besides, understanding intra-salt stratigraphy, salt-sediment interface and the effects of salt dissolution may serve to assess potential drilling hazards and seismic imaging issues that are associated with vertical and lateral changes in seismic velocities (e.g.; Jones and Davison, 2014). This study focuses on the Santos Basin, a salt-dominated sedimentary basin located in eastern offshore Brazil. This basin has been the focus of much attention in recent years due to major hydrocarbon discoveries made beneath a 2 km-thick, stratified salt sequence, known as the Ariri Formation (e.g., Moreira et al., 2007). The reflectivity of this salt sequence and the availability of boreholes that have drilled through it on their way to underlying presalt reservoirs, provide an ideal location to study the stratigraphy of a salt giant. Despite being imaged by high-quality, regionally extensive 2D and 3D seismic reflection data and penetrated by 50-100 boreholes, surprisingly few studies have attempted to characterise the composition and stratigraphic architecture of the Ariri Formation in the Santos Basin, offshore Brazil (e.g, Demercian, 1996; De Freitas, 2006; Gambôa et al., 2008). As a result, it is not clear how this regionally extensive stratigraphic unit records syn-depositional tectonics, or variations in climate, or sea-level or how rapidly was the thick (2 km) salt deposited. Furthermore, the Ariri Formation, has directly controlled the structural evolution and present-day configuration of the post-salt sedimentary overburden. The study area therefore provides spectacular, hitherto undocumented examples of salt tectonic structural style and its control on deep-water sedimentation. In addition, anomalously clear intrasalt reflectivity and exceptional seismic imaging of the crest of large salt structures make it an ideal location to investigate, for the first time, evidence of submarine salt dissolution and its impact in the overburden.

1.2. Research aims

The main aim of this thesis is to constrain the tectonostratigraphic evolution of the Santos Basin salt giant, from its deposition, to its subsequent deformation and eventual partial dissolution. The specific aims of this study are:

(1) To determine the compositional variations and overall intrasalt stratigraphic architecture of a salt giant, with the purpose of answering the following specific questions, (i) how rapidly was the Santos Basin salt giant deposited and what are the implications of this rapid deposition?; (ii) can thickness and stratigraphic variability within a salt giant provide clues to temporal and spatial variations in syndepositional basin physiography?; and (iii) what can salt giants stratigraphic architecture tell us about syndepositional basin hydrology?

(2) To document minibasin development, sediment dispersal, and ultimate stratigraphic architecture on a salt-influenced, deep-water slope, with the purpose of answering the following specific questions, (i) how does salt movement control instraslope deep-water sediment architecture along the Santos Basin slope?; (ii) could previously underexplored postsalt intervals have hydrocarbon exploration significance?; and (iii) what are the implications of these findings for the overall understanding of salt and sediment interactions along salt-influenced slopes?

(3) To identify and characterise any evidence of salt dissolution, with the purpose of answering the following specific questions: (i) what is the role of the intrasalt stratigraphic heterogeneity on the development of local dissolution-related morphologies, and the overall external morphology of salt structures?; (ii) what was the impact of salt dissolution in the postsalt sedimentary overburden?; (iii) what was the mechanism leading to salt dissolution?

1.3. Thesis outline

This section outlines the content of each of the eight chapters comprising this thesis.

Chapter 1 presents the rationale, research aims, thesis outline and publications status.

Chapter 2 puts this research into context by presenting a literature review focused on salt stratigraphy, salt tectonics and salt dissolution.

Chapter 3 highlights the regional geological context of the study area, previous studies, and gaps in current knowledge related to salt deposition, structure and impact

Chapter 4 provides a description of the dataset and the overall approach and methodology used in this thesis. More thorough descriptions of the dataset and methods can be found in the introductions to Chapter 5, 6 and 7.

Chapter 5 presents new insights into the stratigraphy of salt giants, focusing on the intrasalt stratigraphy and seismic expression of the Ariri Formation, Santos Basin, offshore eastern Brazil.

Chapter 6 explores >50 Myrs of salt-sediment interaction in the Santos Basin, highlighting the influence salt movement has on deep-water sediment dispersal and stratigraphic/reservoir architecture, and trap development and hydrocarbon exploration on salt-influenced deep-water margins.

Chapter 7 documents and discusses evidence for and the mechanisms of submarine salt dissolution at the crests of salt structures in the Santos Basin, offshore Brazil, highlighting its implications for basin evolution, hydrocarbon exploration, seismic imaging, and basin modelling.

Chapter 8 summarises the key outcomes of this thesis, highlighting the overall contributions it makes to the understanding of salt giants in general and the tectono-stratigraphic evolution of salt in the Santos Basin, offshore Brazil in particular. This chapter also includes a description of potential future work that may help complement the findings presented in this thesis.

Where possible I have attempted to reduce unnecessary repetition within this thesis. However, some repetition is evident within introductory sections to individual results chapters (i.e., Chapter 4, 5 and 6), principally because these have been submitted or in the process of being submitted to scientific journals.

1.4. Publication status

Chapters 5, 6 and 7 present the main results of this thesis and constitute 'stand-alone' papers (see section 1.3). The author of this thesis is the first author on all three papers, being responsible for the interpretations and material submitted herein. Important contributions to the research are explicitly acknowledged at the end of each chapter. An overview of the main contributions from the various co-authors is outlined below.

Paper 1: Stratigraphy of salt giants: new insights from the Santos Basin, offshore Brazil (Chapter 5)

C. R. Rodriguez, C. A-L. Jackson, A. Rotevatn, R. E. Bell, M. Francis

Submitted to GEOPSHERE

The first author analysed and interpreted the 3D seismic and borehole data. The co-authors critically reviewed and discussed interpretations, and contributed to the revision of the manuscript prior to submission.

Paper 2: Minibasin development and reservoir deposition on a salt-influenced deep-water slope: Santos Basin, offshore Brazil (Chapter 6)

C. R. Rodriguez, C. A-L. Jackson, A. Rotevatn, R. E. Bell, M. Francis

To be submitted to the AAPG Bulletin

The first author analysed and interpreted the 3D seismic and borehole data. The co-authors critically reviewed and discussed interpretations, and contributed to revision of the manuscript prior to submission.

Paper 3: Evidence for and significance of submarine salt dissolution in the Santos Basin, offshore Brazil (Chapter 7)

C. R. Rodriguez, C. A-L. Jackson, R. E. Bell, A. Rotevatn, M. Francis

To be submitted to Basin Research

The first author analysed and interpreted the 3D seismic and borehole data. The co-authors critically reviewed and discussed interpretations, and contributed to revision of the manuscript prior to submission.

1.5. Contributions to other articles

The author of this thesis contributed as a co-author in other research papers broadly focused on Santos Basin salt tectonics. A list of the papers and a description of the main contributions as a co-author are outlined below. The hardcopies of the papers listed can be found in the Appendix.

Paper 4: Geological and geophysical expression of a primary salt weld: An example from the Santos Basin, Brazil.

C. A-L. Jackson, C. R. Rodriguez, A. Rotevatn, R. E. Bell

Published in 2014 in Interpretation in 2014, Vol: 2, Pages: SM77-SM89

The author of this thesis interpreted seismic reflection data, generated the seismic well-tie and stratigraphic correlation, critically reviewed and discussed interpretations, and contributed to revision of the manuscript prior to submission.

Paper 5: Internal structure, kinematics, and growth of a salt wall: Insights from 3-D seismic data.

C. A-L. Jackson, M.P.A. Jackson, M.R. Hudec, C.R. Rodriguez

Published in 2014 in GEOLOGY, Vol: 42, Pages: 307-310

The author of this thesis interpreted seismic reflection data, generated the seismic well-tie

and stratigraphic correlation, critically reviewed and discussed interpretations, and contributed to revision of the manuscript prior to submission.

Paper 6: Enigmatic structures within salt walls of the Santos Basin—Part 1: Geometry and kinematics from 3D seismic reflection and well data.

C. A-L. Jackson, M.P.A. Jackson, M.R. Hudec, C.R. Rodriguez

Published in 2015 in the Journal of Structural Geology, Vol: 75, Pages: 135-162

The author of this thesis interpreted seismic reflection data, generated the seismic well-tie and stratigraphic correlation, critically reviewed and discussed interpretations, and contributed to revision of the manuscript prior to submission.

Paper 7: Enigmatic structures within salt walls of the Santos Basin—Part 2: Mechanical explanation from physical modeling.

T.P. Dooley, A-L. Jackson, M.P.A. Jackson, M.R. Hudec, C.R. Rodriguez

Published in 2015 the Journal of Structural Geology, Vol: 75, Pages: 163-187

The author of this thesis interpreted seismic reflection data, generated the seismic well-tie and stratigraphic correlation, critically reviewed and discussed interpretations, and contributed to revision of the manuscript prior to submission.

Chapter 2

Research Context

This chapter presents a broad review of salt stratigraphy, salt tectonics and salt dissolution highlighting the key aspects that are essential to provide context for the research that is presented in this thesis. Much of the current knowledge about the deposition and evolution of ancient salt giants comes from observations in sub-aerial salt extrusions, mines, 2D and 3D seismic reflection data and boreholes that penetrate subra-salt and salt-bearing sequences.

2.1. Salt deposition and stratigraphy

This section highlights the key controls on the deposition and stratigraphic variability within ancient salt giants.

2.1.1. What is salt?

Salt is a convenient term referring to evaporite rocks (i.e., gypsum, anhydrite, halite and K-Mg-rich salts). The term salt has been especially used to refer to halite, which is the most common evaporite mineral in salt-dominated basins (Warren, 2006). Evaporites form by precipitation from a saturated surface or near surface brine due to solar evaporation. For an evaporite rock to precipitate, arid conditions are needed and the liquid water loss (outflow) from a brine

mass must exceed inflow (e.g, Usiglio, 1849; Clarke 1924; Warren, 2006). Salt is mechanically unstable and tends to flow like a viscous fluid under gravitational forces when it experiences slopes with ≤0.5° dip due to its low density (2.2 gm/cc) and negligible yield strength (e.g., Warren, 2006; Hudec and Jackson, 2007; Archer et al., 2012; Jackson and Hudec, 2017).

2.1.2. Evaporite crystallization sequence

The stratigraphy heterogeneity within salt sequences is mainly controlled by the solubility of different evaporite minerals, which precipitate following an idealised precipitation sequence. In other words, when seawater evaporates a predictable suite of primary evaporites crystallise (Table 2.1). The crystallisation sequence of evaporite minerals has been predicted, documented and revisited by various researchers (e.g.; Usiglio, 1894; Clarke, 1924; Valyashko, 1956; Richter-Bernburg, 1973; Warren, 2006; Mohriak and Szatmari, 2008; Warren, 2010; Babel and Schreiber, 2014). The suite of evaporites that precipitate from modern seawater is predictable and well understood (Warren, 2010). For the experiments, an increasingly concentrated hypersaline solution of modern seawater is evaporated until total dryness is reached (Table 2.1; e.g. Warren, 2010). Ancient salt basins are assumed to have been formed from the evaporation of concentrated seawater. Modern seawater is composed by Na^+ and Cl^- ions and insignificant amounts of SO_4, Mg, Ca, K, and HCO_3 (e.g.; Baar, 2013, Mohriak and Szatmari, 2008). Therefore, in mesohaline marine brines, when salinities reach 1.5-3 times (60%) its original concentration, carbonates ($CaCO_3$) precipitate removing almost all bicarbonate (HCO_3) (Warren, 2010). In penesaline waters, with salinities of 150% or 5-6 times the original concentration, the excess Ca in the remaining brine combines with Sulphate (SO_4) to precipitate gypsum ($CaSO_4.2H_2O$) (Warren, 2010). By the removal of water, gypsum is then later transformed to anhydrite ($CaSO_4$). The onset of halite (NaCl) precipitation occurs in supersaline marine waters, when salinities reach 350%, 10 to 11 times, the original seawater concentration (Warren, 2010). Due to ongoing increase in salinities up to 60-70 times the

original concentration; brines become dominated by Mg-Cl-SO4, promoting the precipitation of a series of magnesium sulphates/chlorides salts or bitterns (Table 2.1; Warren, 2010). As the MgSO4 bittern salts crystallize K becomes dominant and the KCl bitterns or potash salts precipitate, where carnallite and sylvite are the most common in modern seawater (Warren, 2010). Consequently, the stratigraphy of salt basins comprises varying combinations of alkaline carbonates, gypsum or anhydrite, halite and bittern salts like sylvite, carnallite, polyhalite, and tachyhydrite (e.g.; Warren, 2006; 2010).

Table 2.1: Evaporite crystallisation sequence in increasingly concentrated hypersaline solutions. After Warren (2006) and Warren (2012)

	Brine stage	Mineral precipitate	Salinity (%) (onset of precipitation)	Degree of Evaporation
Hypersaline (>35% salinity)	Mesohaline	Alkaline earth carbonates	> 60%	1.5-3x
	Penesaline	Gypsum/Anhydrite(CaSO4)		
		CaSO4 (+- Halite)	>150%	5-6x
	Supersaline	Halite (NaCl)	>350%	10-11x
		Bittern Salts (K-Mg salts)	Extreme and variable	> 60-70x

2.1.3. Ancient Salt giants: Key controls on its deposition and stratigraphic variability

Salt giants consist of more than one thousand-meter-thick, basinwide, evaporite-dominated stratified successions deposited in a variety of tectonics settings and across a wide range of geological time (Fig. 1; e.g.; Schmalz, 1970; Hsü, 1972; Szatmari et al., 1974; Kendall, 1978; Taylor, 1985; Land et al., 1988; Clark, et al., 1998; Krijgsman et al., 1999; Schreiber and Tabakh, 2000; Glennie et al., 2003; Warren, 2006; Hudec and Jackson, 2007; Mohriak et al., 2009; Warren, 2010; Massoth and Tripp, 2011; Trudgill, 2011; Eoff et al., 2013; Babel and Schreiber, 2014; Jackson and Hudec, 2017). Some of the most extensively studied ancient salt giants include the Jurassic Louann salt in the Gulf of Mexico (e.g.; Jackson and Seni, 1984; Bird et al., 2005; Rowan and Vendeville, 2006), the Messinian salt in the Mediterranean Sea (e.g.; Hsü,

(e.g.; Hsü, 1972; Cartwright et al., 2012), the Permian Zechstein Supergroup in northwest Europe (e.g., Taylor, 1985; Clark, et al., 1998; Stewart and Clark, 1999), the Pennsylvanian Paradox Formation in the Western USA (e.g.; Trudgill, 2011; Eoff et al., 2013), and the evaporite-dominated sequences deposited in the circum-South Atlantic salt basins (e.g; De Freitas, 2006; Gambôa et al., 2008; Mohriak et al., 2009).

Our current knowledge of ancient salt giants is constrained by field data (e.g. Jackson et al., 1990; Reuning et al. 2009; Stefano et al., 2010), seismic reflection data that image intrasalt stratigraphy (e.g. Van Gent et al., 2011; Fiduk and Rowan, 2012; Schoenherr et al. 2007; Strozyk et al., 2012; Jackson and Lewis, 2013; Jackson et al., 2014a,b; 2015b), and boreholes that penetrate salt-bearing sequences (e.g. Clark, et al., 1998; De Freitas, 2006; Massoth and Tripp, 2011; Trudgill, 2011; Eoff et al., 2013; Jackson et al., 2014a,b; 2015). Previous studies listed above suggest that depositional thickness and intrasalt stratigraphy are controlled by several factors that may act individually or collectively during the deposition of salt giants; i.e. (i) climate; (ii) sea-level variations; (iv) duration of salt deposition; (iii) syn-depositional tectonics and basin physiography (v) the distance to the basin sill and the direction of seawater inflow and (vi) the location and volume of freshwater river discharge, which may modify brine salinity.

Nevertheless, considerable controversy still exists regarding the deposition and evolution of ancient salt giants as these typically do not have modern analogues with comparable scale, thickness, tectonics and hydrology (e.g.; Warren, 2006, 2010). For comparison, the largest modern salt basin, Salar de Uyuni covers an area of 10,000 km^2; in contrast, the Mediterranean Messinian salt giant is more than six times larger (area of 67,0000 km^2; Warren, 2006). Furthermore, salt is likely to be altered during and/or after deposition due to burial, dissolution and salt tectonics (see sections 2.2 and 2.3; e.g., Schreiber and Tabakh, 2000; Hudec and Jackson, 2007). Thus, for ancient salt giants, the present is not the key to the past, which difficult the characterisation of its depositional stratigraphy and investigating the

key controls on its deposition (Chapter 5).

Three end-member models for the deposition of ancient salt giants have been proposed by previous studies highlighting the role of basin configuration and water depth. These models apply given special conditions over geological time scale, i.e.: isolation from the open ocean and an arid climate where outflow exceeds inflow (Fig. 2.1.; e.g.; Schmalz, 1969; Hsü, 1972; Taylor, 1985; Warren, 2006; Jackson and Hudec, 2017):

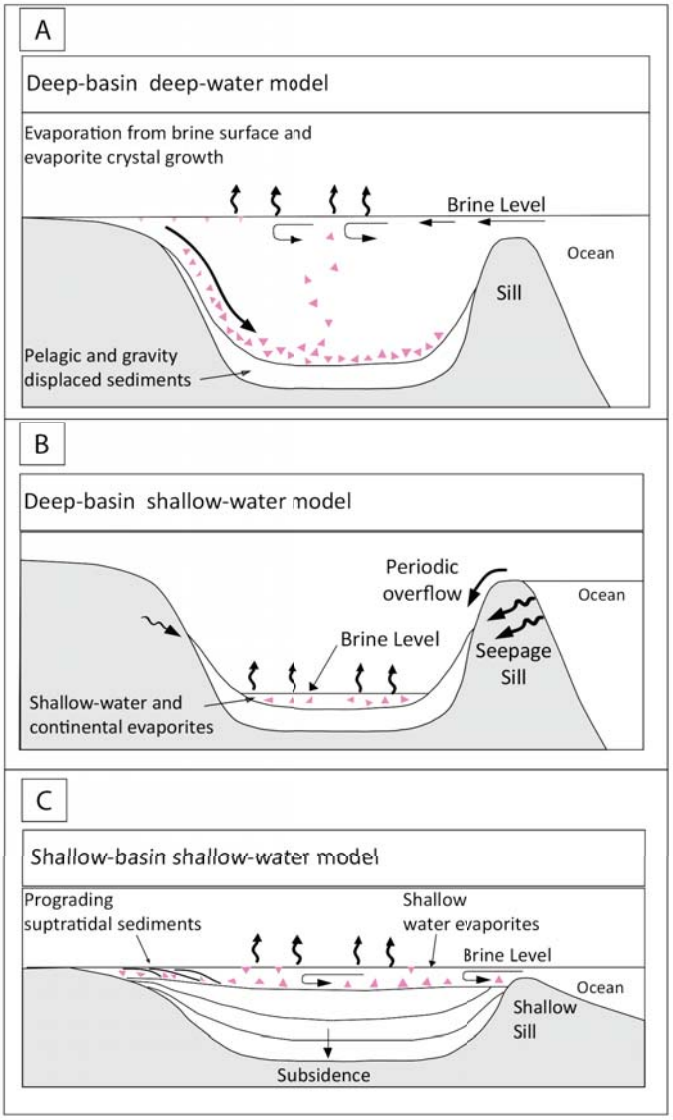


FIGURE 2.1. End-member models for the deposition of ancient salt giants. Modified after Prothero and Schwab (2003) and Warren (2006).

Deep basin and deepwater model

This model assumes an isolated deep basin largely filled with brine and separated from the ocean by a substantial topographic relief (10s-100s m) that prevents free interchange of seawater between the basin and the open ocean (Warren 2006). The brine level is above the sill and thick deposits of certain minerals, such as gypsum, occur due to seaward escape of some brine allowing the specific concentration of brine to be maintained for evaporites to precipitate (Fig. 2.1a; Warren, 2006).

Deep basin-shallow-water model

This model assumes that evaporative drawdown occurs when brine level is reduced below the level of the sill/barrier, hundreds to thousands of meters below sea level (Fig. 2.1b; Warren, 2006). Water interchange with the open ocean occurs by seepage through the sill and/or by periodic overflow of the sill. Thick evaporite basins can also accumulate due to continued subsidence.

Shallow basin-shallow-water model

The shallow-basin shallow-water model assumes that the thick accumulations of evaporites occur in a shallow restricted basin with little topographic relief due to continued subsidence of the basin floor. From shallow bodies of brine or within saline mudflats (Fig. 2.1c; Warren, 2006).

Previous studies thus suggest that the stratigraphic organisation of salt giants is mainly controlled by the solubility of the different evaporite minerals, basin configuration and water depth. This is very well illustrated by Tucker (1991) in his model of a Carbonate-evaporite basin that is subjected to complete drawdown (Fig. 2.2). During the initial stages of partial

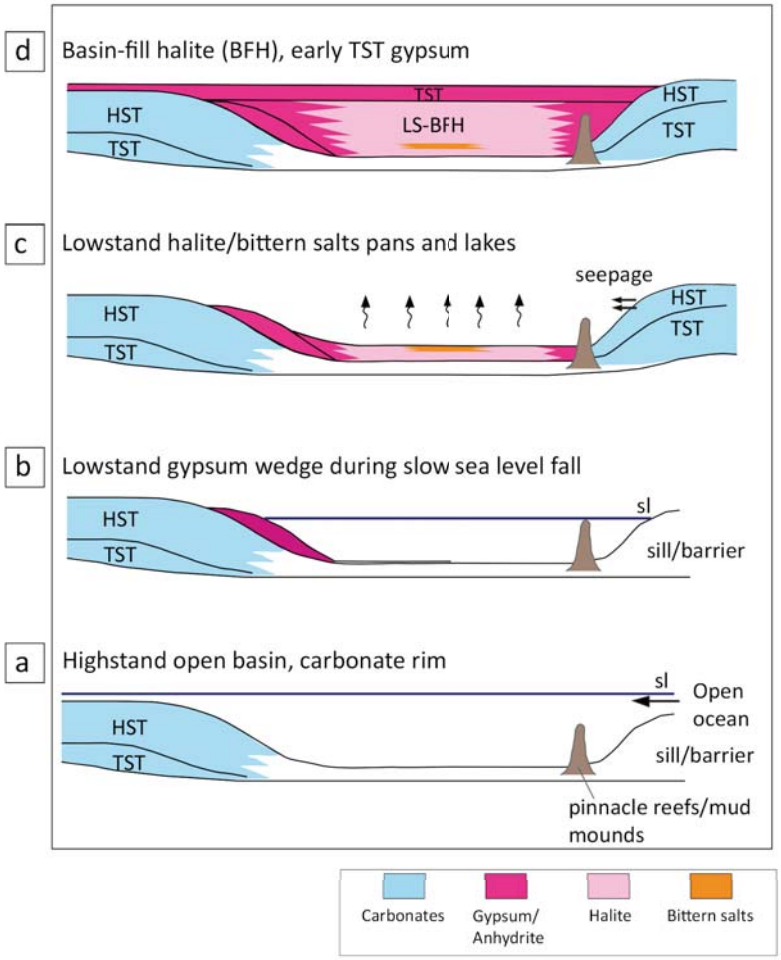


FIGURE 2.2. Carbonate-evaporite basin subjected to complete drawdown. After Tucker (1991). See text for description.

restriction and hydrological drawdown in a carbonate-evaporite basin, carbonate platforms are exposed and gypsum precipitates at the basin margins; if the water level drops below the basin sill, halite and eventually bittern salts may precipitate in salt pans and lakes located in the deepest, most isolated parts of the basin (Fig. 2.2; e.g. Hsü, 1972; Tucker, 1991). Breaching of the sill may recharge the basin with saline fluid and halite may fill the basin removing the original topography (in the absence of any differential subsidence) (Tucker, 1991). A new evaporite cycle starts when the hypersaline basin is reflooded and gypsum is deposited (Fig. 2.2; Tucker, 1991).

Moreover, the total desiccation of a salt basin can occur leading to the sequential deposition of saline minerals forming a bull's eye depositional pattern, if the basin is enclosed; where, carbonates and anhydrites are deposited along the margins of the basin, on slopes, while the more soluble salts, halite and potash salts (K-Mg salts) are deposited in the central parts of the basins or abyssal plains (Fig. 2.3; Schmalz, 1970; Hsü, 1972, Hsü et al., 1973). A teardrop pattern, however can be associated with a restricted basin, where the most soluble salts precipitate far away from the opening of the basin, where the most concentrated brine remains (Fig. 2.3; Hsü 1972).

Nevertheless, the applicability of these models to worldwide ancient salt giants is the subject of controversy, partly due to the lack of modern analogues and considering that salt giants can evolve from one type to the other during the evolution of sedimentary basins (Hsü, 1972; Kendall, 1978; Taylor, 1985; Tucker and Cann, 1986; Schenk et al., 1994; Oard, 2005; Warren, 2010; Jackson and Hudec, 2017). For example, a deep isolated basin can alternate from deepwater to shallow water deposition when the basin is desiccated (Warren, 2006, 2010). Likewise, a deep basin filled with salt will evolve into a shallow-basin-shallow-water

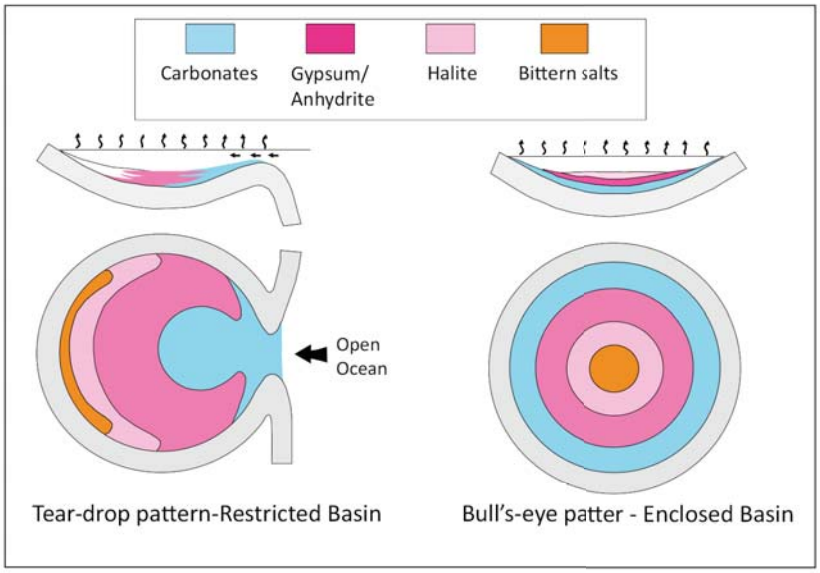


FIGURE 2.3: Patterns of evaporite distribution in desiccating deep basins. Modified from Hsü (1972)

type (Warren, 2006, 2010).

Furthermore, models of ancient salt deposition are generic and oversimplified. Previous studies of worldwide ancient salt giants highlight several other factors controlling salt deposition. For example, deposition of the Paradox Formation (Upper Carboniferous) in North America was primarily controlled by climate and 3rd-order sea-level variations driven by greenhouse (transgressive phases) and icehouse conditions (regressive phases). Thus, deposition of the Paradox Formation highlights the key role of climatic and sea-level variations (Fig. 2.4; Eoff et al., 2013). Transgressive phases were characterised by fully marine conditions and the deposition of organic-rich black shales, whereas regressive phases were characterised by basin desiccation and salt (i.e. anhydrite, halite, bittern salts) deposition. Climate and sea-level variations also influenced the stratigraphy of the Messinian (Upper Miocene) salt in the Mediterranean Sea, where the deposition of gypsum-shale alternations along the basin margins were controlled by periodic changes in salinity due to low-amplitude, high-frequency, 5th-order, precession-driven, climate cycles (e.g.; Krijgsman et al., 1999; Stefano et al., 2010; Manzi et al., 2012).

There is also clear evidence for the impact of syn-depositional tectonics on salt stratigraphy; for example, the foreland basin setting of the Paradox Basin controlled not only bulk thickness but also the distribution of lithologies in the Paradox Formation, with carbonates deposited in the distal forebulge in shallow water depths, whereas halite and other evaporites were deposited in the basin centre during periods of drawdown (Fig. 2.4; e.g., Trudgill, 2011; Eoff et al., 2013). Another example of an ancient salt giant where syn-depositional tectonics controlled stratigraphic variability, is the Zechstein Supergroup in the North Sea. Previous studies suggest that the up to 1.5 km thick, Zechstein Supergroup salt sequence was deposited in a basin that largely formed through post-rift thermal subsidence following a preceding phase of Early Permian extension (e.g.; Tucker, 1991). However, pre-Zechstein faults, inherited from the earlier Permian rift phase or even formed syn-depositionally during Late Permian

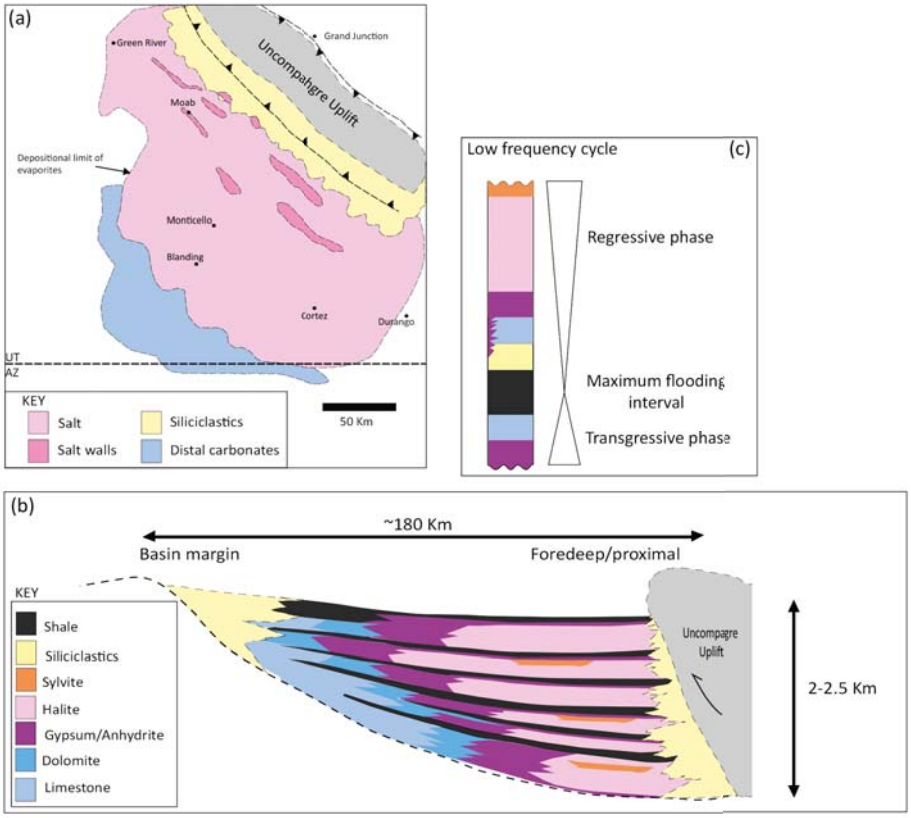


FIGURE 2.4: Example of ancient salt giant: Pennsylvanian Paradox Formation (a) Regional map of the Paradox Basin illustraiting salt distribution. Modified from Trudgill (2011). (b) General cross section through the Paradox Basin, modified from Peterson and Hite (1969), Hite and Buckner (1981), Williams-Stroud (1994); (c) typical evaporite cycle, after Eoff et al., 2012.

rifting, also directly controlled thickness and lithology variations in the salt (Fig. 2.5; e.g.; Clark et al., 1998; Stewart and Clark, 1999; Stewart, 2007; Jackson and Lewis, 2013, 2016). During deposition of the Zechstein salt, periodically submerged intra-basinal highs formed shallow areas where carbonate and anhydrites was deposited (e.g., Taylor, 1990; Tucker, 1991). In deeper waters, an up to 1.5 km thick succession of basin centre facies, comprise mainly of halite, was deposited (e.g.; Clark et al. 1998; Tucker, 1991).

Moreover, ancient sat giants are also characterised by the presence of non-evaporite lithologies (i.e. anoxic shales, marine carbonates, siliciclastics) interfingering and interbedded with the evaporites (e.g.; Warren, 2006; Eoff et al. 2013). The presence of non-evaporite lithologies seem to be the result of a combination of additional elements like syndepositional tectonics,

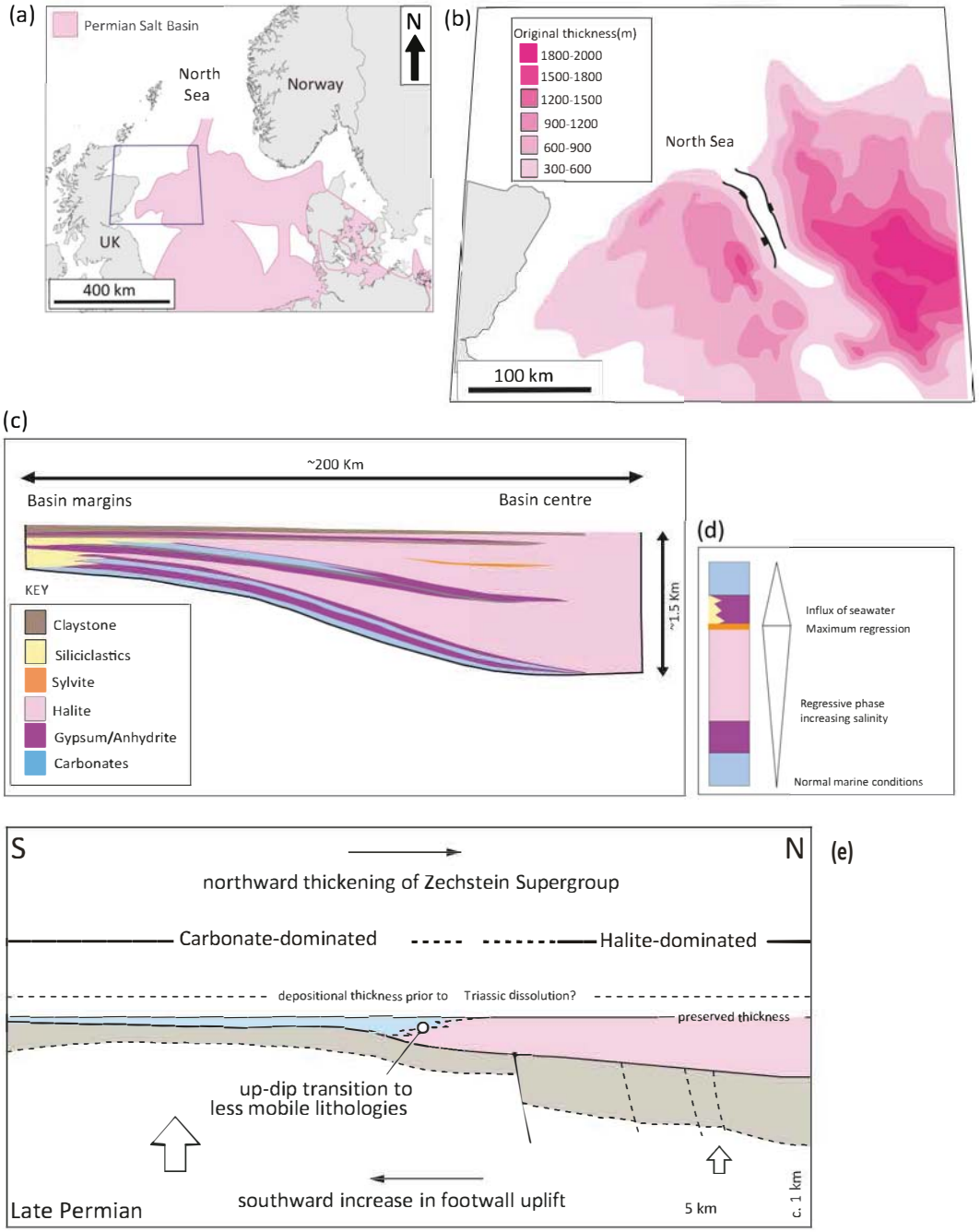


FIGURE 2.5: Example of ancient salt giants, Late Permian Zechstein Supergroup: (a) Location of the Permian salt Basin. (b) Depositional salt thickness distribution of the Zechstein Supergroup. After Glennie et al. (2003). (c)Depositional model of the Zechstein Supergroup, after Clark et al., 1998. (d) Typical evaporite cycle after Taylor (1990); (e) Conceptual model illustrating the Permian tectonostratigraphic evolution of the Stavanger Fault System, after Jackson and Lewis (2013)

marine eustacy and/or river discharge. In particular, during the deposition of the Pennsylvanian Paradox Formation, ongoing syndepositional tectonics (flexural subsidence) triggered the deposition of coarse siliciclastics in peripheral foredeep accommodation sourced by the growing Uncompahgre uplift (Fig. 2.4; e.g. Trudgill, 2011). Similarly, syndepositional tectonics acted as a key controlling factor in the Messinian salt stratigraphy, in the Mediterranean. During deposition of the Messinian salt, ongoing tectonic deformation caused basin margin instability and the erosion of pre-existing salt units that were deposited in distal locations (e.g.; Lugli et al., 2008; Roveri et al., 2008; Stefano et al.; 2010). In addition, river discharge was also an important element promoting reduced salinities during the last phase of Messinian salt and promoting the deposition of alternating evaporites and clastic deposits (e.g.; Lugli et al., 2008; Roveri et al., 2008; Stefano et al.; 2010).

In Chapter 5, I integrate 3D seismic and borehole data to characterise the near-depositional, stratigraphic variability of the Santos Basin salt giant and discuss the likely key controls during its deposition, focusing on the controversies presented in Chapter 3.

2.2. Salt tectonics in passive margins

Salt tectonics is defined as the deformation involving bodies of salt or salt flow (Hudec and Jackson, 2007). In this section, I describe salt-related structural styles, salt-sediment interactions and salt-related trapping styles along passive margins.

2.2.1. Salt and sediment interactions: Key concepts

The geometry of sediments that interact with salt records the history of salt flow during passive margin development (Figs. 2.6, 2.7; e.g.; Rowan and Weimer, 1998; Hudec et al., 2009; Pilcher et al., 2011; Jackson and Hudec, 2017). Lateral **thickness variations** within the overburden can help differentiate areas of **salt inflation**, which feeds the growth of salt structures, compared

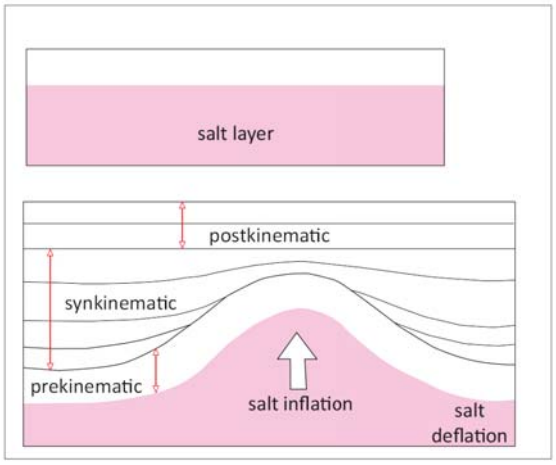


FIGURE 2.6: Overburden strata thickness variations and age relations to underlying salt flow. Modified from Jackson and Hudec (2017).

to, salt deflation, which provides more accommodation for sediment deposition (Fig 2.6; Jackson and Hudec, 2017). The syn-sedimentary depocenters formed above deflated salt and bounded by inflating salt structures are defined as minibasins (Fig. 2.7; e.g., Jackson and Talbot, 1991; Hudec and Jackson, 2007, 2011; Hudec et al., 2009; Pilcher et al., 2011; Goteti et al., 2012). Where salt deflation occurs, if the autochthonous salt is almost or completely removed by salt expulsion or due to dissolution, a primary salt weld is created (Fig. 2.7; e.g.; Jackson et al. 2014 (b); Jackson and Hudec, 2017). Thin overburden can also accumulate above inflating salt structures, thus provides a record of areas where salt rose (Fig. 2.7; Jackson and Hudec, 2017).

The analysis of the thickness and geometry of the stratigraphic units filling the minibasin can, thus, provide insights about sediment interactions with salt flow and its controls on sediment architecture during the evolution of sedimentary basins (e.g., Rowan and Weimer, 1998, Hudec et al., 2009; Pilcher et al., 2011). For example, previous studies of minibasin stratigraphy in the Gulf of Mexico, suggest that the minibasin morphology and the geometry of the stratigraphic units within the minibasins can provide insights into the mechanisms of minibasin subsidence and filling (e.g., Pratson and Ryan, 1994; Rowan and Weimer, 1998; Hudec et al., 2009). For

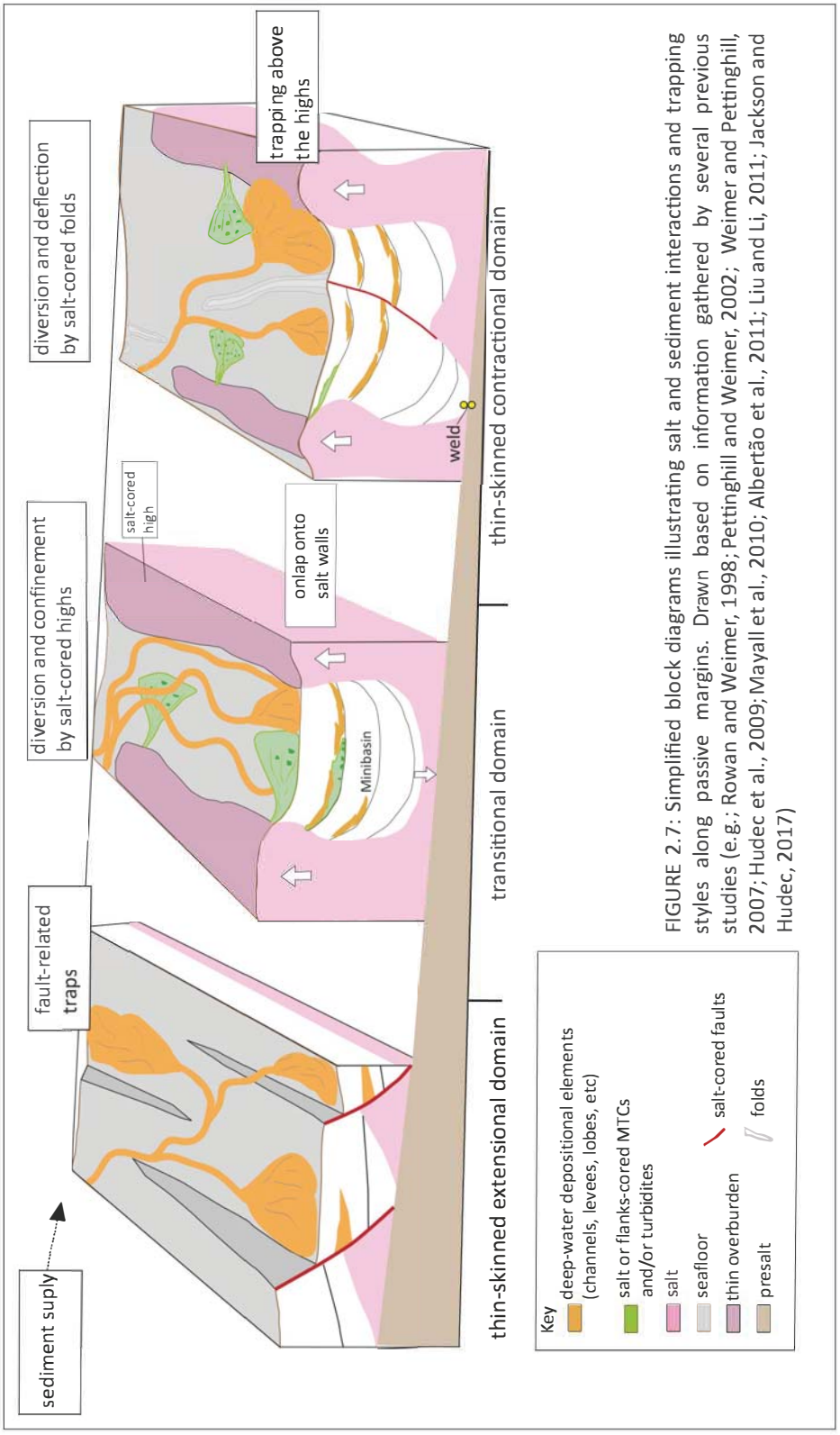


FIGURE 2.7: Simplified block diagrams illustrating salt and sediment interactions and trapping styles along passive margins. Drawn based on information gathered by several previous studies (e.g.; Rowan and Weimer, 1998; Pettinghill and Weimer, 2002; Weimer and Pettinghill, 2007; Hudec et al., 2009; Mayall et al., 2010; Albertão et al., 2011; Liu and Li, 2011; Jackson and Hudec, 2017)

example, intra-minibasin, **bowl-shaped symmetric units** which are thicker in the centre and thinner towards the flanks indicate deposition during **vertical subsidence** onto underlying salt (Fig. 2.7; e.g., Rowan and Weimer, 1998; Hudec et al., 2009). Instead, intra-minibasin, **wedge-shaped units** which thicken asymmetrically towards one side of the minibasin flanks, indicate **preferential salt flow or evacuation** of the underlying salt or **preferential uplift** of the bounding salt structures (Fig. 2.7; e.g., Rowan and Weimer, 1998; Hudec et al., 2009). Hence wedge-shaped units may indicate deposition due to **local welding** of the minibasin floor or **tilting of the minibasin** due to shortening of one of the diapirs bounding the minibasin (Fig. 2.7; e.g., Hudec et al. 2009; Jackson and Hudec, 2017). Welding of the minibasin floor, may also result in inversion of the minibasin stratigraphy and the formation of **turtle anticlines** (e.g.; Jackson and Hudec, 2017). In addition, the **layer-shaped geometry** of units deposited capping minibasins is an indication of **complete salt evacuation** underneath the minibasin floor or welding (e.g.; Rowan and Weimer, 1998).

2.2.2. Salt-related structural styles along passive margins

In salt-dominated passive margins, for example offshore Angola, west Africa, the slope presents a very complex seabed bathymetry resulting in a variety of salt-related structural styles and associated sediment depocenters and trapping styles distributed into domains (Figs 2.7; 2.8). The upslope extensional domain, where thin-skinned extension occurs: salt rollers in the footwalls of listric normal growth faults, triangular-shaped salt walls, salt welds where the salt is thin or absent, turtleback anticlines, and rafts (Figs. 2.7 and 2.8 ; e.g; Demercian et al., 1993; Fort et al., 2004; Mohriak et al., 2012; Rowan et al., 2004). In the central domain, extensional to compressional structures are developed, i.e. salt pillows, salt diapirs, salt welds, salt withdrawal minibasins of varying shapes and sizes and local inversion of post-salt minibasins (Figs. 2.7 and 2.8; e.g; Jackson et al., 2014b; Jackson, 2012; Mohriak et al., 2012). Whereas in the downdip contractional domain, which is a result of thin-skinned shortening,

the salt is relatively thick and characterised by a variety of salt-cored folds and anticlines, asymmetric salt walls, intra-salt thrusts, intra-minibasin thrusts and salt nappes or allocthonous salt tongues (Figs. 2.7 and 2.8; Brun and Fort, 2004; Cobbold and Szatmari, 1991; Demercian et al., 1993; Fiduk and Rowan, 2012; Fort et al., 2004; Adam et al., 2012; Jackson et al., 2014a; Jackson et al., 2015b; Mohriak et al., 2008).

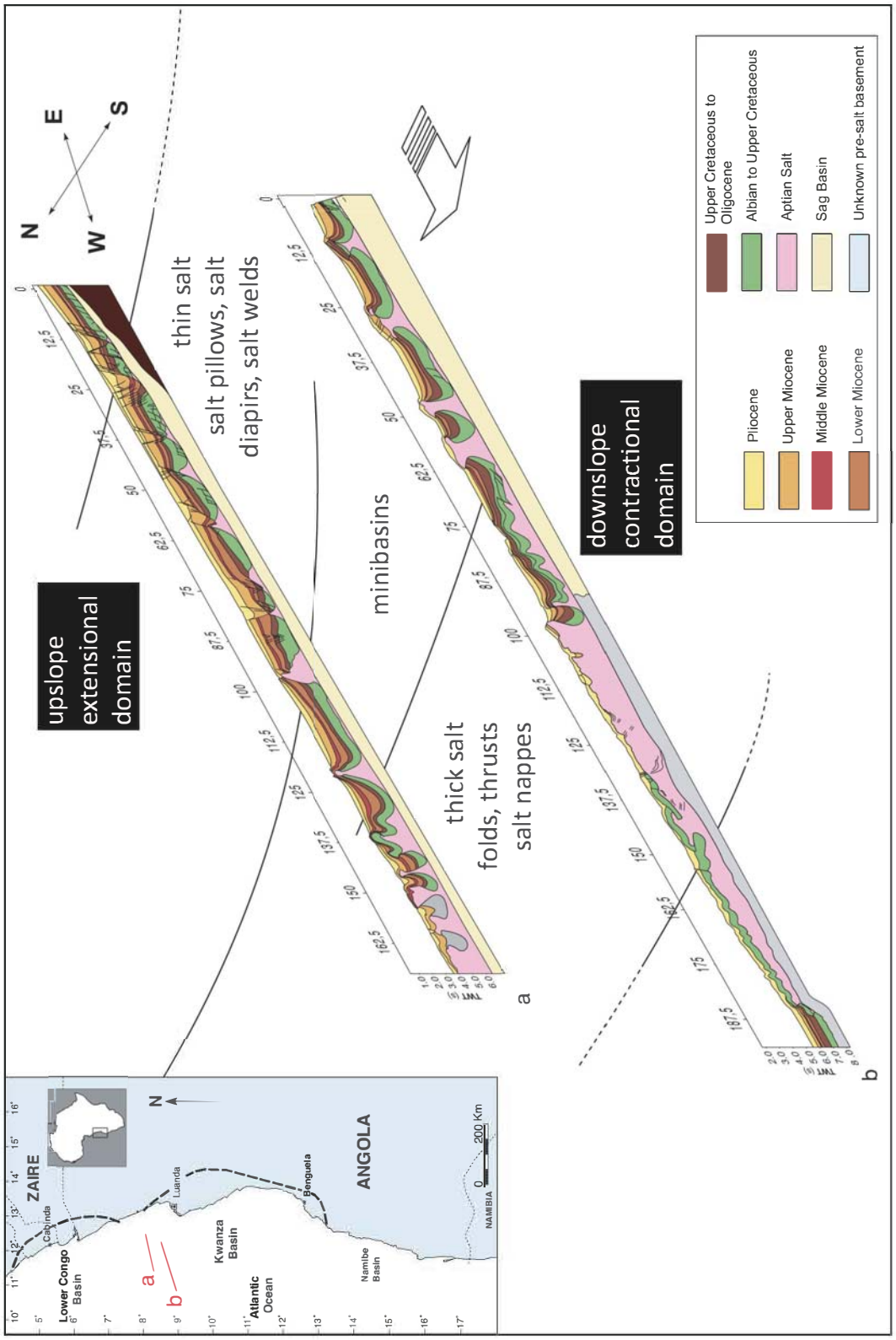


FIGURE 2.8: Salt-related structural styles along the Angola passive margin, offshore West Africa. Modified from Brun and Fort (2004)

2.2.3. Intraslope salt-sediment interactions

During passive margin development, margin tilting, triggered by thermal subsidence and/or continental uplift, drives salt tectonics and controls deep-water sediment dispersal and architecture (Fig. 2.7). Salt-related bathymetric highs along the slope thus can block, confine, divert or deflect deep-water dispersal systems that are flowing downslope synchronous with salt growth (Fig. 2.7; e.g; Clark and Cartwright, 2009, 2011; Gee and Gawthorpe, 2006; Mayall et al., 2010). As channel-levee complexes and their associated downdip lobes approach positive-relief or negative-relief features on the seafloor, transitions in channel geometry and seismic facies generally occur in response to syn-depositional seabed deformation (Fig. 2.7; e.g., Gee and Gawthorpe, 2006, 2007; Clark and Cartwright, 2009, 2011). Continuous salt movement can subsequently uplift and tilt the channels and associated depositional lobes that are closer to the salt-related highs; and sometimes, the erosion of the flows is strong enough that it can incise the growing salt-related highs (Fig. 2.7; e.g; Mayall et al., 2010).

More specifically, upslope, where thin-skinned extension occurs, margin-derived sediment typically is trapped or confined within the hangingwalls of gravity-driven, thin-skinned normal faults (Fig. 2.7 b; e.g. Anderson et al. 2000; Fort et al., 2004; Gee and Gawthorpe, 2006; Alves et al., 2009; Albertão et al., 2011). Basinwards of the extensional domain in the so-called translation domain, where thick autochthonous salt is initially present, minibasins typically form (Fig. 2.7; e.g. Hudec et al., 2009; Jackson et al., 2015a). In the minibasin domain, the relative rates of salt diapir rise and sediment accumulation control the geometry of salt diapirs and associated minibasin subsidence and sediment dispersal (i.e., passive diapirsm; Fig. 2.7; e.g; Giles and Rowan, 2012; Hudec and Jackson, 2007; Hudec et al., 2009). For example, if diapir inflation rate exceeds sediment aggradation rate, diapirs may widen upward and form bathymetric highs that divert or confine deep-water systems that otherwise flow downslope (Fig. 2.7 b; e.g. Gee and Gawthorpe, 2006; Clark and Cartwright, 2009, 2011; Mayall et al., 2010). Deep-water dispersal systems may progressively fill updip intraslope minibasins, before

spilling into neighbouring downdip basins ('fill-and-spill'; e.g. Gulf of Mexico; Winker, 1996; Prather et al., 1998; Smith, 2004). The filling of minibasins and shifting of depocenter can occur due to welding of the minibasin and the eventual inversion of the minibasin stratigraphy, i.e, the formation of turtle structures (e.g.; Jackson and Hudec, 2017). Salt diapir growth relative to slower sediment accumulation can also trigger the emplacement of mass transport complexes (MTCs) within the minibasins (Fig. 2.7); in this case, the MTCs are locally sourced from the unstable salt diapir margins, salt roof and/or the minibasin rotated flanks (e.g; Giles and Rowan, 2012; Jackson, 2012). The emplacement of MTCs, locally sourced or due to more regional shelf-slope failures, is also common on salt-influenced deep-water slopes (Fig. 2.7 b; e.g., Giles and Rowan, 2012; Jackson, 2012). The MTCs can be erosional and overlie intra-minibasin unconformities and tilted and truncated reflections or it can slide with limited erosion of the seafloor (e.g; Giles and Rowan, 2012; Jackson, 2012). A distinct scenario occurs when sediment accumulation outpaces salt diapir rise rate, thus, salt diapirs narrow upward until they get buried (Hudec and Jackson, 2007; Hudec et al., 2009). In this case, the geometry of deep-water dispersal systems may not be greatly affected by coeval salt-related highs. Additionally, in this scenario, local salt and/or flanks sourced MTCs are exceptional due to the overall low relief of the salt-related highs (Giles and Rowan, 2012; Hudec and Jackson, 2007; Hudec et al., 2009). However, if syn-diapiric erosion occurs, reducing sediment accumulation, salt diapirs may pierce the overburden (i.e. active diapirism) and form a slight short-term topographic high on the seabed (Hudec and Jackson, 2007; Koyi, 1998; Mayall et al., 2010). This salt-related topographic high forms a short-term area of bypass or erosion from which local MTCs can also be emplaced (e.g.; Giles and Rowan, 2012; Hearon et al., 2014). Conversely, if the erosion is post-diapiric, possibly due to major geodynamic events, the geometry of salt-related highs and minibasins can also be affected, producing regional erosional unconformities capping salt diapirs and truncating intra-minibasin units (e.g.; Koyi, 1998).

Conversely, where thin-skinned shortening occurs, typically in the downdip contractional

domain or during the latter stages of development of the central, translation domain, diapirs are squeezed and intervening minibasin tilted, causing abrupt shifts in the position of slope depocenters and sediment dispersal pathways (Fig. 2.7; e.g., Hudec et al., 2009). Where thin-skinned shortening is widespread and locally intense, salt-cored folds, anticlines and thrusts develop and are commonly expressed at, and therefore control the local morphology of, the seabed (Fig. 2.7; e.g., Clark and Cartwright, 2009, 2011; Rowan et al., 2004). Salt-cored folds and thrusts expressed at the seabed, thus influence sediment distribution and the geometry of deep-water systems (Fig 2.7; e.g., Brun and Fort, 2004; Hudec et al., 2005; Hudec and Jackson, 2007; Clark and Cartwright, 2009, 2011; Mayall et al., 2010; Jackson et al., 2014; Jackson et al., 2015b).

Understanding the spatial distribution and temporal evolution of deep-water depositional elements relative to the timing and style of salt-induced seabed deformation is key to improving the ability to predict reservoir presence, architecture and potential trapping styles on salt-influenced deep-water slopes. However, seismic reflection-based studies of ancient intra-slope depositional systems that interact with salt are challenging due to the low seismic resolution of deeply-buried depositional elements which limits the level of detail that can be investigated and the poorly imaging of the dipping minibasin flanks which could also be misleading when examining the relative timing of paleoseafloor relief during sedimentation. Most of the current understanding of salt-sediment interactions in deep-water systems thus comes from very shallow, undrilled, relatively young deep-water systems, which are then used as analogues to understand similar salt-sediment interactions in older, more deeply buried systems (e.g.; Beaubouef and Friedmann, 2000; Clark and Cartwright, 2009; 2011).

In Chapter 6, I apply seismic stratigraphy and seismic attribute analysis to characterise the geometry and architecture of Turonian-to-Palaeocene deep-water clastic systems that were deposited on the Santos Basin salt-influenced slope. My results, thus, provides a tectonostratigraphic record of about 60 Ma of salt and sediment interactions.

2.2.4. Salt-related trapping along passive margins

In the previous sections, I reviewed how salt tectonics exerts a direct control in the geometry and architecture of deep-water systems along salt-dominated passive margins. These salt-related controls on deep-water clastic sedimentation also have important implications on trap development (e.g. Fig. 2.9; e.g., Jackson and Hudec, 2017). Trapping of reservoir units near salt structures can occur along minibasin flanks, where sediments onlap the salt structures (Fig. 2.9 a; e.g., Auger and Macaroni fields in the Gulf of Mexico; Booth et al., 2003). Likewise, at the crests of inflating salt pillows or salt diapirs, reservoir-prone units can be trapped by folding or against salt-cored highs and salt-cored faults (Fig. 2.9b; Merluza field, Santos Basin; e.g.; Riddle et al., 1995). Salt-cored fault trapping is also common above salt-pillows in the thin-skinned extensional domain (Fig. 2.9 c; e.g., Campos Basin discoveries such as Marimba, Namorado and Roncador; e.g., Pessoa et al. 1999; Bacoccoli et al., 1979; Bruhn et al., 2003). In addition, trapping of deep-water clastics can also occur within minibasins due to the formation of turtle anticlines where the stratigraphic units become inverted (e.g., east Texas Basin, Wescott and Hood, 1994). Furthermore, intra-salt thrusts and buckle folds which are common in the contractional domain, can also create folding and fault-related trapping in the sedimentary overburden (e.g; Jackson and Hudec, 2017). Combinations of these trapping styles typically exist along salt-influenced passive margins.

In Chapter 6, I use 3D seismic to interpret a variety of salt-related traps within the (previously-overlooked) post-salt sequence in central deep-water Santos Basin (see also section 3.4, Chapter 3).

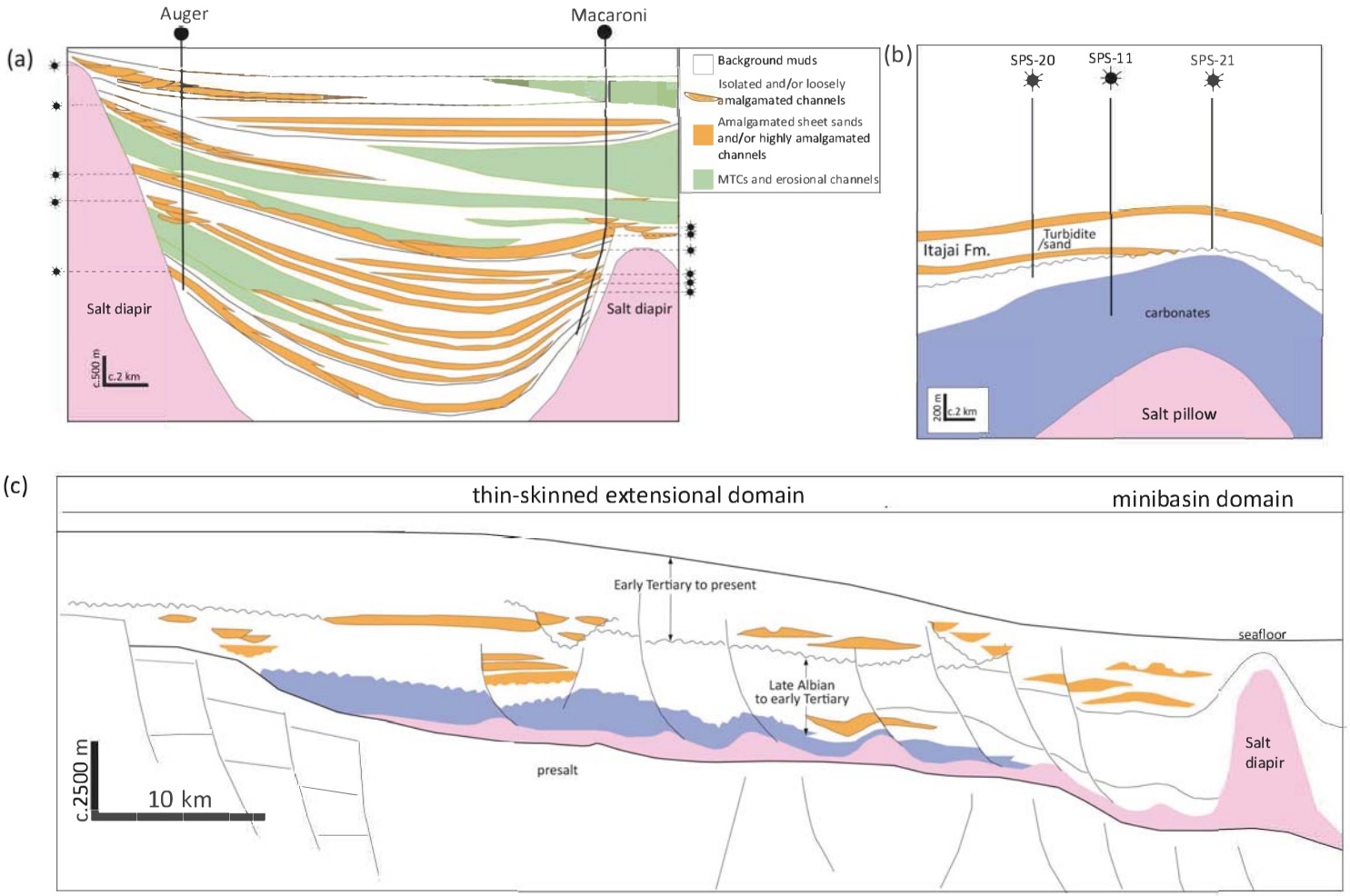


FIGURE 2.9. Examples of trapping along salt-influenced slopes. (a) Onlap trapping within minibasins, Auger and Macaroni fields, Gulf of Mexico. Modified after Booth et al. (2003) (b) Merluza field in the Santos Basin, offshore eastern Brazil, producing from Upper Cretaceous-age sandstone-rich turbidites on a salt-cored high. Modified from Riddle et al. (1995). (c) Examples of post-salt deep-water reservoirs in the Campos Basin, offshore east Brazil. Modified after Bruhn (2003)

2.3. Salt dissolution:

This section explores the significance, current knowledge and outstanding questions about the mechanisms and diagnostics of salt dissolution.

2.3.1. Significance of salt dissolution

Salt dissolution is relevant for the mining and hydrocarbon industry and academic researchers for a variety of reasons:

1. The less-soluble residual evaporite rocks at the crest of dissolved salt structures (i.e, caprock) are the source of economic minerals and have the potential to become reservoir rocks (section 2.3.4; e.g., Posey and Kyle, 1988; Kyle, 1999)
2. Salt dissolution has been related to the creation of local depocenters and faulting within the overburden, potentially promoting reservoir deposition, trapping and compartmentalisation (e.g., Ge and Jackson, 1998; Cartwright et al., 2001; Hudec et al., 2011; Jackson et al., 2010).
3. The collapse and deformation associated with karst can generate mega-pores or reduce the sealing properties of the salt and its overburden, hence its proper characterisation is relevant for evaluating reservoir and seal potential (e.g., Walles, 1993; Vahrenkamp et al., 2004)
4. Accurate seismic imaging requires a proper understanding of the caprock stratigraphy and associated seismic velocities at the crest and lateral margins of salt structures (e.g., Jackson and Lewis, 2012; Jones and Davison, 2014).
5. The amount of salt dissolved from the geological record is often unknown limiting the accuracy in basin restorations and reconstructions (e.g, Koyi et al. 1995; Cartwright et al., 2001).

6. Salt dissolution pose challenges when drilling due to fractures, cavities and diagenetic alterations at the crest and lateral margins of salt structures (eg. Black, 1997; Willson and Fredrich, 2005; Jackson and Hudec, 2017).

However, regardless of its broad significance, surprisingly few studies have used seismic reflection data to investigate salt-related dissolution, characterise seismic-scale karst morphology, and to understand its impact on the overburden and remnant salt (e.g.; Bertoni and Cartwright, 2005; Jackson and Lewis, 2012; Burberry et al., 2016). Seismic-scale salt dissolution studies can be challenging due to seismic imaging issues and the lack of sufficient seismic resolution to precisely analyse salt karst morphologies and deformation within the caprock, overburden and intrasalt units. In addition, there is a limited amount of borehole data to correlate seismic expression to the lithology within caprock and its overburden. Nevertheless, 3D seismic reflection data provide a valuable tool to characterise the expression of salt dissolution compared to 1D- borehole and 2D-seismic reflection data and quasi–three-dimensional outcrops. In Chapter 7 I integrate high quality 3D seismic reflection, 2D seismic and borehole to characterise, for the first time, evidence of salt dissolution in the Santos Basin, offshore Brazil

2.3.2. Solubility of salt

Understanding the solubility of evaporite minerals can provide constrains in the styles and expression of salt dissolution in sedimentary basins (Chapter 7). The most soluble and weaker evaporite minerals are the bittern salts (K and Mg salts, e.g., carnalite, tachyhydrite) followed by halite (NaCl); whereas the less soluble are anhydrite and then gypsum (Warren, 2006). Hence, when evaporites become in contact with NaCl-undersaturated waters, the more-soluble evaporites (bitterns and halite) are dissolved first, resulting in the enrichment of anhydrite, gypsum and carbonate ($CaCO_3$) rocks, which are less soluble than evaporites. The order of solubility is, thus, the reverse to the expected crystallisation sequence of evaporite

minerals (section 2.1.2).

2.3.3. Mechanisms of salt dissolution

The kinematics of salt dissolution are poorly understood, however, there is a general consensus about the three possible mechanisms by which salt structures can get dissolved by NaCl-undersaturated fluids in sedimentary basins (e.g., Warren, 1997; Loucks, 1999; Cartwright et al., 2001; Bertoni and Cartwright. 2005; Warren 2006; Jackson and Lewis, 2012; Burberry et al., 2016):

(1) Superjacent dissolution or epigene mechanisms occur when descending meteoric fluids reach the crest of salt structures or evaporite sequences. Superjacent dissolution has been advocated as the mechanism for the creation of crestal caprock in Zechstein salt structures in the North Sea (e.g., Clark et al. 1998; Cartwright et al., 2001; Jackson et al., 2010) and in salt diapirs in Texas due to exposure at the surface (e.g., Jackson and Seni, 1984, Hudec et al., 2011).

(2) Subjacent dissolution or hypogene mechanism occurs when the salt gets in contact with sub-salt deep basin-related fluids that recharge from below. Subjacent dissolution in the Mediterranean has been attributed to the release of deep overpressure fluids, causing the localised depletion of the overlying evaporite layers (eg., Bertoni and Cartwright, 2005). Subjacent dissolution has also been associated with the migration and expulsion of hydrocarbons (e.g., Machel et al., 2012).

(3) Lateral dissolution occurs when NaCl-undersaturated fluids migrates along the lateral margins of the salt sequence or basin flanks. Migration of deep-basinal fluids up to the lateral margins of a salt diapir has been suggested by Jackson and Lewis (2012) as a possible mechanism for the creation of lateral caprock in the Northern North Sea.

2.3.4. Crestal caprock and solution breccias

Dissolution at the crest of salt structures typically results in the formation of a residual diagenetic caprock (e.g. Posey and Kyle, 1988; Hallager et al., 1990; Warren, 1997; Giles et al., 2012; George et al., 2017; Jackson and Hudec, 2017). Crestal caprocks are commonly formed by superjacent dissolution when salt structures are subaerially exposed and become in contact with meteoric fluids (Warren, 2006). Caprocks that result from halite dissolution typically overlie a nearly-horizontal solution surface or 'table' above which intrasalt stratigraphy is truncated (Posey and Kyle, 1988; Hallager et al., 1990; Warren, 2006; Jackson and Hudec, 2017). The nearly-horizontal surface represents the zone of halite dissolution and contains anhydrite sand and cavities (Fig. 2.10; Posey and Kyle, 1988; Hallager et al., 1990).

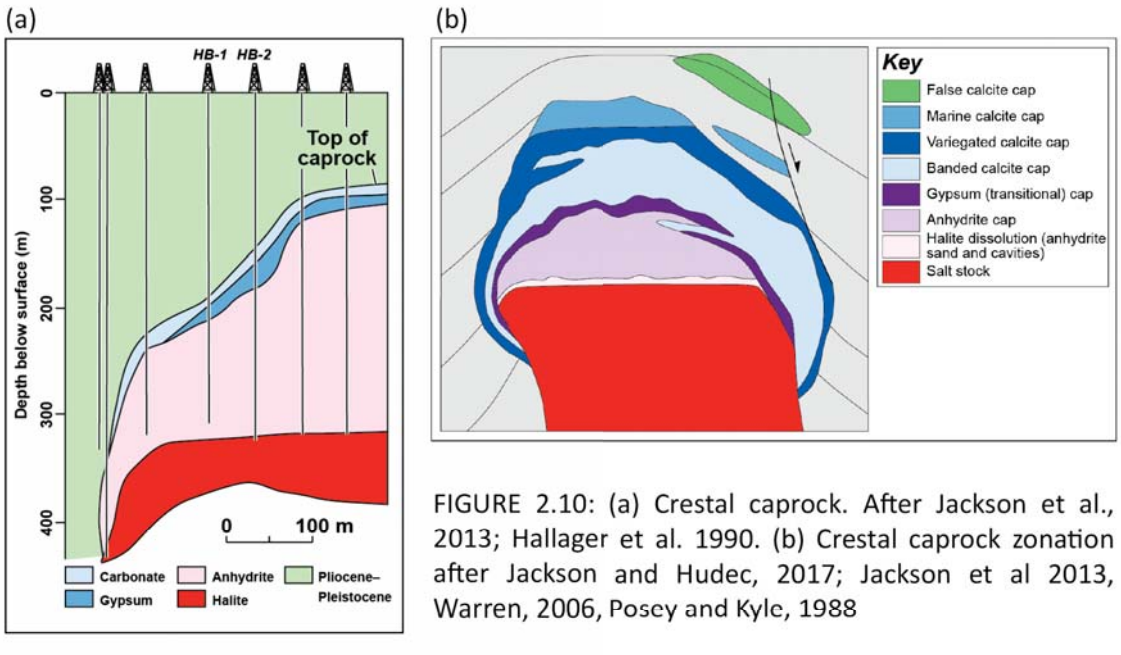


FIGURE 2.10: (a) Crestal caprock. After Jackson et al., 2013; Hallager et al. 1990. (b) Crestal caprock zonation after Jackson and Hudec, 2017; Jackson et al 2013, Warren, 2006, Posey and Kyle, 1988

Caprocks which result from different stages of alteration are highly heterogeneous typically consisting of: (i) a lower anhydrite-dominated zone overlying the halite-dissolution-surface; followed by (ii) a relatively thin gypsum-dominated transitional zone resulting from anhydrite hydration, and an uppermost (iii) highly heterogeneous, relatively thick, carbonate-dominated

cap broadly comprising carbonate clasts, veins, vugs in a fine-grained carbonate matrix (Posey and Kyle, 1988; Jackson and Hudec, 2017). Therefore, the lithological hence acoustic heterogeneity that characterises caprocks difficult the seismic imaging of the crest of salt structures.

Furthermore, the rapid depletion of salt due to widespread and continuous dissolution, creates voids which are consequently filled with clasts of the adjacent or overlying insoluble strata forming a dissolution-related collapse breccia (e.g.; Cooper, 1986; Friedman 1997; Warren, 1997, 2006). Thus, if salt is completely depleted, the downwarping, fracturing and rotation or overlying strata breccia remains as the only evidence of the former evaporites (e.g; Friedman, 1997; Warren, 2006). Solution breccias are a combination of less-soluble and insoluble intrasalt residue and material derived from collapse of the overburden (Laznicka, 1988; Warren, 2006).

2.3.5. Salt dissolution-related local morphologies

Present-day subaerial exposure of salt has also been extensively studied; thus, providing the best documentation of local morphologies likely to result from salt dissolution (i.e, salt karst; e.g., Bruthans et al., 2009; Frumkin, 2013; Gutiérrez and Lizaga, 2016). Remarkable examples of salt karst have been documented in dissolving salt diapirs in the Zagros Mountains in Iran (Fig. 2.11). The exposed salt has recorded the effects of fresh water by forming cm-scale solution grooves (i.e., rillenkarren), m-scale circular depressions (i.e., sinkholes), as well as, up-to-6.5 km-long caves (e.g., Jackson and Hudec, 2017). Furthermore, salt karst morphologies resemble those observed in carbonate karst, which have been imaged by seismic data and extensively studied due to its potential as hydrocarbon reservoirs (Fig. 2.12; e.g. Evans et al., 1994; Vahrenkamp et al., 2004; Sullivan et al. 2006; Zeng et al., 2011; Burberry et al., 2016).



FIGURE 2.11: Collapse sinkhole above a salt dome in the Zagros Mountains, Iran, after Gutierrez and Lizaga (2016)

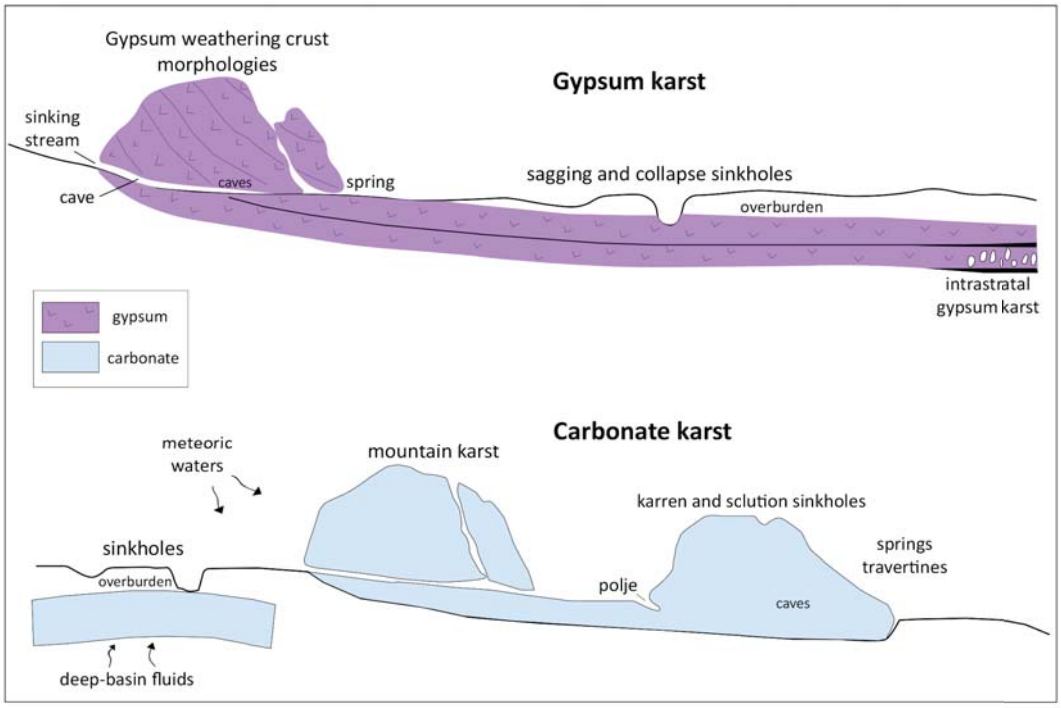


FIGURE 2. 12: Simplified sketch of surface and near-surface karst in gypsum and carbonate settings. Modified from Gutierrez et al. (2014)

2.3.6. Submarine salt dissolution: previous studies

Salt dissolution is not only limited to the near-surface or due to subaerial exposure. Recent studies have described similar rugose morphologies and semicircular depressions related to salt dissolution in submarine settings (e.g., Bertoni and Cartwright, 2005; Talbot and Augustin, 2016). However, seismic-scale submarine salt karst studies are limited. Although potentially dissolved flat-topped and rugose-topped salt walls have been imaged near or at the seabed in the Barents Sea (e.g., Koyi et al. 1995) and in the North Sea (e.g, Duin, 2001), there have been no attempts to document any likelihood of submarine salt karsts morphologies at their crests or to understand if such salt structures have been dissolved by NaCl-undersaturated seawater (except for the recent publication by George et al., 2017). A spectacular example, in the Orca Basin, Gulf of Mexico, reveals a rugose salt canopy exposed at the seabed and potentially being dissolved by seawater (Fig. 2.13; Pilcher and Blumstein, 2007). Dissolution at the crest produce brines that flow downslope into an enclosed submarine brine lake (Fig. 2.13; Shokes et al., 1977; Tompkins and Shephard, 1979; Pilcher and Blumstein, 2007).

In Chapter 7, I demonstrate that salt dissolution at the crest of salt diapirs, in the Santos Basin, occurred in a fully submarine setting (see also section 3.5, Chapter 3).

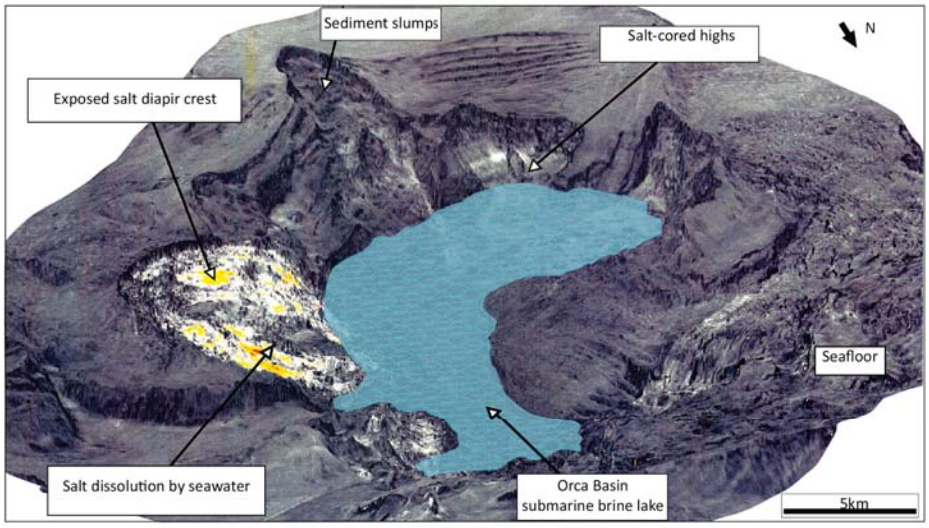


FIGURE 2.13: modern submarine brine lake in the Orca Basin, Gulf of Mexico. After Pilcher and Blumstein (2006).

Chapter 3

Study area:
Santos Basin, offshore eastern Brazil

This Chapter describes the regional context, previous studies and key uncertainties and controversies in the study area.

3.1. Regional context

The Santos Basin is the widest (c. 500 km) of the South Atlantic salt basins with an area of 350,000 km2 (Fig. 3.1; e.g. Davison et al., 2012; Guerra & Underhill, 2012), and is bounded to the west by the Brazilian mainland, and to the north by the Cabo Frio High and the Campos Basin (Fig. 3.2). To the south, the basin is bounded by the Florianopolis High, and the volcanic belt north of the Florianopolis Fracture Zone and the São Paulo Ridge, and to the east by the Jean Charcot volcanic seamounts (Fig. 3.2). The São Paulo Plateau is the main structural element in the Santos Basin, forming a c. 500 km wide area that is characterised by relatively deep water (2000-3000 m) and the presence of a prominent intra-basinal structural high, the Outer High (Fig. 3.2) (Gomes et al., 2002; Gomes et al., 2009). The Outer High is characterised by half-grabens developed during Barremian rifting, when non-marine to shallow marine sediments of the Guaratiba Group were deposited (Demercian, 1996; Meisling et al., 2001; Gomes et al., 2002; Moreira et al., 2007; Carminatti et al., 2009; Gomes, et al., 2009; Scotchman, et al.,

2010) (Fig. 3.3). Episodic marine incursions and basin desiccation events led to the deposition of an up to 2.5 km of Aptian salt (called the Ariri Formation in the Santos Basin; Modica and Brush, 2004; Moreira, 2007). The salt was deposited on extended continental crust at the base of a 1500 km-long, N-trending rift-related valley located between the eastern Brazilian and West African conjugate margins, north of a volcanic belt represented by the proto-Rio Grande Rise and the Walvis and São Paulo ridges (Gladczenko et al., 1997; Fig. 3.4). These volcanic features acted as oceanographic sills, impeding influx of saline marine waters into the developing Santos Basin, facilitating evaporation and salt deposition (Fig. 3.4; e.g. Szatmari 2000; Dias 2004; Davison 2007; Karner and Gambôa, 2007; Carminatti et al., 2009; Davison et al., 2012). During the Aptian, the proto-South Atlantic rift-related valley was up to 500 km wide in the Santos Basin, narrowing northward to <50 km in the Sergipe-Alagoas Basin (Fig. 3.2; e.g. Jackson et al., 2000; Szatmari, 2000; Dias, 2004).

During the Albian, a shallow-marine carbonate platform was established near the basin margin, with deep-water marls deposited basinward in deeper waters (Itanhaem Formation; Figs. 3.3; e.g., Modica and Brush, 2004). Salt-related deformation commenced in the Albian, with margin tilting and the downslope flow of salt causing stretching and faulting of the carbonate platform, and the development of normal fault-bound rafts in the upslope extensional domain (Fig. 3.5; e.g.; Guerra and Underhill, 2012; Davison et al., 2012; Jackson, 2012).

In the Late Cretaceous, periodic uplift and erosion of the onshore Serra do mar mountain belt drove progradation of a thick clastic wedge into the Santos Basin (Itajai-Acu Formation; Fig. 3.3 and 3.5; e.g., Modica and Brush, 2004; Moreira et al., 2007; Guerra and Underhill, 2012). Late Campanian-Maastrichtian uplift of the Serra do Mar deflected the Paraiba do Sul river drainage system to the NE, starving the central deep-water Santos Basin of sediment (e.g.; Cobbold et al., 2001; Modica and Brush, 2004; Guerra and Underhill, 2012). Subsequently, during the Eocene, sediment supply to the basin was thus largely derived from catastrophic failure of the middle Eocene shelf margin, which produced debris flows and turbidites of the

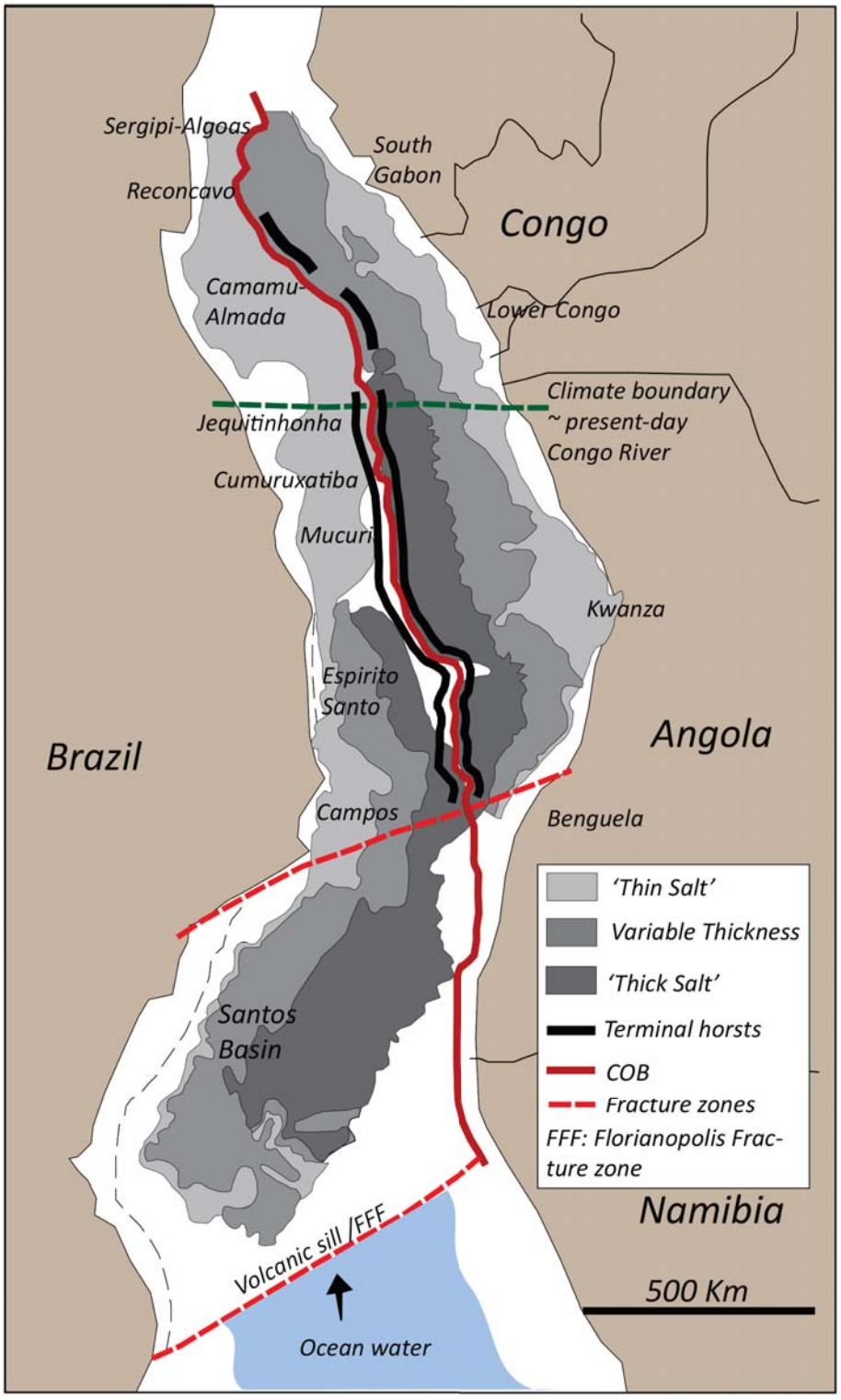


FIGURE 3.1. Early Cretaceous paleogeography illustrating the South Atlantic salt giant and the location of the Santos Basin (after Lentini et al., 2012)

Lower Marambaia Formation that were locally trapped in the proximal domain (Modica and Brush, 2004). Previous studies also suggest the upper Marambaia Formation varies little in thickness and is dominated by fine-grained sediments, recording a global marine flooding event and sea level highstand (e.g.; Modica and Brush, 2004; Moreira et al., 2007; Guerra and Underhill, 2012).

3.2. South Atlantic salt deposition: Key controversies

The Aptian-age salt giant deposited during opening of the South Atlantic Ocean covered c. 741,000 km2 and was up to 2.5 km thick (Fig. 3.1; e.g. Dias 2004; Davison 2007). Although the tectonics and geodynamics of South Atlantic opening have been extensively studied, several key questions remain regarding deposition of the Aptian salt giant, including: (i) how rapidly was the thick (2.5 km) salt deposited?; (ii) what mechanism or mechanisms generated accommodation for thick salt deposition, thus in what tectonic context was the salt deposited?; (iii) was the salt deposited in shallow or deep water?; and (iv) was the seawater inflow into the Santos Basin from the north or south? Chapter 5 addresses these questions by the analysis of the intrasalt stratigraphy in the Santos Basin, offshore Brazil.

The age of the South Atlantic salt giant is poorly constrained, previous studies suggest a depositional age of between 0.4 and 10 Ma (Jackson et al. 2000; Szatmari, 2000; Dias, 2004; De Freitas, 2006; Davison, 2007; Karner and Gambôa, 2007; Moreira et al., 2007; Montaron and Tapponier, 2010). However, most authors agree on a rapid deposition period (< 600 kyr) based on analysis of core data (Dias, 2004), correlation of evaporite stratigraphy with Milankovitch cycles (De Freitas, 2006), and by comparison to other salt basins (Davison, 2007) and the predictions of numerical models (Montaron and Tapponier, 2012).

In terms of accommodation for thick salt deposition, three main mechanisms have been proposed: (i) salt deposition occurred within a pre-existing basin during tectonically quiescent

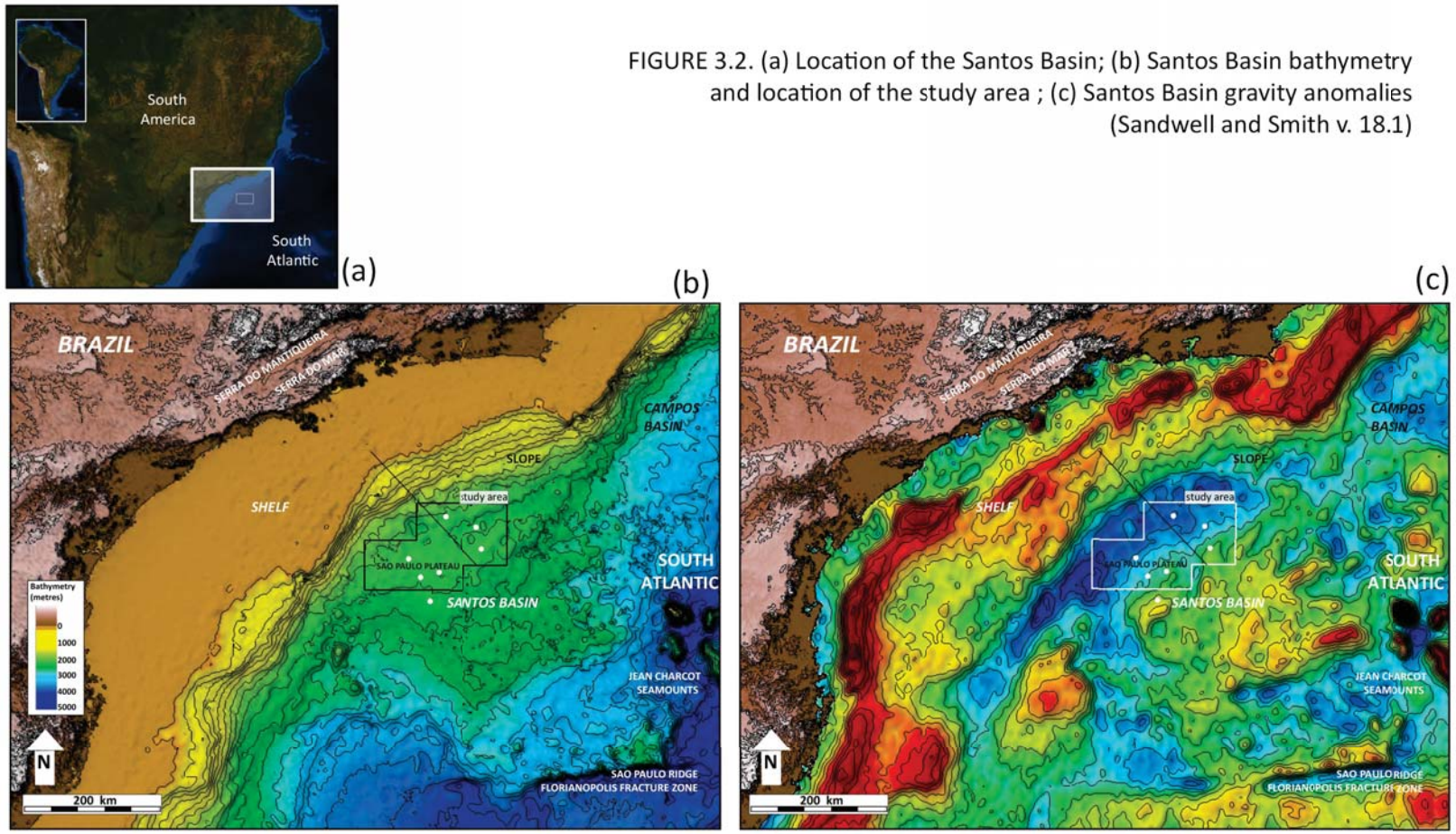


FIGURE 3.2. (a) Location of the Santos Basin; (b) Santos Basin bathymetry and location of the study area ; (c) Santos Basin gravity anomalies (Sandwell and Smith v. 18.1)

conditions (Szatmari, 2000; Burke et al., 2003; Dias, 2004; Davison, 2007; Davison et al., 2012); (ii) salt deposition occurred during rifting (i.e. it is a syn-rift deposit), prior to the onset of post-rift thermal subsidence (Karner et al., 2003; Karner and Gambôa, 2007; Gambôa et al., 2008; Torsvik et al., 2009; Scotchman et al., 2010) and; (iii) loading of the crust by thick salt drove local subsidence and led to the development of accommodation (e.g.; Dias, 2004; Karner and Gambôa, 2007; Davison et al., 2012). The first mechanism suggests that rift-related faulting had ceased at the onset of salt deposition, with deformation giving rise to a pre-existing basin defined by several discrete lakes and which lay up to 2 km below sea-level (Szatmari, 2000; Burke, 2003). The lakes were flanked by pre-existing, normal fault-related scarps that controlled salt thickness across the basin, with thicker (<2 km) salt within the lows and with thinner (<1 km) salt over the highs (Dias, 2004; Davison, 2007; Davison et al., 2012). In contrast, studies favouring a syn-rift salt interpretation postulate that salt deposition occurred during the latest phase of rifting, characterised by minor late Aptian normal faulting and thermal subsidence (Karner et al., 2003; Karner and Gambôa, 2007; Torsvik et al., 2009; Reston, 2010; Scotchman, 2010). In addition, local faulting during salt deposition was possibly due to salt loading, which may have increased accommodation (Dias, 2004; Karner and Gambôa, 2007; Davison et al., 2012).

Despite the controversies regarding the Aptian salt giant, there is a general consensus with regards to the water depth within which the salt was deposited. Except for Karner and Gambôa (2007) and Montaron and Tapponier (2010), who suggest salt deposition in relatively deep waters (1.5-3 km), many other authors support a shallow-water (< 1 km) depositional environment based on the following evidence: (i) the stratigraphic context of the salt, above continental/lacustrine deposits and below shallow-water limestones (e.g, Szatmari, 1979; Moreira et al., 2007; Palagi, 2008); (ii) sedimentological features (chevron and cornet halite crystals) identified in cores in the Espirito Santo Basin, indicating that evaporite precipitation occurred in 'very shallow waters' (Dias, 2004); (iii) subaerial exposure and karstification of the pre-salt sag sequence (Gomes et al., 2009); and (iv) palaeontological evidence from the base

of Aptian carbonates capping the salt on the Angolan margin, suggesting water depths of <500 m (Marton et al., 2000).

Therefore, within this deep-basin/shallow-water depositional context (section 2.1.3, Chapter 2), the proto-South Atlantic was occupied by lakes of varying salinity and, as salinity increased, these lakes were replaced by hypersaline lagoons (e.g., Szatmari et al., 1979; Burke et al. 2003; Aslanian et al., 2009). The transition from a lacustrine to a lagoonal depositional environment, conducive to salt deposition, was the result of partial filling of isolated basins by saline waters, as the basin became connected to the open ocean during rifting, becoming entirely evaporitic by the Late Aptian (e.g., Bate 1999; Dingle 1999; Karner & Gambôa 2007; Reston 2010).

Most studies suggest that the connection to the open ocean and recurrent seawater inflow was from the south, where a barrier comprised by the Rio Grande Rise, Walvis/São Paulo Ridges confined the evolving South Atlantic, thus providing the condition necessary to permit salt deposition and preservation (Figs. 3.1; 3.5; e.g.; Evans, 1978; Jackson et al., 2000; Karner and Gambôa, 2007; Gambôa et al., 2008; Davison et al., 2012). These volcanic ridges formed during Paraná -related volcanism in the Barremian, shortly before salt deposition, and are believed to have collectively acted as a barrier to ocean water circulation before open marine conditions were established in the Albian (Evans, 1978; Karner and Gambôa, 2007; Gambôa et al., 2008; Davison et al., 2012). However, a somewhat more controversial model suggests intermittent seawater incursions flooded from the north via a series of early rifts or seaways formed in the central Atlantic (Dingle, 1999; Bate, 1999; Scotchman et al., 2006; Arai, 2014). For example, according to Scotchman et al. (2006), analysis of ostracod data suggests that the volcanic Walvis Ridge was not breached until Cenomanian-Turonian times, hence preventing marine waters entering during the estimated period of salt deposition. An alternative entry point for seawater is thus postulated suggesting seawater percolation through fracture zones in the volcanic ridges to the south, thus recharging the salt basin (Jackson et al., 2000; Nunn and Harris, 2007; Montaron and Taponier, 2012).

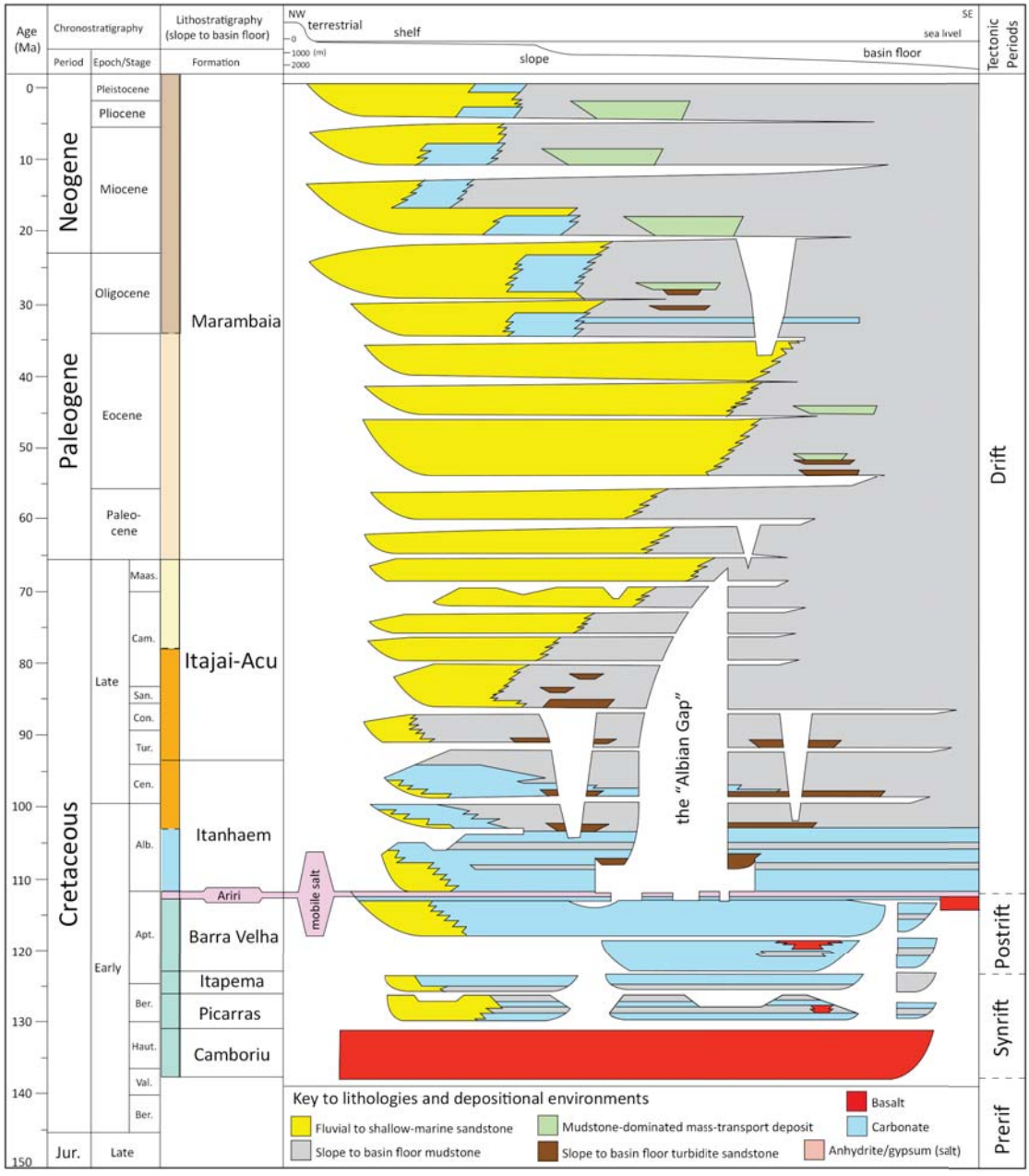


FIGURE 3.3. (a) Stratigraphic column for the Santos Basin, after Modica and Brush (2004), Duarte and Viana (2007), Moreira et al. (2007), and Jackson (2012).

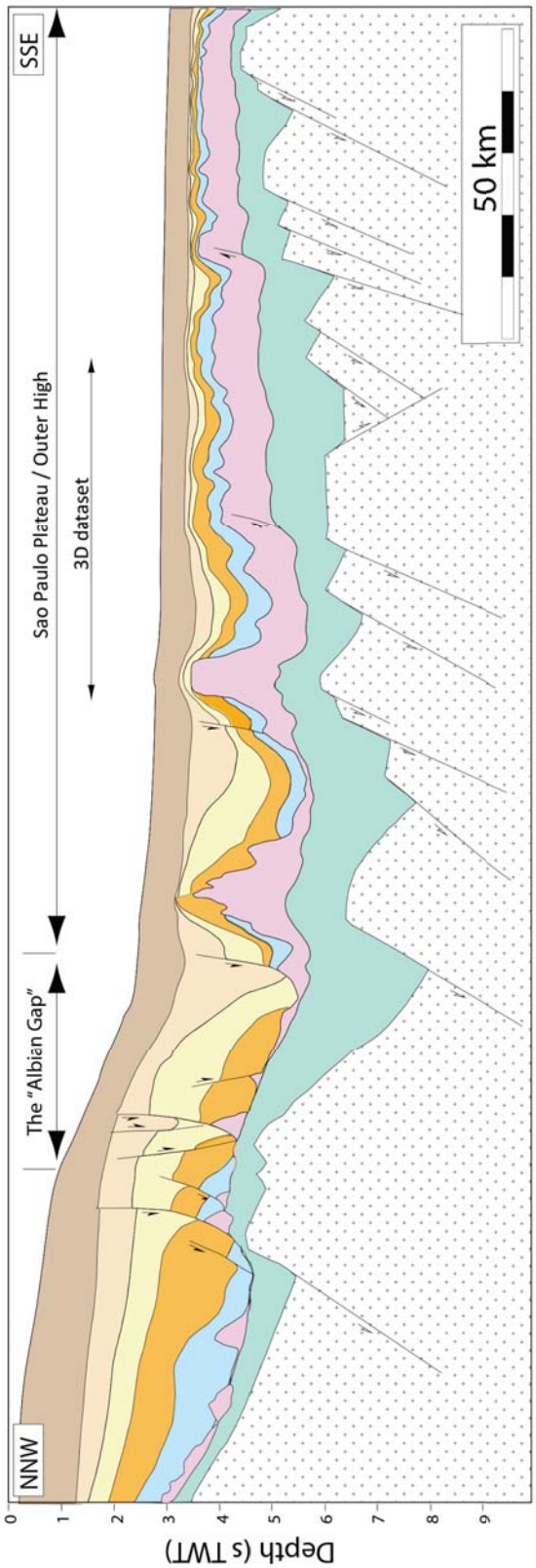


FIGURE 3.3. (b) Cross-section across the Santos Basin, after Modica and Brush (2004), and Jackson (2012). Location is shown in Figure 3.2.

3.3. Stratigraphy of the Ariri Formation: Previous studies and unanswered questions

The Ariri Fm. has been studied in the past, with the principal emphasis being on salt-related structural styles and its impact on hydrocarbon exploration (Cobbold and Szatmari, 1991; Demercian et al., 1993; Cobbold et al., 1995; Mohriak et al., 1995; Demercian, 1996; Szatmari et al., 1996; Ge et al., 1997; Modica and Brush, 2004; Freitas, 2006; Davison, 2007; Davison et al., 2012; Fiduk and Rowan, 2012; Jackson et al., 2014; 2015). Seismic and borehole data from the São Paulo Plateau, which is the major structural element in the Santos Basin, indicate that the Ariri Formation is characterised by highly-reflective, multi-layered evaporites. The unusual seismic character of the Ariri Formation was first recognized on 2D seismic reflection data by Cobbold et al. (1995) and was assumed to be composed of interbedded halite, anhydrite and clastics (Davison, 2007). An exploration borehole drilled in 2002 revealed the Ariri Formation was composed of at least 2.5 km of interbedded evaporites, including halite, anhydrite and bittern salts (e.g. carnallite, bishofite, sylvite and tachyhydrite; Poiate et al., 2006; Scotchman et al., 2010; Mohriak et al., 2012).

De Freitas (2006) correlation of two boreholes separated >200 km apart indicate that halite and bittern salt layers thicken basinwards, whereas interbedded anhydrite layers thicken landwards (Fig. 3.6). De Freitas (2006) suggests this pattern reflects overall lower salinities near the land due to the periodic input of freshwater. Lateral variations in lithology in the Ariri Formation have also been described by Moreira et al. (2007) and Gambôa et al. (2008), with halite, anhydrite, tachyhydrite, carnallite and locally silvite in the basin centre, thinning and passing into main dolomite and anhydrite in the basin margins.

In addition, seismic facies analysis of high-quality seismic reflection data covering the São Paulo Plateau also allowed Gamboa et al. (2008) to divide the Ariri Formation into five units; (i) a 20 m thick basal anhydrite layer; (ii) a ‘thick’ lower halite; (iii) a stratified interval composed

of anhydrite, halite and bittern salt (carnallite, tachyhydrite and sylvite) layers; (iv) a 'thin', halite-rich interval; and (v) an upper interval of interbedded anhydrite, halite and bittern salts. Using 3D seismic reflection data, Fiduk & Rowan (2012) divide the Ariri Formation into six mechano-stratigraphic intervals based on the inferred rheological behaviour of the evaporites, i.e. ductile detachment zones (D3, D2 and D1), defined by acoustically transparent, poorly continuous reflections, and more competent layers or 'beams' (B3, B2 and B1), defined by high-amplitude, continuous reflections. Variability in the proposed units may be related to lateral variations in stratigraphy and/or location within the study area.

Even though the detailed stratigraphic architecture of the Ariri Formation remains very poorly constrained, previous regional studies in the South Atlantic, based largely on 2D seismic reflection data and sparse or no borehole data, suggest that a >2 km thick, halite-dominated succession was deposited in the rapidly subsiding basin centre, whereas thinner (c. 200 m) carbonate-, anhydrite-, sylvite- and tachydydrite-bearing successions were deposited on highs along the basin margins (e.g., Chang et al. 1992; Karner & Gambôa, 2007; Lentini et al., 2010).

It is clear that, due to a lack of focus on the salt as a depositional entity and the unavailability of borehole data, previous studies have been unable to constrain the regional compositional variations or the overall stratigraphic architecture of the Ariri Formation. Furthermore, due to the lack of previous studies, it is still uncertain how the syn-depositional tectonics or variations in climate and water depth controlled salt deposition. It is this what forms part of the focus of Chapter 5.

3.4. Post-salt sequence in the Santos Basin: is there any overlooked hydrocarbon exploration potential?

Significant post-salt hydrocarbon discoveries have been made within deep water (up to 3000

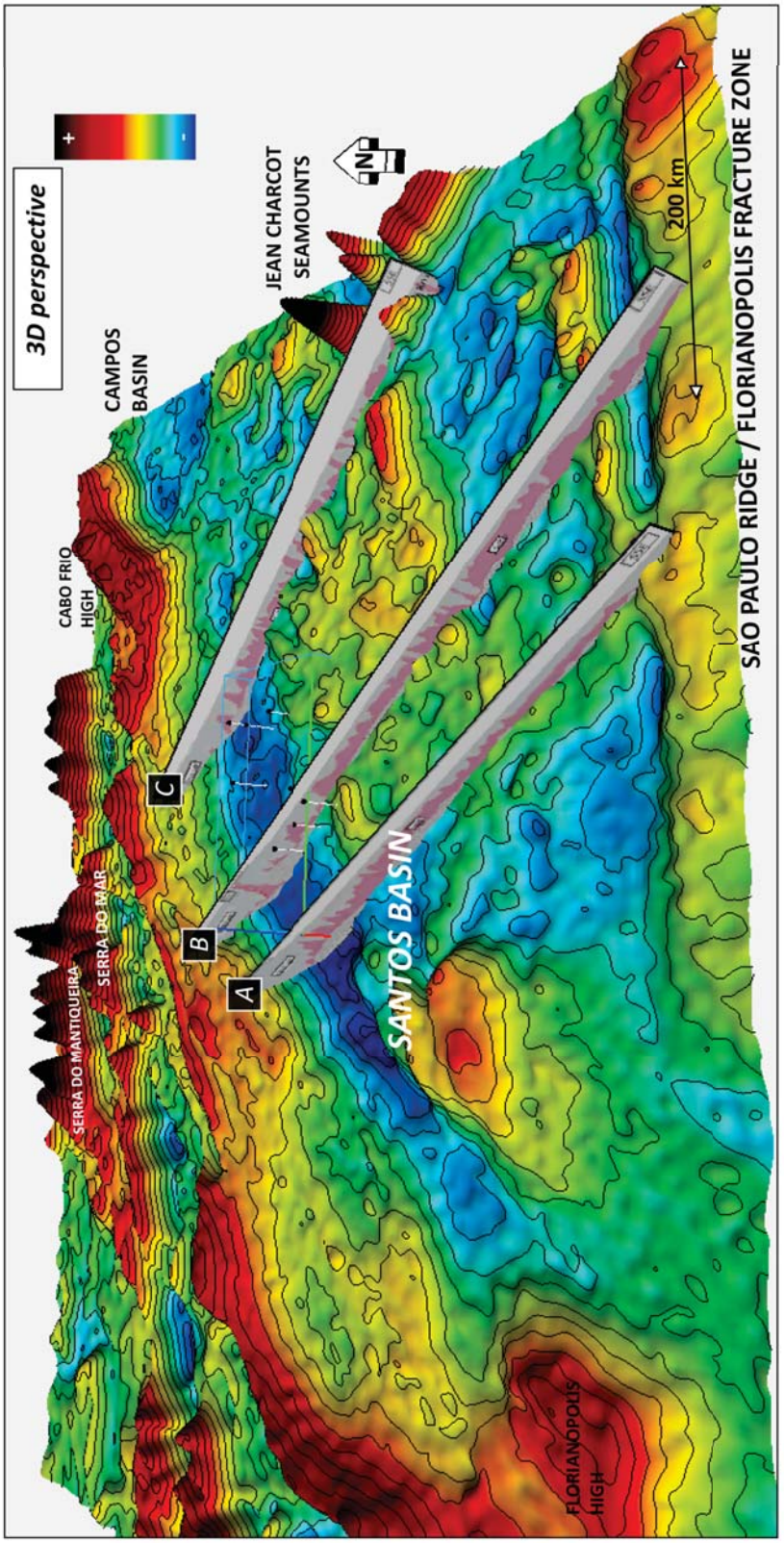


FIGURE 3.4. Gravity anomalies by Sandwell and Smith v. 18.1 scaled to depth of basement showing the limits of the Santos Basin. Basinwide geoseismic sections illustrating salt thickness variations are after Davison et al., 2012 (see Figure 3.5 for vertical scale)

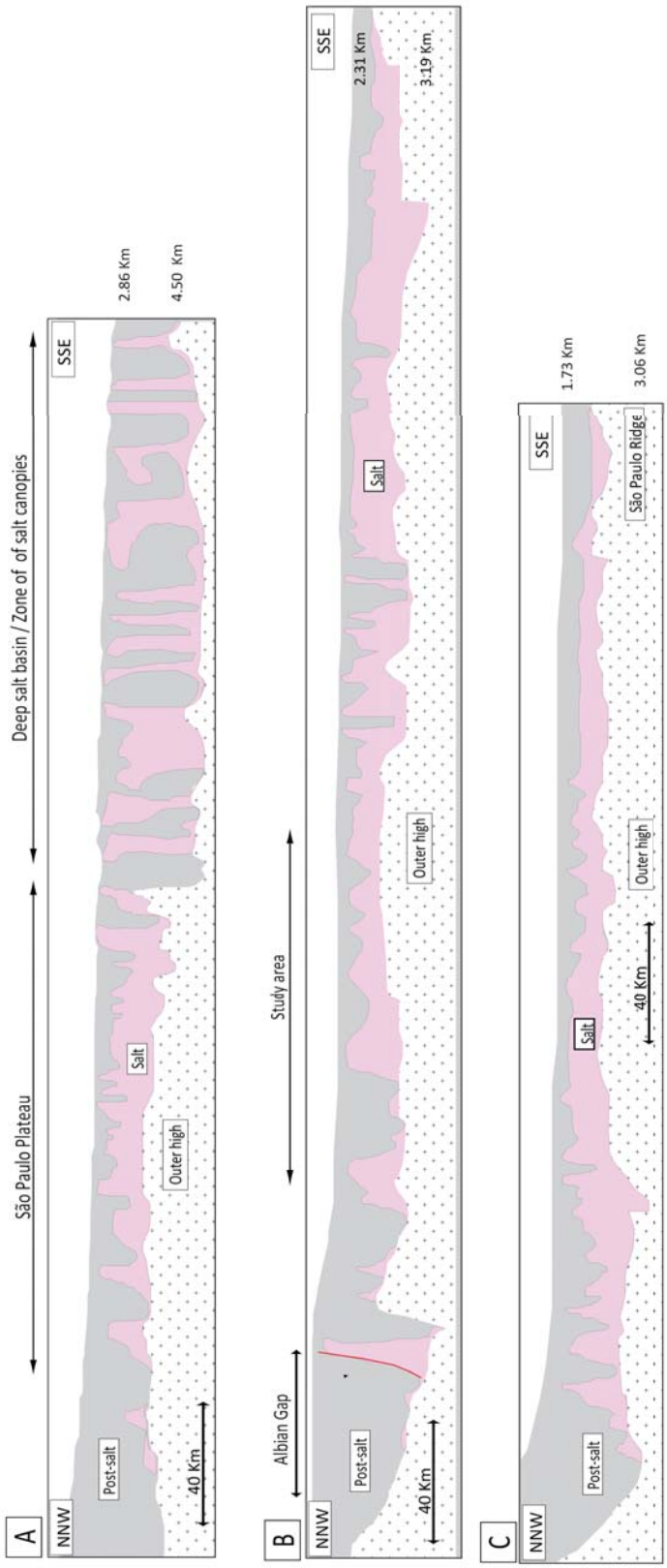


FIGURE 3.5. Basinwide geoseismic sections. After Davison et al. (2012)

m water depth) Brazilian offshore basins (Fig. 3.1). For example, in the Campos Basin alone, >30 deep-water fields produce from, Late Cretaceous, Palaeocene, Eocene, Oligocene and Miocene turbidite reservoirs, with a small contribution coming from locally developed MTCs (Horschutz et al., 1978; Bacoccoli et al., 1979; Bacoccoli et al., 1980; Figueiredo et al., 1985; Guardado et al., 1989; Moraes, 1989; Mohriak et al., 1990; Candido and Cora, 1992; Bruhn and Walker, 1995; Lopes et al., 1999; Guardado et al., 2000; Meisling et al., 2001; Bruhn et al., 2003; Machado et al., 2004; Moraes et al., 2004; Winter et al., 2007; Waisman, 2008; De Gasperi and Catuneanu, 2014). Unlike the Gulf of Mexico, where significant discoveries have been made within minibasins and fold-belt plays, post-salt discoveries in the Campos Basin are mainly located within the thin-skinned extensional domain, up to 150 km downdip from the present Brazilian coastline (section 2.2, Chapter 2). Discoveries in the Campos Basin are mainly in unconfined deep-water channels and lobes occurring in stratigraphic traps, or more confined channels and lobes occurring in structural traps related to salt-cored thin-skinned faults (e.g., Bruhn et al., 2003; Albertao, 2011). For example, in the giant oilfield of Albaroca, Barracuda, Caratinga and Marlim, stratigraphic trapping occurs due to lateral pinchout and differential compaction of turbidite sandstones (e.g., Figueiredo et al., 1985; Pessoa et al., 1999; Guardado et al., 2000; Cobbold et al., 2001; Meisling et al., 2001; Bruhn et al., 2003; Winter et al., 2007; Waisman, 2008; Contreras et al., 2010; De Gasperi and Catuneanu, 2014). Structural trapping by salt-cored faults occurs in other Campos Basin discoveries such as Marimba, Namorado and Roncador (e.g., Pessoa et al. 1999; Bacoccoli, 1979; Bruhn et al., 2003).

In contrast to the prolific Campos Basin, no significant post-salt discoveries have yet been made in the neighbouring Santos Basin, except for in Upper Cretaceous and Tertiary turbidite plays in very shallow waters (i.e. Merluza gas field and Oliva oilfield; Mohriak et al., 2012). Regional studies suggest that, in the central deep-water Santos Basin, siliciclastic wedges never prograded beyond a large, shoreline-parallel, salt-controlled intra-slope depocentre called the 'Albian Gap' or the seaward limit of the extensional domain (Figs.3.3, 3.5; e.g.,

Modica and Brush, 2004; Guerra and Underhill, 2012). As a result, these studies predict little or no sand was deposited basinward within the translation or contractional domains. Chapter 6 challenges the results of previous studies and shows conclusive evidence for the existence of Late Cretaceous, ultra-deep water depositional elements up to 100 km from the coeval shelf margin. Furthermore, Chapter 6 demonstrates that syn-depositional, salt-induced deformation of the seabed controlled sediment dispersal, potential reservoir presence and trapping styles along the Santos Basin slope.

3.5. Salt dissolution in the Santos Basin

The salt-related structural styles and kinematics within salt structures in the Santos Basin have been previously documented (e.g.; Fiduk and Rowan, 2012; Jackson et al, 2014, 2015). However, there are currently no published studies describing any occurrence of salt dissolution in deep-water Santos Basin despite the highly-reflective nature of the evaporite-interbedded salt sequence and the absence of complexity within the overburden revealing remarkable intra-salt structures. This makes it an ideal location to analyse the intra-salt stratigraphy and its relationship with any potential dissolution at the crest of salt walls (section 2.3, Chapter 2). This work contributes, for the first time, to the broad understanding of submarine salt dissolution in the Santos Basin, and even more importantly to the understanding of the eventual partial dissolution of salt giants and its implications for hydrocarbon exploration, seismic imaging and basin modelling.

Chapter 4
Data and methods

This chapter provides a description of the dataset and the methodology used in this thesis. The overall approach used for this work focused in the throughout integration of geophysical and geological information available. An in-depth description and significance of the methods used are presented in this chapter and additional complementary details are included in Chapter 5-7.

4.1. Data

This study is based on interpretation of a 20,122 km2 high quality, three-dimensional, post-stack time-migrated, seismic reflection dataset located in the central deepwater Santos Basin. The study area is located basinwards of the Albian Gap and covers a large area of the Sao Paulo plateau and the Outer High (Fig. 4.1a). Water depths vary from 1600 to 2200 metres in the study area (Fig. 4.1 b). The 3D seismic volume provided by CGG Veritas contains trace information from sea level down to 5.5 second two-way time (TWT), with a vertical sample rate of 4ms, inline spacing (east-west) of 18.75 m and crossline spacing (north-south) of 25.0 m. Three regional 2D Kirchoff pre-stack depth migrated lines were provided by WesternGeco for this study. The 2D depth seismic profile that intersects the 3D survey and some of the boreholes available, is c. 350 km long and has a record length of 16 km providing a good

quality regional image along the central deep-water Santos Basin. This 2D depth seismic profile have been used to illustrate the regional salt thickness distribution, to tie borehole data outside the 3D survey area, to adjust depth converted maps at the 2D line locations and for basin reconstruction.

Seismic profiles are displayed in SEGY normal polarity using two different colour tables. For basinwide-scale 2D profiles and intrasalt seismic-well tie, a downward increase in acoustic impedance is represented by a positive reflection event (black) and a downward decrease in

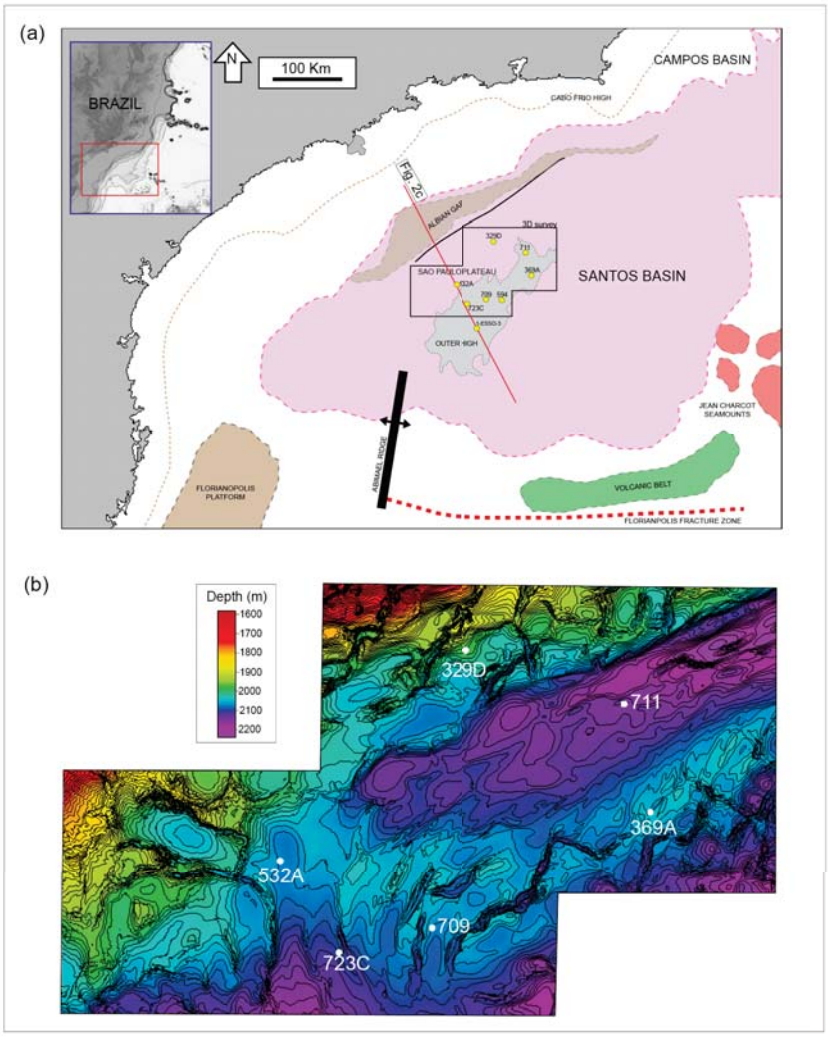


FIGURE 4.1: (a) Study area and dataset. See location of 3D survey relative to key structural elements like the Outer High, and the Albian Gap. (b) Seabed depth-structural map highlighting the present-day bathymetry in the study area.

acoustic impedance is represented by a negative reflection event (red). Instead, for 3D seismic stratigraphic interpretations, a downward increase in acoustic impedance is represented by a positive reflection event (yellow-to-red) and a downward decrease in acoustic impedance is represented by a negative reflection event (blue).

Data from 8 boreholes provided by Statoil Brazil and ANP (Agência Nacional do Petróleo, Gás Natural e Biocombustíveis) have been used to constrain the age and lithology of the mapped reflection events and stratigraphic units within the salt (Chapters 5 and 7) and the post-salt sequences (Chapters 6 and 7). Only two of the boreholes contain a comprehensive set of electrical logs (eg. GR, Neutron, Density and P-Sonic) recorded for the salt sequence and these have been used for seismic-well tie and to assign lithology information to the intrasalt intervals (Chapter 5).

It is important to recognise that the use of time- rather than depth-migrated seismic data, where extreme lateral variations in velocities are not accounted for, can result in ambiguous interpretations especially in areas of steep dips, complex folding and salt overhangs. However, for the academic objectives of this research thesis and with a proper integration of the borehole data provided, the time-migrated seismic volume is sufficient to understand the stratigraphic heterogeneity and thickness variations within the salt and post-salt sequences (e.g, see section 4.8).

4.2. Data preparation and integration

The boreholes, 2D seismic profiles and 3D seismic reflection data provided were integrated in the Petrel software by Schlumberger. Raw log DLIS data was revised and converted to LAS using the Schlumberger toolbox before it was loaded and merged in Petrel for lithological and stratigraphic interpretation and seismic-borehole tie (Chapter 5). For the boreholes where the density log was missing, a density log was calculated using a neural network estimation model

(e.g., Helle et al., 2001). For the method, a combination of logs (GR, Neutron, sonic, density) was used as input training data to create a function that was later applied to similar input data in wells were the density was missing to compute a reasonable density log.

In addition to the data provided, publicly available regional bathymetry and gravity anomalies from Sandwell and Smith v.18.1 were integrated in the project to provide relevant and complementary information. Furthermore, previous studies in the Santos Basin were also georeferenced in the Petrel project; i.e, paleogeography by Modica and Brush, 2004; regional top salt structural map by Guerra and Underhill, 2012; basinwide geoseismic sections by Davison et al., 2012 (e.g.; Fig. 4.2). Geo-referencing and integrating previous studies was essential to locate the study area into the regional-scale context of the Santos Basin (Fig. 4.2; see also Fig. 3.4).

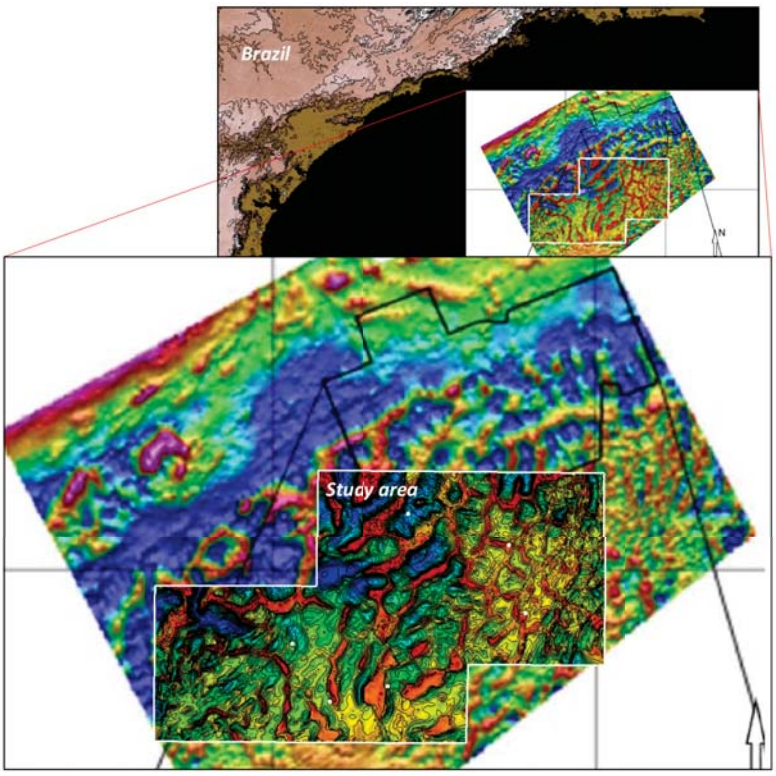


FIGURE 4.2: Example of integration of previous studies: Regional salt structre map by Guerra and Underhill (2012) overlapped by the new Top salt time-structure map interpreted using the data available in the study area.

4.3. Vertical seismic resolution estimations

Vertical seismic resolution was estimated for the intrasalt and post-salt sequences with the purpose of getting an insight about the level of geological detail imaged by the 3D seismic reflection data available (e.g., Chopra et al., 2006). In this study, understanding the values of seismic resolution was essential as an input for calibrating the borehole information with the seismic expression (Chapter 5). In addition, vertical seismic resolution was estimated across the study area to get insights during the analysis of the deep-water depositional elements within the post-salt and the salt karst morphologies at the crest of salt walls (Chapters 6 and 7, respectively).

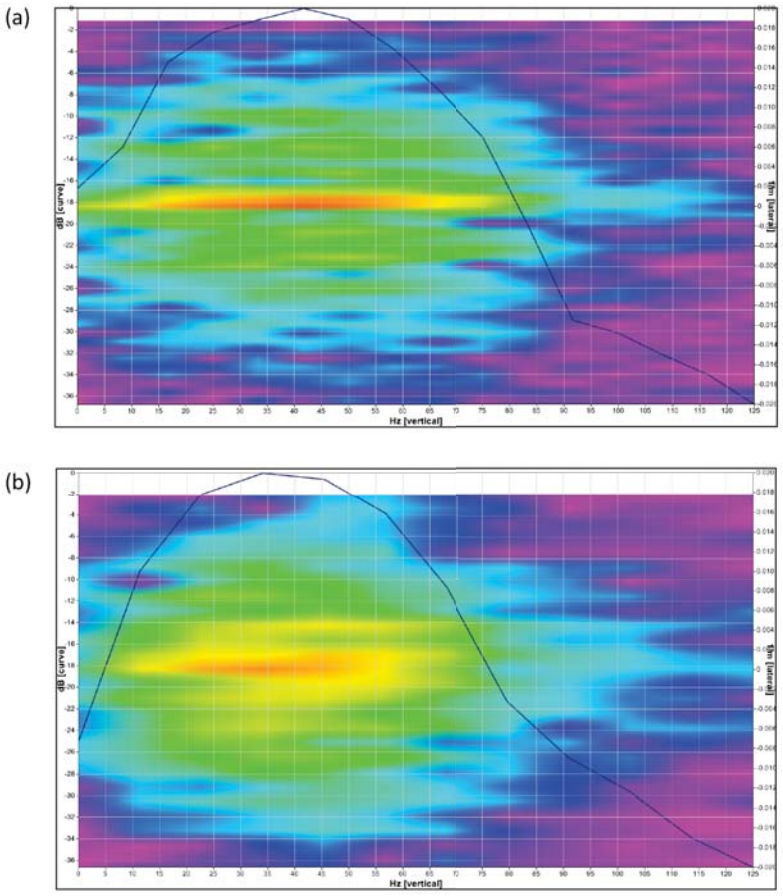


FIGURE 4.3. Examples of frecuency spectrums calculated for the postsalt (a) and the intrasalt (b).

To estimate the vertical seismic resolution, dominant frequency values were calculated from frequency spectrum plots for each of the intervals of interest (Fig. 4.3). Frequency spectrums were generated using the Blueback Geophysics toolbox plugin for Petrel. To estimate the interval velocities within the units of interest, interval velocities were calculated using calibrated checkshot velocity surveys available at the boreholes.

Vertical seismic resolution estimated for the intrasalt (Ariri Formation, Chapter 5) was found to be within the range of 23 m - 30 m based on analysis at five borehole locations (i.e., 723C, 709, 532A, 711, 369A; Fig. 4.1). Dominant frequencies range between 25 Hz – 50 Hz within the salt at the same boreholes. Intrasalt interval velocities obtained from the borehole time-depth curves are of the order of 3000 m s-1 - 4500 m s-1. Vertical seismic resolution within the post-salt sequence decreases from c. 8 m at relatively shallow depths (<2500 ms TWT), to up to 31 m where the post-salt sequence is relatively thick (4500 ms TWT), to up to 64 m where the post-salt sequence is thickest (>5000 ms TWT) (see variations in Table 6.1 and Fig. 6.5; Chapter 6).

4.4. Seismic-well tie

Two key wells (709 and 723C) containing a complete and comprehensive set of well logs within the salt (Density, P-Sonic, Neutron, GR) were used for intrasalt seismic well-tie in the study area (Fig. 4.4 a). For an accurate seismic-well tie, a zero-phase wavelet was extracted from the seismic volume and used for forward modelling (i.e.; post-stack seismic inversion; (e.g., Veeken and Da Silva, 2004) and to calculate the relative acoustic impedance. The relative acoustic impedance was used to identify and map lithology away from areas of well control (Fig. 4.4 b). For the salt sequence, individual seismic reflectors were tied and correlated to individual evaporite layers (c. 20-25 metres thick) interpreted at the wells (see also section 4.5; and Fig. 5.8; Chapter 5). Thinner layers of evaporites, below seismic resolution, are not imaged in the

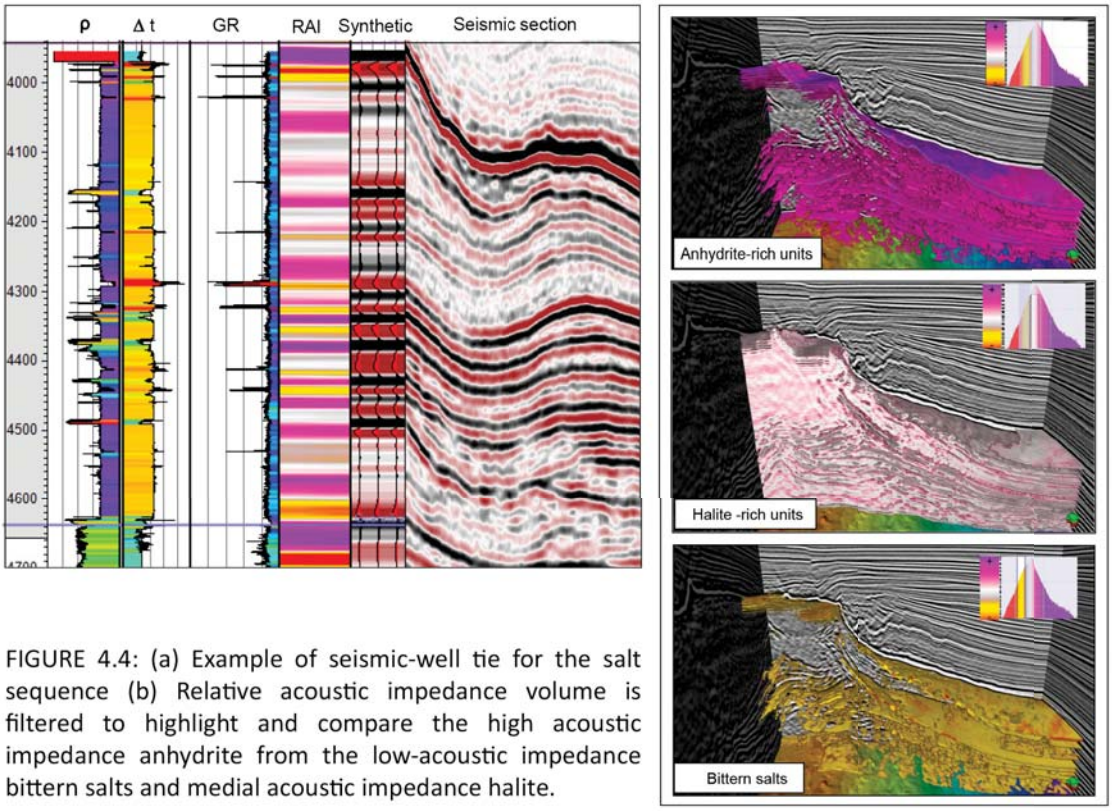


FIGURE 4.4: (a) Example of seismic-well tie for the salt sequence (b) Relative acoustic impedance volume is filtered to highlight and compare the high acoustic impedance anhydrite from the low-acoustic impedance bittern salts and medial acoustic impedance halite.

seismic. Due to limited well logs availability for the post-salt sequence, the checkshot velocity survey was used to estimate the time-depth relationship along the well. Subsequently, the wells logs, well markers and lithology (in TWT, ms) were correlated to the seismic data.

4.5. Intrasalt lithology interpretation and stratigraphic correlation

To identify and interpret the lithology within the salt at each well location, the typical well log response expected from a combination of wireline logs was used, including density (RHOB), sonic (DT), neutron porosity (NPHI) and gamma-ray (GR) (Table 4.1; Schlumberger, 1991; Charts Halliburton Log Interpretation, 1994; Mohriak et al. 2009). Crossplot analysis of wireline log data was also conducted to assist in the identification of clusters of values related to a

particular lithology or type of evaporite (Fig. 4.5). Observations from crossplots were used to guide lithological interpretation and stratigraphic correlation. A distinctive cluster of low densities and significant high GR value were identified as potash salt, mainly carnallites. Low-density tachyhydrites are easily identified from low-density carnallites due to the former characteristic high sonic values (Fig. 4.5). The GR values and neutron porosities for halite and anhydrites are insignificant, however, these can be identified based on the high-density values that characterise the anhydrites (average 2.98) in comparison with the halite (average 2.03) (Table 4.1; Schlumberger, 1991; Charts Halliburton Log Interpretation, 1994; Mohriak et al. 2009; Chapter 5). Lithology interpretation was also verified from information from cuttings descriptions available in the well composite logs provided.

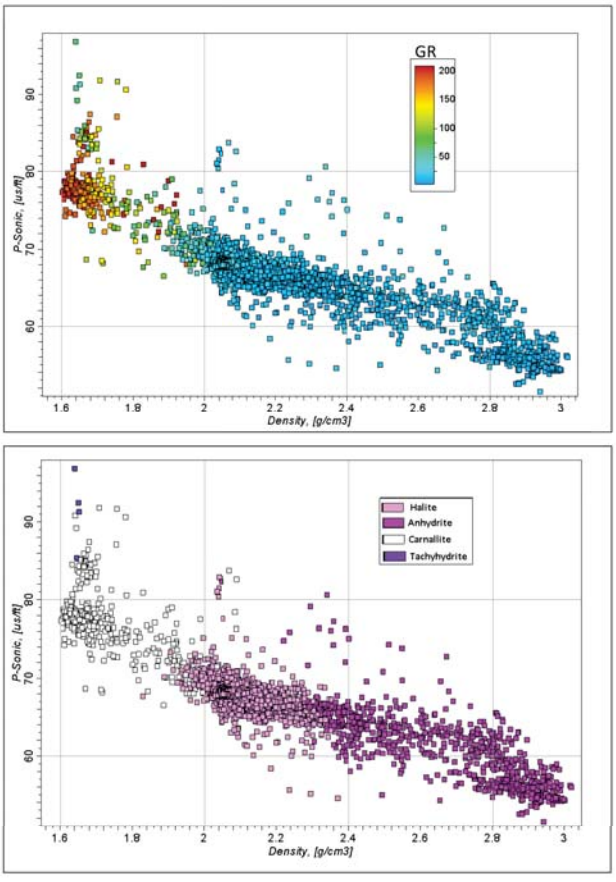


FIGURE 4.5. Crossplot analysis used to interpret lithology at the well locations (a) Sonic vs. density coloured with GR values; (b) Sonic vs. density coloured with the evaporites interpreted.

The intrasalt lithology interpreted at the well locations was subsequently used to construct regional well correlations across the study area (Fig. 4.6). For a more accurate and integrated approach for the intrasalt well correlation, the maps of borehole-calibrated individual evaporite layers and the relative acoustic impedance were integrated to assess the extent of the evaporites during correlation (Figs. 4.4 b and 4.6)

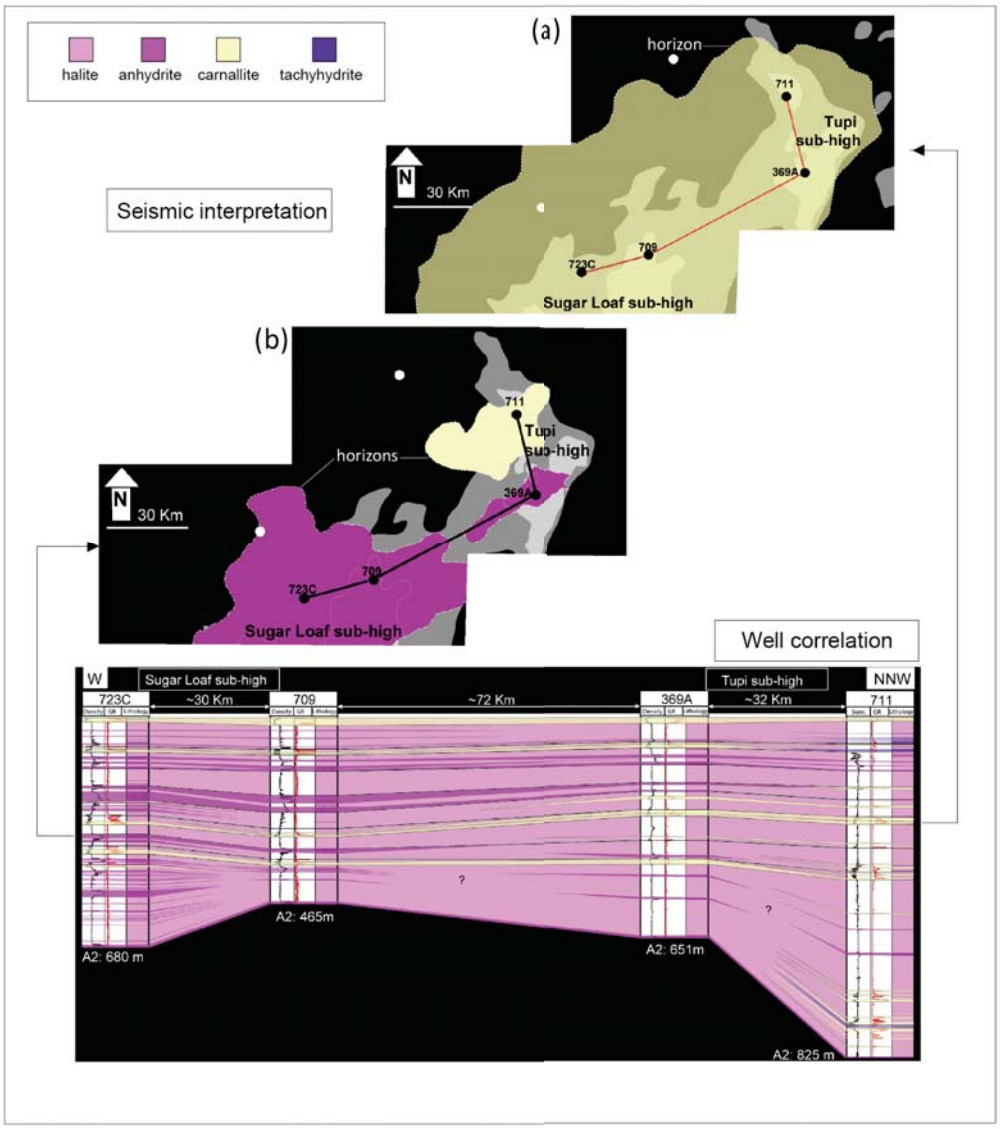


FIGURE 4.6. Integrated approach used for the regional well correlation: (a) laterally extensive carnallite layer identified at the wells and interpreted using the seismic; (b) anhydrite layers pinching and thinning towards the North and Tupi sub-high.

4.6. Horizon interpretation and mapping

Horizons and time-structure maps (i.e, grids) were constructed synchronously during the seismic interpretation. The mapping while interpreting method aid in the early quality control of the horizons and provided the primary three-dimensional insights into the geological information in the seismic data. More than 20 key seismic horizons where interpreted and mapped to accomplish the aims of this thesis. The horizons interpreted correlate to stratigraphic information from boreholes (i.e.; lithology and age) or define clear vertical changes in seismic facies. The horizons interpreted vary in scale and purpose:

(i) Main horizons defining the regional seismic stratigraphic framework in the study area (Fig. 5.4; Chapter 5): Base Salt (top Guaratiba Group); Top Salt (top Ariri Formation); Top Albian-Cenomanian (Top Itanhaem Formation); Mid-Oligocene unconformity (intra-Marambaia Formation); Seabed (top Marambaia Formation)

(ii) Intrasalt horizons defining key stratigraphic intervals within the salt sequence (Fig. 5.4, Chapter 5): Top A1; Top A2; Top A3.

(iii) Intrasalt horizons tied to individual evaporite layers at the borehole locations were interpreted to aid in the well correlation (Fig. 4.6; section 4.4).

(iv) Post-salt horizons correlated to stratigraphic information from boreholes or defining vertical variations in seismic facies (Fig. 6.5; Chapter 6): Top Unit 2 (intra-upper Itajai Acu Formation); Top Unit 3 (intra-Lower Marambaia Formation).

(v) Intra-minibasin horizons interpreted locally and defining sub-units with significant vertical changes in seismic facies (Fig 6.11a; Chapter 6): Top Unit 3a (Intra-upper Itajai Acu Formation); Top Unit 4a (intra- Lower Marambaia Formation); Top Unit 4b (intra-Lower Marambaia Formation).

(vi) Intra-minibasin horizons used for seismic attribute analysis and highlighting

deep-water depositional systems (Fig. 6.11b; Chapter 6).

(vii) Post-salt horizons at the crest of salt walls defining variations in the geometry and seismic facies within the overburden.

(viii) Basinwide-scale horizon interpreted along the regional 2D depth seismic profile and used for basin reconstruction: Basement.

4.7. Thickness maps

Thickness maps were constructed using the gridded horizons. Time- and depth- thickness maps (i.e., isochrons and isochores) construction and analysis were essential to:

(i) provide a broad understanding of salt-related thickness distribution and structural deformation at basinwide scale.

(ii) characterise intrasalt thickness variations and highlight the magnitude of deformation relative to the main salt diapirs (Fig. 5.9; Chapter 5)

(iii) reconstruct the regional scale tectonostratigraphic evolution of the post-salt sequence (e.g., Fig. 6.9; Chapter 6).

(iv) examine the temporal and spatial evolution of the minibasins. The integration of intra-minibasin isochrons and attribute analysis (section 4.9) provided an understanding about depocenters migration within the minibasins (e.g., Fig. 6.12; Chapter 6).

(v) interpret the geometry and the variations, in time and space, of deep-water depositional elements relative to present-day salt structures (e.g., Fig. 6.20; Chapter 6).

4.8. Velocity model and depth conversion

A Depth conversion was carried out to estimate salt thickness distribution and to assess the

present-day configuration of the base of salt by minimising the effects of high velocity pull-ups (Fig 4.7). To convert time-structure maps to the depth domain a three-dimensional velocity model was constructed. The interval velocity assigned to each layer was estimated from the time-depth curves from five of the seven boreholes. Depth values from stratigraphic markers in all six boreholes, together with the pre-stack depth migrated 2D seismic sections, were used to check the accuracy of the depth conversion (Fig. 4.7).

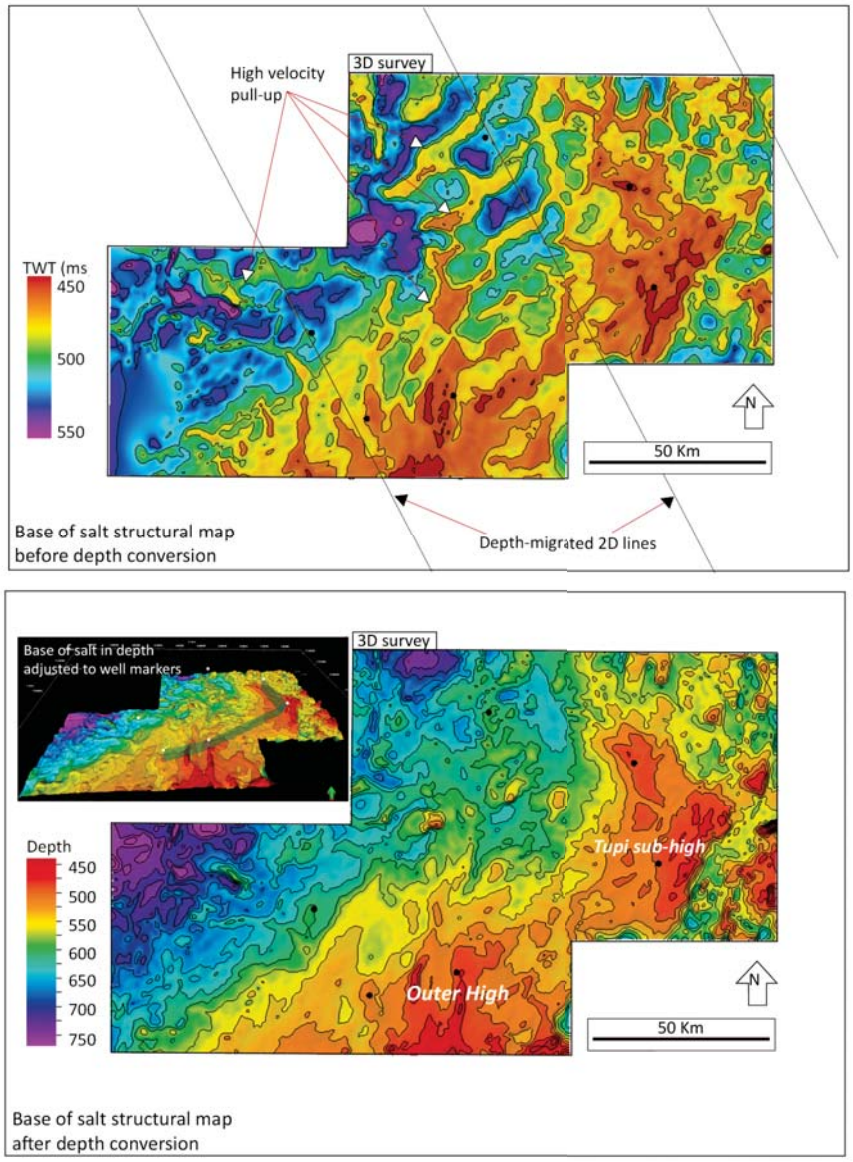


FIGURE 4.7. Depth conversion of the base salt structure map to minimise or eliminate velocity pull ups effects caused by salt structures

4.9. Seismic attribute analysis for the geological interpretation

The seismic attributes used in this thesis and its geological significance are described in this section.

Sweetness: integrates amplitude strength (envelope) and instantaneous frequency to highlight lateral changes in seismic facies variations related to inferred changes in lithology (e.g.; Hart, 2008). Sweetness is mainly used for the identification of features where the overall energy signatures change in the seismic data. The Instantaneous amplitude (envelope in Petrel) is the total instantaneous energy of the analytic signal (the complex trace) and it is generally use for detecting major lithological changes caused by strong energy reflections and sequence boundaries. The instantaneous frequency is defined as the time derivative of phase and it is used to measure cyclicity of geological intervals. Therefore, sweetness was used to highlight, interpret and/or isolate strongly-reflective stratigraphic intervals in 3D seismic reflection data. More specifically, in this study, sweetness was used to:

(i) identify, interpret and correlate Intrasalt cyclic evaporites (Fig. 4.8; Chapter 5)

(ii) identify and map deep-water depositional elements (Chapter 6).

(iii) to highlight lateral and vertical facies variations (in section) along the crest of salt walls and between and within the key intrasalt intervals (Chapter 7)

Chaos: is a texture attribute used to map disorganized seismic traces within a 3D window (Randen and Sønneland, 2005). The chaos attribute measures the 'lack of organization' within the seismic data (e.g.; Hart, 2008). In this study, chaos was used for different purposes:

(iv) Halite-rich acoustically-transparent seismic stratigraphic units can easily be distinguished using the chaos attribute, which is negligible in cyclic interbedded evaporites (Chapter

5)

(v) chaos, it was key in this study to investigate intra-salt facies variations along the salt crests;

Amplitude contrast: This seismic attribute calculates amplitude derivatives between neighbouring seismic traces. In this study, the amplitude contrast was used

(i) to highlight salt structures, faults and mass transport complexes (MTCs) (Chapter 6; Schlumberger, 2012).

(ii) to characterise discontinuities associated with dissolution along the top salt (Chapter 7)

Variance: identifies abrupt lateral changes in seismic reflection continuity (Hart, 2008). It was mainly used in this study for visual blending with the sweetness.

The combination or **visual blending** of two independent attributes was used as a method to

(i) to aid in the identification and mapping of lithology-calibrated horizons away from areas of well control

(ii) Interpret intrasalt seismic facies variations (Fig. 4.8)

(iii) interpret the seismic geomorphology of deep-water depositional systems and identify edges of channels and lobes (Chapter 6; see also Hart, 2008).

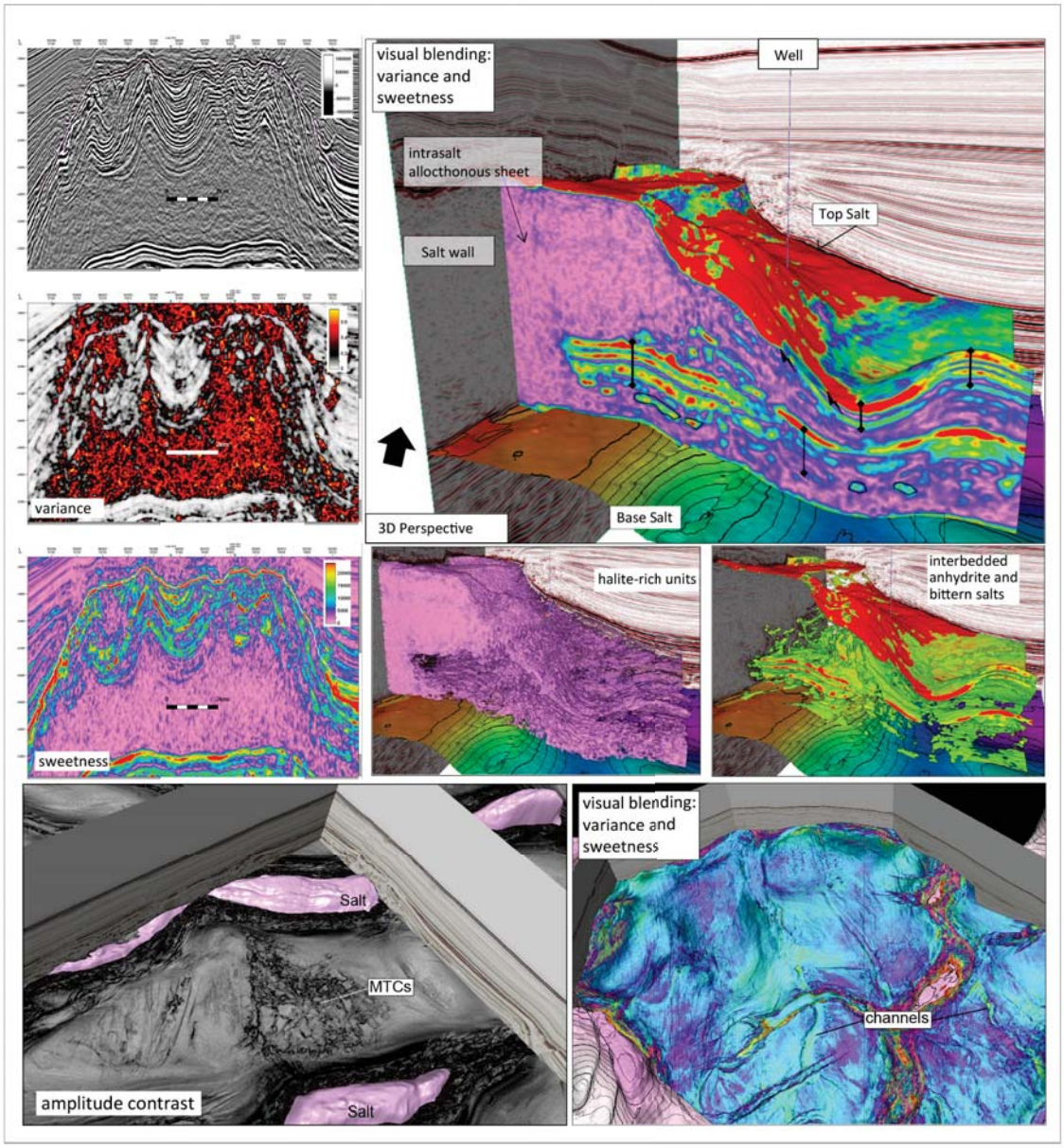


FIGURE 4.8. Examples of seismic attributes used for this study

Chapter 5

Stratigraphy of salt giants:
New insights from the Santos Basin, offshore Brazil

This Chapter is written as a scientific paper and documents compositional variations and overall intrasalt stratigraphic architecture of the Santos Basin salt giant. This section also provides insights into the temporal and spatial variations in basin physiography, salinity variations and basin hydrology during salt deposition in the Late Aptian. As this Chapter is written as a 'stand-alone' paper, some of the material presented in the 'Introduction', 'Tectono-stratigraphic framework' and 'Data and methods' sections overlap with that in Chapters 3-4.

5.1 Abstract

The stratigraphic evolution of ancient salt giants is controversial, mainly due to the absence of modern analogues that are of comparable scale and thickness, and which occur in similar tectonic and hydrological settings. Furthermore, investigating the original stratigraphy of salt giants is often made difficult by post-depositional flow and dissolution. Layered evaporites of the Ariri Formation in the Santos Basin (offshore Brazil), deposited during opening of the South Atlantic Ocean, form part of one such salt giant. Despite being well-imaged in seismic data and being penetrated by >50 boreholes, little work has explored the stratigraphic architecture of this unit and what this may tell us about the syn-depositional tectonics, basin physiography

and variations in climate and sea-level. Here I integrate 3D seismic and borehole data from the São Paulo Plateau, deep-water Santos Basin, to document the intrasalt stratigraphy of the Ariri Formation. My analysis suggests that a combination of an arid paleo-climate, low-amplitude local sea-level variations and basin physiography controlled deposition of this thick (2.5 km) salt sequence, during a short time span < 530 ka. The Ariri Formation records at least 12 cycles of basin desiccation and filling, resulting in the deposition of four key units (A1-A4) that have a distinct composition and therefore, seismic expression; i.e. low-frequency, transparent, chaotic seismic facies represent relatively halite-rich (>85%) units (A1 and A3), whereas high-frequency, highly-reflective seismic facies represent still relatively halite-rich (65-85% halite) units, but which contain relatively high proportions (15-35%) of anhydrite and carnallite (A2 and A4 units). My findings suggest that during salt deposition the Santos Basin was characterized by a series of sub-basins of varying water depth; as a result, the thickness and composition of these units vary laterally and are spatially related to structural domains. Overall, thinner salt (c. 1.8 km) and higher anhydrite net thickness (c. 350 m) occur towards the structurally high Sugar Loaf domain, compared to flanking, structurally lower domains where the mean salt thickness is >2.2 km and anhydrite net thickness are less (c. 180 m). Additionally, stratigraphic variations in the basin, suggest seawater incursions came from the south, through the São Paulo-Walvis ridge; consequently, more anhydrite was deposited closer to the ridge, whereas more bittern salts were deposited in more distal and restricted locations. The results of my study, although based on an analysis of Aptian salts preserved offshore Brazil, offers valuable insights into the sedimentology, and stratigraphic architecture and evolution of other ancient salt giants.

5.2 Introduction

Ancient ‘saline giants’ (sensu Hsü, 1972) or ‘salt giants’ (sensu Hübscher et al., 2007) are areally extensive (>100,000 km2), hundreds to thousands of metres thick, evaporite-dominated

successions, deposited in hydrologically restricted basins in a wide range of tectonic settings (Hudec and Jackson, 2007; Warren, 2010). The stratigraphy of salt giants is mainly controlled by the solubility of different evaporite minerals, which precipitate following an idealised precipitation sequence, i.e. first carbonates, then sulphates, followed by chlorides, with carbonates typically being the volumetrically dominating rock type, and then gypsum/anhydrite, followed by halite, and ending with bittern salt (K- and Mg-rich salts; e.g. Usiglio, 1849; Clarke, 1924). During the initial stages of partial restriction and hydrological drawdown in a carbonate-evaporite basin, carbonate platforms are exposed and gypsum precipitates at the basin margins; if the water level drops below the basin sill, halite and eventually bittern salts may precipitate in salt pans and lakes located in the deepest, most isolated parts of the basin (Fig. 5.1) (e.g. Hsü, 1972; Tucker, 1991). Breaching of the sill may recharge the basin with saline fluid and halite may fill the basin. A new evaporite cycle starts when the hypersaline basin is reflooded and gypsum is deposited (Fig. 5.1; Tucker, 1991). The applicability of this general model to ancient salt giants is uncertain, partly reflecting the lack of modern analogues that are of comparable scale and thickness, and which occur in similar tectonic and hydrological settings. In addition, the original stratigraphy of salt giants is likely to be altered during and/or after deposition due to dissolution, changes in mineral phase (i.e. anhydrite to gypsum and vice versa) and salt flow, which can result in tectonic modification of the primary depositional stratigraphy due to preferential expulsion of low-viscosity units (Kupfer, 1968; Warren, 2006; Hudec and Jackson, 2007; Cartwright et al., 2012; Jackson et al., 2014a).

Our current knowledge of ancient salt giants is constrained by field data (e.g. Jackson et al., 1990; Reuning et al. 2009; Stefano et al., 2010), seismic reflection data that image intrasalt stratigraphy (e.g. Van Gent et al., 2011; Fiduk and Rowan, 2012; Schoenherr et al. 2007; Strozyk et al., 2012; Jackson and Lewis, 2013; Jackson et al., 2014a; Jackson et al., 2014b; 2015), and boreholes that penetrate salt-bearing sequences (e.g. Clark, et al., 1998; De Freitas, 2006; Massoth and Tripp, 2011; Trudgill, 2011; Eoff et al., 2013; Jackson et al., 2014a,b; 2015). These data suggest that depositional thickness and intrasalt stratigraphy are controlled by several

factors that may act individually or collectively during salt giant deposition; i.e. (i) climate; (ii) sea-level variations; (iv) duration of salt deposition; (iii) syn-depositional tectonics and basin physiography (v) the distance to the basin sill and the direction of seawater inflow and (vi) the location and volume of freshwater river discharge, which may modify brine salinity. For example, deposition of the Paradox Formation (Upper Carboniferous) in North America was primarily controlled by climate and 3rd-order sea-level variations driven by greenhouse (transgressive phases) and icehouse conditions (regressive phases), thus highlighting the key role of climatic and sea-level variations (Eoff et al., 2013). Transgressive phases were characterised by fully marine conditions and the deposition of organic-rich black shales, whereas regressive phases were characterised by basin desiccation and salt (i.e. anhydrite, halite, bittern salts) deposition. Climate and sea-level variations also influenced the stratigraphy of the Messinian (Upper Miocene) salt in the Mediterranean Sea, where the deposition of gypsum-shale alternations along the basin margins were controlled by periodic changes in salinity due to low-amplitude, high-frequency, 5th-order, precession-driven, climate cycles (Krijgsman et al., 1999; Stefano et al., 2010; Manzi et al., 2012). There is also clear evidence for the impact of syn-depositional tectonics on evaporite stratigraphy; for example, the foreland basin setting of the Paradox Basin controlled not only bulk thickness but also the distribution of lithologies in the Paradox Formation, with carbonates deposited in the distal forebulge in shallow water depths, whereas halite and other evaporites were deposited in the basin centre during periods of drawdown (Trudgill, 2011; Eoff et al., 2013). Syn-depositional tectonics also controlled the thickness and stratigraphic development of the Zechstein Supergroup (Upper Permian) in NW Europe. During deposition of the Zechstein Supergroup, basin physiography was controlled by pre- and syn-depositional, rift-related normal faulting, with halite-rich units occurring in the basin centre, whereas on intra-basinal highs, carbonate- and anhydrite-rich units were deposited (e.g. Taylor, 1990; Tucker, 1991; Clark et al., 1998; Stewart and Clark, 1999; Stewart, 2007; Jackson and Lewis, 2013).

In this study, I integrate and analyse 3D seismic reflection and borehole data from the deep-

water Santos Basin, offshore Brazil to provide new insights into the deposition and evolution of salt giants. My results show that basin physiography and sea-level variations can play key roles during the deposition of thick (2.5 km) salt sequences.

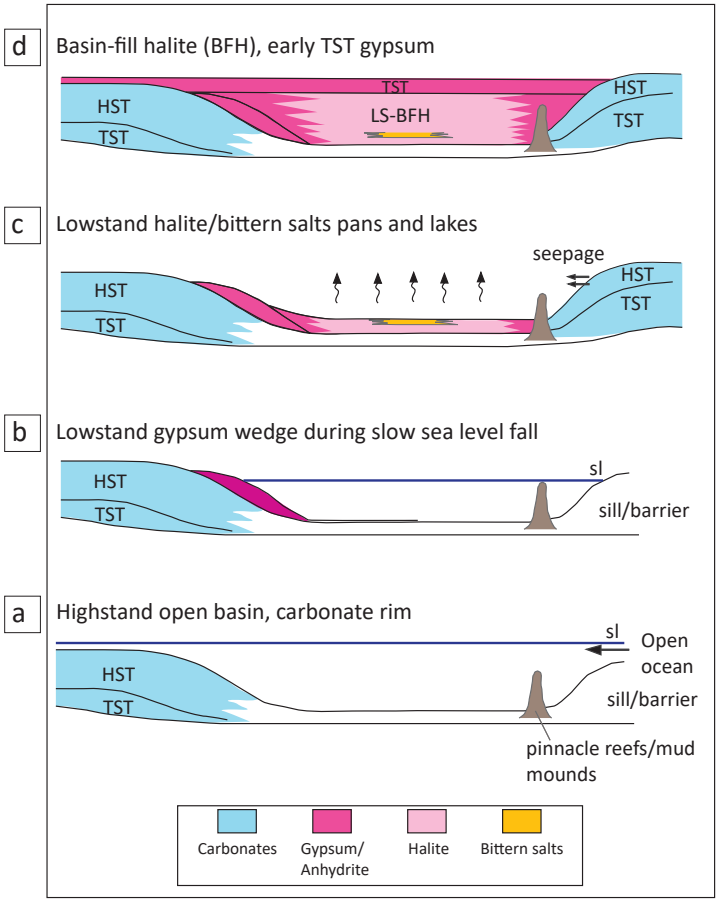


FIGURE 5.1: Conceptual model for the stratigraphic architecture of a carbonate-evaporite basin subjected to complete drawdown (after Tucker, 1991). (a) carbonate deposition during highstands; (b) gypsum deposition during slow sea level fall; (c) halite and bittern salts are deposited during lowstands and basin desiccation; (d) gypsum is deposited during refill of the basin.

5.2.1 Early Cretaceous salt of the South Atlantic: Previous studies and controversies

An Aptian salt giant was deposited during opening of the South Atlantic Ocean covering c. 741,000 km2 and was up to 2.5 km thick (Fig. 5.2a; e.g. Dias 2004; Davison 2007). Although

the tectonics and geodynamics of South Atlantic opening have been extensively studied, several key questions remain regarding deposition of the Aptian salt giant, including: (i) how rapidly was the thick (2.5 km) salt deposited?; (ii) what mechanism or mechanisms generated accommodation for thick salt deposition, thus in what tectonic context was the salt deposited?; (iii) was the salt deposited in shallow or deep water?; and (iv) was the seawater inflow into the Santos Basin from the north or south? In this study, I contribute to this debate by analysing the intrasalt stratigraphy in the Santos Basin, offshore Brazil, but first I review some of the previous studies.

The age of the South Atlantic salt giant is poorly constrained, previous studies suggest a deposition between 0.4 and 10 Ma (Jackson et al. 2000; Szatmari, 2000; Dias, 2004; De Freitas, 2006; Davison, 2007; Karner and Gambôa, 2007; Moreira et al., 2007; Montaron and Tapponier, 2010). However, most authors agree on a rapid deposition (< 600 ka) based on analysis of core data (Dias, 2004), correlation of evaporites stratigraphy with Milankovitch cycles (De Freitas, 2006), and by comparison to other salt basins (Davison, 2007) and the predictions of numerical models (Montaron and Tapponier, 2012).

In terms of accommodation for thick salt deposition, three main mechanisms have been proposed: (i) salt deposition occurred within a pre-existing basin during tectonically quiescent conditions (Szatmari, 2000; Burke et al., 2003; Dias, 2004; Davison, 2007; Davison et al., 2012); (ii) salt deposition occurred during rifting (i.e. it is a syn-rift deposit), prior to the onset of post-rift thermal subsidence (Karner et al., 2003; Karner and Gambôa, 2007; Gambôa et al., 2008; Torsvik et al., 2009; Scotchman et al., 2010) and; (iii) loading of the crust by thick salt drove local subsidence and led to the development of accommodation (e.g.; Dias, 2004; Karner and Gambôa, 2007; Davison et al., 2012). The first mechanism suggests that rift-related faulting had ceased at the onset of salt deposition, with deformation giving rise to a pre-existing basin defined by several discrete lakes and which lay up to 2 km below sea-level (Szatmari, 2000; Burke et al., 2003). The lakes were flanked by pre-existing, normal fault-related scarps that

controlled salt thickness across the basin, with thicker (<2 km) salt within the lows and with thinner (<1 km) salt over the highs (Dias, 2004; Davison, 2007; Davison et al., 2012). In contrast, studies favouring a syn-rift salt interpretation postulate that salt deposition occurred during the latest phase of rifting, characterised by minor late Aptian normal faulting and thermal subsidence (Karner et al., 2003; Karner and Gambôa, 2007; Torsvik et al., 2009; Reston, 2010; Scotchman et al., 2010). In addition, local faulting during salt deposition was possibly due to salt loading, which may have increased accommodation (Dias, 2004; Karner and Gambôa, 2007; Davison et al., 2012).

Despite the controversies regarding the Aptian salt giant, there is a general consensus with regards to the water depth within which the salt was deposited. Except for Karner and Gambôa (2007) and Montaron and Tapponier (2010), who suggest salt deposition in relatively deep waters (1.5-3 km), many other authors support a shallow-water depositional environment based on the following evidence: (i) the stratigraphic context of the salt, above continental/ lacustrine deposits and below shallow-water limestones (e.g, Szatmari et al., 1979; Moreira et al., 2007; Palagi, 2008); (ii) sedimentological features (chevron and cornet halite crystals) identified in cores in the Espirito Santo Basin, indicating that evaporite precipitation occurred in very shallow waters (Dias, 2004); (iii) subaerial exposure and karstification of the pre-salt sag sequence (Gomes et al., 2009); and (iv) palaeontological evidence from the base of Aptian carbonates capping the salt on the Angolan margin, suggesting water depths of <500 m (Marton et al., 2000).

Therefore, within this deep-basin/shallow-water depositional context, the proto-South Atlantic was occupied by lakes of varying salinity and, as salinity increased, these lakes were replaced by hypersaline lagoons (e.g., Szatmari et al., 1979; Burke et al. 2003; Aslanian et al., 2009). The transition from a lacustrine to a lagoonal depositional environment, conducive to salt deposition, was the result of partial filling of isolated basins by saline waters, as the basin became connected to the open ocean during rifting, becoming entirely evaporitic by the Late

Aptian (e.g., Bate 1999; Dingle 1999; Karner and Gambôa 2007; Reston 2010).

Most studies suggest that the connection to the open ocean and recurrent seawater inflow was from the south, where a barrier comprised by the Rio Grande Rise, Walvis/São Paulo Ridges confined the evolving South Atlantic, thus providing the condition necessary to permit salt deposition and preservation. These volcanic ridges formed during Paraná -related volcanism in the Barremian, shortly before salt deposition, and are believed to have collectively acted as a barrier to ocean water circulation before open marine conditions were established in the Albian (Evans, 1978; Karner and Gambôa, 2007; Gambôa et al., 2008; Davison et al., 2012). However, a somewhat more controversial model suggests intermittent seawater incursions flooded from the north via a series of early rifts or seaways formed in the central Atlantic (Dingle, 1999; Bate, 1999; Scotchman et al., 2006; Arai, 2014). For example, according to Scotchman et al. (2006), analysis of ostracode data suggests that the volcanic Walvis Ridge was not breached until Cenomanian-Turonian times, hence preventing marine waters entering during the estimated period of salt deposition. An alternative entry point for seawater is thus postulated suggesting seawater percolation through fracture zones in the volcanic ridges to the south, thus recharging the salt basin (Jackson et al., 2000; Nunn and Harris, 2007; Montaron and Tapponier, 2012).

5.2.2 Stratigraphy of the Ariri Formation: Previous studies

Despite being imaged by high-quality, regionally extensive 2D and 3D seismic reflection data and penetrated by 50-100 boreholes, surprisingly few studies have attempted to characterise the composition and stratigraphic architecture of the Ariri Formation in the Santos Basin, offshore Brazil (Demercian, 1996; De Freitas, 2006; Davison, 2007; Davison et al., 2012); as a result, it is not clear how this regionally extensive stratigraphic unit, which spans much of the Brazilian margin, records syn-depositional tectonics, or climatic and sea-level variations. Seismic and borehole data from the São Paulo Plateau, which is the major structural element

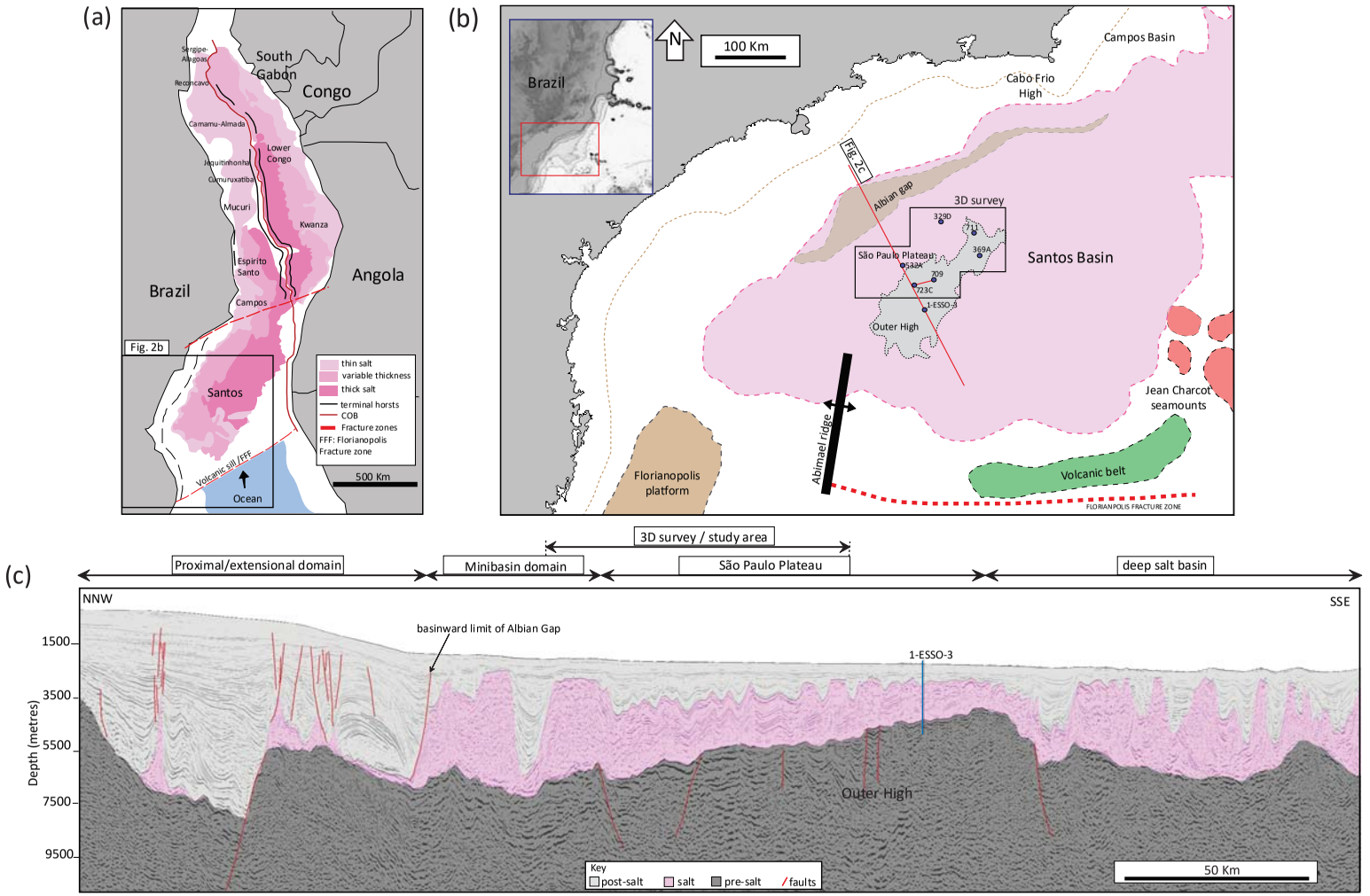


FIGURE 5.2: (a) Early Cretaceous paleogeography illustrating the South Atlantic salt giant (after Lentini et al., 2012); (b) Study area (c) Geoseismic section illustrating the salt-related structural domains and the salt thickness variations across the Santos Basin. 2D seismic line courtesy of WesternGeco.

in the Santos Basin, indicate that the Ariri Formation is characterised by highly-reflective, multi-layered evaporites. The unusual seismic character of the Ariri Formation was first recognized on 2D seismic reflection data by Cobbold et al. (1995) and was assumed to be composed of interbedded halite, anhydrite and clastics (Davison, 2007). An exploration borehole drilled in 2002 revealed the Ariri Formation was composed of at least 2.5 km of interbedded evaporites, including halite, anhydrite and bittern salts (e.g. carnallite, bishofite, sylvite and tachyhydrite; Poiate et al., 2006; Scotchman et al., 2010; Mohriak et al., 2012).

De Freitas (2006) correlation of two boreholes separated >200 km apart indicate that halite and bittern salt layers thicken basinwards, whereas interbedded anhydrite layers thicken landwards (Fig. 5.3). De Freitas (2006) suggests this pattern reflects overall lower salinities near the land due to the periodic input of freshwater. Lateral variations in lithology in the Ariri Formation have also been described by Moreira et al. (2007) and Gambôa et al. (2008), with halite, anhydrite, tachyhydrite, carnallite and locally silvite in the basin centre, thinning and passing into main dolomite and anhydrite in the basin margins. In addition, seismic facies analysis of the Ariri Formation has divided the succession into four key seismic-stratigraphic units (Fig. 5.4; Gambôa et al., 2008) or six mechano-stratigraphic intervals (Fig. 5.4; Fiduk and Rowan, 2012).

Even though the detailed stratigraphic architecture of the Ariri Formation remains very poorly constrained, previous regional studies in the South Atlantic, based largely on 2D seismic reflection data and sparse or no borehole data, suggest that a >2 km thick, halite-dominated succession was deposited in the rapidly subsiding basin centre, whereas thinner (c. 200 m) carbonate-, anhydrite-, sylvite- and tachydydrite-bearing successions were deposited on highs along the basin margins (e.g., Chang et al. 1992; Karner and Gambôa, 2007; Lentini et al., 2010).

It is clear that, due to a lack of focus on the salt as a depositional entity and the unavailability of borehole data, previous studies have been unable to constrain the regional compositional

variations or the overall stratigraphic architecture of the Ariri Formation, nor the role syn-depositional tectonics or variations in climate and water depth played during salt deposition; it is this what forms the focus of my study.

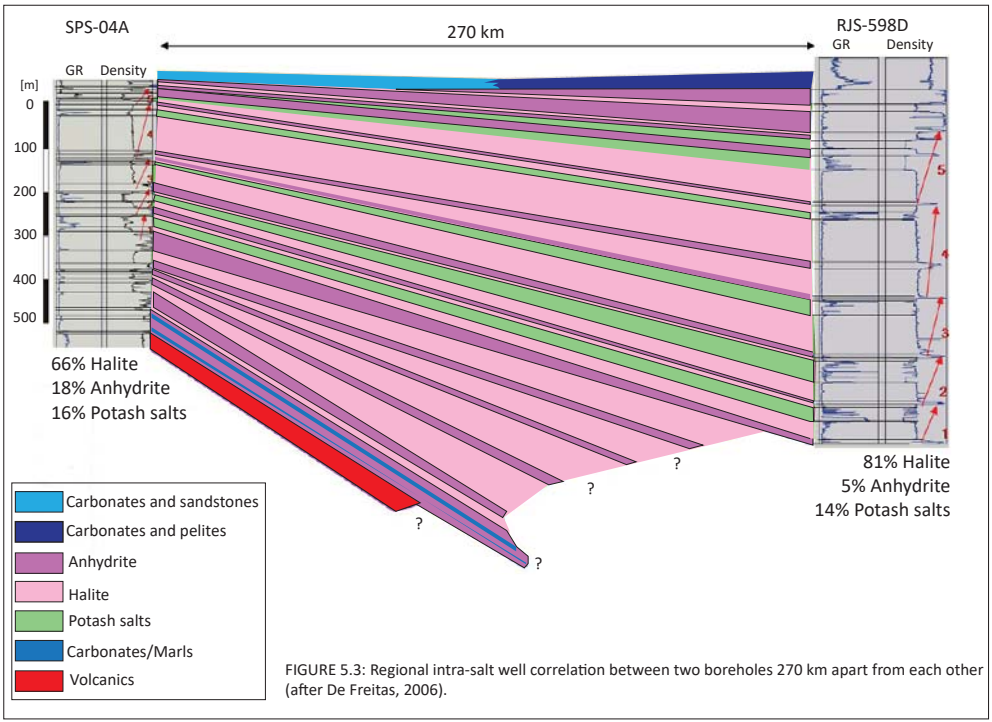


FIGURE 5.3: Regional intra-salt well correlation between two boreholes 270 km apart from each other (after De Freitas, 2006).

5.3 Tectono-stratigraphic framework

The Santos Basin (350,000 km2) is the widest (c. 500 km) of the South Atlantic salt basins (Fig. 5.2a; e.g. Davison et al., 2012; Guerra and Underhill, 2012), and is bounded to the west by the Brazilian mainland, and to the north by the Cabo Frio High and the Campos Basin (Fig. 5.2b). To the south, the basin is bounded by the Florianopolis High, and the volcanic belt north of the Florianopolis Fracture Zone and the São Paulo Ridge, and to the east by the Jean Charcot volcanic seamounts. The São Paulo Plateau is the main structural element in the Santos Basin, forming a c. 500 km wide area that is characterised by relatively deep water (2000-3000 m) and the presence of a prominent intra-basinal structural high, the Outer High (Fig. 5.2b, c) (Gomes et al., 2002; Gomes et al., 2009). The Outer High is characterised by half-grabens

developed during Barremian rifting, when non-marine to shallow marine sediments of the Guaratiba Group were deposited (Demercian, 1996; Meisling et al., 2001; Gomes et al., 2002; Moreira et al., 2007; Carminatti et al., 2009; Gomes, et al., 2009; Scotchman, et al., 2010) (Figs. 5.2c and 5.4) . Episodic marine incursions and basin desiccation events led to the deposition of an up to 2.5 km of Aptian salt (called the Ariri Formation in the Santos Basin). The salt was deposited on extended continental crust at the base of a 1500 km-long, N-trending rift-related valley located between the eastern Brazilian and West African conjugate margins, north of a volcanic belt represented by the proto-Rio Grande Rise and the Walvis and São Paulo ridges (Gladczenko et al., 1997; Fig. 5.2 and 5.4). On the other hand, some authors have suggested that the southern boundaries of the salt basin correspond to exhumed mantle rocks (Zalán et al., 2011). These volcanic features acted as oceanographic sills, impeding influx of saline marine waters into the developing Santos Basin, facilitating evaporation and salt deposition (Fig. 5.2a, b; e.g. Szatmari 2000; Dias 2004; Davison 2007; Karner and Gambôa, 2007; Carminatti et al., 2009; Davison et al., 2012). During the Aptian, the proto-South Atlantic rift-related valley was up to 500 km wide in the Santos Basin, narrowing northward to <50 km in the Sergipe-Alagoas Basin (Fig. 5.2a; e.g. Jackson et al., 2000; Szatmari, 2000; Dias, 2004). During the Albian, a shallow-marine, carbonate platform became established (Guaruja Formation) (Figs 5.2c and 5.4) (Moreira et al., 2007). Rapid eustatic sea-level rise during the Upper Cretaceous and Palaeocene-Eocene led to the deposition of shelfal clastics, shales and marls of the Itanhaem Formation and the development of a major clastic-dominated progradational basin margin (upper Itajai-Acu Fm.; Figs 5.2c and 5.4; Modica and Brush, 2004; Moreira et al., 2007).

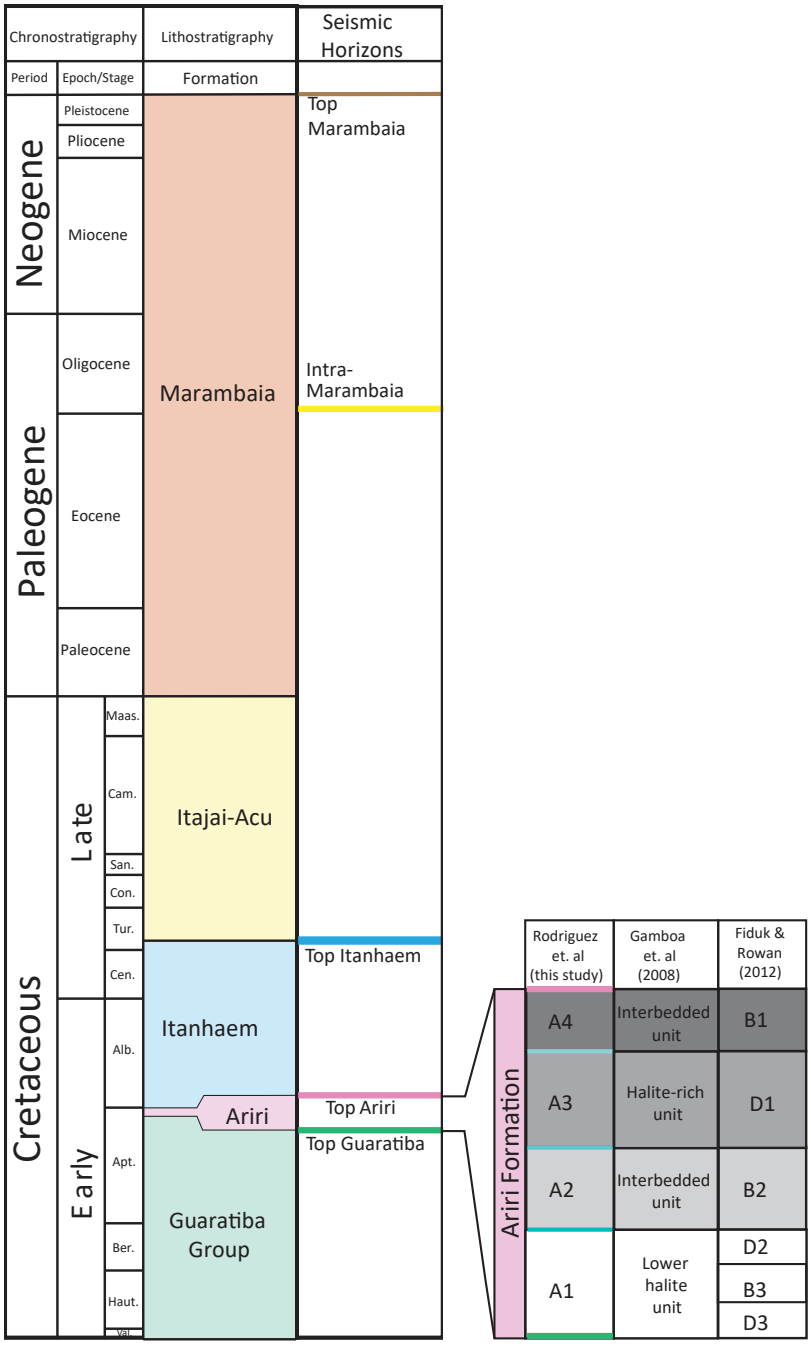


FIGURE 5.4: Santos Basin seismic stratigraphic framework.
Intrasalt key stratigraphic intervals are specified for this and previous studies. B1, B2 and B3 refer to competent layers or 'beams' defined by high amplitude continuous reflections. D1, D2 and D3 refer to ductile detachment zones defined by acoustically transparent, poorly continous reflections (Fiduk and Rowan, 2012)

5.4 Data and methods

My study uses a 20,122 km2, high-quality, three-dimensional, post-stack time-migrated, seismic reflection dataset located in the central deep-water Santos Basin, covering a large area of the São Paulo Plateau and the Outer High (Fig. 5.2b). The 3D seismic volume, courtesy of CGG, contains trace information from sea level down to 5.5 second two-way time (s TWT), with a vertical sample rate of 4 ms, inline spacing (east-west) of 18.75 m and crossline spacing (north-south) of 25 m. Data from five boreholes within the study area indicate that the intrasalt vertical seismic resolution is c. 30 m, based on an average intrasalt interval velocity of c. 4400 m s-1 and average dominant frequency of 36 Hz. Interval velocities were estimated using calibrated checkshot velocity surveys available at the boreholes locations. The intrasalt interval velocities are low when compared to typical salt velocities of 4500-5500 m/s; this is due to the presence of acoustically-low-velocity (3500 m s-1) carnallite layers. Seismic profiles are displayed in SEGY normal polarity, where a downward increase in acoustic impedance is represented by a positive reflection event (black) and a downward decrease in acoustic impedance is represented by a negative reflection event (red). Three regional 2D Kirchoff pre-stack depth-migrated lines were also used in this study, principally to help illustrate the regional salt thickness distribution and to tie borehole data located outside the area imaged in the 3D survey (Figs. 5.2b, 5.2c).

Data from seven boreholes have been used to constrain the age of the mapped reflection events and the lithology of intrasalt stratigraphic units (Fig. 5.2b). These data also allow us to construct regional stratigraphic correlations depicting the stratigraphy and thickness of the salt. Synthetic seismograms were constructed in order to calibrate borehole lithology with the intrasalt seismic reflections. Only two of the boreholes contain a comprehensive set of electrical logs (eg. GR, Neutron, Density and P-Sonic), and these have allowed us to tie seismic and borehole data, and to assign lithology information to the mapped intervals (Figs. 5.5, 5.8). Identification of intrasalt lithology is based on the typical borehole log response expected from a combination of wireline logs, including density (RHOB), sonic (DT), neutron porosity

(NPHI) and gamma-ray (GR) (Table 1; Schlumberger, 1991; Charts Halliburton Log Interpretation, 1994; Mohriak et al. 2009). Lithology interpretation was also verified with information from cuttings descriptions available in borehole composite logs.

To establish the regional thickness and stratigraphic framework of the salt, five well-calibrated regional horizons were mapped (Figs. 5.4 and 5.5): (i) Top Guaratiba Group (base salt); (ii) Top Ariri Formation (top salt); (iii) Top Itanhaem Formation; (iv) Intra-Marambaia Formation; and (v) Seabed. Seismic facies analysis and borehole data allowed us to constrain the four main intrasalt stratigraphic intervals (A1 to A4) and to map three intrasalt seismic horizons: Top A1, Top A2 and Top A3 (Figs. 5.4 and 5.5) (see also Jackson et al., 2015). To convert time-structure maps to the depth domain a velocity model was constructed. The interval velocity assigned to each layer was estimated from the time-depth curves from five of the seven boreholes. Depth values from stratigraphic markers in all six boreholes, together with the pre-stack depth migrated seismic sections, allowed us to check the accuracy of the depth conversion of the generated depth maps. Intrasalt seismic facies interpretations and stratigraphic correlations were supported using seismic attribute analysis (i.e. sweetness and variance; Hart, 2008) and seismic inversion (i.e. relative acoustic impedance; Fig. 5.8). These seismic attributes and variations in relative acoustic impedance have been used to identify and map lithology away from areas of well control. The relative acoustic impedance was estimated using the zero-phase wavelet extracted at the well location and also used to identify and correlate the lithology between the wells (Figs. 5.8, 5.10).

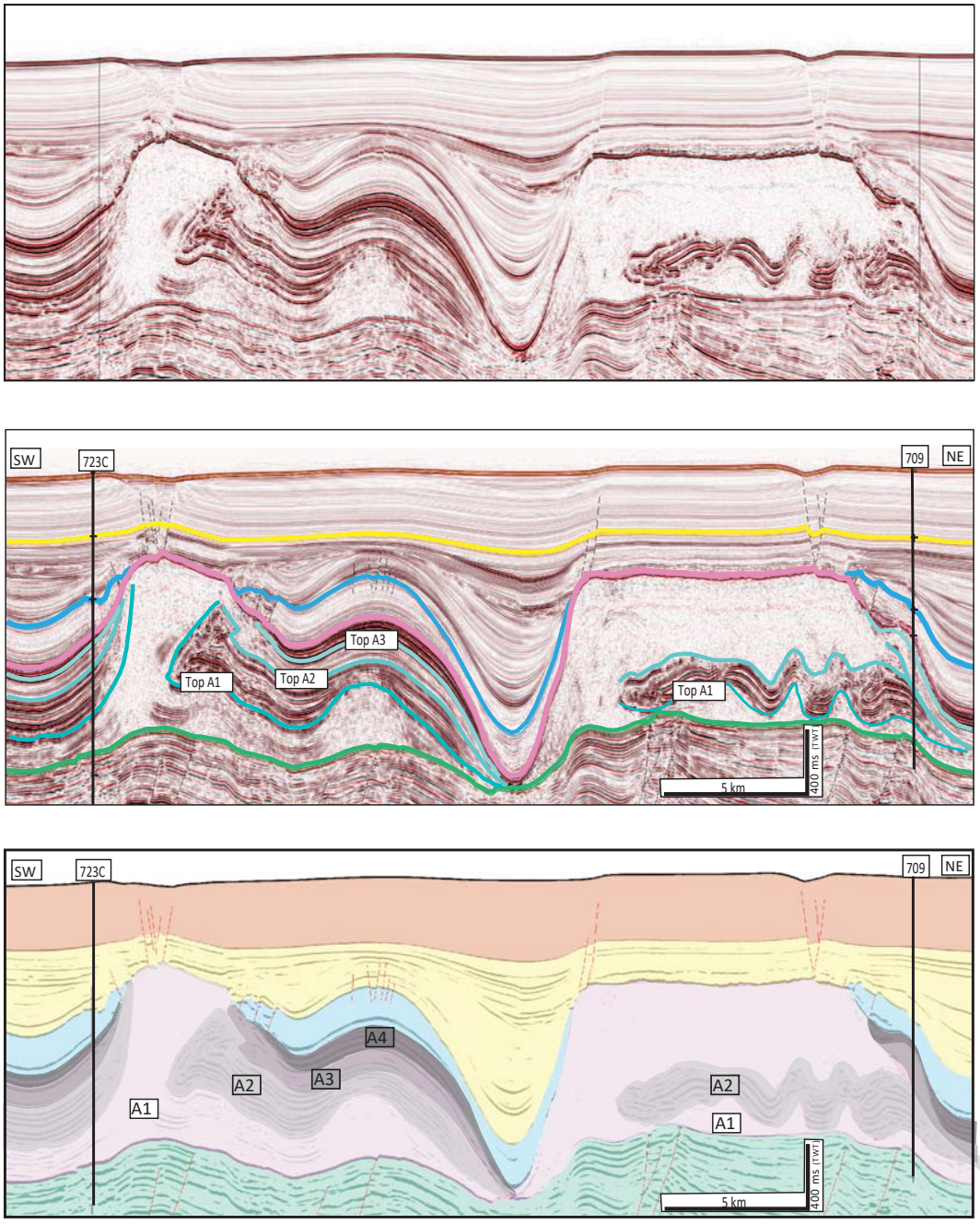


FIGURE 5.5: Seismic and geoseismic profiles across 2 boreholes in the study area. Seismic data courtesy of CGG. See Figure 5.2b for location

5.5 Structural framework

Overall, the base and top of the salt are represented by continuous, high amplitude, regionally mapable seismic reflections (Figs. 5.4 and 5.5). The high amplitudes are produced by the high acoustic impedance contrast between the salt and the underlying lacustrine shales and carbonates (Guaratiba Group; i.e. base salt), and between the salt and the overlying carbonates and deep-water marls (Guaruja Formation; i.e. top salt). Lateral changes in base salt reflectivity likely reflect changes in the lithology of rocks underlying and overlying this boundary.

The base salt depth map illustrates the present subsalt structure of the basin, indicating the presence of two prominent structural highs in the south (the Sugar Loaf sub-high) and east (the Tupi sub-high) of the study area (Fig. 5.6a) (e.g., Gomes et al., 2009). North and northwest of the highs, the base salt dips gently (5-7°) landward, with this dip estimated using the base salt depth map (Fig. 5.6a). Overall, base salt is concordant with underlying subsalt seismic reflections (Fig. 5.7). However, over some parts in the Sugar Loaf and Tupi sub-highs, underlying units are truncated against base salt in the footwalls of subsalt, rift-related normal faults (Fig 5.7a). Moreover, in the Outer High, a series of predominately NNE-SSW-striking fault systems offset the base of the salt by as much as 100 ms TWT (c. 450 m) (Figs 5.6a and 5.7). The Top Ariri depth-structure map illustrates the present salt-related structure of the basin and salt thickness variations (Fig. 5.6b). The salt is up to 4.9 km thick in the cores of large salt diapirs and is possibly absent in apparent welds underlying deep minibasins (Figs 5.6c, 5.7b) (see also Jackson et al., 2014a).

Based on the base salt geometry, and variations in salt thickness and salt-related structural styles, I identify four main structural domains in the São Paulo Plateau, (Table 2; Figs 6c and 7). The thick salt domain - this domain is characterised by the greatest mean salt thickness (c. 2.2 km), with very thick salt (up to 4.9 km) present in salt walls. Furthermore, the base salt is at its deepest in this domain (7.5 km) and no welds are developed, with the minimum salt

thickness being c. 2 km. The Sugar Loaf domain – this overlies a semi-regional structural high at the base of salt (i.e. the Sugar Loaf sub-high; Fig. 5.6a). The mean salt thickness in this domain is c. 1.8 km and characterised by the development of N- and NE-trending salt walls, within which salt is up to c. 3 km thick (Table 2, Fig. 5.6c). Some of these salt walls have flat tops beneath which the intrasalt stratigraphy is truncated. Complex intrasalt folding and thrusting is also observed in salt walls in the Sugar Loaf domain (Fig. 5.7b; see also Fiduk and Rowan, 2012; Jackson et al., 2014, 2015b). The minibasin domain – this is defined by a structural low at base salt level, a mean salt thickness of c. 2 km, and thick minibasins enclosed by large, N-, E- and NE-trending salt walls (Fig. 5.6b, c). The walls are 50 km long, 5-10 km-wide and up to 4.9 km thick, with salt welds developed beneath many of the minibasins (Table 2, Fig. 5.6b) (see Jackson et al., 2014a). And the Tupi domain – this overlies the Tupi sub-high, a semi-regional structural high at the base of salt. The mean salt thickness in the Tupi domain is c. 1.9 km and the salt-tectonic structural style is characterised by a network of minibasins arranged in a polygonal pattern, enclosed by c. 20 km long, c. 2-4 km wide, N-, E- and NW-trending salt walls (Figs. 5.6b, c and 5.7c). Salt diapirs in the Tupi domain are of lower amplitude (up to c. 2.7 km) than those in the minibasin domain (up to 4.8 km). No welds are observed in the Tupi domain, where the minimum salt thickness is c. 1 km. Salt-related structural styles and thickness variations suggest that less salt flow occurred here than in the highly-deformed minibasin domain (Fig. 5.7c). In the transition between the structurally-high Tupi and Sugar Loaf domains and the structurally-low minibasin domain and thick salt domain, the base salt dips landwards and shortening-related salt-cored buckle folds are observed (Fig. 5.7a, b) (Cobbold and Szatmari., 1991; Jackson et al., 2015).

My observation suggests that intrasalt deformation is relatively mild in the locations of borehole 532A and 723C where little post-depositional salt flow has occurred. It is these two boreholes that are the key to describing intrasalt evaporite cycles and the associated impact syndepositional basin physiography had on salt deposition (Table 2). For example, near borehole 532A, intrasalt deformation is modest and expressed by several low-relief, locally

developed, salt-cored buckle folds; whereas borehole 723C is located near the flank and at the tip of a salt wall, where internal deformation is overall less than observed elsewhere. In addition, mean salt thickness at borehole 532A (2.3 km) is also consistent with previous estimations made of the depositional salt thickness in central deepwater Santos Basin (Davison et al., 2012). Previous studies have also documented shortening of the salt layer in the study area in the form of low-amplitude buckle folds, intrasalt shear zones, diapir squeezing and local thickening of the salt layer and support that no major translation of the salt layer occurred within the study area after salt deposition (e.g., Cobbold et al., 1995; Gambôa et al., 2008; Jackson et al., 2015a).

TABLE 5.1: Evaporites typical borehole log response expected from wireline logs. Information gathered from literature review (After Mohriak et al. 2009; Schlumberger, 1991; Halliburton, 1994)

	Mineral	Formula	Density (gr/cm3)	Δt (μs/ft)	Neutron porosity	Gamma Ray
	Halite	NaCl	2.03	67	0	0 - Very low
	Anhydrite	CaSO4	2.98	50	From -1 to 0	0
	Gypsum	CaSO4 (H2O)2	2.35	52.5	49	0
Bittern Salts (K- Mg salts)	Sylvite	KCl	1.86	74	0	500+
	Polyhalite	K2SO4.MgSO4.2CaSO4.2H2O	2.79	57.5	15	180-200
	Carnalite	KMgCl3.6H2O	1.57	78	65	200-220
	Tachhydrite	CaCl2(MgCl2)2(H20)12	1.66	92	-	Low

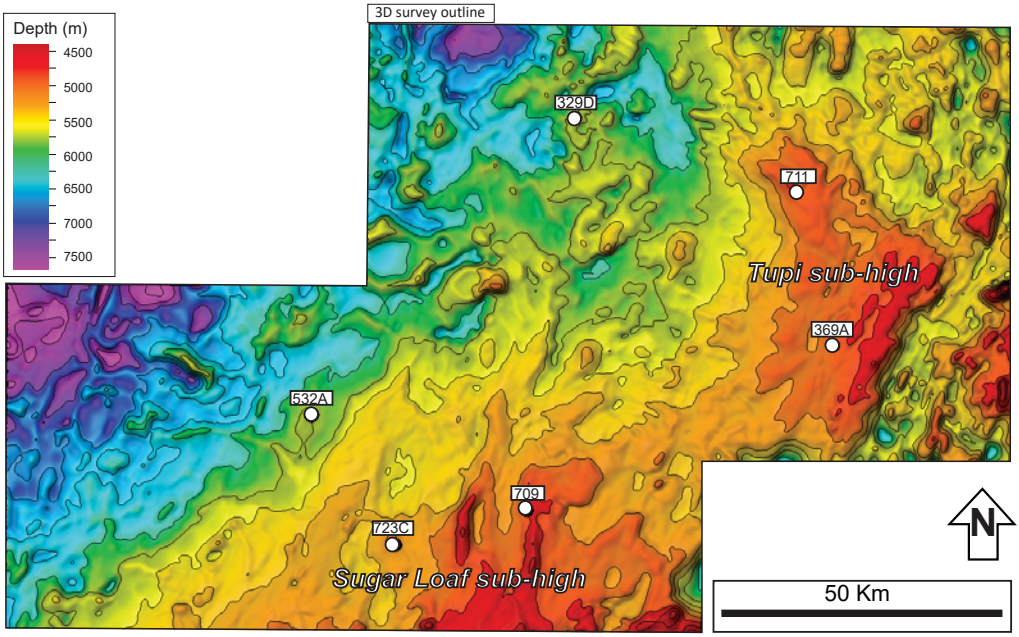


Figure 5.6 a: Base of salt depth-structure map

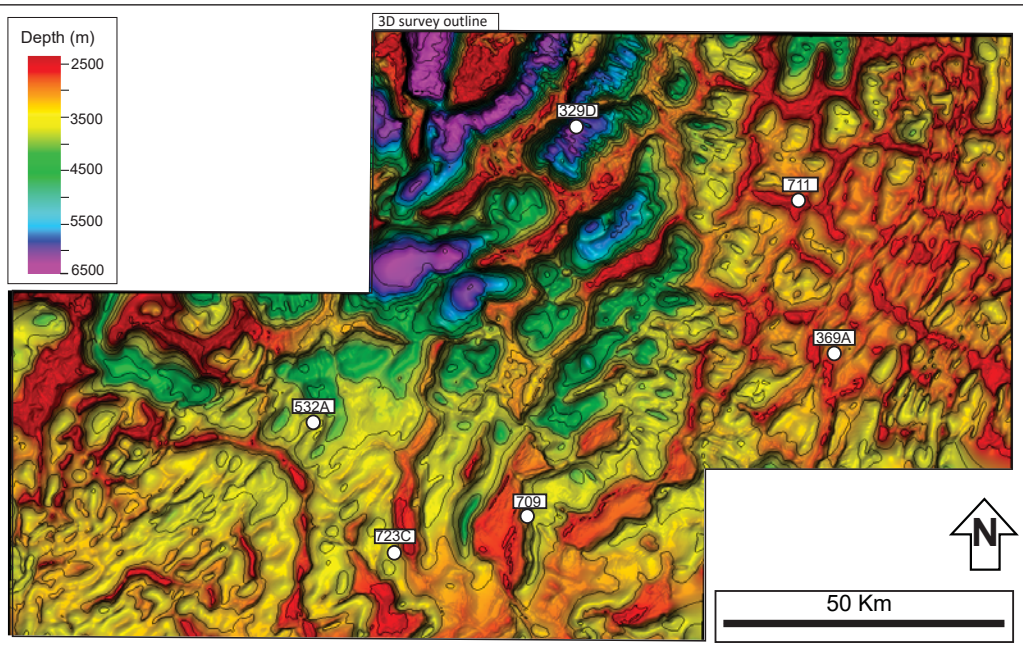


Figure 5.6 b: Top of salt depth-structure map

FIGURE 5.6: Present-day structural framework of the study area: (a) Base of salt depth-structural map illustrating the sub-salt basin physiography and the presence of the Sugar loaf and Tupi sub-highs; (b) Top of salt depth-structure map illustrating the salt-related structural domains; and (c) Salt thickness map in depth.

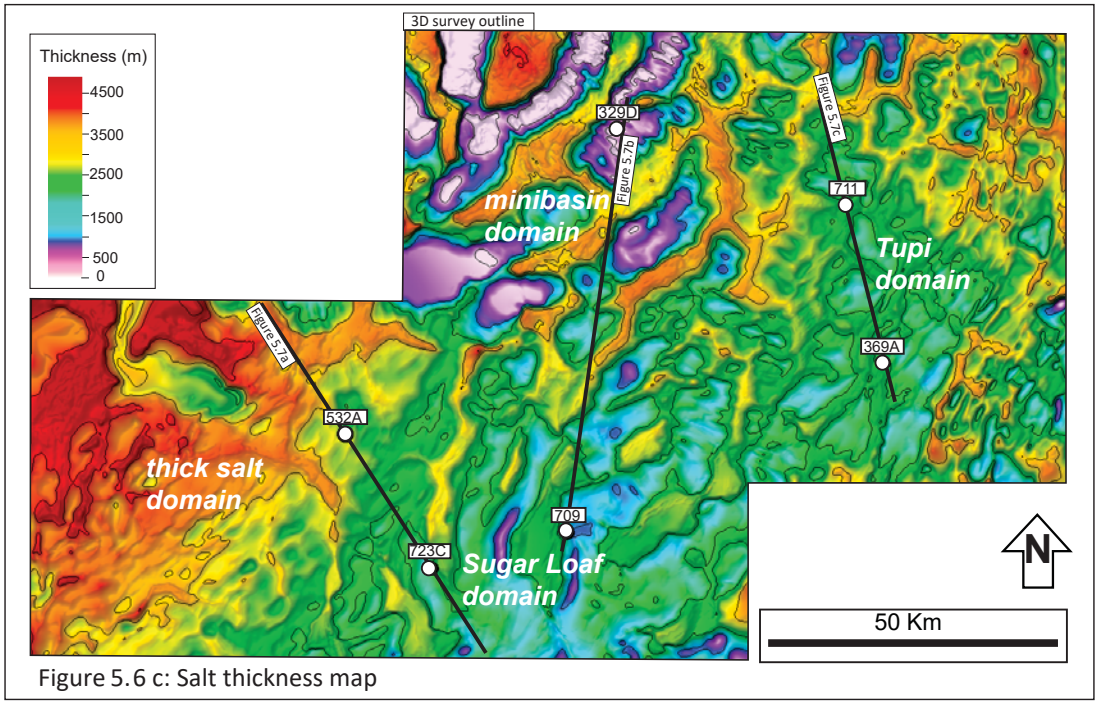


Figure 5.6 c: Salt thickness map

TABLE 5.2: Structural domains

Structural domains	Depth to base salt	Mean salt thickness	Borehole	Salt-related deformation at the borehole location	Salt thickness(at the borehole location)
thick salt domain	6 km - 7.5 km	2.2 km	532 A	area characterised by locally developed salt-cored buckle folds	2.3 km
Sugar Loaf domain (overlies the Sugar Loaf sub-high)	4.4 km - 5.5 km	1.8 km	723C	located near the flank and at the southern tip of a salt wall	1.8 km
			1-ESSO-3	area characterised by locally developed salt-cored buckle folds (2D seismic line)	1.3 km
			709 C	near a salt wall flank	1.4 km
minibasin domain	5.5 km - 7.5 km	2 km	329D	penetrates a salt weld within a deep minibasin	22 m
Tupi domain (overlies the Sugar Loaf sub-high)	4.4 km - 5.5 km	1.9 km	711	penetrates a salt-cored diapir	2.2 km
			369A	near the flank of a salt-cored high	1.9 km

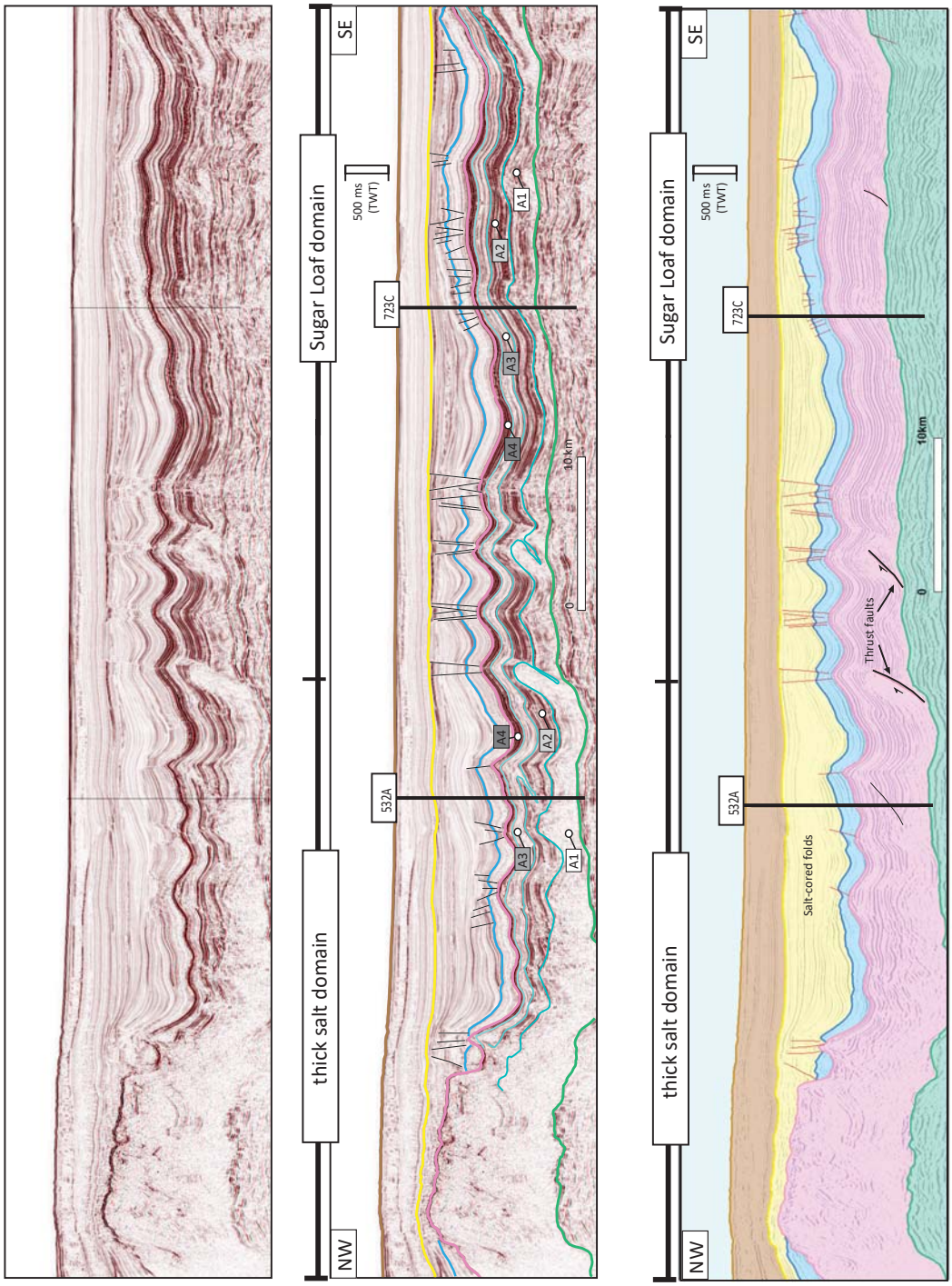


FIGURE 5.7a. NW-SE seismic and geoseismic cross-sections and mapped horizons illustrating the salt thickness variations and the seismic expression of the intrasalt key stratigraphic intervals across the Thick Salt and Sugar Loaf domains

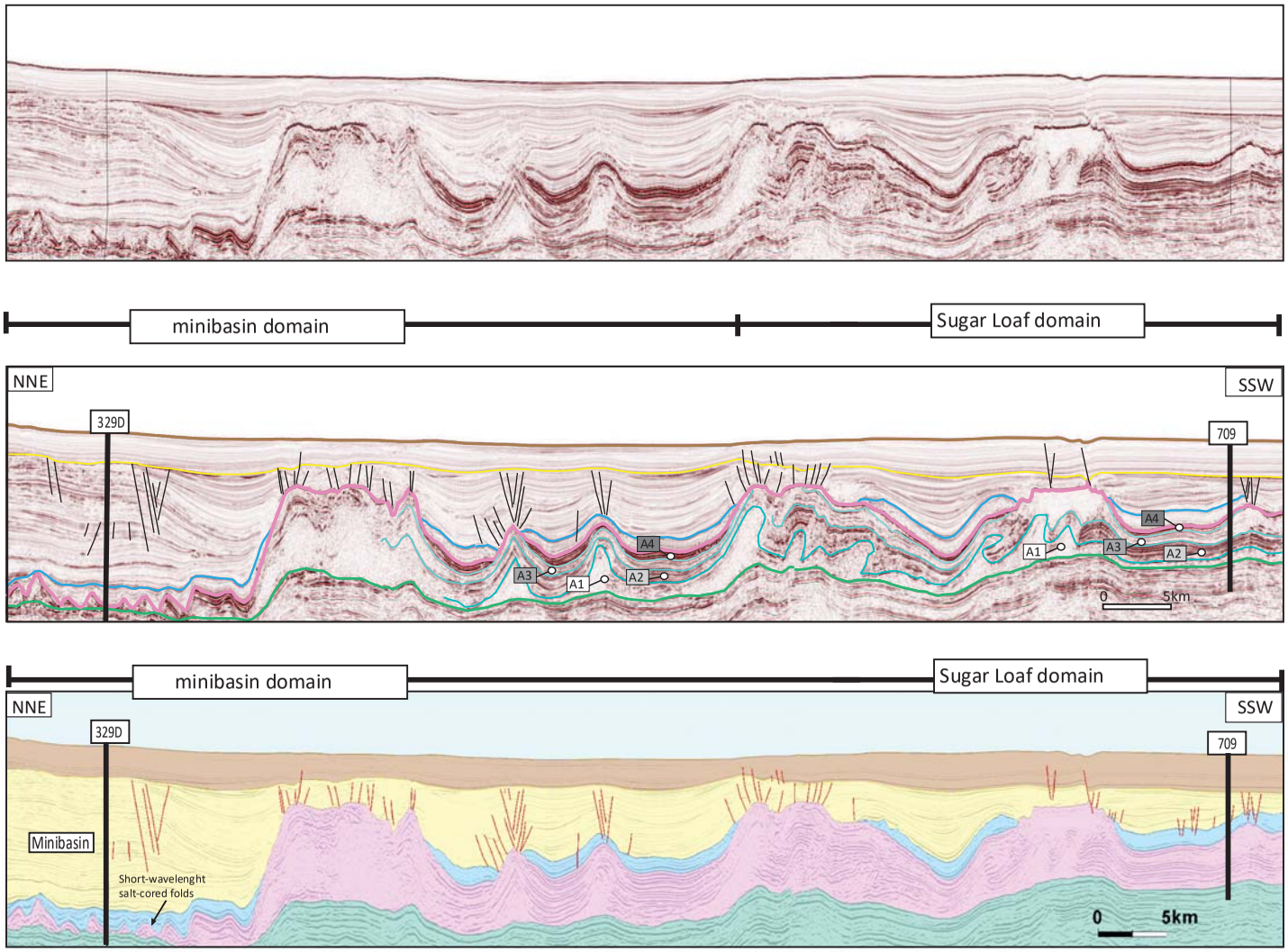


FIGURE 5.7b. NNE-SSW seismic and geoseismic cross-sections with the mapped horizons illustrating the salt thickness variations and intrasalt seismic expression from the minibasin domain towards the Sugar Loaf domain

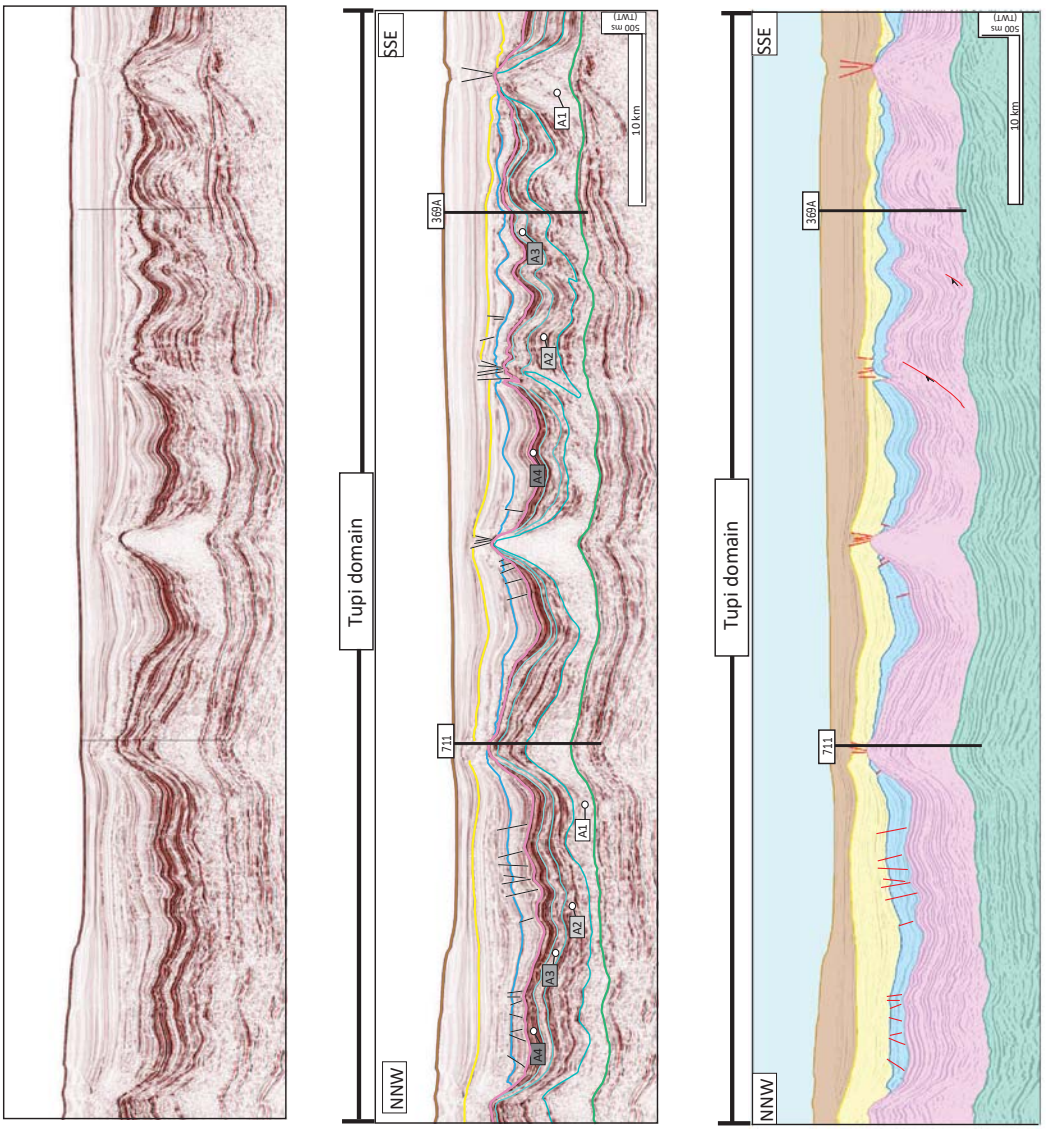


FIGURE 5.7c. NNW-SSE seismic and geoseismic cross-section illustrating the salt thickness variations and intrasalt seismic expression across the Tupi domain. See Figure 5.5c for locations. 3D seismic data courtesy of CGG

5.6 The Ariri Formation: Composition and seismic expression

Before I can investigate the controls on salt deposition, I need to understand the intrasalt composition and architecture. In this section, I describe the overall composition and seismic expression of the Ariri Formation before describing its constituent sub-units.

5.6.1 Composition

Borehole data available indicate that the Ariri Formation is mainly composed of halite (82%), anhydrite (11%) and bittern salts (7%), the latter being composed of mainly carnallite (6%) and tachyhydrite (1%) (Fig. 5.9). The borehole located in the minibasin domain penetrates a relatively thin (c. 22 m), halite-absent salt sequence, with the Ariri Formation composed of anhydrite (40%; c. 8.7 m) and non-evaporitic lithologies (i.e. sandstone - c. 3.5 m or 16%; carbonate - c. 8.9 m or 40%; and marl - c. 0.8 m or 4%) (borehole 329D, Fig. 5.9b, see also Jackson et al. 2014b).

5.6.2 Seismic expression of intrasalt units

The good seismic resolution within the salt (c. 29-33 m) permits evaporite layers of specific composition to be tied to individual reflections or reflection packages (Fig. 5.8). Overall, high-density anhydrite layers tie with high-amplitude positive reflections (black peaks), whereas low-density carnallite layers tie with high-amplitude negative reflections (red trough) (Fig. 5.8). Thinner (<24 m) carnallite and anhydrite layers interpreted from the borehole logs are not resolvable in seismic data, whereas thicker (c. 34-100 m), halite-rich layers broadly correlate with packages of low-amplitude, moderately chaotic reflections (Fig. 5.8). Evaporite beds of varying composition can also be identified in a Relative Acoustic Impedance (RAI) volume (Savic 2006; Suarez et al. 2008), with carnallite and anhydrite defined by low and high acoustic impedance values respectively.

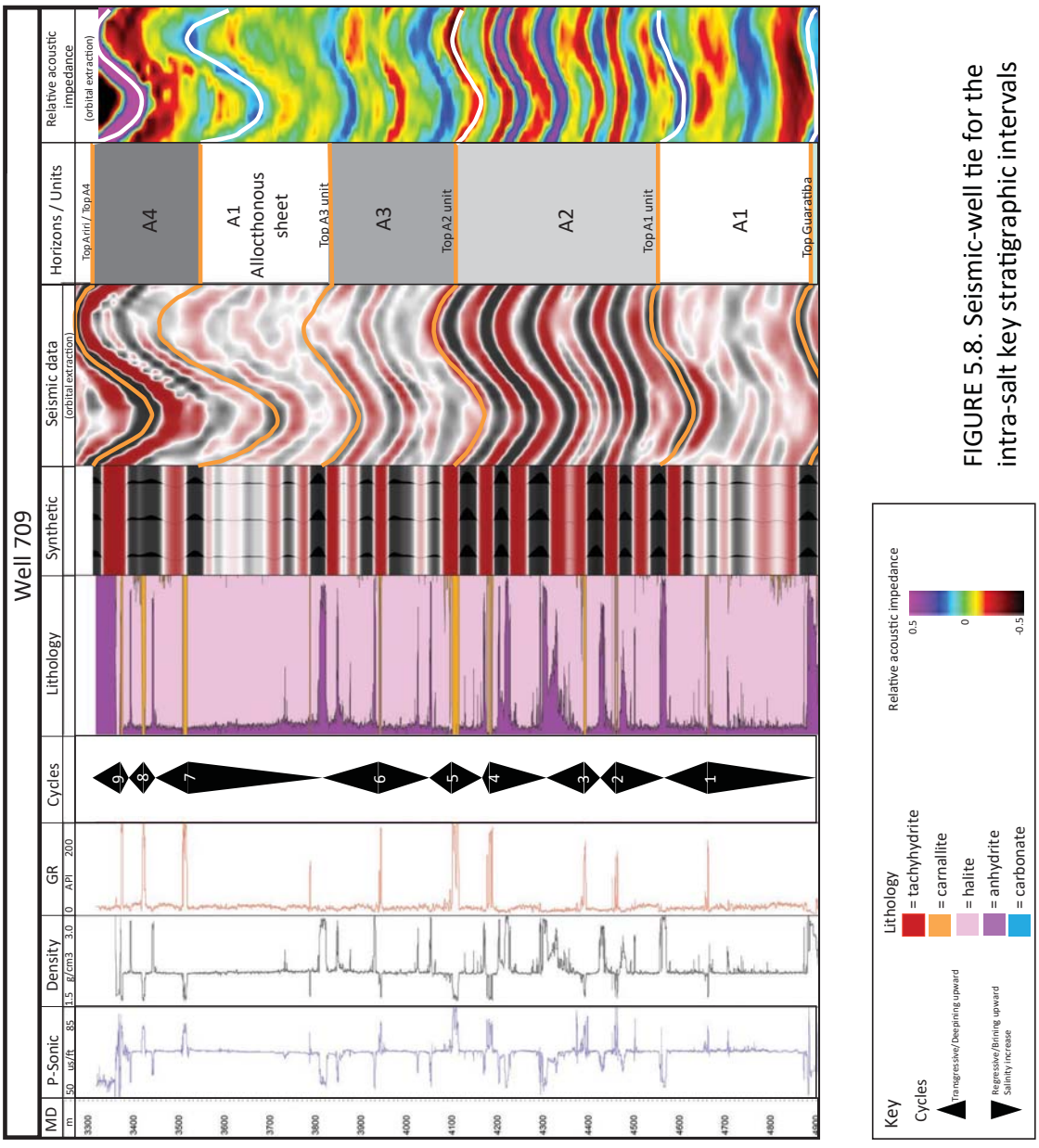


FIGURE 5.8. Seismic-well tie for the intra-salt key stratigraphic intervals

5.7 The Ariri Formation: Key stratigraphic intervals

Based on seismic reflection and borehole data, I define four intra-Ariri Formation stratigraphic intervals (A1-A4; Figs. 5.5 and 5.8). Although considerable post- and possibly syn-depositional salt flow has occurred in the Santos Basin (e.g., boreholes 329D, 709, 711) the near-depositional evaporite stratigraphy seems to be reasonably preserved away from the main diapirs; even within these structures the intrasalt stratigraphic intervals can be mapped with reasonable confidence (Figs. 5.7 and 5.9; see also Jackson et al., 2014b, 2015a). As described above, the seismic expression of the key stratigraphic intervals can be correlated to the composition of the salt from the boreholes, where highly reflective continuous intervals like A2 and A4 correspond to high acoustic impedance anhydrites interbedded with low acoustic impedance carnallite and halite; these units are also characterised by several complete evaporite cycles (boreholes 709 and 723C, Figs. 5.8 and 5.9). In contrast, A1 and A3 are more relatively halite-rich and contain lesser proportions of anhydrite and bittern salts, hence contain less complete evaporite cycles (boreholes 709 and 723C, Figs. 5.8 and 5.9). Detailed variations in the thickness and composition, and the seismic expression of the intrasalt units are described below.

A1: Seismic expression, thickness and composition

The top of A1 is defined by a positive reflection that correlates to an anhydrite layer (Fig. 5.8). The base of A1 is defined by a positive seismic reflection, which correlates to an anhydrite layer overlying the carbonates and shales of the Barra Velha Formation (Figs. 5.8 and 5.10). Seismic data indicate that A1 is generally characterised by low-frequency, discontinuous to locally transparent, chaotic seismic facies, although stronger, more continuous reflections are locally observed (Figs. 5.5 and 5.7). The chaotic seismic facies are particularly evident in the proximal, structurally lower domains (near boreholes 532A and 711 in the thick salt domain and Tupi domain; Fig. 5.7). Conversely, continuous, high-amplitude reflections are more

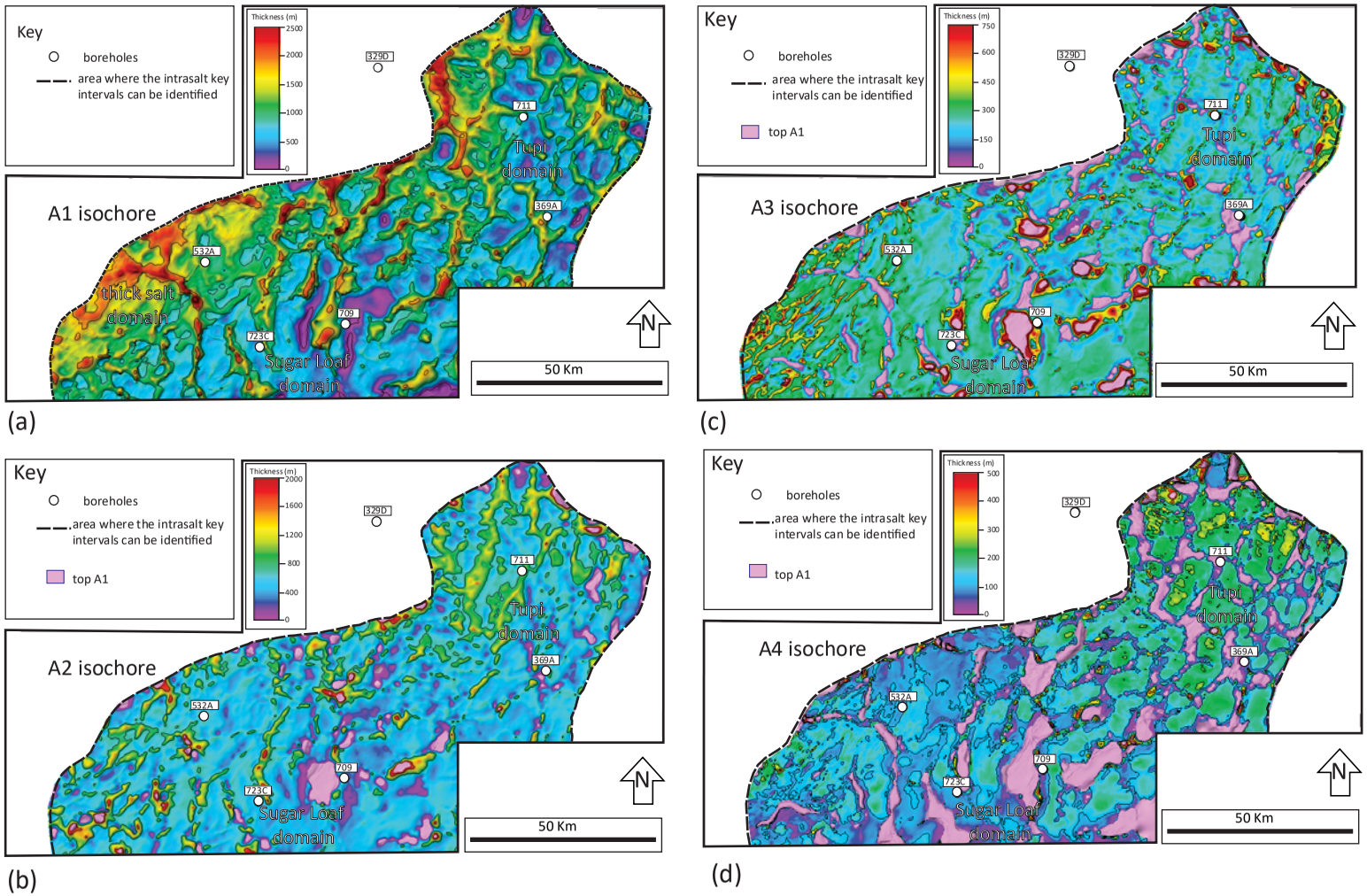


Figure 5.9: (a) A1 thickness map in depth; (b) A2 thickness map in depth; (c) A3 thickness map in depth; (d) A4 thickness map in depth. The isochores illustrate intra-salt diapirsm by A1 (in pink)

Table 5.3. Key stratigraphic intervals. Thickness ranges estimated from isochores and borehole data in areas where less post-depositional salt flow has occurred. Evaporite proportions across domains are also included.

		Thickness (m)*	Evaporite cyles (723C)	Anhydrite net thickness (m)			Halite net thickness (m)			Bittern salts net thickness (m)		
				TSD	Tupi	Sugar Loaf	TSD	Tupi	Sugar Loaf	TSD	Tupi	Sugar Loaf
Key intervals	A1	500 m - 1200 m	3	40	40	100	720	950	400	20	50	10
	A2	400 m - 750 m	5.5	50	40	100	560	650	400	90	85	30
	A3	150 m - 300 m	2	10	15	35	350	140	240	10	95	5
	A4	150 m - 250 m	1.5	65	15	20	90	15	120	40	25	20
Ariri Formation		1200 m - 2500 m	12	165	145	255	1720	1755	1160	160	255	65

*Thickness estimated from the boreholes and isochores in less-deformed areas

common on structurally-higher locations (near borehole 723C and 369A in the Sugar Loaf domain and Tupi domain; Fig. 5.7).

Seismic data indicate pronounced thickness variations (0-2500 m) in A1, principally related to salt tectonics (Fig. 5.9a). Where A1 can be identified in the study area, major thickness variations occur in the thick salt domain and locally on the Sugar Loaf domain where this unit has been expelled from below minibasins into flanking walls (borehole 709; Fig. 5.9a). In contrast, thickness variations and, I infer, salt flow is more subtle in the structurally higher Tupi domain, the Sugar Loaf domain near borehole 723C and in the thick salt domain near borehole 532A (Fig. 5.9a). In these areas, where the salt seems to have moved less, seismic and borehole data suggest A1 thickness range between 500 and 1200 m (Figs. 5.9a and 5.10). Overall, A1 is moderately thinner (by c. 200 m) in the distal, structurally higher domains than in the proximal, structurally deeper domains (boreholes 532 and 723C, Fig. 5.10a).

Borehole data available indicate that A1 is dominated by halite (87%), and relatively small amounts of anhydrite (10%), bittern salts (2.7%) and carbonate (0.3%) (Fig. 5.10). Although A1 is generally halite-rich, lateral stratigraphic variations are observed between boreholes located on different structural domains. Anhydrite net thickness increase by more than 50 m

from structurally deeper locations (borehole 532A) towards, structurally higher locations (borehole 723C; Figs. 5.7a and 5.10a). An increase in anhydrite proportion towards the Sugar Loaf domain is complemented by a decrease in the amount of halite and bittern salts (Table 5.3; Fig. 5.10a). Bittern salts are rare in Al, especially in distal boreholes located in the structurally high Sugar Loaf domain. However, bittern salts are volumetrically important (> c. 23 m) in the present-day structurally high Tupi domain (Table 5.3; Fig. 5.10b). I identify three complete evaporite cycles where borehole data penetrates A1 (borehole 723C, Fig. 5.10a).

A1: Interpretation

My analysis reveals an overall link between the seismic expression, thickness and composition of A1 (Table 5.3). Where A1 is more continuous, highly reflective and thinner (c. 500 m), anhydrite is more common (>15%) and bittern salt is rare (<1%). In contrast, where A1 is discontinuous, transparent and thicker (>600 m), bittern salt is more common (>3%) and anhydrite is relatively rare (<8%).Based on this relationship I interpret that the syn-depositional basin physiography directly controlled deposition of A1, with gypsum (now anhydrite) deposition occurring preferentially in the Sugar Loaf domain, which I suggest, was structurally higher than the surrounding domains at the onset and during A1 deposition thus promoting vertical salinity variations in the São Paulo Plateau. In contrast, the Tupi domain, minibasin domain and the thick salt domain were structurally lower and more hydrologically isolated than the Sugar Loaf domain, thus promoting more halite and bittern salt deposition (Fig. 5.12). I suggest that higher anhydrite deposition in the Sugar Loaf domain occurred during highstands due to renewed seawater inflow and lower salinities. In contrast, the basin was more isolated and deeper towards the minibasin domain, Tupi domain and the thick salt domain, thus promoting higher salinities during lowstands and hence more halite and bittern salt deposition when the salt basin became partially or almost completely desiccated. The number of evaporite cycles I identify in A1 suggest the basin was almost or completely desiccated (lowstands) and refilled

(highstands) at least three times during the deposition of this unit.

A2: Seismic expression, thickness and composition

The top of A2 is defined by a negative reflection and correlates with a laterally extensive carnallite layer (Fig. 5.8). Seismic data indicate that A2 is characterised by high-frequency, highly-reflective, sub-parallel to parallel reflections (Figs. 5.7 and 5.8). The highly-reflective packages within A2 are more evident in the distal and structurally higher Sugar Loaf domain (i.e., near boreholes 723C and 709; Fig. 5.7). In the thick salt domain and Tupi domain, A2 is characterised by more transparent or lower-amplitude seismic facies (i.e. near boreholes 532A, 369A and 711; Fig. 5.7). Seismic data indicates that A2 varies from 0 to 2000 m (Fig. 5.9b). However, local thickening of A2 is associated with shortening, folding and thrusting of the entire salt sequence, whereas localised thinning of A2 is associated with expulsion of A1 into diapirs and, in and some cases, allochthonous salt sheets (Figs. 5.5 and 5.7; see also Jackson et al. 2014a). In areas where I infer the salt has moved less, seismic and borehole data indicate that A2 ranges between 400 m and 700 m (Figs. 5.7a and 5.9b). Overall, A2 is thinner (by c. 65 m) in the distal, structurally higher domains than in the proximal, structurally deeper domains (see boreholes 532 and 723C, Figs. 5.7a and 5.10a). It is important to note that this estimation takes into consideration structurally-induced thickness variations, such as the intrasalt shear zone-related stratigraphic repetition observed in borehole 532A (Fig. 5.7a).

Borehole data available indicate that A2 is also relatively halite-rich (79%), although it contains slightly less halite than A1 (i.e. 87%) and, as a result, more anhydrite (12%) and bittern salt (9%). I observe lateral compositional variations between boreholes located in different structural domains. For example, anhydrite thickness increases (by >50 m) and halite and bittern salt decreases (by c. 250 m and c. 55 m, respectively) from structurally deeper (i.e. boreholes 532A, 369A and 711) to structurally higher locations (borehole 723C, Table 5.3, Figs 5.7a, 5.10a and 5.11). I identify at least five and a half evaporite cycles within A2; this is almost

twice the number of cycles identified within A1 (Boreholes 532A and 723C, Fig. 5.7a).

A2: Interpretation

Like A1, my analysis reveals a strong link between the seismic expression and composition of A2, with the high-frequency and strongly-reflective nature of this unit reflecting vertical changes in acoustic impedance related to the interbedded nature of the contained lithologies (i.e. anhydrite, halite and bittern salts). I suggest that the higher proportion of anhydrite and bittern salt in A2 than A1 are due to more and greater magnitude of water depths variations, hence salinity fluctuations in the basin during this time. More specifically, based on the occurrence of at least six intra-A2 evaporite cycles, I infer that, during A2 deposition, the basin was partially or completely desiccated and refilled at least six times (borehole 723C, Fig. 5.7a).

I interpret that the syn-depositional basin physiography controlled deposition of A2, in a similar manner to that inferred for A1. A thinner salt sequence and more gypsum (now anhydrite) was deposited onto the structurally higher and shallower Sugar Loaf domain, in comparison with the surrounding domains where the salt sequence was thicker, anhydrite-poor and halite-rich (Figs. 5.11 and 5.12). However, more subtle thickness and stratigraphic variations in A2, in comparison to A1, suggest subtler basin relief and broadly similar water depths between structural domains at this time (Figs. 5.11 and 5.12).

A3 interval: Seismic expression, thickness and composition

The top of A3 is defined by a positive reflection event and, in some locations, like in the Tupi domain, intra-A3 reflections are truncated beneath top salt (borehole 711, Figs. 5.7c. Overall, A3 is characterised by transparent, discontinuous, sub-parallel reflections (Figs. 5.5 and 5.8). Although the seismic expression varies across the study area, in the distal and structurally-high Sugar Loaf domain, A3 highly reflective and dominated by continuous reflections, whereas in

the more proximal Tupi domain and structurally-lower thick salt domain, it is defined by more transparent, chaotic reflections (Fig. 5.7).

Seismic and borehole data indicate that A3 varies between 0 and 750 m and it is characterised by structurally-induced thickness changes related to shortening of the salt sequence, and associated folding and thrusting (Fig. 5.9b; see also Jackson et al. 2014a). A3 is thinner and truncated near and on top of some of the large salt-structures. For example, 12% thinning of A3 from borehole 369A to borehole 711 in the Tupi domain is due to erosion/dissolution at the crest of a salt wall (Figs. 5.7c). Apparent thickening of A3 in borehole 709 in the Sugar Loaf domain is due to the emplacement of an A1-sourced allochthonous salt sheet (Figs. 5.5 and 5.8; see also Jackson et al. 2014a). Seismic data and boreholes that penetrate A3 away from areas of major intrasalt deformation indicates that A3 thickness ranges between 150 m and 300 m and that only minor lateral thickness variations are observed between structural domains (Fig. 5.9c). For example, A3 thins by only c. 21 m (5%) from the proximal and structurally low thick salt domain towards the distal and structurally-high Sugar Loaf domain (boreholes, 532A and 723C Figs. 5.7a and 5.10a).

A3 is composed of halite (87%), anhydrite (8%) and bittern salts (5%), although lateral variations in the proportions occur between structural domains (Table 5.3). Higher proportions of anhydrite occur in the distal and structurally-high Sugar Loaf domain (average c. 35 m; boreholes 723C, 1-ESSO-3) when compared with the structurally-low thick salt domain (c. 10 m; borehole 532A) and more distal Tupi domain (c. 15 m; boreholes 711 and 369A; Table 5.3, Fig. 5.10). I identify two evaporite cycles in locations where A3 is less deformed (borehole 723C, Fig. 5.10a).

A3: Interpretation

I interpret that the weakly reflective, chaotic seismic expression of A3 reflects the fact this unit

is more halite-dominated, and thus compositionally and acoustically homogeneous than A1 or A2. In turn, this interpretation suggests that, during A3, the Santos Basin saw an increase in halite precipitation and overall consistently higher salinities than during deposition of A2 (Fig. 5.12). During A3 deposition, the basin was desiccated only once as suggested by the intra-A3 evaporite cycles (borehole 723 C, Fig. 5.10a). My analysis shows that syn-depositional basin physiography likely influenced A3 thickness and stratigraphy, but to a more limited extent than for A1 or A2; this interpretation is based in the more subtle thickness and compositional changes that occur between structural domains in A3. From this, one may infer that A1 and A2 had largely filled the pre- or syn-depositional relief, thus resulting in an overall flatter basin (Fig. 5.12).

A4: Seismic expression, thickness and composition

The top of A4 (top salt) is interpreted as a positive reflection event. Locally, the top of A4 is defined by an angular and erosional unconformity, with intra-A4 and A3 reflections being truncated beneath it (Fig. 5.7). Borehole data indicate that Top A4 correlates to a thick anhydrite layer (Figs. 5.8 and 5.10). Seismic data indicate that A4 is generally characterised by high-frequency, highly reflective, sub-parallel reflections. No significant lateral changes in intra-A4 seismic facies are observed between structural domains (Fig. 5.7).

Seismic and borehole data indicate that A4 thins towards and is absent at the crest of salt walls, and thickens towards the flanking minibasins ranging in thickness from 0 and 500 m (Fig. 5.9d). Post-depositional, structurally-induced variations in the thickness of A4 are particularly clear in borehole 709C, where they are related to the emplacement of an A1-salt sheet (see also Jackson et al. 2014a; Figs 5.7b; 5.8). Seismic data and boreholes that penetrate A4, indicate that in less-deformed areas A4 thickness ranges between 150 m and 250 m. In areas where A4 is not truncated at top salt, borehole data indicates that only very minor thinning (c. 1 m; 0.8%) of the unit occurs between the structurally low thick salt domain (borehole 532A) and

the structurally higher Sugar Loaf domain (borehole 723C) (Figs. 5.7a and 5.10a).

Borehole data indicate that A4 is composed by halite (64%), anhydrite (17%) and bittern salts (19%); A4 is thus the most halite-poor, bittern salt-rich unit developed within the Ariri Formation. However, in contrast to A1-A3, A4 contains significantly lower proportions of anhydrite and carnallite proportions in the structurally higher Sugar Loaf domain (c. 20 m, c. 20 m) when compared to the structurally lower thick salt domain (c. 65 m, c. 40 m) (Table 5.3; Fig. 5.10a). I identify one and a half evaporite cycles in A4 (borehole 723C, Fig. 5.10a).

A4: Interpretation

The highly reflective character of A4 reflects its compositional and acoustically heterogeneous characters, with halite being interbedded with high acoustic impedance anhydrites and low acoustic impedance carnallite (Fig. 5.8). I interpret that the heterogeneous character of A4 reflects higher salinity fluctuations in the basin during its deposition, with these fluctuations perhaps being of a similar magnitude to those occurring during A2 deposition. During A4 deposition, the basin was partially or completely desiccated at least twice, based on my identification of evaporite cycles in a location where the salt is relatively undeformed (borehole 723C; Fig. 5.10a). I suggest that thinning of A4 towards the largest salt walls is due to post-depositional salt flow, erosion and dissolution (Figs. 5.7 and 5.10). The top of A4 defines the end of evaporite deposition, and a transition to more fully marine conditions characterised by deposition of deepwater carbonates and marls. The Albian thus defines a relatively desalinisation of the basin related to basin deepening and an influx of seawater (Modica and Brush, 2004; Moreira et al., 2007).

Assessing the role of basin physiography on A4 deposition is difficult due to the significant post-depositional variations in thickness caused by salt flow and related dissolution. However, only minor thinning of A4 towards the structurally-higher Sugar Loaf domain may indicate that

earlier-deposited units (A1-A3) had filled and smoothed out any pre- or syn-depositional relief by the onset of A4 deposition (Fig. 5.12).

5.8 The Ariri Formation: Key controls on the composition and stratigraphic architecture and their significance

I found that the composition and stratigraphic architecture of the Ariri Formation directly controls its seismic expression. Low-frequency, acoustically transparent, chaotic seismic facies represent relatively halite-rich (>80%) units, whereas high-frequency, highly-reflective seismic facies represent still relatively halite-rich (65-85% halite) units, but which contain relatively high proportions (15-35%) of anhydrite and carnallite (Fig. 5.7). Additionally, my findings suggest that variations in the thickness and composition, the latter inferred from seismic expression or directly constrained by boreholes, of the Ariri Formation are spatially related to structural domains. Overall, thinner salt (mean salt thickness <1.9 km) and higher anhydrite net thickness (c. 350 m) occur towards the structurally high Sugar Loaf domain, compared to flanking, structurally lower domains where the mean salt thickness is >2.4 km and anhydrite net thickness are less (c. 180 m). I also note that anhydrite proportions substantially differ between the Tupi (5% average) and Sugar Loaf (19% average) domains, even though both occur in the Outer High and have comparable depths to present-day base of salt.

I observe three key controls on the compositional variations and overall stratigraphic architecture; i.e. climate and sea-level, syn-depositional basin physiography and hydrology. These results raise some key questions: (i) can these elements provide any clues about duration of deposition? how rapid was the thick salt deposited?; (ii) can the basin physiography be constrained using the observed stratigraphic and thickness variability, and what does this reveal regarding the basin origin and accommodation development? ; (iii) Are there any indications of freshwater inflow from the continent during salt deposition, or any evidence

about the direction of seawater inflow?

5.8.1 Climate, water depth and duration of deposition

I suggest that the compositional variations that define the four intrasalt units (A1 to A4) arose due to changes in water depth and the frequency of marine incursions and near desiccation episodes during the Late Aptian in the Santos Basin. I thus suggest the Santos Basin was characterised by very low water depths and then refilled at least 12 times, based on the identification of 12 more-or-less complete evaporite cycles. During deposition of the up to c. 1000 m thick, halite-rich A1 unit, I infer that the salt basin was partly or completely desiccated and refilled three times; in contrast, during deposition of the thinner (up to c. 600 m), relatively halite-poor A2 unit, the basin was partly or completely desiccated and refilled at least six times. Similar intervals are interpreted in the northern Espirito Santo Basin, where analysis of 345 m of cores from five boreholes indicates that the lower part of the Aptian Ibura salt sequence is dominated by halite, suggesting it was deposited during a relative sea-level lowstand, whereas the upper part is dominated by anhydrite deposited during periods of rising relative sea-level (Dias, 2004). My analysis of the salt in the Santos Basin indicate that each filling episode was immediately followed by an increase in the salinity of the brine due to lower water depths with partial or complete desiccation of the basin. I suggest that anhydrite deposition occurred during periods of relatively high water-depth, which were associated with lower salinities due to episodic marine incursions; in contrast, I infer that halite was precipitated during periods of relatively low sea-level when brine salinity was higher. During periods of extreme or complete desiccation, bittern salts were deposited in the more isolated parts of the salt basin.

My analysis suggests that at least part of the Ariri Formation (i.e., A2) is characterised by regular; high frequency, short-term cycles (≤30ka; assuming a depositional rates ≥ 0.4 cm/a) (boreholes 532 A; borehole 723 C; Fig. 5.13). I propose that the regular cyclicity characterising

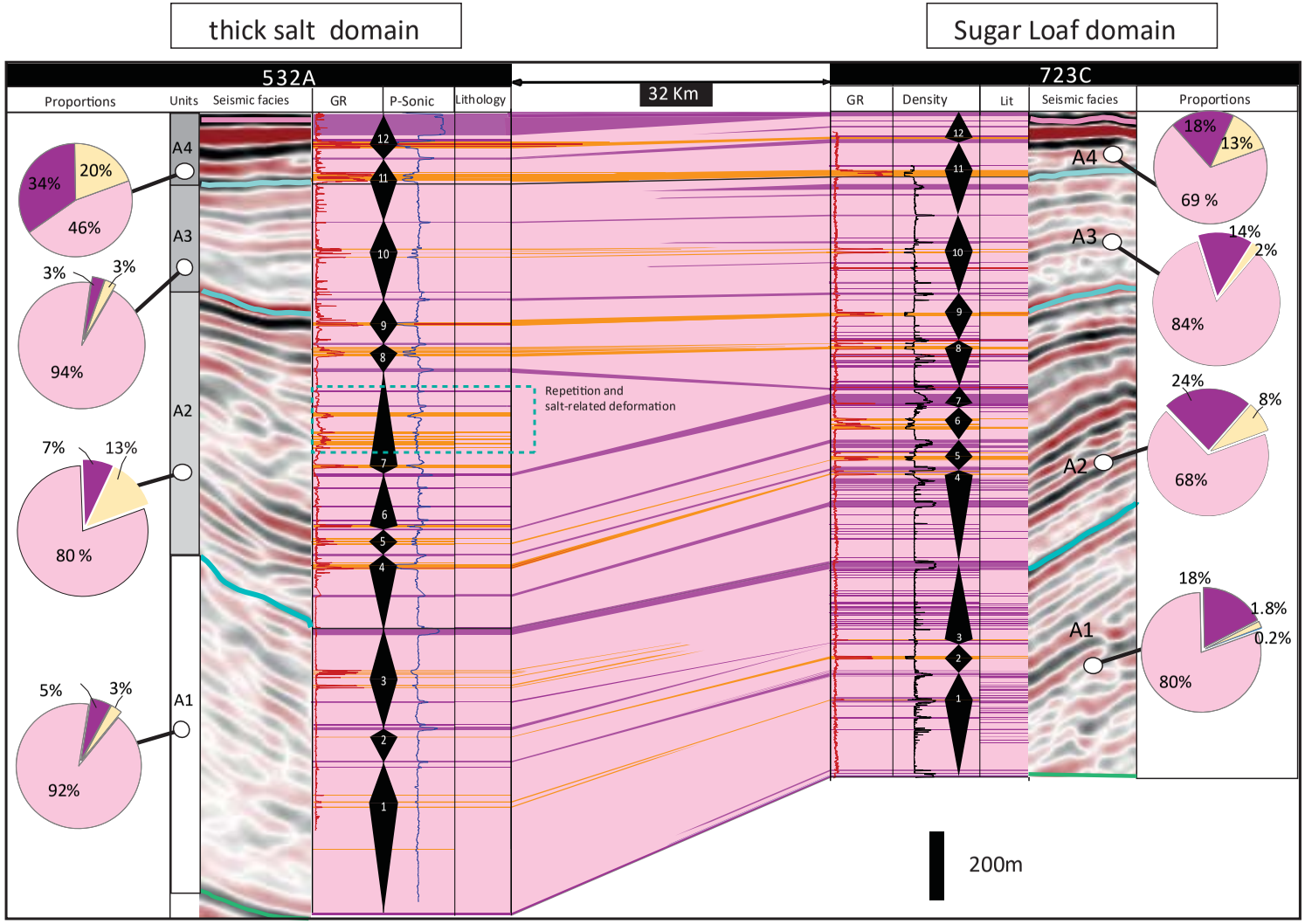


FIGURE 5.10a. Well correlation across the Thick Salt and Sugar Loaf domains illustrating variations in intra-salt thickness and lithology proportions

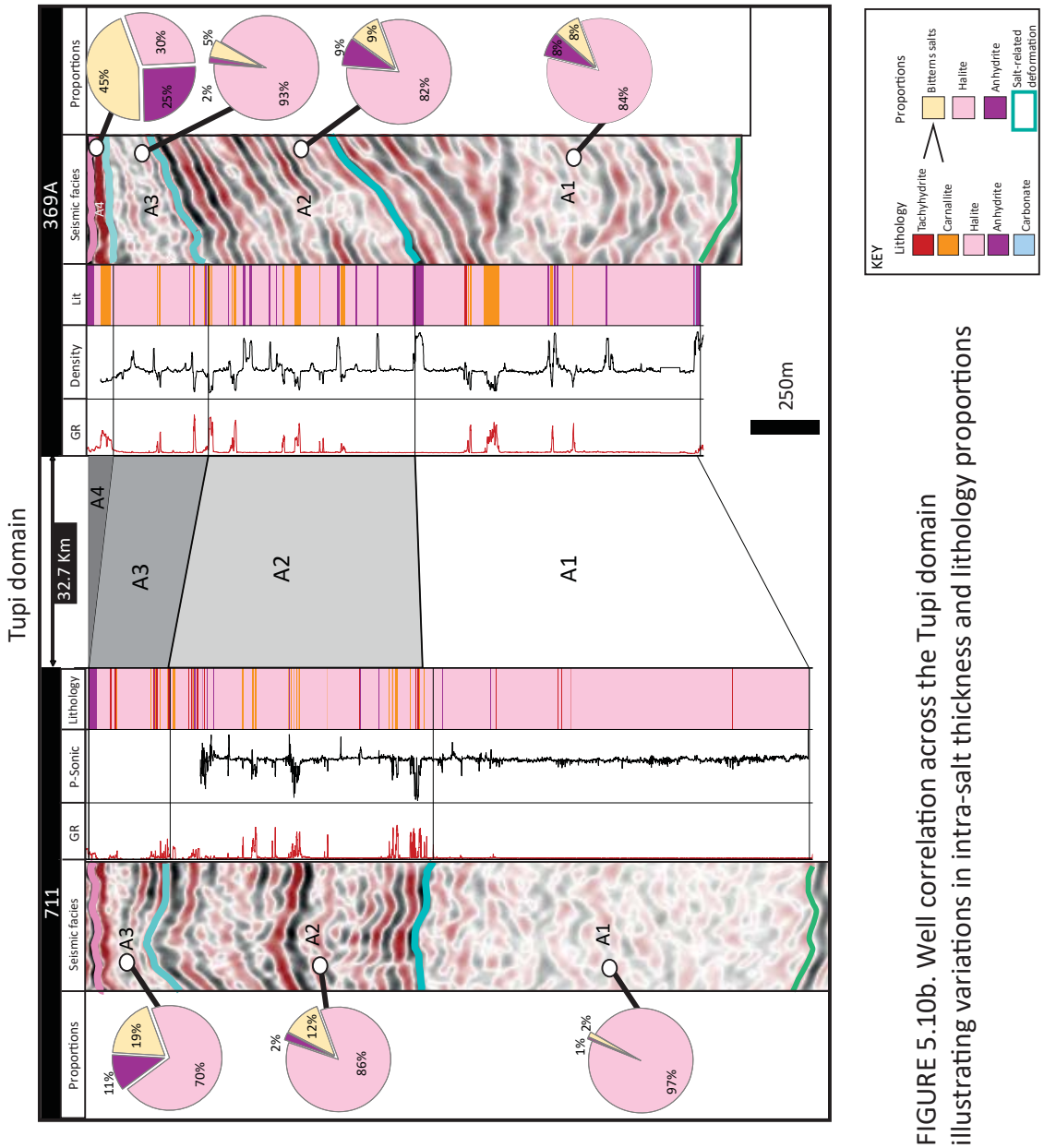


FIGURE 5.10b. Well correlation across the Tupi domain illustrating variations in intra-salt thickness and lithology proportions

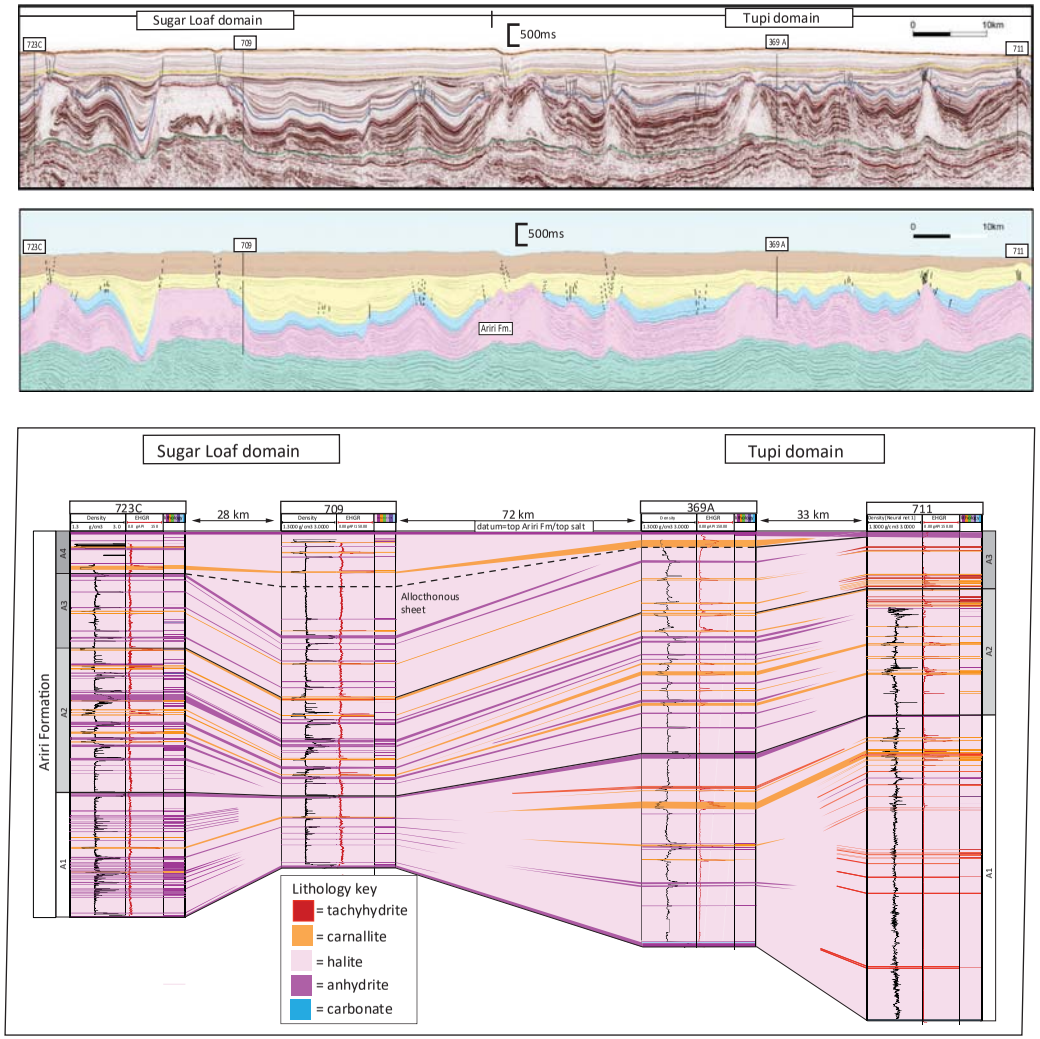


FIGURE 5.11. SW-NE detailed intrasalt well correlation across the Outer High. The detailed correlation was done based on the seismic expression and the relative acoustic impedance to identify evaporite layers betwen the boreholes

A2 can be tentatively linked to short-term climate cycles, with bittern salts being deposited during aridity peaks and anhydrite during the humid phases. Based on the evaporite cycles interpreted and assuming depositional rates measured in analogue ancient salt giants (i.e.; Paradox Formation, 0.4 cm/a; Trudgill, 2011; Mediterranean salt, 0.66 cm/a; Clauzon et al., 1996) and a modern rift-related salt basin, Lake Assal (1 cm/a; Imbert and Yann, 2005); I suggest the salt sequence in the central deepwater Santos Basin was deposited between 190 ka – 529 ka (Fig. 5.13). Considering the duration of each cycle (Fig. 5.13), and based on the fact salt is almost entirely composed of evaporites (e.g. Fig. 5.10a), I suggest this deposition timescale may have been driven by low-amplitude, 4th- to 5th-order sea level changes, such as those characterising the greenhouse conditions and an arid paleoclimate; such conditions have previously been proposed for the Late Aptian of the South Atlantic (e.g., Evans 1978; Dias, 2004; Gambôa et al, 2008).

A depositional timescale of <500 ka is also broadly consistent with the high rates of deposition scenario proposed by Dias (2004) (600 ka), De Freitas (2006) (500-800 ka), and Davison (2007), Davison et al. (2012) and Montaron and Tapponier (2012) (500 ka). A lithology-time-climate correlation is suggested for the Messinian salt in the eastern Mediterranean, by correlating observed lithological variations to precessional climate cycles of c. 21 ka duration (Stefano et al., 2010). Astronomical tuning of the Primary Lower Gypsum of the Messinian salt allows banded selenites to be correlated to the acme of the aridity peak in the precessional climate cycle (insolation minima), whereas shale layers (comparable to anhydrite layers in my model) are correlated to humid phases (Stefano et al. 2010).

I suggest that a combination of an arid paleo-climate, low-amplitude sea-level changes, and relatively rapid deposition (ca. 190 ka – 529 ka) of a thick (1.2 km -. 2.5 km) salt sequence also prevented the deposition of non-evaporite lithologies in the central deepwater Santos Basin. Although broadly similar in terms of overall thickness, the depositional timescale and at least the sea-level controls I infer for salt deposition in the Santos Basin, is unlike that suggested for

the Zechstein Supergroup, NW Europe (c. 1.5 km thick and deposited in in 5 Myr) and the Paradox Formation, North America (c. 2 km thick and deposited in 7 Myr). The presence of non-evaporite lithologies (e.g. sandstone, mudstone) within the Zechstein Supergroup and the Paradox Formation suggest that fully marine conditions periodically occurred in the basins and the salt sequences were deposited during less arid conditions, higher amplitude sea-level changes and relatively slower deposition (> 5 Myr).

5.8.2 Syn-depositional basin physiography

My results show that thickness and stratigraphic variations within the salt were directly controlled by the depth of the basin at the onset and during salt deposition. I propose that A1 was deposited in an irregular sub-basin, within which the Sugar Loaf sub-high represented an intra-basin structural high covered by relatively shallow water (Fig. 5.10). Given the potentially rapid depositional timeframe estimated for the salt (c. 500 ka), I propose A1 largely filled pre-existing, rift-related relief and that A2 was also deposited in a basin defined by accordingly more subdued relief (Fig. 5.10). The heterogeneous, cyclic, bittern salt-rich character of A2 was probably the result of a combination of reduced accommodation in a sub-basin with subtle relief, low-magnitude episodic marine incursions, and an overall slow increase in accommodation mainly driven by salt loading. A combination of these factors may have promoted higher-frequency desiccation of the salt basin when compared with A1 deposition (Figs. 5.4 and 5.10). A3 and A4 display more subdued thickness and compositional variability, suggesting that A1 and A2 had filled most of the pre-existing relief. Hence, I propose that a series of sub-basins, defined by pre-existing, rift-related relief existed at the onset of salt deposition. The associated relief of such sub-basins promoted vertical salinity variations that controlled the thickness and stratigraphic variations within the salt. During periods of relatively high sea-level, thinner salt and higher proportions of gypsum/anhydrite were deposited along the basin margins and on shallow, intra-basinal structural highs such as the Sugar Loaf domain.

In contrast, during periods of relatively low sea-level, thicker salt and higher proportions of halite and bittern salts were deposited in the basin centre and deeper isolated sub-basins, such as those now represented by the thick salt, minibasin and Tupi domains. These lateral intra-A1 stratigraphic variations have been previously defined as separate/individual units for the Ariri Formation (i.e. B3 of Fiduk and Rowan, 2012). My interpretation that changes in basin physiography controlled regional changes in salt thickness and intra-salt stratigraphic variations are consistent with those previously proposed from regional analysis of the South Atlantic salt basins and discussed in the introduction (Davison and Bate, 2004; Dias, 2004; Davison, 2007; Davison et al., 2012). In addition, my observations support previous studies suggesting that the Santos Basin Outer High has been a longstanding, positive structural element, initially uplifted at the end of the early syn-rift phase and which may have been at least periodically emergent before and during salt deposition (Gomes et al., 2002; Carminatti et al., 2009; Gomes et al., 2009; Scotchman et al., 2010). Although my results are not conclusive regarding the influence of tectonic events on salt deposition, I suggest that syn-salt subsidence and accommodation was driven by a combination of salt loading, post-rift thermal subsidence and/or fault-related subsidence, as suggested by previous regional studies (Karner et al., 2003; Dias, 2004; Davison, 2007; Davison et al. 2012; Karner and Gambôa, 2007; Torsvik et al., 2009). Other ancient salt giants evolved under the influence of similar controls to those inferred for the Ariri Formation. For example, the 1.5 km thick, Zechstein Supergroup salt sequence in the North Sea was deposited in a basin that largely formed through post-rift thermal subsidence following a preceding phase of Early Permian extension (Tucker, 1991). However, pre-Zechstein faults, inherited from the earlier Permian rift phase or even formed syn-depositionally during Late Permian rifting, also directly controlled thickness and lithology variations in the salt (Clark et al. 1998; Jackson and Lewis, 2013, 2016). Periodically submerged intra-basinal highs formed shallow areas where carbonate and anhydrites was deposited (Taylor, 1990). In deeper waters, an up to 1.5 km thick succession of basin centre facies, comprise mainly of halite, was deposited (Clark et al. 1998).

5.8.3 Basin hydrology

De Freitas (2006) proposes that anhydrite is thicker and more voluminous in the west of the Santos Basin due to freshwater influx from the continent during the Aptian. Conversely, eastwards on the São Paulo Plateau, away from this freshwater source, salinities were higher and halite and bittern salts were thicker. However, I argue that the impact of continental river discharge was likely to have a minor impact on basin salinity and thus salt composition, given that the study area is located a considerable distance (> c. 100 km) from the coeval coastline. Nevertheless, I observe salt thickness and stratigraphic variations between the two structurally higher domains (i.e. the Sugar Loaf and Tupi sub-highs) that, at present, have similar depths to base salt (Fig. 5.9). If both the Sugar Loaf and Tupi sub-highs were shallower than the surrounding domains at the onset of salt deposition, then the main factor controlling salinity variations and thus lithologies found on the Outer High may be the position of this area with respect to the putative sill controlling seawater influx into the basin (Figs. 5.9 and 5.10). More specifically, to the south, closer to the seawater entry point (i.e, in the Sugar Loaf domain), gypsum/anhydrite was precipitated in larger quantities, whereas larger amounts of halite and bittern salts were deposited farther away from the sill, towards the north, in the deeper, more isolated domains (i.e. Tupi domain) (Figs 5.9 and 5.10). My observations are consistent with those of Demercian (1996), who suggested that gypsum/anhydrite deposition was controlled by the position and direction of the seawater inflow from the southern Florianopolis high (São Paulo Ridge), with concentrations increasing northwards. Additionally, my interpretation agrees with previous studies that suggest seawater recharge from the south probably percolated through fractures in the volcanic barrier (see Jackson et al., 2000 and Nunn and Harries, 2007).

Similar salinity variations to these interpreted for the Outer High have been observed in Lake Asal, Djibouti, which represents a modern example of a marine-fed rift basin actively accumulating interbedded evaporites (Jackson et al., 2000). Here, seawater incursions occur

through a highly fractured, 10 km wide volcanic ridge that bounds the southeastern margin of the lake. Close to the seeps that bring seawater to the surface, gypsum precipitation dominates, whereas stacked halite crusts characterise the opposite side of the lake where salinities are higher; in this location, a 60 km wide, up to 80 m thick halite body has developed (Warren, 2006).

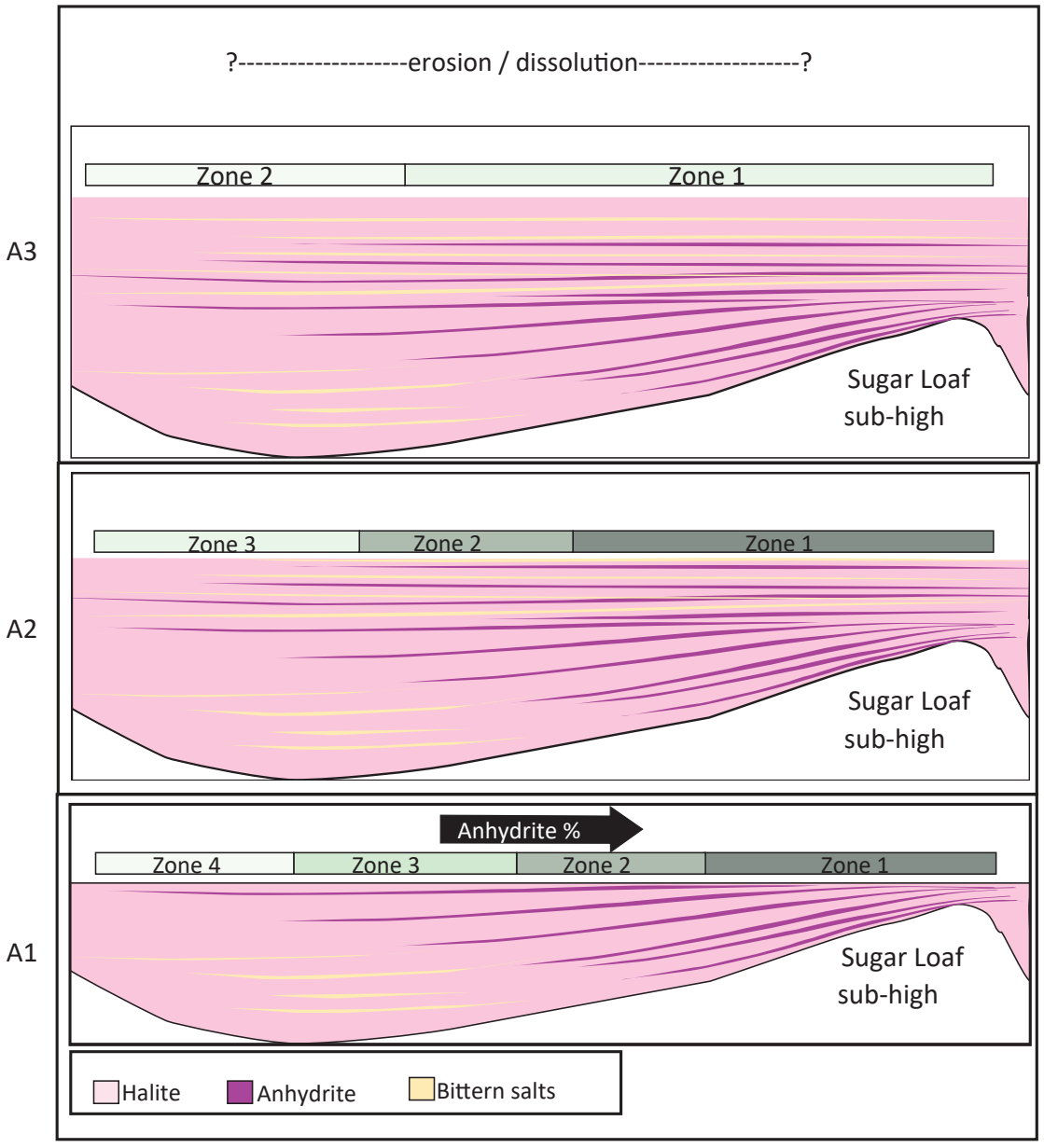


Figure 5.12: Proposed model for A1, A2 and A3 intrasalt key stratigraphic intervals illustrating the influence of the syn-depositional basin physiography in the resulting stratigraphic architecture

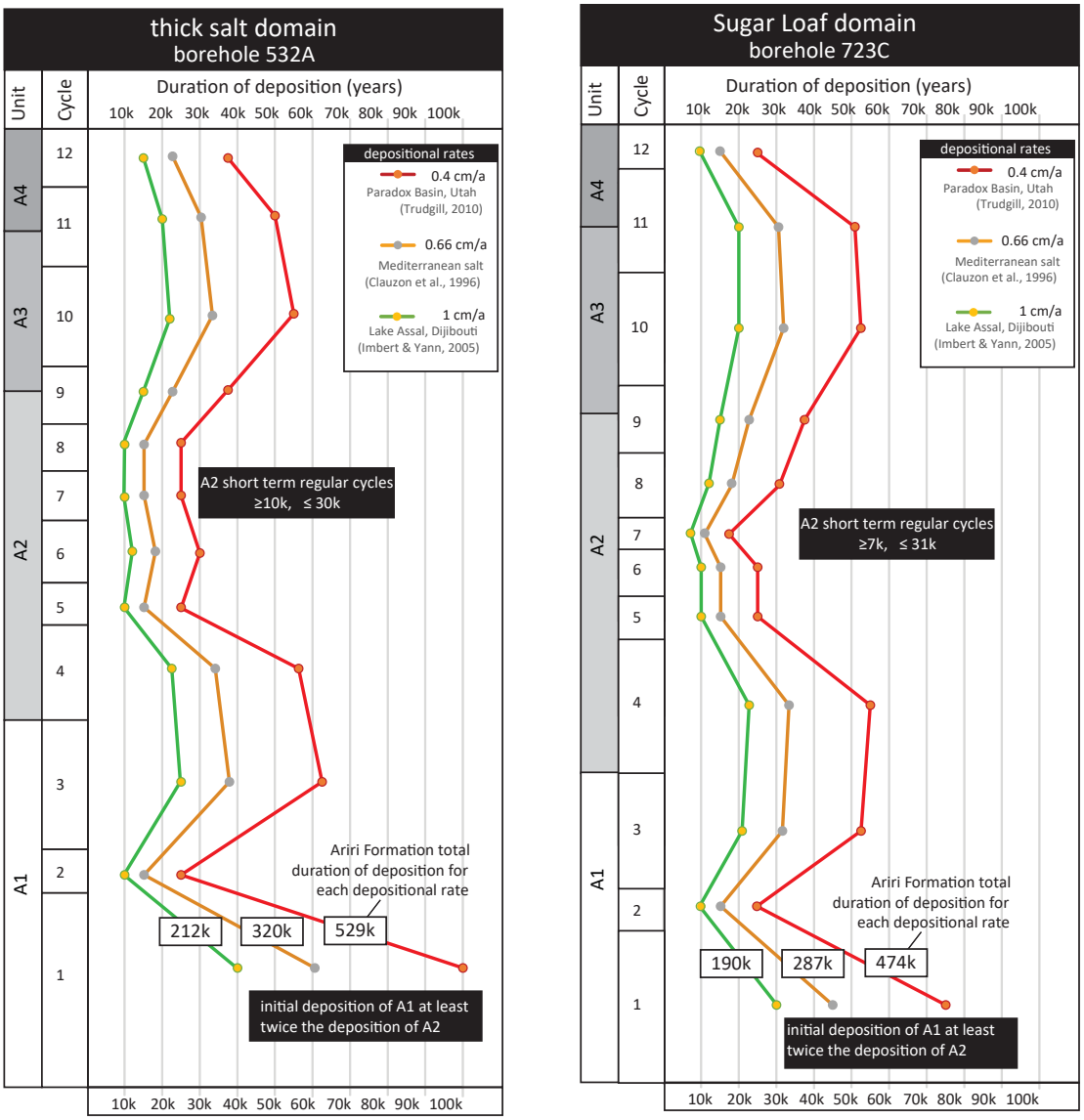


FIGURE 5.13: Duration of salt deposition estimated based on the thickness of each evaporite cycle and depositional rates from ancient and modern salt basins

5.9 Conclusions

The integration of 3D seismic reflection data and borehole data from the São Paulo Plateau, Santos Basin, offshore Brazil, has allowed us to investigate the lithology and stratigraphy of a salt giant (i.e., the Ariri Formation), as well as the key controls on the depositional thickness distribution and intrasalt stratigraphic variability. The key conclusions of my study are:

1. The Ariri Formation in the São Paulo Plateau is mainly composed of halite interbedded with significant proportions of anhydrite and bittern salts (carnallite and tachyhydrite) as well as minor proportions of carbonates, marls and sandstones locally.

2. The Ariri Formation can be subdivided into four key stratigraphic intervals based on seismic facies: i) A1: a variably thick and highly deformed lower unit mostly characterized by chaotic and transparent seismic facies which varies laterally and locally to sub-parallel and more continuous seismic facies, ii) A2: A thick highly-reflective unit characterized mainly by continuous parallel to sub-parallel seismic facies, iii) A3: a relatively thin unit characterized by transparent seismic facies and sub-parallel continuous reflections and iv) A4: A thin, highly-reflective unit that thins and is truncated beneath the top of salt and towards the main salt structures.

3. Seismic facies within the salt are directly controlled by salt composition; where acoustically transparent chaotic seismic facies are associated with higher halite proportions (> 80%); whereas high-frequency, highly-reflective continuous seismic facies represent lower halite proportions (<80%) cyclically interbedded with high-density anhydrite and low-density carnallite

4. The Santos salt basin was completely desiccated and refilled at least 12 times in < 530 ka, as suggested by the 12 complete evaporite cycles that have been identified within the salt. The Ariri Formation stratigraphy and cyclicity suggests that the sea-level variations controlling

the cyclicity during salt deposition where low-amplitude, rapid, 4th to 5th order sea-level changes, i.e. few meters to decimetres in c.10ka to c. 100ka, potentially associated to precessional climatic changes with the deposition of gypsum/anhydrite during the humid phase and bittern salts during the dry phase.

5. Lateral depositional thickness and stratigraphic variations occur within the salt and between structural domains, which I defined based on mean salt thickness and depth to base of salt structure; i.e. i) the minibasin domain, ii) the Tupi domain, iii) the Sugar Loaf domain and the vi) thick salt domain.

6. I suggest that an irregular deep basin existed at the onset of salt deposition with sufficient accommodation for A1 and potentially A2 deposition. This basin was characterized by a series of shallower and deeper sub-basins, where the Sugar Loaf sub-high was shallower with respect to surrounding areas. This syn-depositional basin physiography controlled depositional thickness and stratigraphy; overall, thinner salt (mean salt thickness < c.1.8 km), highly reflective and continuous seismic facies and higher anhydrite proportions (> c. 10%) characterise the salt in the Sugar Loaf domain, whereas thicker salt (mean salt thickness of c. > 2.2 km), discontinuous, acoustically transparent seismic facies and higher bittern salt and halite characterise the structurally lower domains (minibasin and thick salt domains).

7. Stratigraphic variations exist between the Sugar Loaf domain and the Tupi domain with higher gypsum (now anhydrite) proportions precipitated closer to the entry on seawater whereas higher bittern salts were deposited in a more restricted and distal Tupi domain. This also suggests that seawater incursions came from the South through the São Paulo ridge/Walvis ridge.

8. In this study I provide new insights into the deposition and evolution of an ancient salt giant. My results suggest that an arid paleo-climate, low-amplitude sea-level variations and syn-depositional basin physiography controlled the deposition of this thick (1.2-2.5 km) salt giant, even though the depositional timespan was relative short (< 530 ka) and sediment

accumulation rates were correspondingly high. There is no clear evidence of influence from river discharge of freshwater influx and further studies are required to understand how salt loading and syn-depositional tectonics may have also controlled salt deposition.

5.10 Acknowledgments

I would like to thank CGG for providing access to the 3D seismic data and for granting permission to publish the results of this study. I also thank Statoil and ANP Brazil for providing access to the borehole data. Schlumberger WesternGeco is also gratefully acknowledged for providing 2D seismic regional data, partial funding and support of this work.

Reviewers Ian Davison and Webster Mohriak are thanked for insightful reviews that greatly improved the final manuscript.

Chapter 6

Minibasin development and reservoir deposition on a salt-influenced deep-water slope

This Chapter is written as a scientific paper and documents minibasin development, and deep-water sediment dispersal and ultimate stratigraphic architecture by exploring > 60 Myrs of salt-sediment interaction along the Santos Basin salt-influenced, deep-water slope, offshore Brazil. This section also evaluates the exploration significance of these observations, highlighting the influence of salt movement on hydrocarbon trap development. As this Chapter is written as a 'stand-alone' paper, some of the material presented in the 'Introduction', 'Geological Setting' and 'Methods' sections overlaps with that in Chapters 3-4.

6.1 Abstract

Salt tectonics controls sediment dispersal and, ultimately, the stratigraphic architecture of deep-water systems in salt-influenced sedimentary basins. However, it is typically difficult to study deeply buried, ancient, salt-influenced intra-slope depositional systems due to the lack of seismic reflection resolution and problems with imaging steeply dipping deposits preserved on the flanks of salt structures. These issues limit the level of stratigraphic detail that can be imaged and investigated. Previous studies in the Santos Basin, offshore Brazil suggest that, following drowning of an Albian-Cenomanian carbonate platform, most clastic sediment was

trapped behind the so-called 'Albian Gap', a salt-controlled, intra-slope depocentre. As a result, no exploration wells have deliberately targeted post-salt, deep-water reservoirs basinward of this depocentre. In this study, I integrate high-quality 3D seismic reflection and borehole data to challenge the notion that little post-salt reservoir potential exits basinward of the Albian Gap, showing that a range of deep-water reservoir types are indeed present. The study area therefore provides spectacular, hitherto undocumented examples of the salt tectonic structural style of this basin, and the control of salt related-deformation on deep-water sedimentation. In details, I identify six main seismic facies types that I relate to the following deep-water depositional elements; (i) channels, (ii) levees, (iii) lobes, (iv) mass-transport complexes (MTCs) and (v) 'background' deposits. These elements form the building blocks of three main tectono-stratigraphic phases of clastic deposition. During the first phase (Turonian-middle Campanian), sand-rich channels and lobes, and MTCs of unconstrained composition were confined within proximal minibasins and to the hangingwalls of landward-dipping, salt-detached listric faults. During the second phase (middle Campanian-Paleocene), sand-rich channels and lobes eventually filled and bypassed proximal minibasins, with coarse clastic deposition then occurring further downslope in distal minibasins, >100 km from the coeval shelf margin. Syn-depositional seabed deformation, driven by passive and active diapirism, and salt-detached thrusting and folding, caused: (i) channel deflection and diversion around salt-cored highs; (ii) channel and levee uplift and rotation on the flanks of rising salt-cored anticlines and diapirs; (iii) progressive lateral channel migration, expressed in the form of lateral accretion packages (LAPs); (iv) local ponding and long-distance confinement of channels, levees and lobes. During the third and final phase (Paleocene-to-middle Oligocene), continued rise of proximal salt walls dissected previously deposited deep-water systems, with deposition from diapir- and shelf-edge sourced MTCs becoming increasingly important. The deep-water depositional elements I have identified have important implications for post-salt hydrocarbon prospectivity in the Santos Basin, with a range of reservoir types and trapping styles being developed in this previously underexplored interval. In addition, the results of my

study can be applied to other deep-water basins, where syn-depositional salt-induced seabed deformation controls reservoir deposition and architecture.

6.2 Introduction

Minibasins are relatively small (5-30 km) syn-sedimentary depocenters formed due to sediment subsidence into salt (e.g. Jackson and Talbot, 1991; Hudec and Jackson, 2007, 2011; Hudec et al., 2009; Goteti et al., 2012). The initiation and evolution of minibasins in deep-water sedimentary basins control sediment dispersal and the ultimate stratigraphic architecture of deep-water deposits, in addition to hydrocarbon trapping styles (offshore West Africa, e.g. Anderson et al., 2000; Broucke et al. 2004; Gee and Gawthorpe, 2006, 2007; Mayall et al., 2010; Jones et al., 2012; Janocko et al., 2013; Oluboyo et al., 2014; eastern Mediterranean, e.g., Loncke et al., 2006; Clark and Cartwright, 2009, 2011; offshore eastern Brazil, e.g., Alves et al., 2009; Albertão et al., 2011; Guerra and Underhill, 2012; the Gulf of Mexico, e.g., Prather et al., 1998; Rowan and Weimer, 1998; Badalini et al., 2000; Beaubouef and Friedmann, 2000; Booth et al., 2003; Hearon et al., 2014; the North Sea, e.g., Stewart and Clark, 1999; Argent et al., 2000; Stewart, 2007; Jackson et al., 2010). Several of the studies listed here indicate that the style of salt-sediment interaction is mainly controlled by; i) the nature (e.g. grainsize, erosive power, etc) and temporal evolution of deep-water sediment dispersal systems; ii) downdip changes in salt-related structural style (i.e., from predominantly thin-skinned extensional styles near the updip basin margins, to thin-skinned contractional styles towards the basin centre), with a key control being the orientation, scale and growth rate of structures relative to the incoming deep-water systems (Fig. 6.1); and iii) the timing of sediment deposition relative to the formation, growth and decay of salt-induced seafloor deformation (e.g., Koyi, 1998; Booth et al., 2003; Gee and Gawthorpe, 2006; Clark and Cartwright, 2009, 2011; Hudec et al., 2009; Mayall et al., 2010; Jackson, 2012; Oluboyo et al., 2014). Hence, understanding the spatial distribution and temporal evolution of deep-water depositional elements relative to

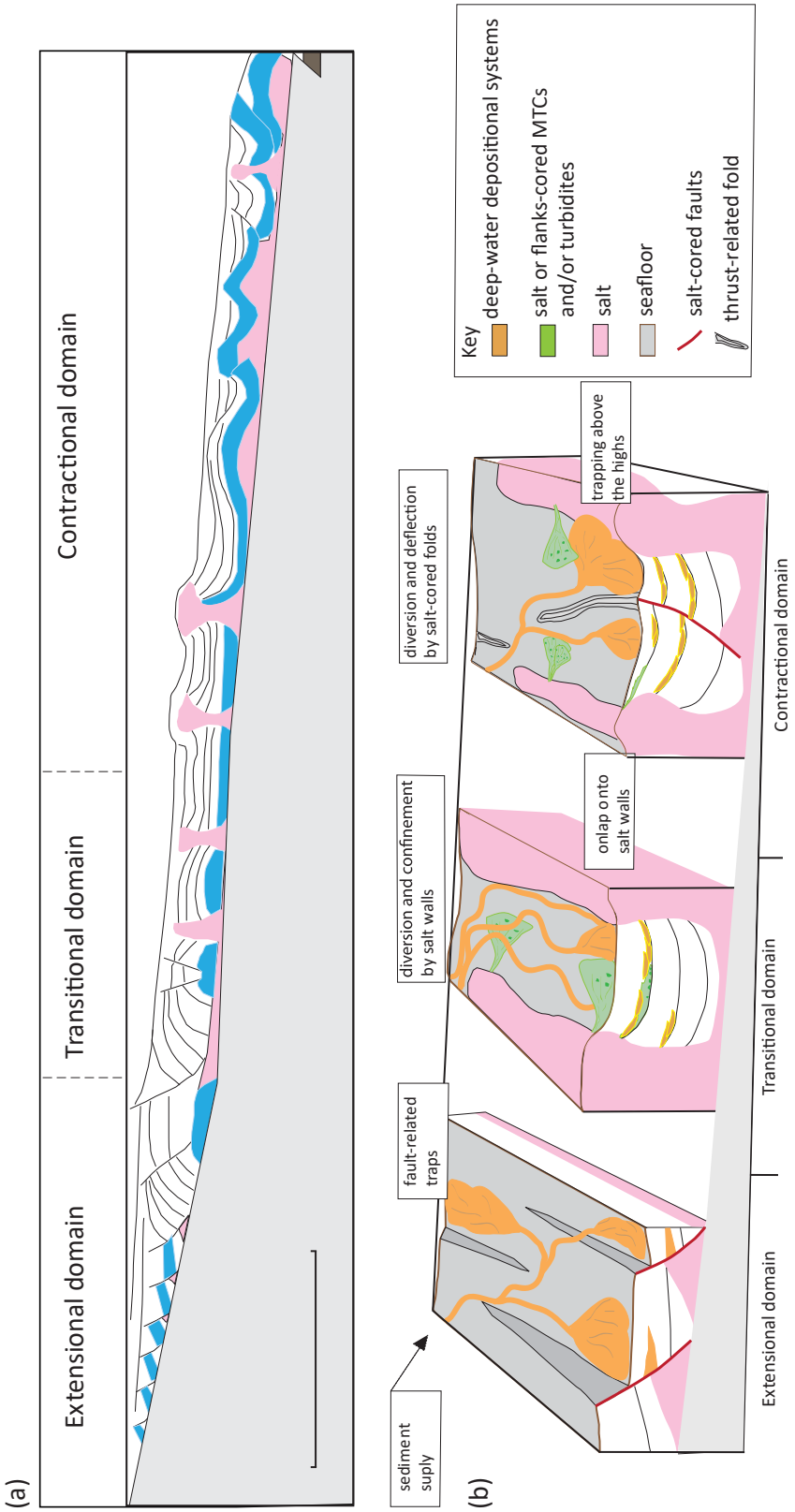


FIGURE 6.1: (a) Passive margin salt-related domains. After Brun and Fort (2011) (b) Block diagrams illustrating examples of deep-water depositonal systems interacting with salt and potential trapping styles along the passive margin.

the timing and style of salt-induced seabed deformation is key to improving the ability to predict reservoir presence, architecture and potential trapping styles on salt-influenced deep-water slopes. However, seismic reflection-based studies of ancient intra-slope depositional systems that interact with salt are challenging due to the low seismic resolution of deeply-buried depositional elements which limits the level of detail that can be investigated and the poorly imaging of the dipping minibasin flanks which could also be misleading when examining the relative timing of paleoseafloor relief during sedimentation. Most of the current understanding of salt-sediment interactions in deep-water systems thus comes from very shallow, undrilled, relatively young deep-water systems, which are then used as analogues to understand similar salt-sediment interactions in older, more deeply buried systems (e.g.; Beaubouef and Friedmann, 2000; Clark and Cartwright, 2009; 2011).

This study focuses on central deep-water Santos Basin, offshore eastern Brazil. Here, high-quality seismic reflection and borehole data provide a rare opportunity to analyse Turonian-to-Palaeocene deep-water clastic systems that were deposited on a salt-influenced slope. Previous studies in the Santos Basin predict that little or no sand was deposited basinward in relatively distal positions due to the presence of a salt-controlled intra-slope depocentre called the 'Albian Gap' (e.g.; Modica and Brush, 2004; Guerra and Underhill, 2012). In this study, I challenge the results of previous studies and show conclusive evidence for the existence of deepwater depositional elements up to 100 km from the coeval shelf margin. More specifically, we: i) document the spatial and temporal variations in the size and type of deep-water depositional elements within the post-salt succession; ii) assess the key controls on minibasin development, paleo-seafloor relief and deep-water stratigraphic architecture; and iii) determine the exploration significance of this hitherto poorly explored succession. This study improves the current understanding of the distribution of and controls on depositional systems along salt-influenced deepwater slopes and provides new insights into the tectono-stratigraphic evolution of this salt-dominated basin.

6.3 Geological Setting

The study area is located on the São Paulo Plateau (SPP), Santos Basin, offshore eastern Brazil (Fig. 6.2). The Santos Basin formed during opening of the South Atlantic in the earliest Cretaceous, with the main Hauretivian rift phase being characterised by the development of half-graben filled with fluvial and lacustrine sediments (Guaratiba group; Fig. 6.2c) (Meisling et al., 2001; Modica and Brush, 2004; Moreira et al., 2007). The end of the rift phase was marked by the deposition of the main source rocks and reservoirs in the Santos Basin; these included organic-rich lacustrine mudstones and carbonates of the Barremian 'sag' sequence (upper Guaratiba group), which largely filled and smoothed relict rift-related topography (Fig. 6.2c; Meisling et al., 2001; Modica and Brush, 2004; Moreira et al., 2007). Episodic marine incursions and an arid climate during the Aptian promoted deposition of the Ariri Formation, an up-to-2.5 km-thick evaporite-dominated succession (Fig. 6.2c, 6.3; e.g. Modica and Brush, 2004; Davison, 2007; Karner and Gambôa, 2007; Moreira et al., 2007; Gambôa et al., 2008; Davison et al., 2012; Fiduk and Rowan, 2012; Jackson et al., 2014; Rodriguez et al., in press/ CHAPTER 5). During the Albian, a shallow-marine carbonate platform was established near the basin margin, with deep-water marls deposited basinward in deeper waters (Itanhaem Formation; Figs. 6.2c, 6.3, 6.4a; e.g., Modica and Brush, 2004). Salt-related deformation commenced in the Albian, with margin tilting and the downslope flow of salt causing stretching and faulting of the carbonate platform, and the development of normal fault-bound rafts in the upslope extensional domain (Fig. 6.2c; e.g.; Davison et al., 2012; Guerra and Underhill, 2012; Jackson, 2012).

In the Late Cretaceous, periodic uplift and erosion of the onshore Serra do mar mountain belt drove progradation of a thick clastic wedge into the Santos Basin (Itajai-Acu Formation; Fig. 6.2c, 6.3; e.g., Modica and Brush, 2004; Moreira et al., 2007; Guerra and Underhill, 2012). Regional paleogeographic mapping based on widely spaced 2D seismic reflection and limited borehole data suggest large volumes of sediment were supplied by the Paraiba do Sul river

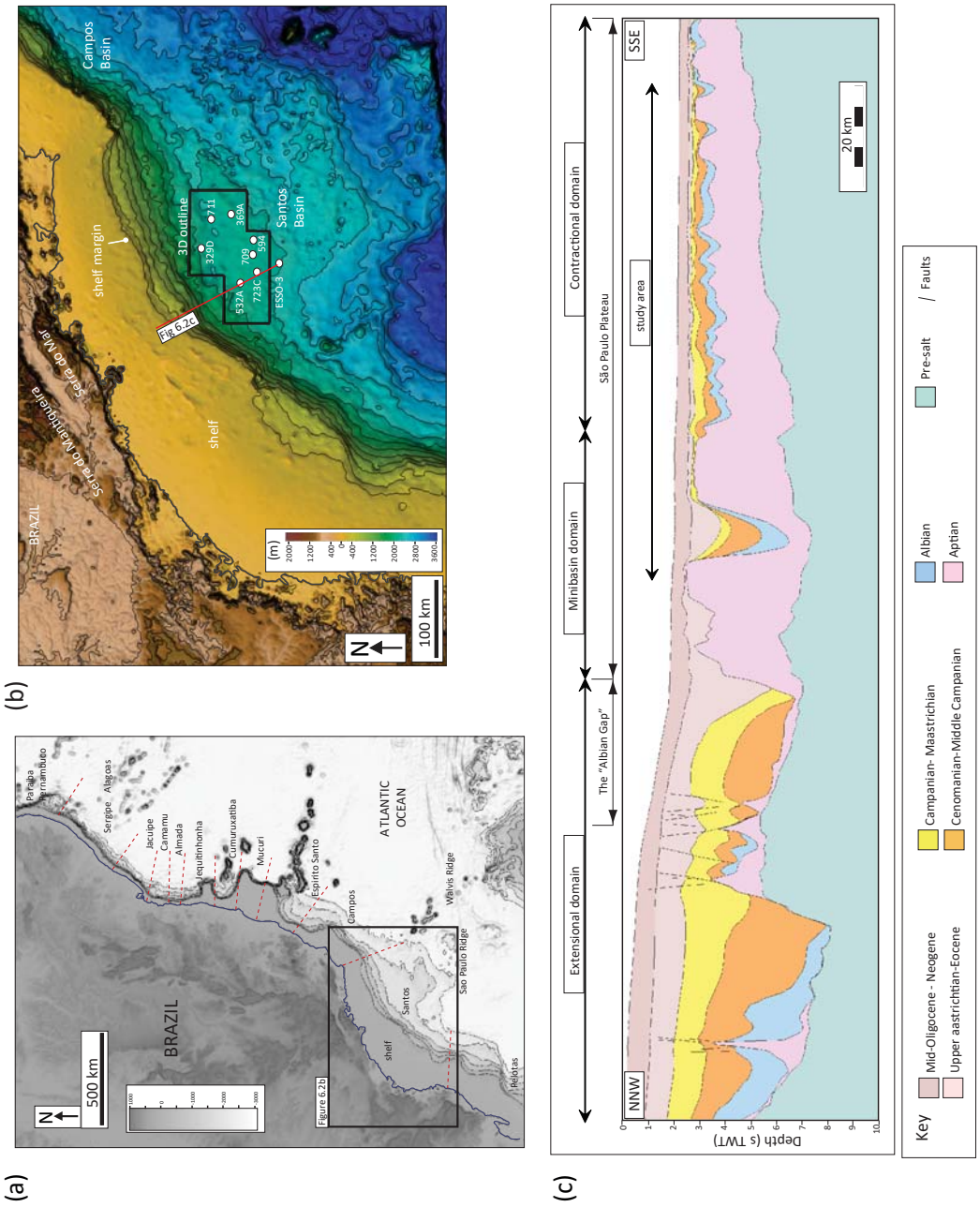


FIGURE 6.2: (a) Brazilian sedimentary basins; (b) Study area and dataset; (c) Geoseismic profile accross the study area, after Modica and Brush, 2004; Jackson, 2012

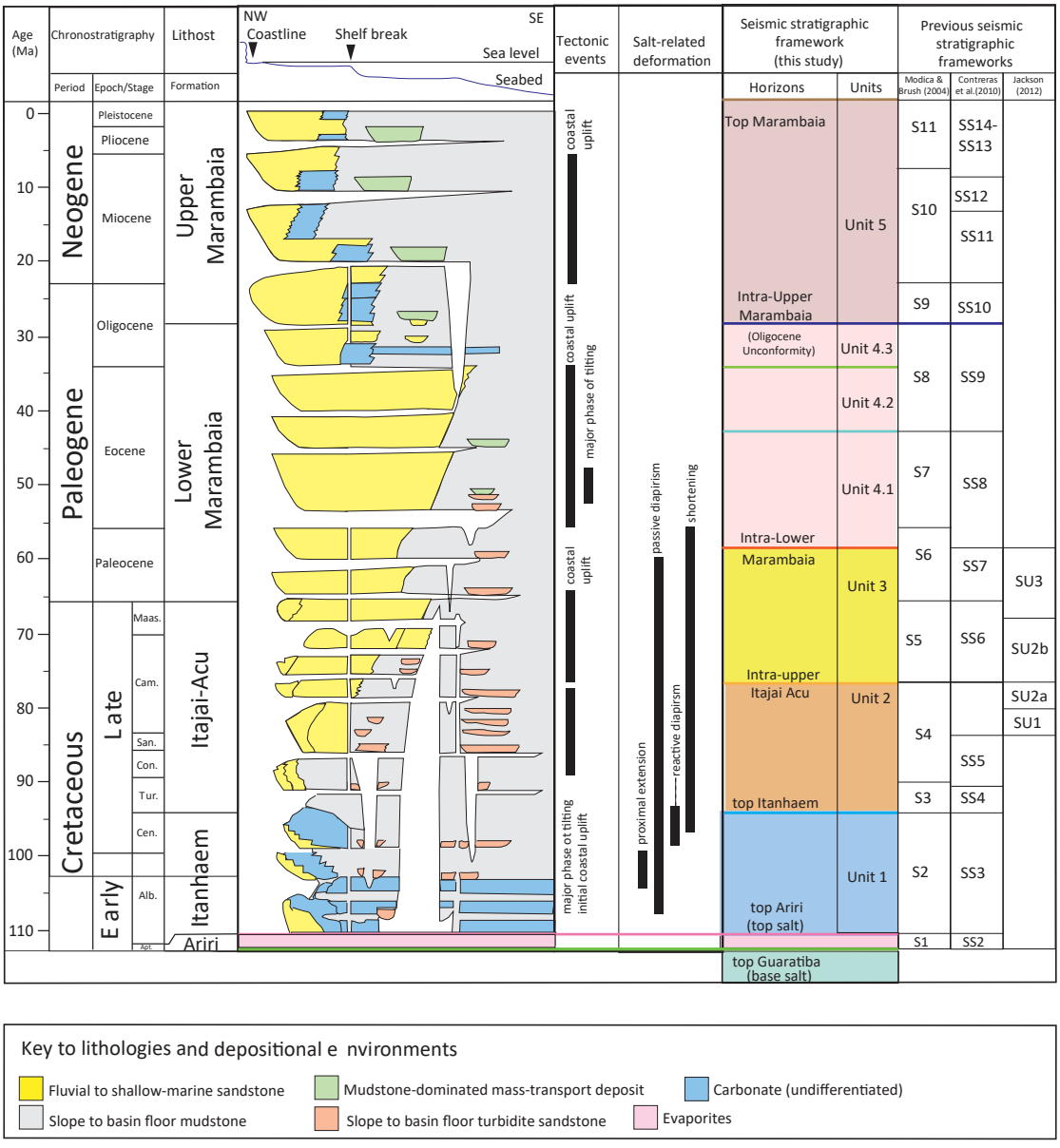


FIGURE 6.3: Chrosnostratigraphic table. After Moreira, 2007 and Jackson, 2012

drainage system, which at this time lay to the N and NW of the São Paulo Plateau (Fig. 6.4b, Modica and Brush, 2004). However, according to Modica and Brush (2004), much of this sediment was trapped in a relatively proximal setting due to formation of the Albian Gap, a large (4 km thick, 200 km long, 10 km wide), salt-controlled, intraslope depocentre bounding the seaward limit of the extensional domain (Figs. 6.2c, 6.4b; Jackson et al., 2015a). The interpretation of Modica and Brush (2004) thus argues for limited deep-water sediment dispersal to the slope during the Late Cretaceous, implying limited deep-water prospectivity on the São Paulo Plateau (Fig. 6.4b). Late Campanian-Maastrichtian uplift of the Serra do Mar deflected the Paraiba do Sul river drainage system to the NE, starving the central deep-water Santos Basin of sediment (Figs. 6.4c; Cobbold et al., 2001; Modica and Brush, 2004; Guerra and Underhill, 2012). Subsequently, during the Eocene, sediment supply to the basin was thus largely derived from catastrophic failure of the middle Eocene shelf margin, which produced debris flows and turbidites of the Lower Marambaia Formation that were locally trapped in the proximal domain (Figs. 6.2d and 6.4d). Previous studies also suggest the upper Marambaia Formation varies little in thickness and is dominated by fine-grained sediments, recording a global marine flooding event and sea level highstand (Figs. 6.2c, 6.3; Modica and Brush, 2004; Moreira et al., 2007; Guerra and Underhill, 2012).

By integrating 3D seismic reflecting and borehole data I here show that: (i) deep-water systems of the Itajai-Acu Formation were deposited on the São Paulo Plateau, some distance seaward of the Albian Gap and the coeval Late Cretaceous shelf edge; and (ii) large thickness variations occur within the Marambaia Formation due to continue salt diapirism, and the emplacement of relatively small, intra-minibasin and larger, shelf-derived mass transport complexes (MTCs).

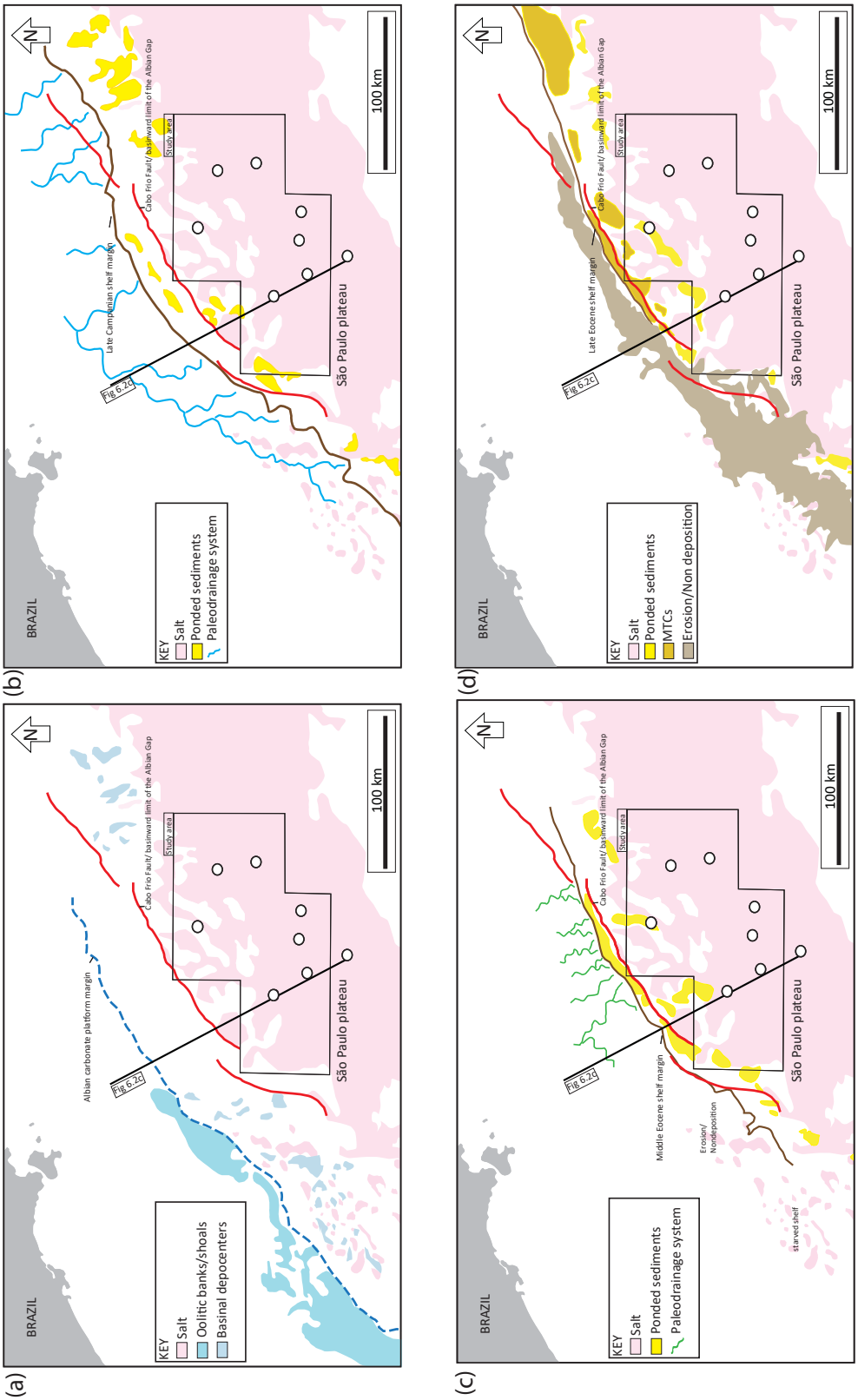


FIGURE 6.4: Deepwater Santos Basin Paleogeography. After Modica and Brush, 2004. (a) Albian paleogeography; (b) Late Campanian paleogeography; (c) Middle Eocene paleogeography; (d) Late Eocene paleogeography

6.4 Data and methods

In this study I integrate a 20,122 km2, high-quality, three-dimensional, post-stack time migrated seismic reflection dataset provided by CGG, and eight publically available boreholes (Fig. 6.2b). The dataset is located in the central deep-water Santos Basin, 200 km southeast of the present Brazilian shelf edge and 200 km southwest of the Campos Basin (Fig. 6.2b). The seismic dataset contains trace information from sea level down to 5.5 second two-way time (s, TWT), with a vertical sample rate of 4 ms, inline spacing (east-west) of 18.75 m and crossline spacing (north-south) of 25 m. Data from four boreholes indicate that vertical seismic resolution within the post-salt varies not only with depth, but also spatially due to variations in composition (Fig. 6.5, and Table 6.1). Vertical resolution within the post-salt sequence decreases from c. 8 m at relatively shallow depths (<2500 ms TWT), to up to 31 m where the post-salt sequence is relatively thick (4500 ms TWT), to up to 64 m where the post-salt sequence is thickest (>5000 ms TWT) (Fig. 6.5 and Table 6.1). This decrease in seismic resolution limits the opportunity to identify and map depositional systems occurring deep within the post-salt sequence. Seismic profiles are displayed with SEGY normal polarity, where a downward increase in acoustic impedance is represented by a positive reflection event (red) and a downward decrease in acoustic impedance is represented by a negative reflection event (blue) (inset on Fig. 6.5). The boreholes contain lithology information and formation markers. Well-log data are restricted to the presalt and salt sequences. Only borehole 329D, which penetrates the centre of a minibasin encircled by salt diapirs, contain age data for the post-salt interval (Figs. 6.5).

I mapped nine main seismic horizons and correlated these to stratigraphic information (e.g. age, lithology) provided by borehole 329D (Fig. 6.5). I chose horizons defining clear vertical changes in seismic facies, or which correlated to major lithological breaks or unconformities identified in boreholes. Some of these horizons are of high-amplitude and are regionally mappable, whereas others can only be locally interpreted within a few proximal minibasins

in the north of the study area (e.g.; unit 4.2, Fig. 6.5). These seismic horizons were used to generate isochrons (time-thickness maps) of key stratigraphic intervals; these were used to illustrate how syndepositional, salt-induced subsidence and uplift varied in space and time, and how this then impacted the development of deep-water depositional systems.

TABLE 6.1: Vertical seismic resolution of intervals of interest and accross structural domains

Structural Domains	Borehole	Formation	Interval Velocity (m/s)	Frequency (Hz)	Resolution (m)
Proximal deep minibasins	329D	Marambaia	2125	52	10
		Itajai-Acu	3525	37	24
		Itanhaem	4300	17	63
Medial shallow minibasins	369A	Marambaia	1700	37	11
		Itajai-Acu	2300	30	19
		Itanhaem	3700	23	42
Distal elongated minibasins	723C	Marambaia	1500	45	8
		Itajai-Acu	1900	42	11
		Itanhaem	2750	30	23
	709	Marambaia	1500	48	8
		Itajai-Acu	2200	42	13
		Itanhaem	2300	30	19

I use a range of volume- and surface-based seismic attributes to identify and map deep-water depositional elements (Table 6.2); i.e.; (i) *amplitude contrast*, which calculates amplitude derivatives between neighbouring seismic traces in order to highlight salt structures, faults and mass transport complexes (Schlumberger, 2012); (ii) *variance*, which identifies abrupt

lateral changes in seismic reflection continuity (Hart, 2008); and (iii) *sweetness*, which integrates amplitude strength (envelope) and instantaneous frequency to highlight lateral changes in seismic facies variations related to inferred changes in lithology (Hart, 2008). I visually blend sweetness and variance to identify and analyse the seismic geomorphology of deep-water depositional elements (Fig. 6.5; see also Hart, 2008).

By integrating seismic reflection and borehole data I identify three main seismic facies (Fig. 6.5): (i) Seismic Facies 1 (SF1): intervals of high-amplitude, laterally continuous seismic facies characterised by moderate-to-high sweetness (light blue to red colours) and low variance (grey to white colours). SF1 correlates with intervals of sandstone (c. 40%) interbedded with mudstone (c. 56%), with minor intervals of siltstone, marl and carbonate (c. 4%); (ii) Seismic Facies 2 (SF2): intervals of moderate-to-high amplitude, discontinuous seismic facies, characterised by medium sweetness (light blue colour) and high variance (black colour). SF2 corresponds to intervals of interbedded sandstone (c. 56%), mudstone (c. 28%), and a higher proportion of marl and carbonate than encountered in SF1 (c. 16%); and (iii) Seismic Facies 3 (SF3): consists of intervals of low-amplitude, discontinuous seismic reflections that are characterised by low sweetness (dark-blue-to-dark-pink colours) and high variance (black-to-red colours). SF3 is mudstone-dominated (c. 70%), containing significantly less sandstone (c. 25%) than observed in SF1 and SF2. The integration of map- (i.e. seismic geomorphology) and section- (i.e. seismic stratigraphy) views with borehole-derived lithology data was core to my interpretation of deep-water depositional elements along the slope.

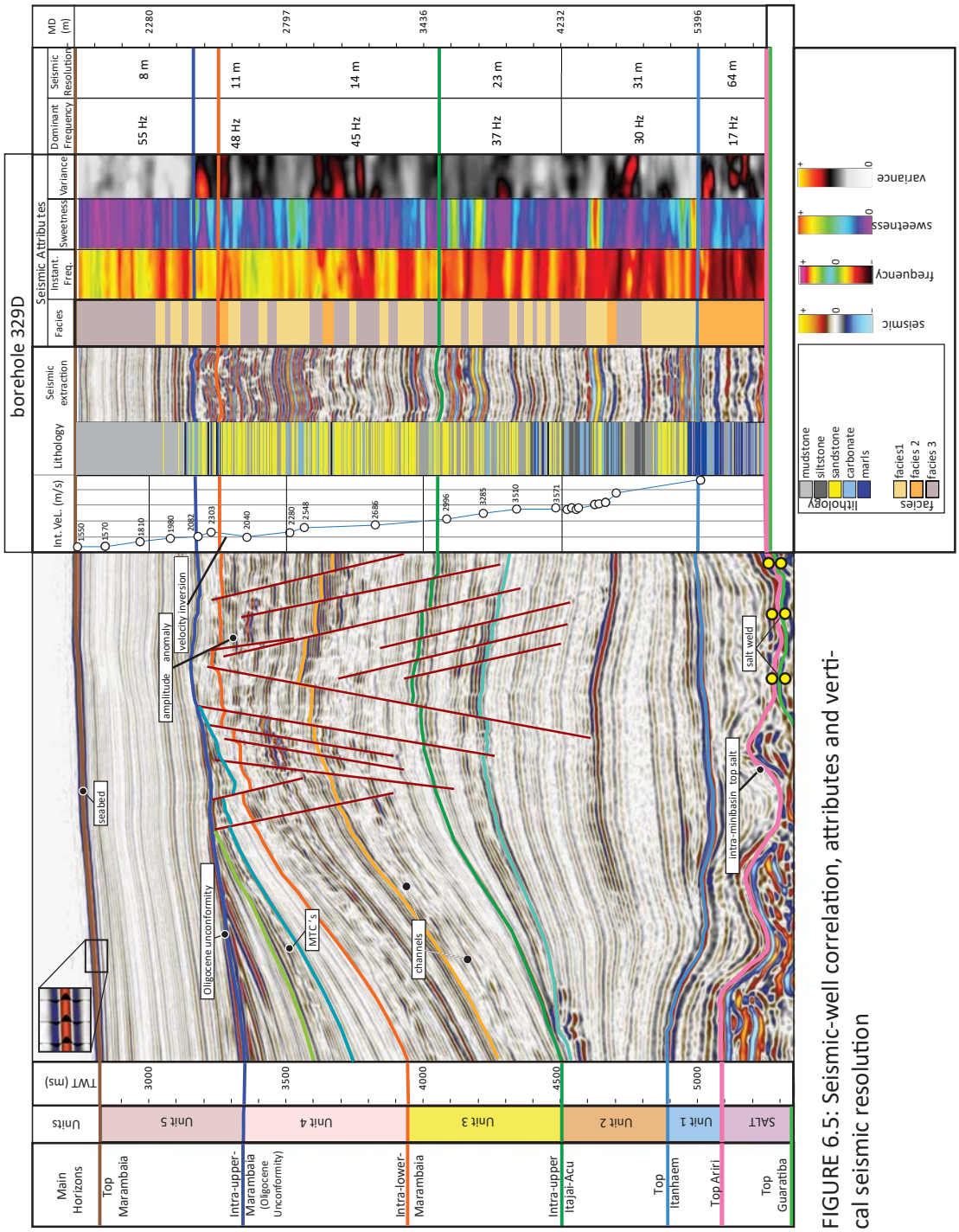


FIGURE 6.5: Seismic-well correlation, attributes and vertical seismic resolution

6.5 Minibasin structure and stratigraphy

Based on their location relative to the present shelf-edge, their map-view geometry, and the thickness of sediment they contain, I recognise three intraslope minibasin types: (i) *proximal thick minibasins* (e.g; minibasins A, B, C, D, E; Figs. 6.6b and 6.7a); (ii) *medial shallow minibasins* (e.g.; minibasins F, G, H; Figs. 6.6b and 6.7b); and (iii) *distal elongated minibasins* (e.g.; minibasins I, J, K, L, M; Figs. 6.6b and 6.7c). Seismic facies mapping and borehole-derived lithological data also indicate minibasin structure, bulk composition, and, therefore, likely depositional environment, vary in time and space (Figs. 6.6 and 6.7). I define five key stratigraphic units based on vertical seismic facies variations within the minibasins (i.e., Units 1-5; Figs. 6.5 and 6.7). The approximate age of each unit is largely based on a tie to stratigraphic age information provided by boreholes 329D and 723C (Figs. 6.5 and 6.8b). My age assignments are broadly consistent with and are thus supported by, regional seismic and stratigraphic data presented in several previous studies (e.g. Modica and Brush, 2004; Moreira et al. 2007; Contreras et al., 2010; Guerra and Underhill, 2012). In this section, I describe the structure and bulk stratigraphy of these minibasins, before outlining their tectono-stratigraphic development and the geomorphology of the deep-water depositional elements they contain.

6.5.1 Proximal thick minibasins:

Structure: The northern, most proximal part of the study area, immediately seawards of the Albian Gap, is characterised by relatively thick (>2.5 km) minibasins that are underlain by relatively thin (<500 m) or apparently welded salt (e.g.; minibasins A-E; Figs. 6.6, 6.7a; see also Jackson et al., 2014). The minibasins trend N to NE, are up to 30 km long and 5 km wide, and are bound by similarly trending, upright salt walls that are up to 5 km wide. Internally, the bases of most minibasins are defined by 'bowl'-shaped packages (*sensu* Rowan and Weimer, 1998), which appear to record deposition of Unit 1 during simple vertical subsidence into

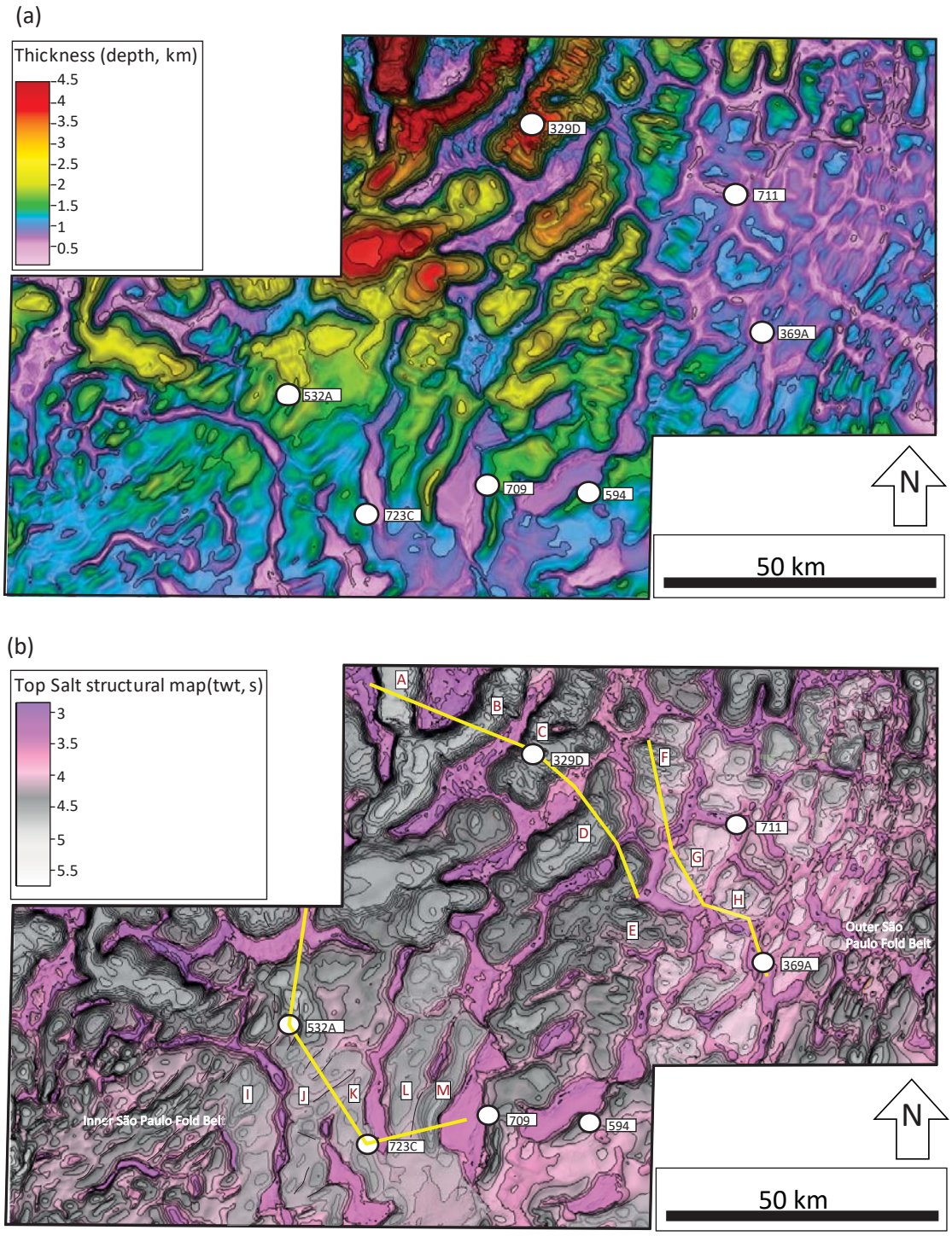


FIGURE 6.6: (a) Postsalt isophach (Seabed to top salt depth thickness map); (b) Minibasin types

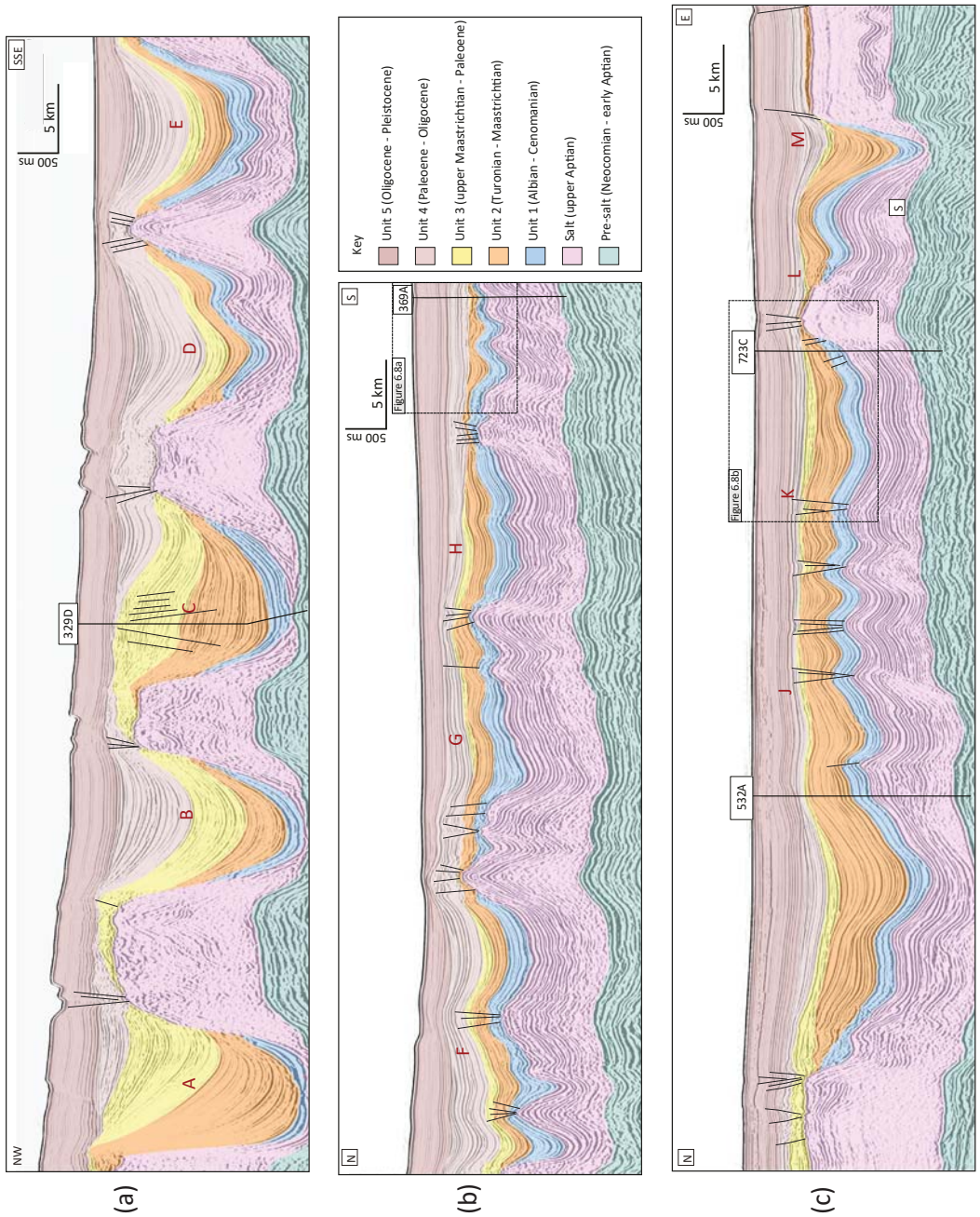


FIGURE 6.7: Minibasins (a) Proximal thick minibasins; (b) Medial shallow minibasins; (c) Distal elongated minibasins

underlying thick salt (Fig. 6.7a). Units 2 and 3 within minibasins B, D and E were also deposited during simple vertical subsidence as suggested by the 'bowl-like' shape of the deepest seismic-stratigraphic units. In contrast, rather than being dominated by bowl-shaped packages, the middle and upper parts of some minibasins are defined by 'wedge'-shaped packages, suggesting the latter stages of subsidence were characterised by asymmetric subsidence and minibasin tilting, possibly due to the onset of welding (e.g.; Units 2, 3 and 4 in minibasins A, C; Fig. 6.7a) (see Rowan and Weimer, 1998). My interpretation that minibasin welding was responsible for asymmetric subsidence and the deposition of wedge-shaped packages is also supported by the local development of turtle structures, which reflect structural inversion of minibasin stratigraphy (minibasin C, Fig. 6.7a; see Jackson & Hudec, 2017).

Stratigraphy: A borehole penetrates the central, deepest part of a partly-enclosed proximal deep minibasin (minibasin C, Figs. 6.5, 6.7a). This borehole indicates the Unit 1 is dominated by interbedded Albian-Cenomanian marl and mudstone (c. 87%), with lesser proportions of coarser-grained carbonate (c. 12%) and clastics (c. 1%). In contrast, overlying units are relatively sandstone-rich (c. 45%), although very fine-grained lithologies (i.e. mudstone) still dominate (>50%; Unit 2 and Unit 3; Fig. 6.5). The unit capping the minibasins (i.e., Unit 5) is mudstone-dominated (Fig. 6.5).

6.5.2 Medial shallow minibasins:

Structure: The eastern, most distal part of the study area, which bounds the western flank of the Outer São Paulo Fold belt (*sensu* Jackson et al. 2015b), is characterised by minibasins that are thinner (<1.5 km) than those further west (e.g., minibasins F, G, H; Figs. 6.6, 6.7b). The shallow minibasins are underlain by relatively thick salt (> 2 km); welds are absent. The minibasins are sub-circular to oval, are up to 20 km long and 10 km wide, and are enclosed by narrow (<2 km), nearly-triangular diapirs and salt-cored buckle folds (Fig. 6.7b). The salt-cored structures bounding the shallow minibasins trend either NE or NW, thus defining a crudely

polygonal pattern (Fig. 6.6). Internally, Units 1, 2 and 4 are characterised by negligible thickness variations along the shallow minibasins, although local 'bowl'-shaped packages are suggestive of deposition during simple vertical subsidence into underlying thick salt (e.g., minibasin F; Fig. 6.7b). Instead, Unit 3 is defined by thin (<200 m) 'wedge-shaped' packages indicating deposition during asymmetric subsidence (e.g., minibasins F, H; Fig. 6.7b).

Stratigraphy: A borehole penetrating a distal shallow minibasin indicates that Unit 1 comprises only interbedded mudstone and marl (borehole 369A, Fig. 6.8a). Likewise, the overlying post-Cenomanian units (2-4) are also dominated (c. 80%) by very fine-grained lithologies (i.e. mudstone and marl). However, even in this relatively distal location, some sandstone (40 m net thickness) occurs within Unit 3 (i.e. borehole 369A, Figs. 6.7b, 6.8a). The unit capping the minibasins comprises only mudstone and marl (Unit 5, Fig. 6.8b).

6.5.3 Distal minibasins:

Structure: The most distal location of the study area includes part of the Inner São Paulo Plateau Fold Belt (ISPFB, *sensu* Jackson et al. 2015b). This area is characterised by N-striking, up to 30 km long and 5 km wide, relatively thin (<1.5 km) minibasins, which are typically underlain by relatively thick salt (c. 1 km; Fig. 6.6). Some thicker (up to 2.5 km), nearly welded minibasins are also locally developed (e.g. minibasin M, Fig. 6.7c). The distal minibasins are bound by salt walls that have flat or rugose-tops, or broadly N-trending, salt-cored anticlines (e.g., minibasins L, M, Fig. 6.7c; e.g., Jackson et al. 2014, 2015b). The distal minibasins are internally deformed by NE-trending, salt-cored buckle folds that are spaced c. 5 km (e.g, minibasins J and K, Fig. 6.7c). Internally, Unit 1 and Unit 2 are concordantly folded above the salt-cored buckle folds with local development of bowl-shaped packages characteristic of deposition during vertical minibasin subsidence (e.g., minibasin M; Fig. 6. 7c). In contrast, Unit 3 is of variable thickness, defining relatively thin (<200 m), wedge- and bowl-shaped packages that overlie Unit 2 across an erosional surface (Fig. 6.7c). Unit 4 and Unit 5 cap the distal

minibasins and the flat-topped, bounding salt walls (Fig. 6.7c).

Stratigraphy: Most of the boreholes penetrating the Inner São Paulo Fold Belt and the distal minibasins indicate Unit 1 comprises interbedded mudstone and marl (Itanhaem Formation; boreholes 532A, 723C, 709, 594, Fig. 6.6). However, a notable exception occurs on the eastern flank of minibasin K, where Unit 1 contain relatively coarse-grained lithologies (e.g. c. 63 m net thickness of siltstone and c. 22 m net thickness of sandstones; borehole 723C, Fig. 6.8b). The overlying post-Cenomanian units are also dominated by fine-grained lithologies (mudstone, c. 70% of total unit thickness), except on the eastern flank of minibasin K where relatively coarse-grained lithologies occur (i.e., siltstone, borehole 723C, 80% of total unit thickness, 170 m net thickness; Fig. 6.8b). Sandstone is rare (<5% of total unit thickness), with volumetrically minor proportions only locally developed (i.e. 723C, c. 27 m net thickness, Unit 3, Fig. 6.8b). In a similar way to the more proximal minibasins, the unit capping the distal minibasins is mainly composed of mudstone (>81% of total unit thickness), although interbedded carbonate, sandstone and siltstone occur in its lower part (Fig. 6.8b)

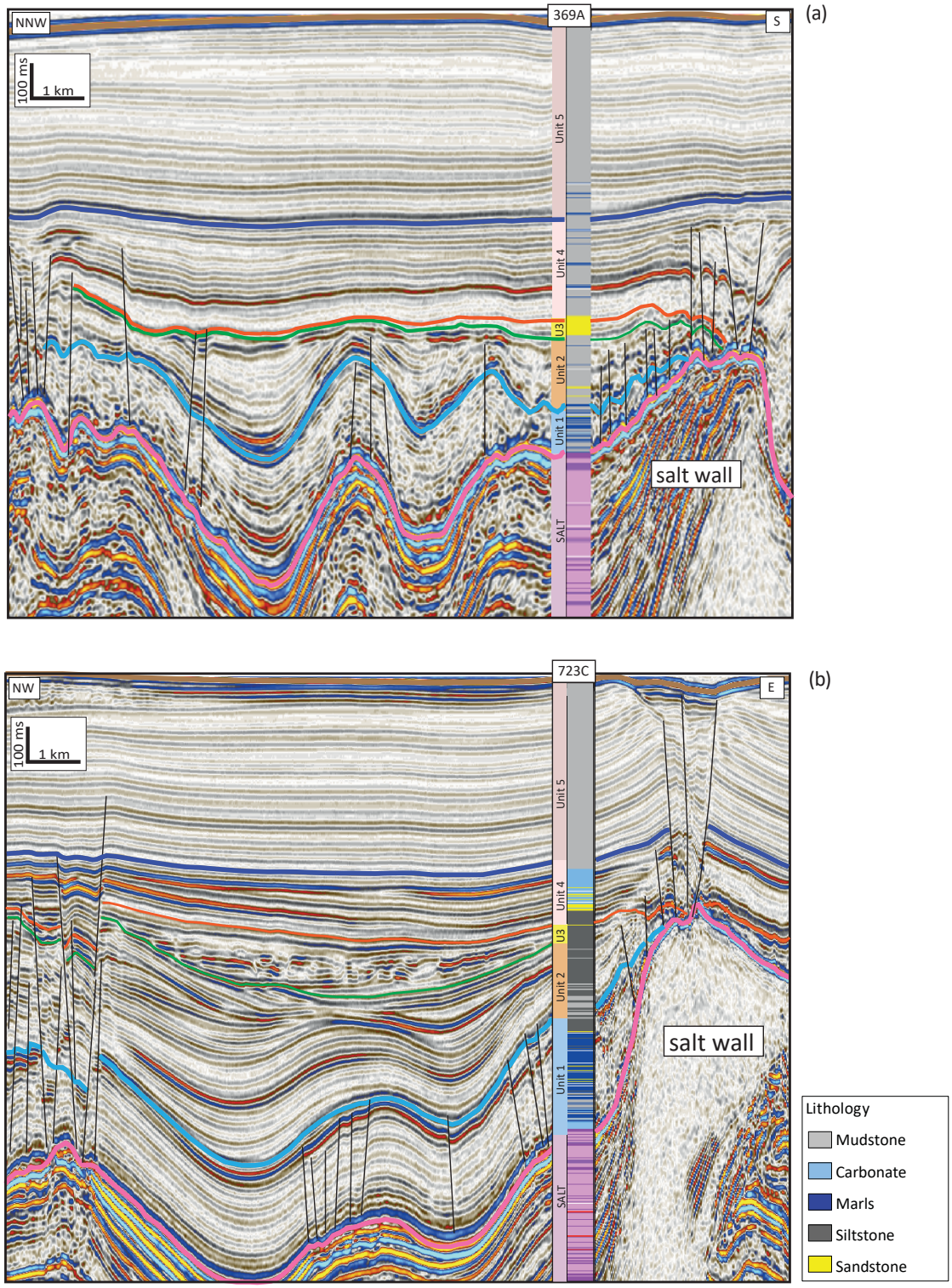


FIGURE 6.8: Seismic-well tie. (a) Borehole 369a penetrating a shallow minibasin. See Figure 6.7b for location. (b) Borehole 723C penetrating the flank of a distal minibasins. See Figure 6.7c for location.

6.6 Minibasins deep-water depositional elements

Having defined the key types and bulk lithological trends within the intraslope minibasins, I here integrate seismic stratigraphy and seismic attribute analysis to identify, describe and map the deep-water depositional elements they contain (Table 6.2). I identify five main seismic facies types, which I infer represent the following deep-water depositional elements; i) channels (with and without lateral accretion packages (LAPs); ii) levees; iii) lobes; iv) MTCs; and v) background deposits (Table 6.2).

Channels

In cross-section, this depositional element is characterised by 20-150 m thick packages of parallel, continuous, flat-lying, moderate-to-high amplitude seismic reflections (Table 6.2). Package bases are flat and only weakly erosional (Table 6.2). In plan-view, these packages define relatively narrow (0.2-3 km), elongate (up to 200 km), low sinuosity (<1.5), channel-like forms that pass downdip into lobe-shaped depositional elements. I note these channel-like forms are defined by SF1, i.e., relatively high amplitudes, and high sweetness and low variance values, suggesting they are sandstone-prone. This interpretation is supported by borehole 329D, which penetrates a channel-like feature and that indicates high-amplitude, continuous seismic facies correspond to the presence of sandstone (SF1; Fig. 6.5). Based on this observation and by comparison to other borehole-calibrated, seismic reflection-based studies (e.g. Prather 2003; Samuel et al., 2003), I infer channel-like depositional elements defined by relatively moderate-to-low amplitudes are filled by finer-grained lithologies such as siltstone or mudstone.

Based on their seismic expression, geometry and scale, and by comparison to notable examples from other deep-water margins, this depositional element is interpreted as the seismic expression of turbidite-fed, relatively low-sinuosity, submarine channels (e.g. Prather, 2003; Nile Delta, Samuel et al., 2003, Espirito Santo Basin; Alves et al., 2009; Lower Congo

Basin, offshore Angola; Kolla et al. 2000; Mayall and Stewart; 2000; Fonnesu, 2003; Mayall and O'Byrne, 2002; Gee and Gawthorpe; 2006, 2007).

The flanks of some of the channels described above are characterised by up to 100 m thick, laterally stacked packages of moderate-to-high-amplitude reflections that dip in towards the channel axis. Attribute maps illustrate these dipping reflections are up to 1 km wide and 5 km long, and have a crescent-shaped form, flanking the inner bends of the more sinuous channels(i.e. sinuosity index c. 1.5 or above) (Table 6.2). None of the boreholes available penetrate these dipping reflections, which are characterised by high amplitudes and high sweetness values, suggesting they are too sandstone-dominated. Based on their geometry and occurrence on the inner side of the channel bends, these depositional elements are interpreted as lateral accretion packages (LAPs) that developed due to lateral migration of the adjacent channel, similar to point bars in sinuous fluvial channels (cf. Kolla et al., 2000; Abreu et al. 2003; Janocko et al. 2013).

Levees

Some of the submarine channels are locally flanked by wedge-shaped seismic packages of subparallel, low-to-moderate amplitude seismic reflections that are thickest (up to 150 m but typically thinner) immediately adjacent to the channels (Table 6.2). Due to the predominantly low-amplitude seismic reflections these elements are not clearly imaged by surface attributes. However, isochrons indicate this depositional element is up to 5 km wide, up to 10 km long in dip extent, and are typically asymmetrically developed on both sides of the channel (Table 6.2). None of the boreholes available penetrate this depositional element; however, these wedge-shaped seismic packages are characterised by low-to-moderate- amplitudes and sweetness values, suggesting they are composed of relatively fine-grained lithologies such as siltstone or mudstone.

Based on their seismic expression, geometry, scale and development adjacent to submarine

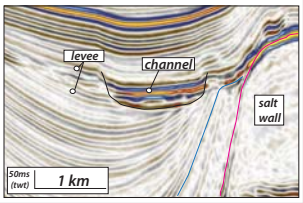
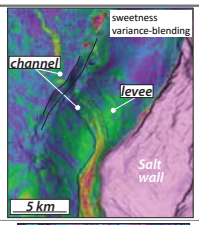
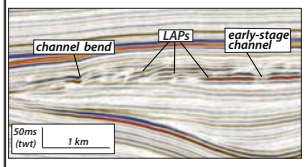
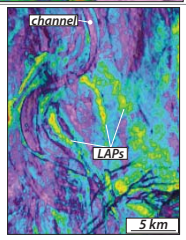
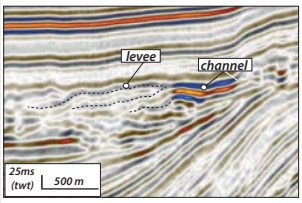
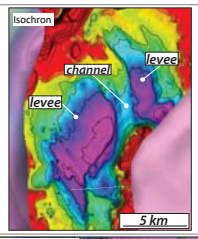
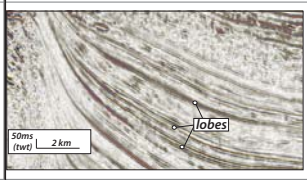
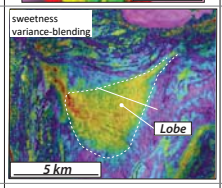
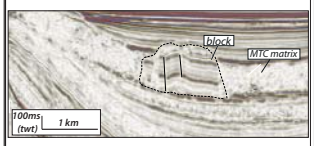
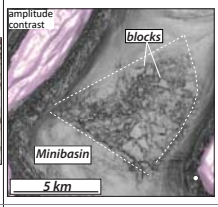
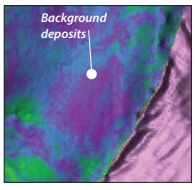
Seismic facies and depositional elements					
	Seismic stratigraphy	**Seismic geomorphology**	**Reflection character**	**Geometry**	**Interpretation/ composition**
Channels			Parallel, continous, moderate-to-high amplitude seismic reflections. Some low-amplitude channels also observed Bases are flat, weakly erosional or strongly erosional ***20 - 150 m thick***	Relatively narrow,elongate, low sinuosity, channel-like forms ***0.2 - 3 km wide*** ***up to 200 km long*** ***sinuosity (<1.5)***	Turbidite-fed submarine channels Sandstone-prone channel-axis if highly reflective, high sweetness and low variance Siltstone and mudstone if moderate to low amplitude and low sweetness values
			Laterally stacked moderate-to high amplitude seismic reflec-tions dipping in towards the channel axis ***up to 100 metres thick***	Crescent-shaped forms flanking the inner bend of more sinous channels ***up to 1 km wide*** ***up to 5 km long***	Lateral accretion packages developed due to the channel lateral migration Sandstone/siltstone based on high amplitude, high sweetness and low variance values
Levees			Wedge-shaped seismic packages of subparallel, low-to-moderate amplitude seismic reflections adjacent to the channels ***up to 150 metres thick but mostly thinner***	Asymmetrically developed on both sides of the channels ***up to 5 km wide*** ***up to 10 km long***	Levees deposited by sediment gravity-currents that escaped from the submarine channels Generally fine-grained mudstone or siltstone composition based on low seismic amplitudes and sweetness values
Lobes			Tabular to mounded packages of subparallel, continous moderate to high-amplitude seismic reflections. thinning towards the fringes downlap ***Up to 200 m thick***	Sub-rounded, to lobate to elongate ***up to 5 km wide*** ***up to 10 km long***	Lobes deposited at the mouth of submarine channel Composed largely of sandstone based on high amplitude, attributes and differential compaction
MTCs			Packages of discontinuous to chaotic, low-to-moderate amplitude seismic reflections ***Up to 200 m thick*** Basal surfaces are sharp and not erosional or highly irregular with v-shaped grooves Blocks are parallel continuous high amplitude reflections ***up to c. 200 m thick***	Fan-shaped or subparallel lineations ***up to 50 km long*** Small semi-circular to angu-lar blocks of various sizes, ***0.2 to 1 km long*** ***0.1 to 2 m wide***	Mass transport complexes Marls, mudstone and sandstone composition based on borehole data
Background deposits			Parallel, continous, high frequency, low-to-moderate amplitude reflections	Continuous with slight variattions in seismic amplitudes and sweetness values	Mudstone and marls deposited during low-energy conditions

Table 6.2: Seismic facies and depositional elements identified within the post-salt sequence in central deep-water Santos Basin. Interpretation is mainly based on the analysis of the seismic stratigraphy and seismic geomorphology

channels, I interpret these depositional elements as levees, deposited by sediment gravity-currents that escaped from their channels. Geometrically similar features are identified in many deep-water basins (e.g. Fonnesu, 2003; Viana et al., 2003; Gee and Gawthorpe, 2006, 2007; Clark and Cartwright, 2009, 2011; Janocko et al., 2013; Oluboyo et al., 2014).

Lobes

This depositional element is defined by tabular to mounded packages of subparallel, continuous, moderate-to-high-amplitude reflections. These packages are up to 10 km long, 5 km wide and 200 m thick, thinning towards their fringes. Bidirectional downlap onto underlying strata is also observed in distal locations (e.g., Fig. 6.19b). The plan-view morphology of this element ranges from sub-rounded, to lobate, to elongate occurring at the mouth of channel depositional elements (Table 6.2, Figs. 6.12 and 6.15). Based on their high-amplitude character and moderate-to-high-sweetness values, I infer this depositional element is sandstone-dominated. This inference is supported by borehole data, which indicates some of the units containing these depositional elements are sandstone-bearing (Unit 2, Unit 3, 329D and Unit 3 in 723C, 369A; Figs. 6.5, 6.8). Further support for a sandstone-dominated composition comes from the mounded externally morphology of these features, which may reflect differential compaction between the lobes and adjacent finer-grained sediment.

Based on their geometry in map- and section-view, I interpret these depositional elements as lobes that occur at the mouth of and are genetically linked to updip submarine channels (cf. Gee and Gawthorpe, 2006, 2007; Jones et al. 2012; Oluboyo et al. 2014).

MTCs – Mass transport complexes

This depositional element is characterised by up to 200 m thick, 50 km long packages of discontinuous to chaotic, low-to-moderate amplitude reflections (Table 6.2). The basal surface of this element is either sharp and apparently not erosional, or highly irregular and defined by

'v'-shaped grooves. The upper surfaces are invariably rugose. The plan-view morphologies of these elements are fan-shaped, defined by laterally extensive subparallel lineations or locally ponded within the minibasins (Table 6.2; 6.23). Within these chaotic intervals I recognise laterally restricted 'blocks' of parallel, continuous moderate-to-high-amplitude reflectivity. These blocks are up to 100 m thick, 1 km long and 5 km wide.

Based on the seismic stratigraphy and geometry, I interpret these depositional elements as MTCs. The chaotic seismic facies likely represent highly disaggregated, debritic material, whereas the coherent packages represent relatively coherent slide blocks (cf. Posamentier and Kola, 2003; Gee and Gawthorpe, 2006, 2007; Gamboa et al. 2010; Jones et al. 2012; Oluboyo et al. 2014).

Background deposits

This depositional element dominates the stratigraphic fill of all minibasins, encasing the depositional elements described above. This depositional element is characterised by parallel, continuous, high-frequency, low-to-moderate amplitude reflections, although subtle variations in amplitude and sweetness occur (SF2; Table 6.2). Borehole data indicate these seismic facies consists of fine-grained lithologies (i.e. mudstone and marl, e.g., unit 5; Fig. 6.5). Based on the seismic stratigraphy and the integration with borehole data I interpret this depositional element as fine-grained slope deposits emplaced by dilute turbidity currents or suspension setting. (cf. Hadler-Jacobson et al. 2007; Oluboyo et al. 2014).

6.7 Tectono-stratigraphic development of intraslope minibasins

The key seismic stratigraphic units defined within the post-salt succession document the tectono-stratigraphic development of the intraslope minibasins (Fig. 6.7). Here I interpret the isochron-derived thickness variations and depositional elements occurring within each unit; this allows us to understand minibasin filling history and, more specifically, to assess how syn-depositional, salt-induced seabed deformation controlled deep-water sediment dispersal and sediment architecture. Based on previous regional studies (e.g., Modica and Brush, 2004;

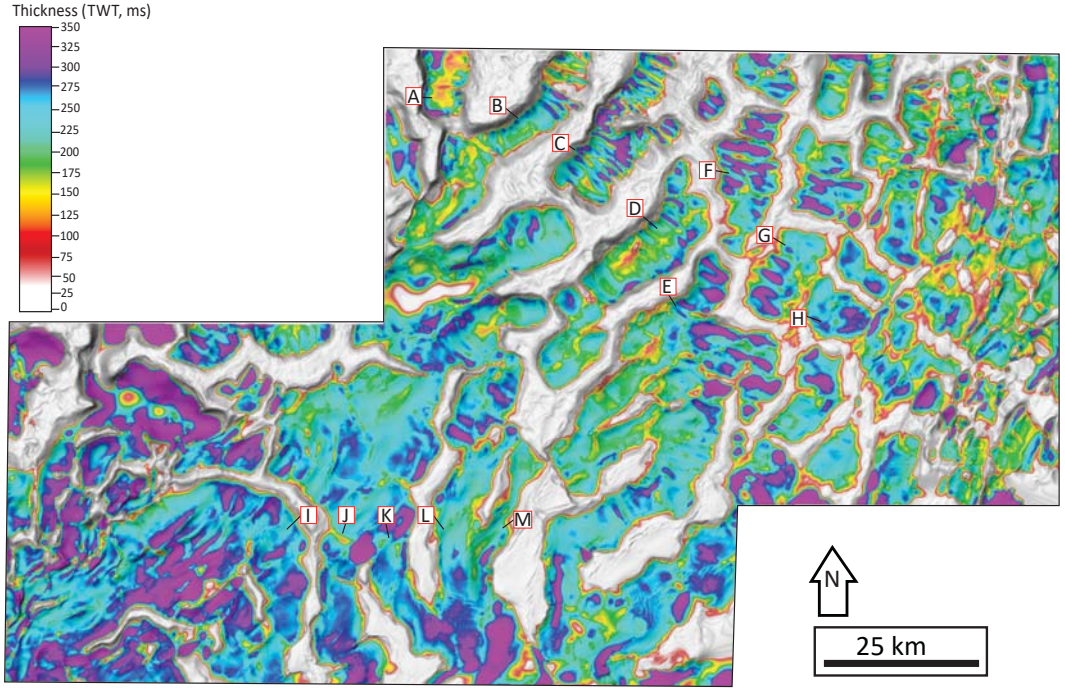


FIGURE 6.9a: Unit 1 time thickness map

FIGURE 6.9: Regional isochrons illustrating deposition and salt-related deformation in the post-salt of central deep-water Santos Basin. (a) Albian-Cenomanian unit 1 twt thickness map; (b) Turonian to Mid-Campanian Unit 2 twt thickness map; (c) Campanian to Paleocene Unit 3 twt thickness map; (d) Paleocene to Mid Oligocene Unit 4 twt thickness map; (e) Mid-Oligocene to present-day Unit 5 twt thickness map.

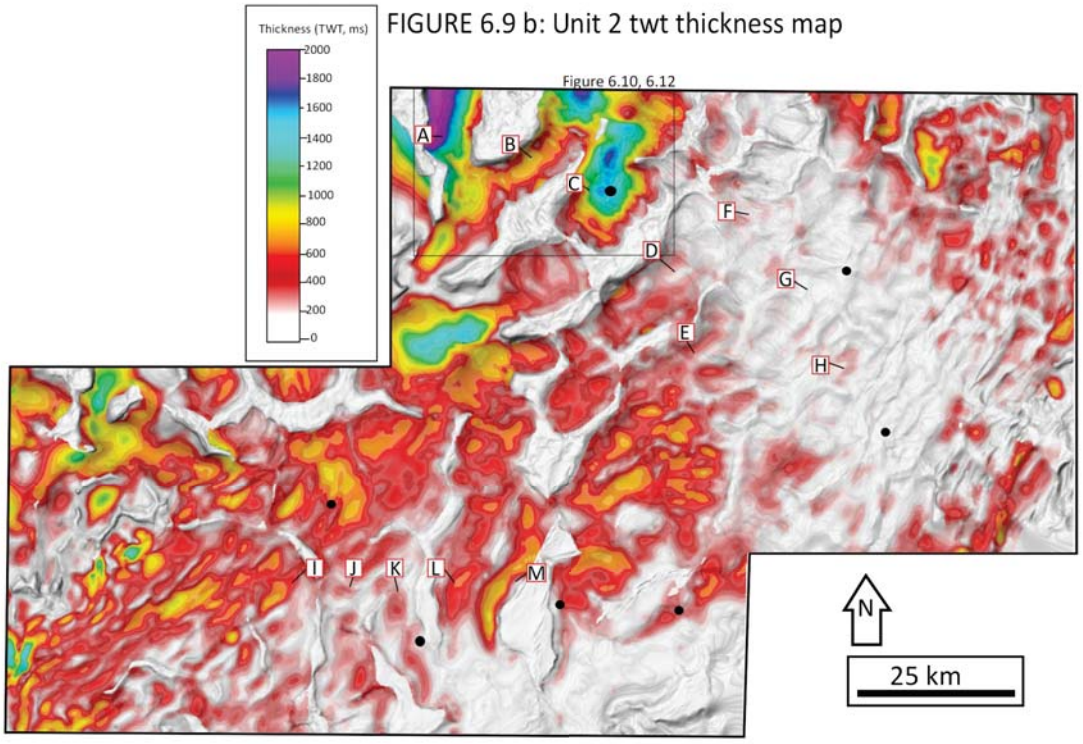


FIGURE 6.9 b: Unit 2 twt thickness map

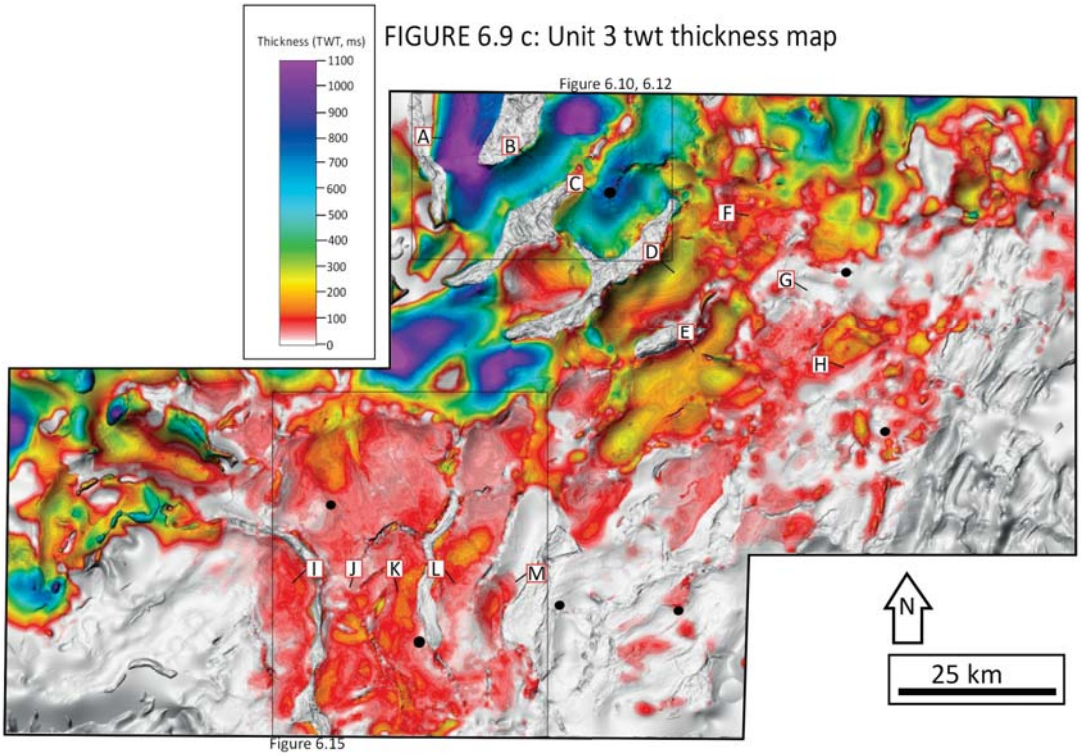


FIGURE 6.9 c: Unit 3 twt thickness map

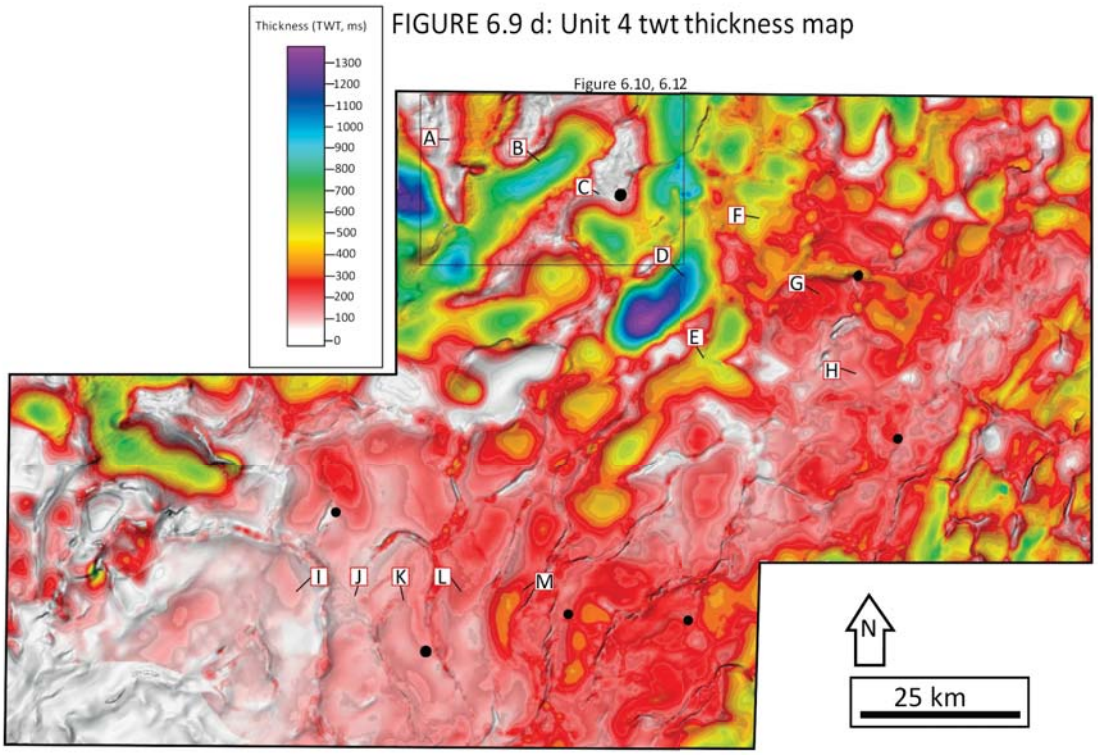


FIGURE 6.9 d: Unit 4 twt thickness map

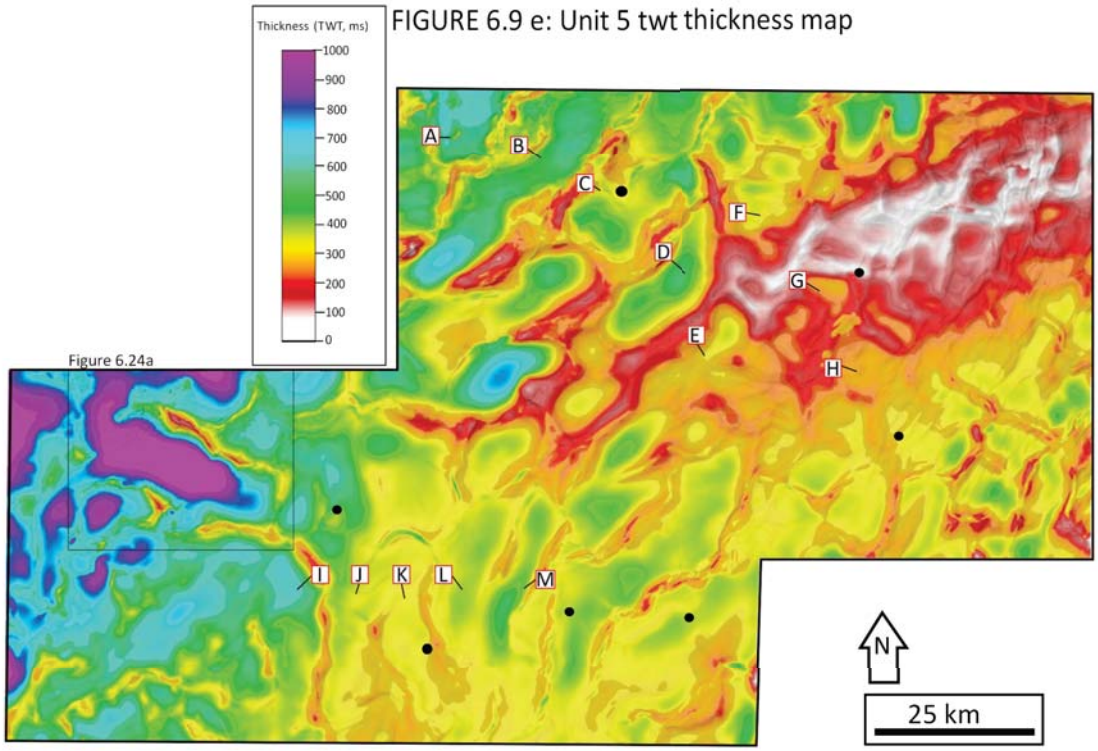


FIGURE 6.9 e: Unit 5 twt thickness map

Guerra and Underhill, 2012), I infer that the dominate sediment transport direction was from N-S and NW-SE, although I recognise local diversions from this within minibasins due to syn-depositional deformation.

6.7.1 Unit 1: Albian - Cenomanian

The Unit 1 isochron indicates this unit is areally extensive and displays significant thickness variations (Figs. 6.7, 6.9a). Overall, I observe a central thinner wedge or 'tongue' of relatively thin strata, which is surrounded by areas of thicker strata (up to 350 ms, TWT) (Fig. 6.9a). Seismic stratigraphic and attribute analysis provide no evidence for at least seismic-scale deep-water depositional systems within unit 1.

Based on seismic reflection and borehole data (Figs. 6.7, 6.8), I interpret Unit 1 represents the distal expression of the Albian-Cenomanian shallow-marine carbonate platform (Fig. 6.4a). Thickness variations across the study area possibly reflects differences in the timing and style of salt tectonics (e.g., Jackson et al. 2015b).

6.7.2 Unit 2: Turonian to Mid-Campanian

Unit 2 is less extensive than unit 1, with the main depocenters focused within proximal minibasins presently encircled by salt walls (minibasins A, C; Fig. 6.9b). Locally thick succession is observed, however, occurring landward of a salt pillow within minibasin B (depocenters B1; Figs. 6.10a, 6.11b). In contrast, within the Inner Fold Belt and more distal minibasins, thinner successions occur (Figs. 6.9b).

In unit 2, deep-water depositional elements, such as channels and lobes, occur only within proximal thick minibasins (Figs. 6.12 a, b). Low sinuosity (<1.5), narrow (<1 km wide) submarine channels enter from the north of and are vertically stacked within, minibasin A (Figs. 6.12 a, b)

(Figs. 6.12 a, b). Channels of similar dimensions and sinuosities trend WNW in the proximal part of minibasin B and N in minibasin C, changing to NNE towards the south where they encounter the salt wall bounding the minibasins eastern margin (Figs. 6.12 a, b). At the downdip mouths of some of the channels I identify lobes, with these being particularly well-developed within depocenter C1 where they correlate with SF1 in borehole 329D and are interpreted to be sandstone-rich (Figs. 6.5; 6.11a; 6.12 a, b).

The distribution of deep-water sediments within unit 2 was clearly controlled by salt-related deformation, with isochron, seismic attribute and borehole data (Fig. 6.5) indicating Turonian to Mid-Campanian, relatively coarse-grained channels only extended downdip into and were at least partly ponded within, proximal minibasins (minibasins A and northern para of minibasin B). In addition, I interpret that channels within minibasin C are now separated from their updip counterparts in depocenter B1 by a large salt wall that pierces the stratigraphic interval within which they are developed (Figs. 6.10a; 6.12 a, b)

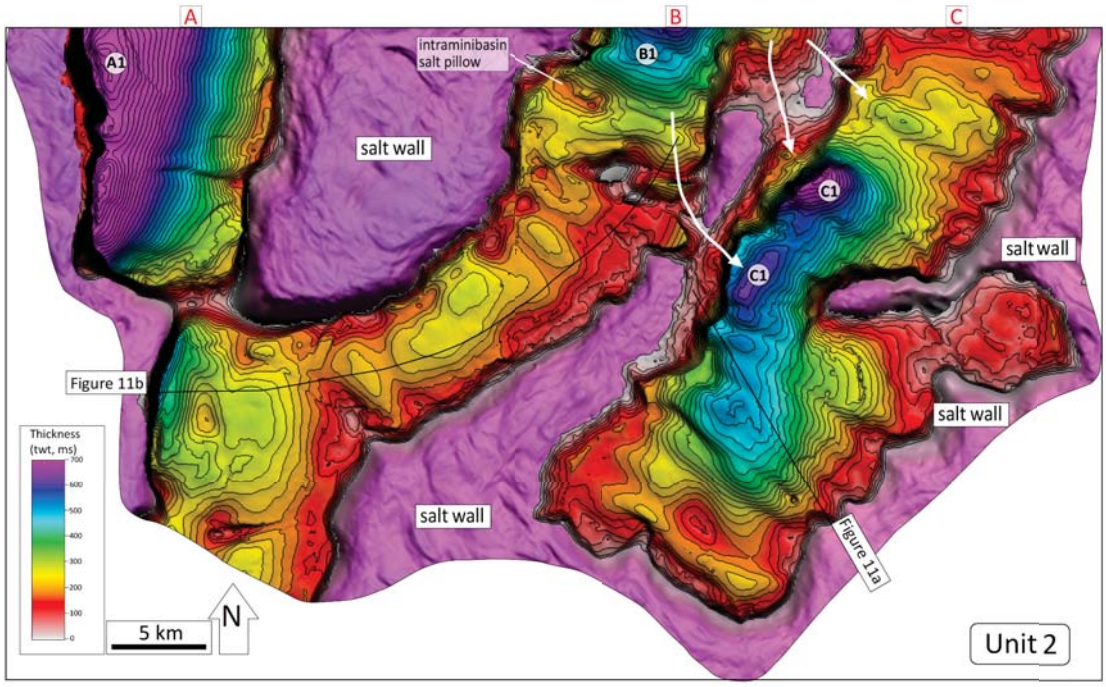


FIGURE 6.10: Detailed thickness maps of the proximal minibasins (A-C) illustrating local intra-minibasins depocenters and shifting of depocenters during minibasin development: (a) Unit 2 thickness map and initial depocenters (b) Sub-unit 3a thickness map and main depocenters; (c) Sub-unit 3b time thickness map and main depocenters; (d) Sub-unit 4a time thickness map and main depocenters; (e) Sub-units 4b and 4c and main depocenters.

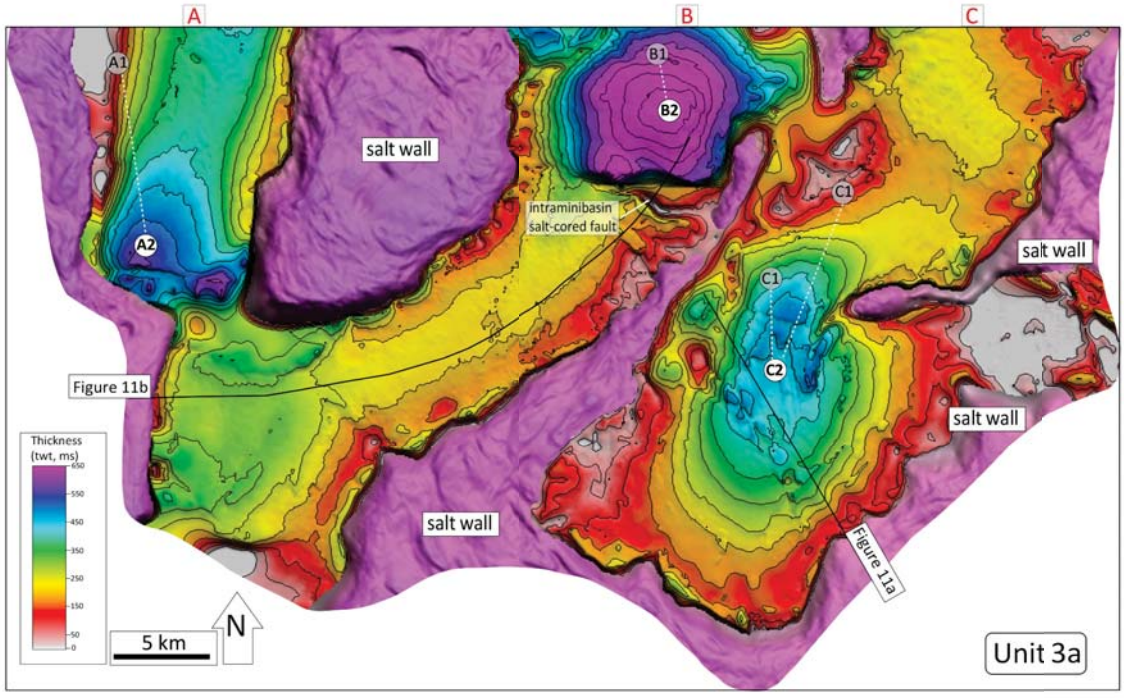


FIGURE 6.10b: Proximal thick minibasins - Unit 3a isochron

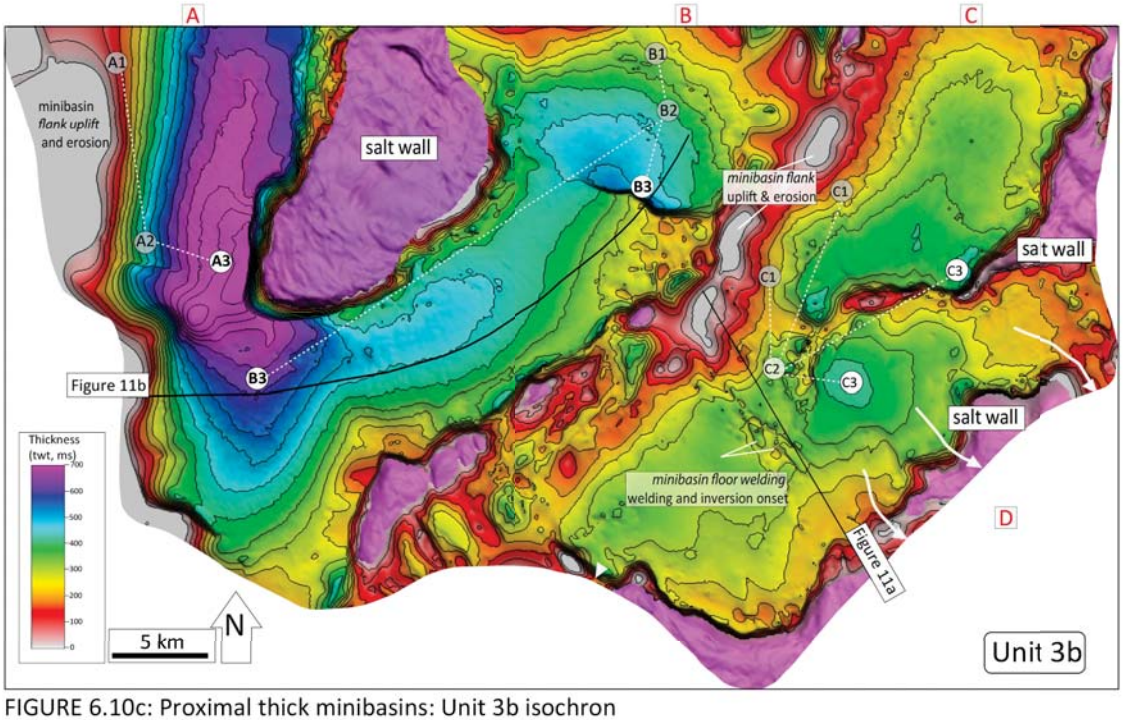


FIGURE 6.10c: Proximal thick minibasins: Unit 3b isochron

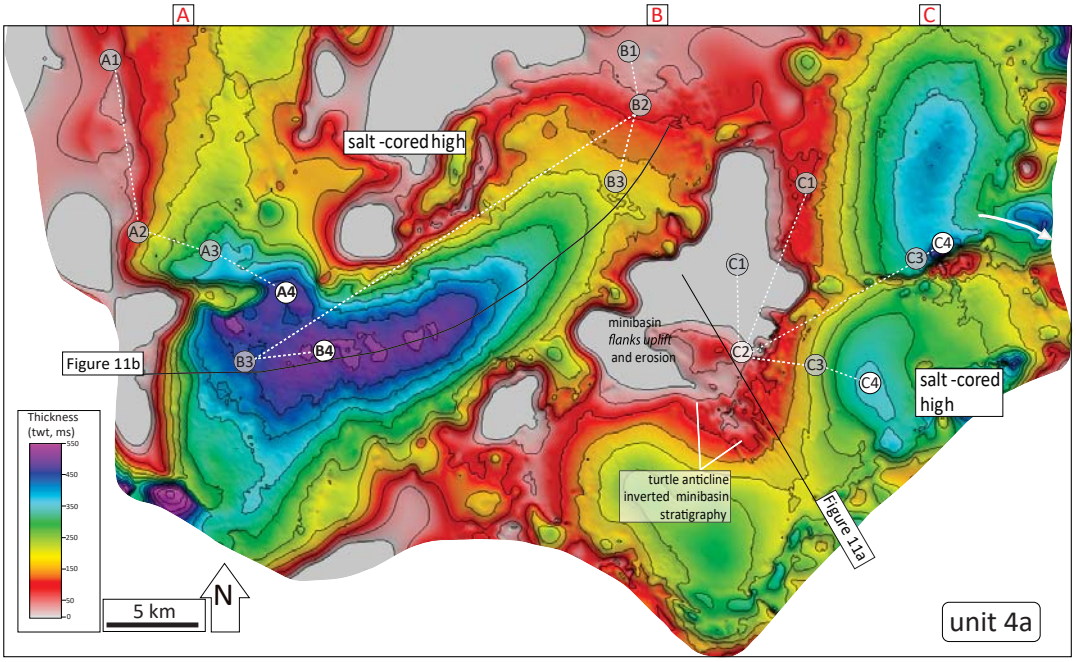


FIGURE 6.10d: Proximal thick minibasins - Unit 4a isochron

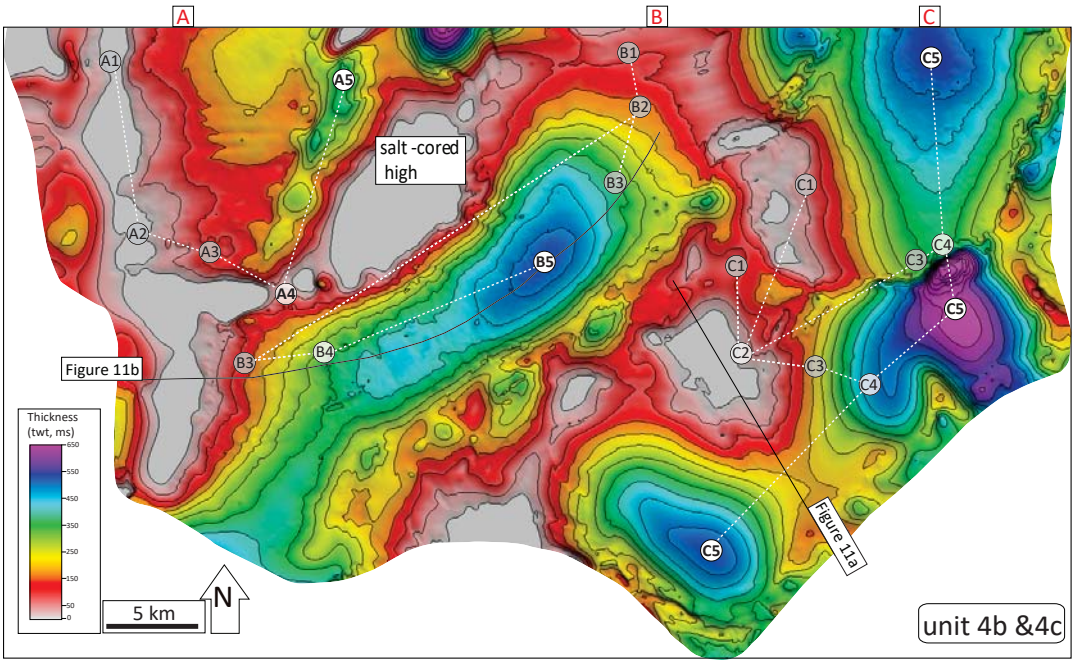


FIGURE 6.10e: Proximal thick minibasins - Unit 4b and 4c isochron

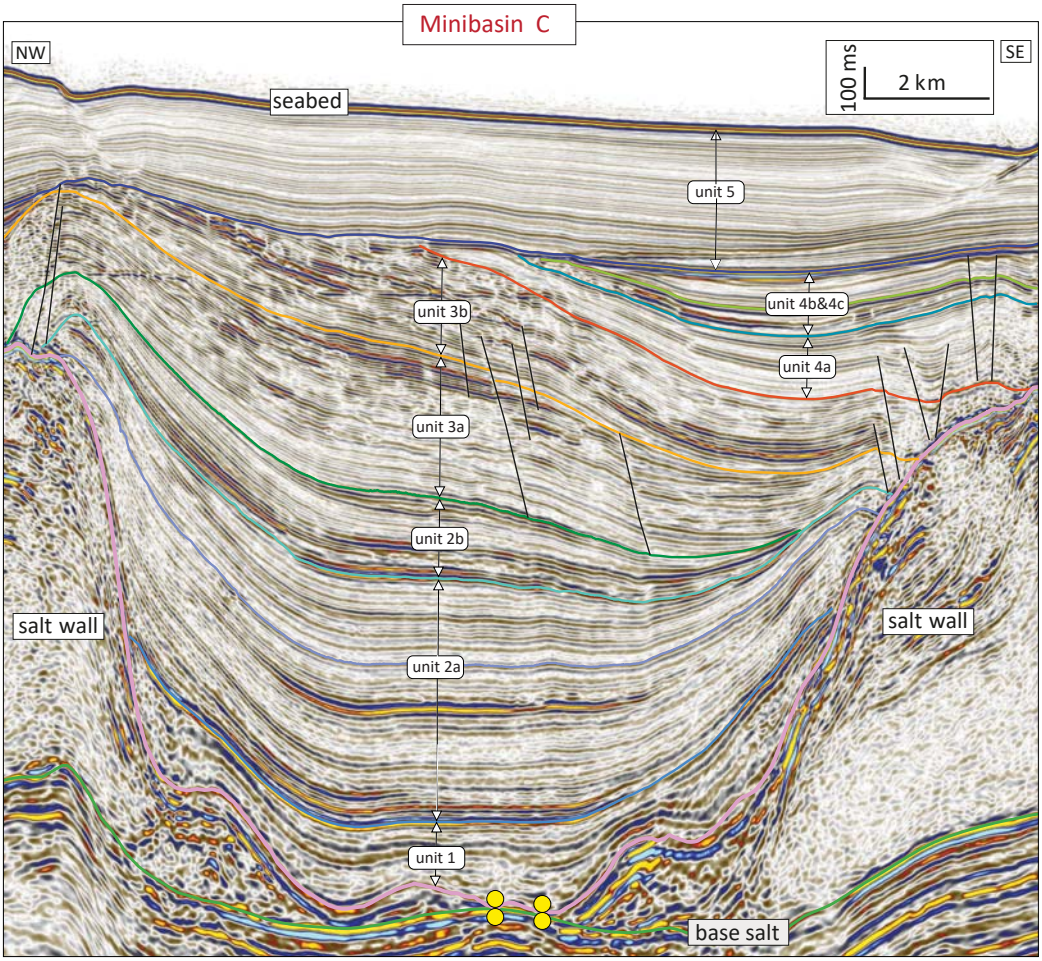


FIGURE 6.11. (a) Seismic profile across minibasin C. (b) Seismic profile along minibasin B. See Figures 6.10 and 6.12 for locations. (c) Geoseismic profile along minibasin B illustrating the main depositional elements within the key units. (d) Sweetness attribute in the proximal part of minibasin B illustrating the main depositional elements identified. (e) Sweetness attribute south of minibasin B illustrating the main depositional elements identified.

6.7.3 Unit 3: Mid-Campanian to Palaeocene

Overall, Unit 3 is more extensive than Unit 2, with major intraslope depocenters still present in actively subsiding proximal minibasins (minibasins A-C; Fig. 6.9c). More specifically, local increases in sediment thickness occur next to intra-minibasin salt pillows and thin-skinned normal faults, and along minibasin flanks associated with growing salt walls (Figs. 6.10 b, c). However, in contrast to Unit 2, significant thicknesses of strata are now preserved in downdip minibasins, especially in synclines flanking folds, above salt-cored faults, and along minibasin flanks (minibasins D-M; Figs. 6.9c; 6.16 a, 6.18a and 6.20)

Deep-water depositional systems are widespread in unit 3 (Figs. 6.12, 6.13 and 6.15). Minibasins A-C are still dominated by relatively low sinuosity (<1.5), narrow (<1 km wide) submarine channels. However, these channels extend further downdip than those in Unit 2. For example, channels in minibasin A are no longer restricted to the northern part of the depocentre, now extending c. 10 km further south to the junction between minibasins A and B, where they appear to pass downslope into a lobe (Figs. 6.11b, c; 6.12c). Likewise, channels and lobes initially ponded in depocenters B1-B2 extend further downslope along minibasin B, depositing lobes in depocenter B3 (Fig. 6.12d). In a manner similar to that identified in unit 2, some of the channels entering minibasin B in Unit 3 extend downslope towards minibasin C, although channels along the western flank of the minibasin appear to be diverted towards depocenter B3 at their southern end (Figs. 12d, e, f). During deposition of unit 3, lobes are also deposited against the salt wall bounding the SE margin of the minibasin (depocenters C2, Fig. 6.12 c-e). Continued filling of minibasin C was accompanied by the shifting of depocenters C2 to C3 related to deposition of SE-trending submarine channels, which apparently terminate abruptly against the salt wall defining the southern limit of minibasin C; however, further downslope, on the other side of this structure, channels of similar dimensions, orientation and morphology occur in minibasin D and E (Figs. 6.12f, g, 6.13, 6.14).

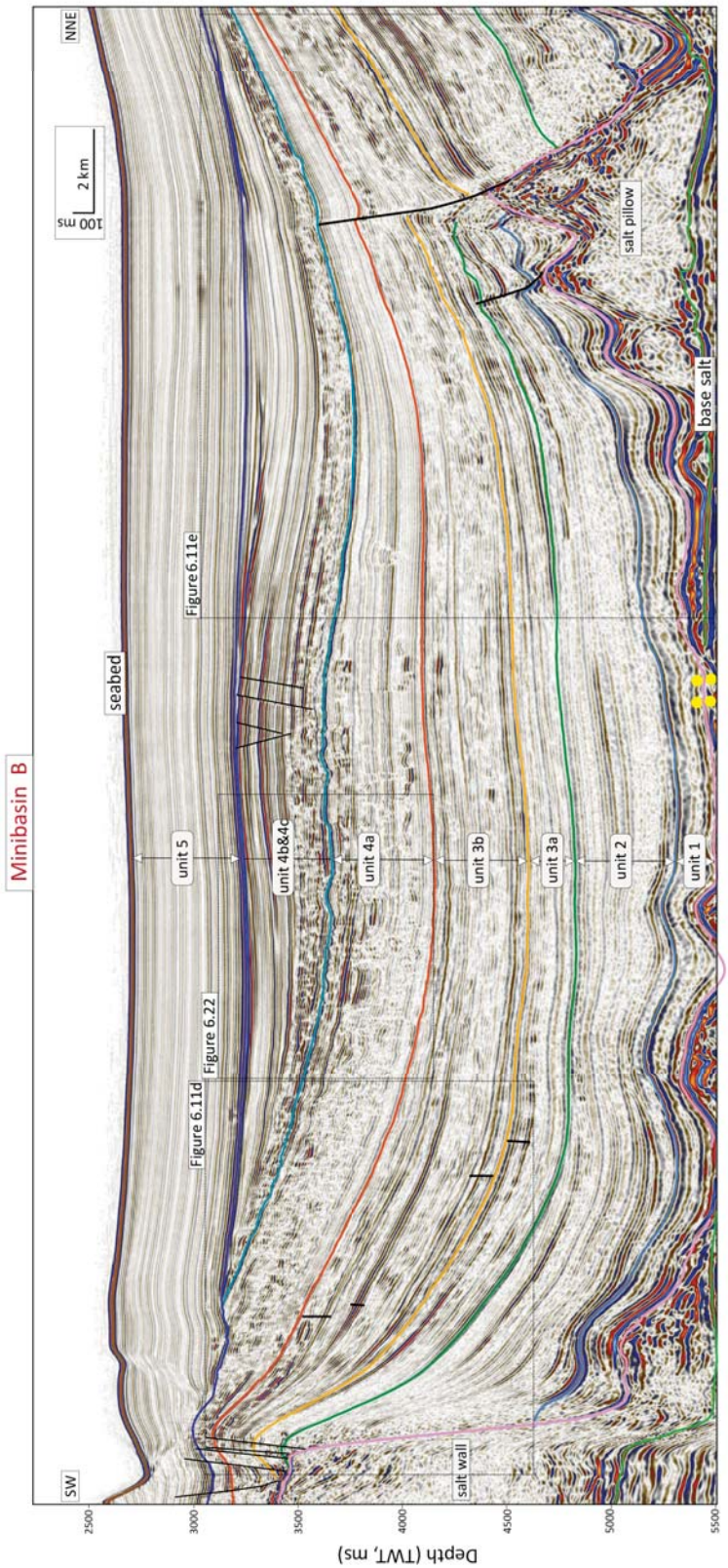


FIGURE 6.11 b: Seismic section along Minibasin B. Mapped attribute intervals in Figure 12 are shown with black lines. Location of section is shown on Figures 10 and 12.

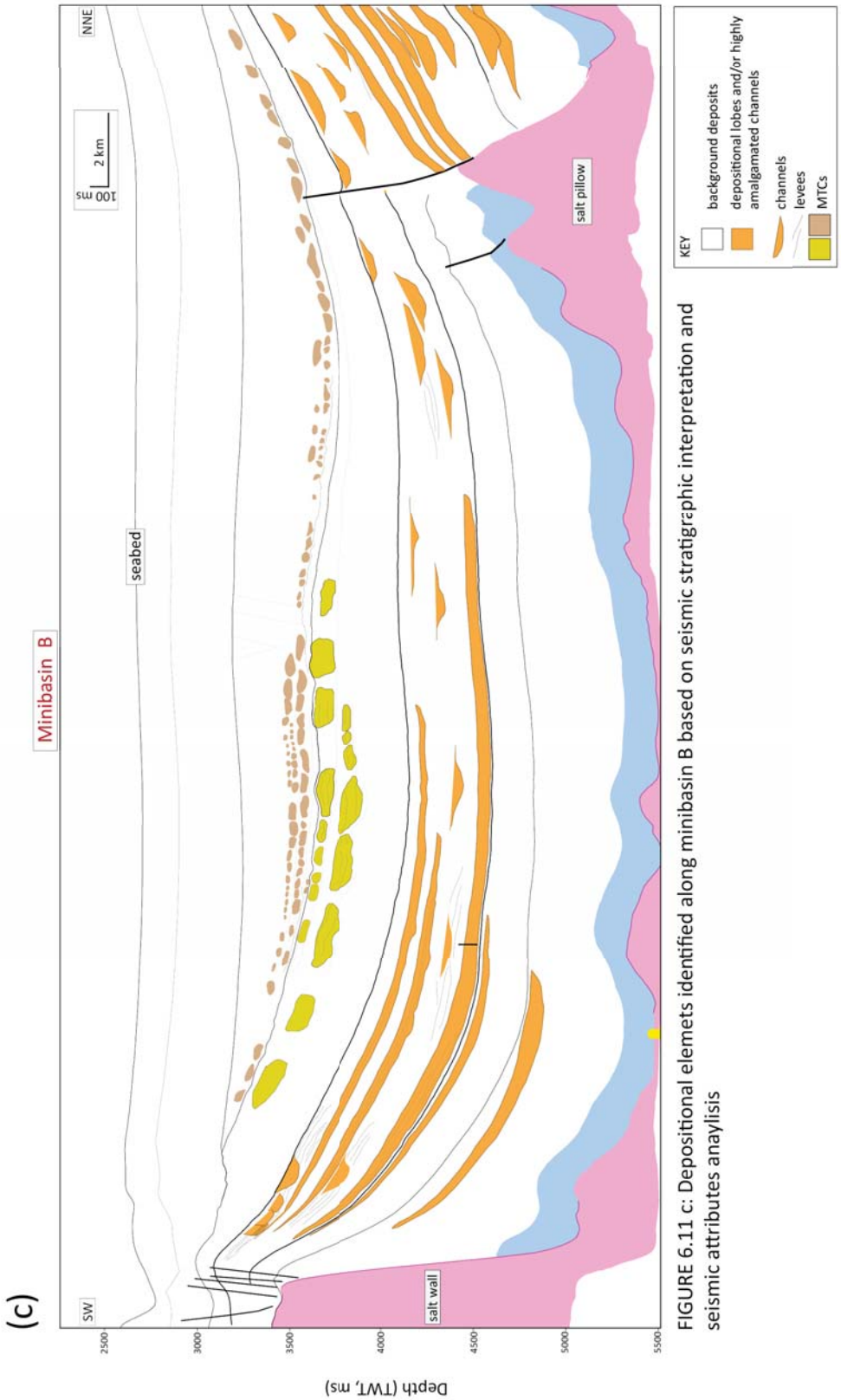


FIGURE 6.11 c: Depositional elemets identified along minibasin B based on seismic stratigrɾphic interpretation and seismic attributes anaylisis

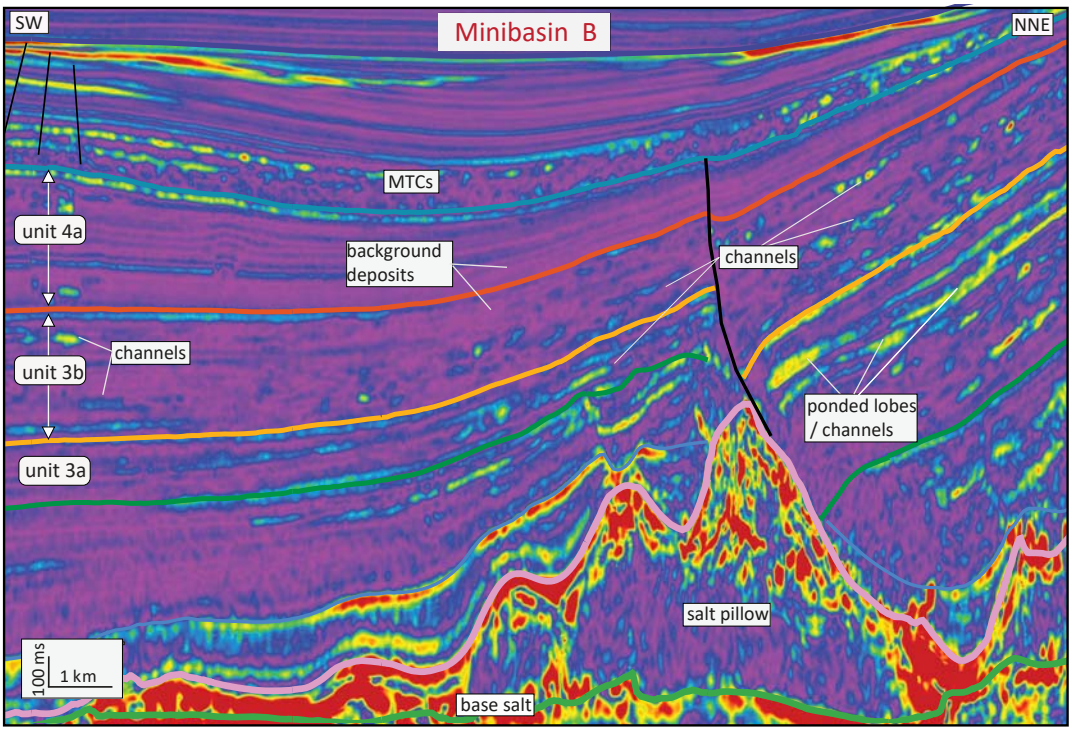


FIGURE 6.11d: Sweetness attribute highlighting the depositional elements within the proximal part of Minibasin B. See location on Fig. 6.11b

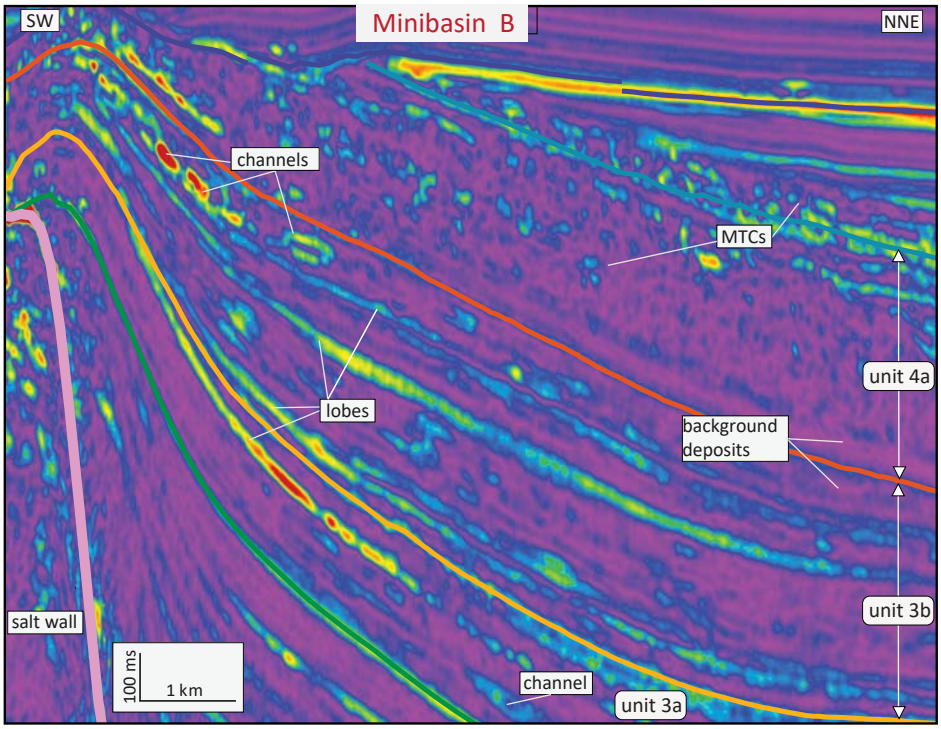


FIGURE 6.11e: Sweetness attribute highlighting the depositional elements within the distal part of minibasin B. See location on Fig. 6.11b

In distal regions, N-trending, slightly sinuous channels occur within and trend parallel to the long axes of several broadly N-trending minibasins (channels 1, 2 and 3 in minibasins I-K; Figs. 6.15 and 6.18). Channels that trend at a relatively high angle (>30°) to bounding salt walls and salt-cored anticlines change course within the minibasins, becoming parallel to the minibasin axis and bounding salt walls (channels 4 and 5 in minibasins L-M; Figs. 6.15 and 6.20). Locally, channel bends also occur next to salt-cored folds, in some cases leading to the deposition of LAPs (channel 2; Figs. 6.16c, 6.18b). Within distal minibasins, lobes are confined to minibasin flanks and within fold-bounded synclines, downlapping onto the lows and onlapping and converging towards salt-cored highs (Figs. 6.18, 6.19 a,b).

Channel continuity between adjacent minibasins across bounding salt walls is observed downslope in distal minibasins (e.g. channel 5 between minibasins L and M; Figs. 6.15 and 6.20). However, changes in channel geometry are evident between, for example, minibasin L to M. In minibasin L I identify an erosionally based, up to 1 km wide, 50 m thick, WNW-trending channel, flanked by levees and overlying an intra-minibasin MTC (channel 5 in Figs. 6.20, 6.21 a). Within minibasin M, this channel increases in reflectively, width (to 5 km) and thickness (to 200 m), in addition to bending to trend NE, sub-parallel to the minibasin axis (Figs. 6.20, 6.22). The asymmetric levees flanking channel 5 onlap onto and are seemingly rotated on the limbs of, the western salt-cored anticline (Fig. 6.22).

During deposition of Unit 3, the locus of subsidence in minibasin A shifted towards the centre and eastern margin of the depocenter due to welding (Fig. 6.10 b, c). In addition, the cessation of activity on landward-dipping listric faults at the southern end of minibasin A meant that channels were able to spill southwards and flow axially beyond the junction within minibasin B. Continued deposition drove welding of minibasin C and shifting of the main depocenter within minibasin C from C2 to C3, leading to eventual inversion of the minibasin stratigraphy and the formation of a turtle anticline (Fig. 6.10 c). Eventual filling of minibasin C resulted in sediment spilling downslope to the SE into minibasin D and E (Figs. 6.12 f, g, 6.13, 6.14).

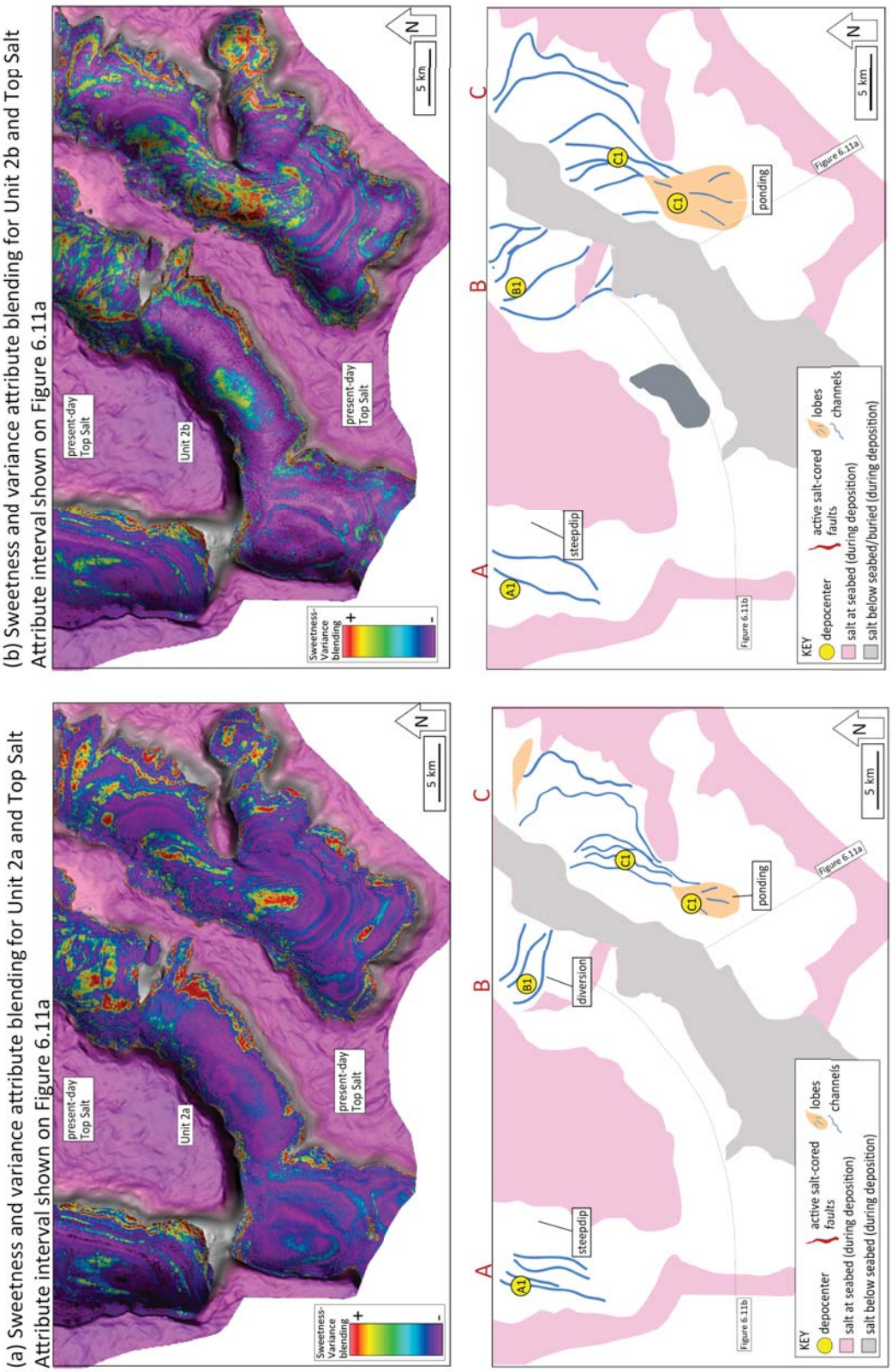

(a) Sweetness and variance attribute blending for Unit 2a and Top Salt
Attribute interval shown on Figure 6.11a
present-day Top Salt
Unit 2a
present-day Top Salt
Sweetness-Variance blending
+
-
N
5 km
(b) Sweetness and variance attribute blending for Unit 2b and Top Salt
Attribute interval shown on Figure 6.11a
present-day Top Salt
Unit 2b
present-day Top Salt
Sweetness-Variance blending
+
-
N
5 km
A
B
C
A1
steepdip
B1
diversion
C1
ponding
Figure 6.11a
Figure 6.11b
KEY
depocenter
active salt-cored faults
lobes
channels
salt at seabed (during deposition)
salt below seabed/buried (during deposition)
A
B
C
A1
steepdip
B1
C1
ponding
Figure 6.11a
Figure 6.11b
N
5 km

Figure 6.12

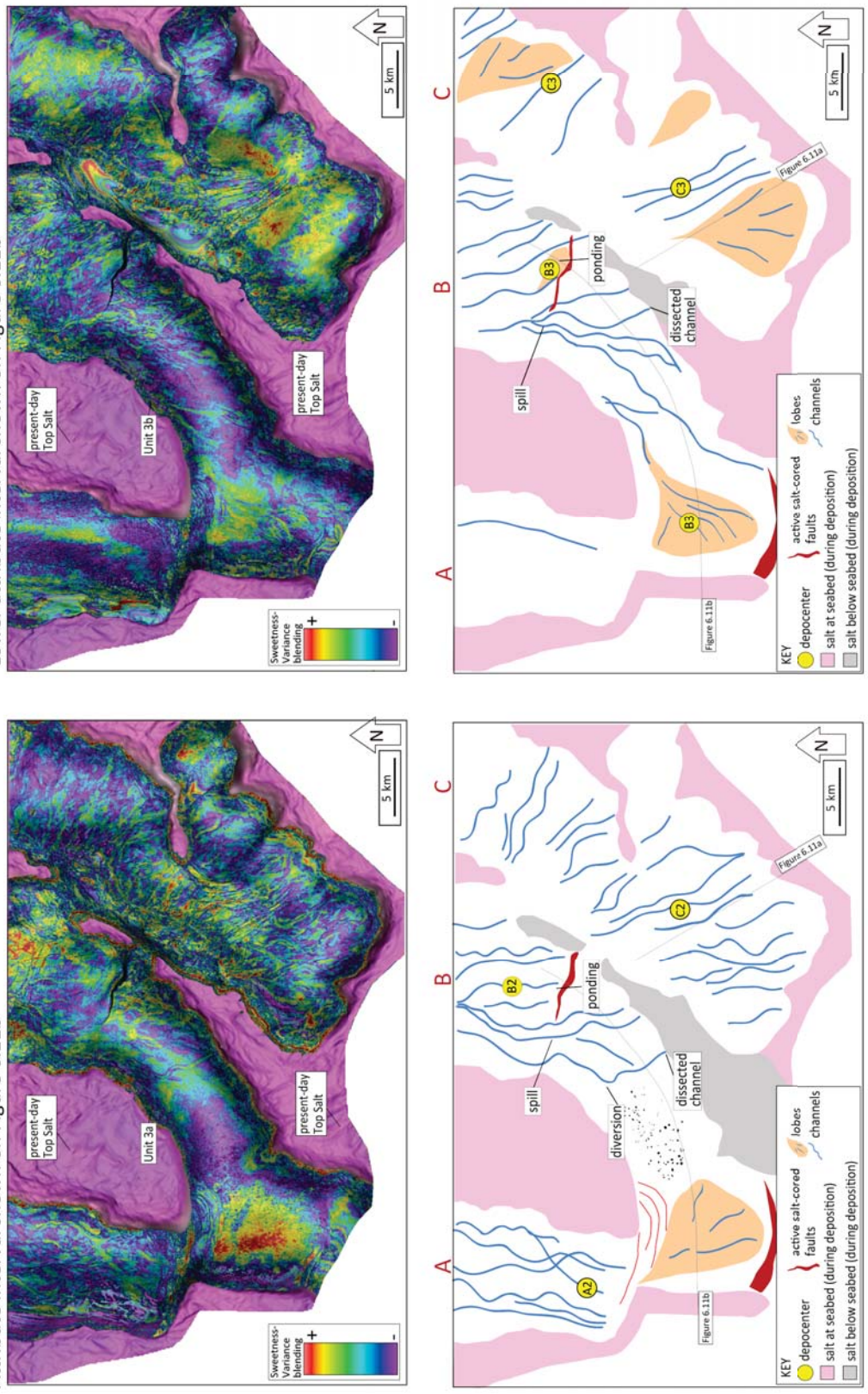

(c) Sweetness and variance attribute blending for Unit 3a and Top Salt
Attribute interval shown on Figure 6.11b
(d) Sweetness and variance attribute blending for Unit 3b and Top Salt
Lower attribute interval shown on Figure 6.11b
present-day Top Salt
Unit 3a
Unit 3b
Sweetness-Variance blending
5 km
N
A
B
C
A2
B2
C2
B3
C3
spill
ponding
diversion
dissected channel
Figure 6.11a
Figure 6.11b
KEY
depocenter
active salt-cored faults
lobes
channels
salt at seabed (during deposition)
salt below seabed (during deposition)

Figure 6.12

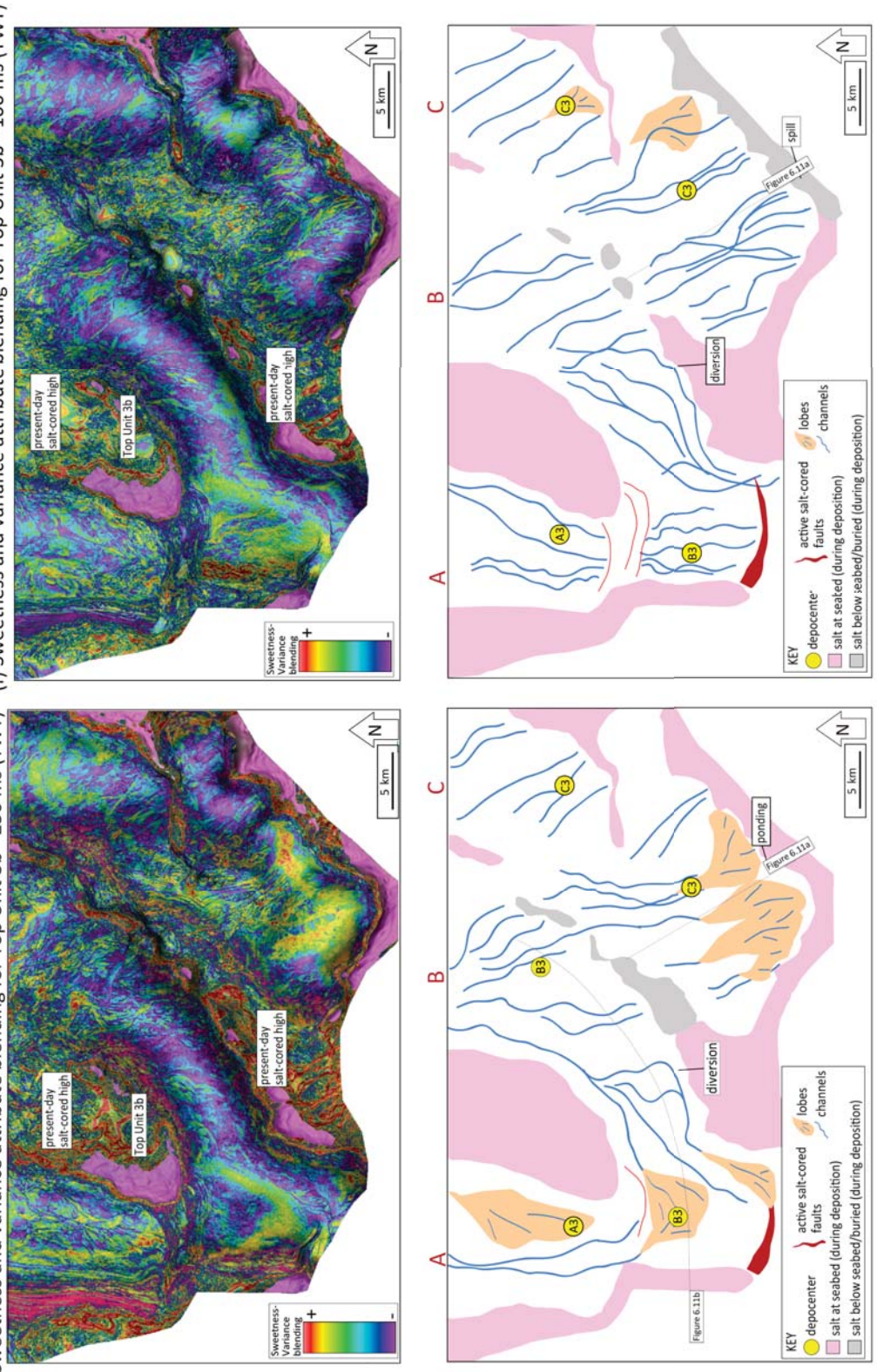
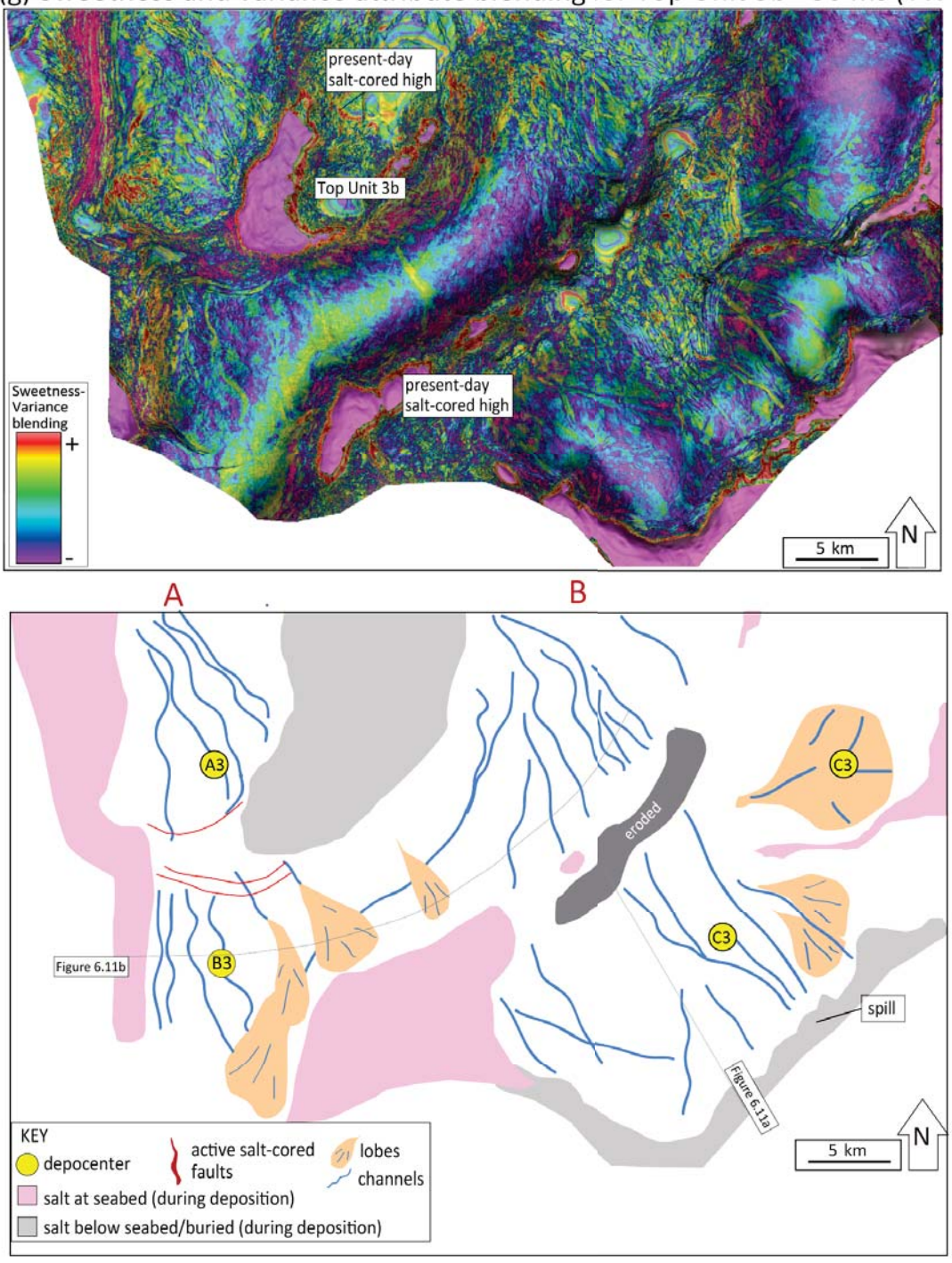

(e) Sweetness and variance attribute blending for Top Unit 3b - 250 ms (TWT)
(f) Sweetness and variance attribute blending for Top Unit 3b - 100 ms (TWT)
present-day salt-cored high
Top Unit 3b
Sweetness-Variance blending
5 km
N
A
B
C
A3
B3
C3
diversion
ponding
spill
Figure 6.11a
Figure 6.11b
KEY
depocenter
active salt-cored faults
lobes
channels
salt at seabed (during deposition)
salt below seabed/buried (during deposition)

Figure 6.12

Figure 6.12

(g) Sweetness and variance attribute blending for Top Unit 3b - 50 ms (TWT)



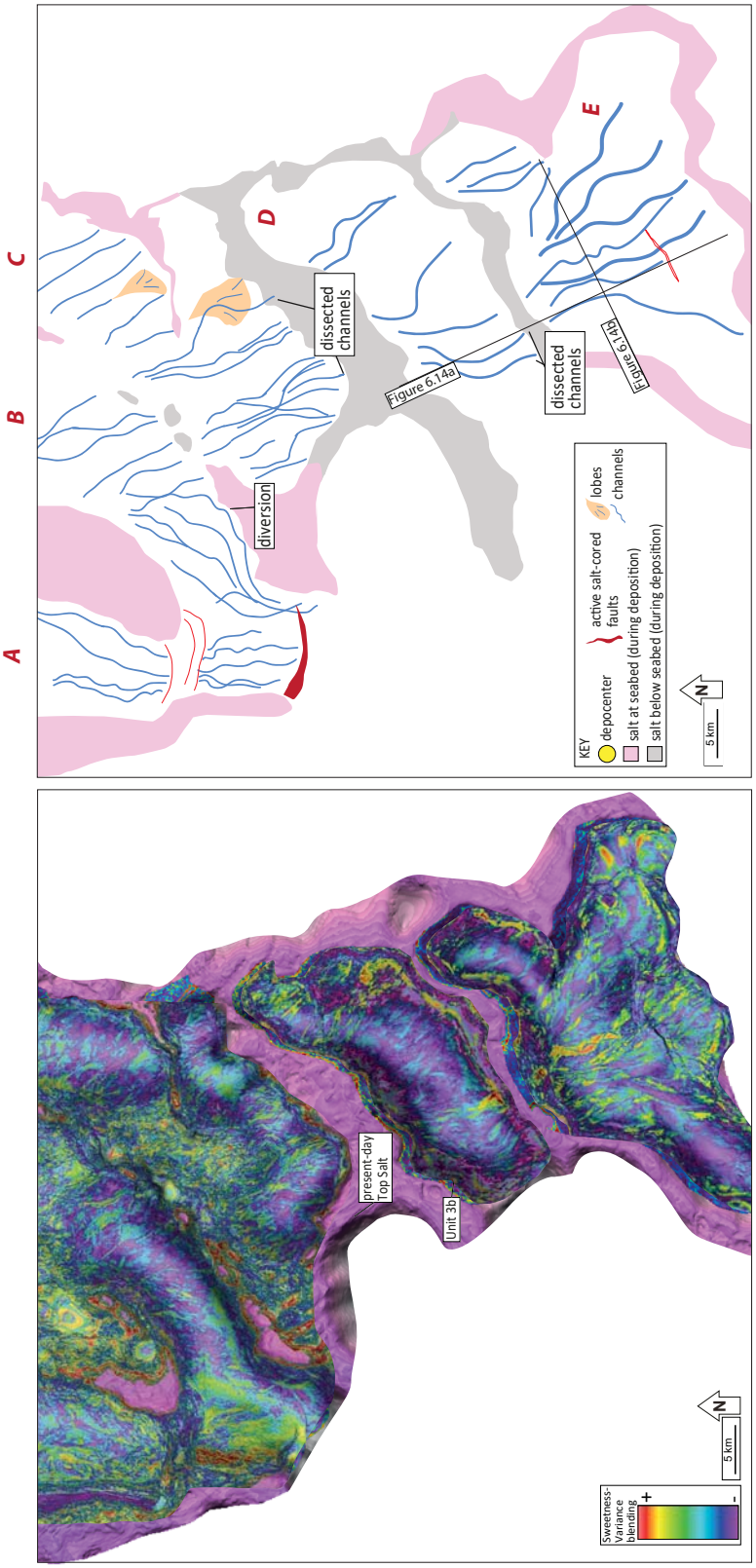


FIGURE 6.13. Unit 3b: Sweetness and variance attribute blending illustrating dissected channels by present-day salt walls

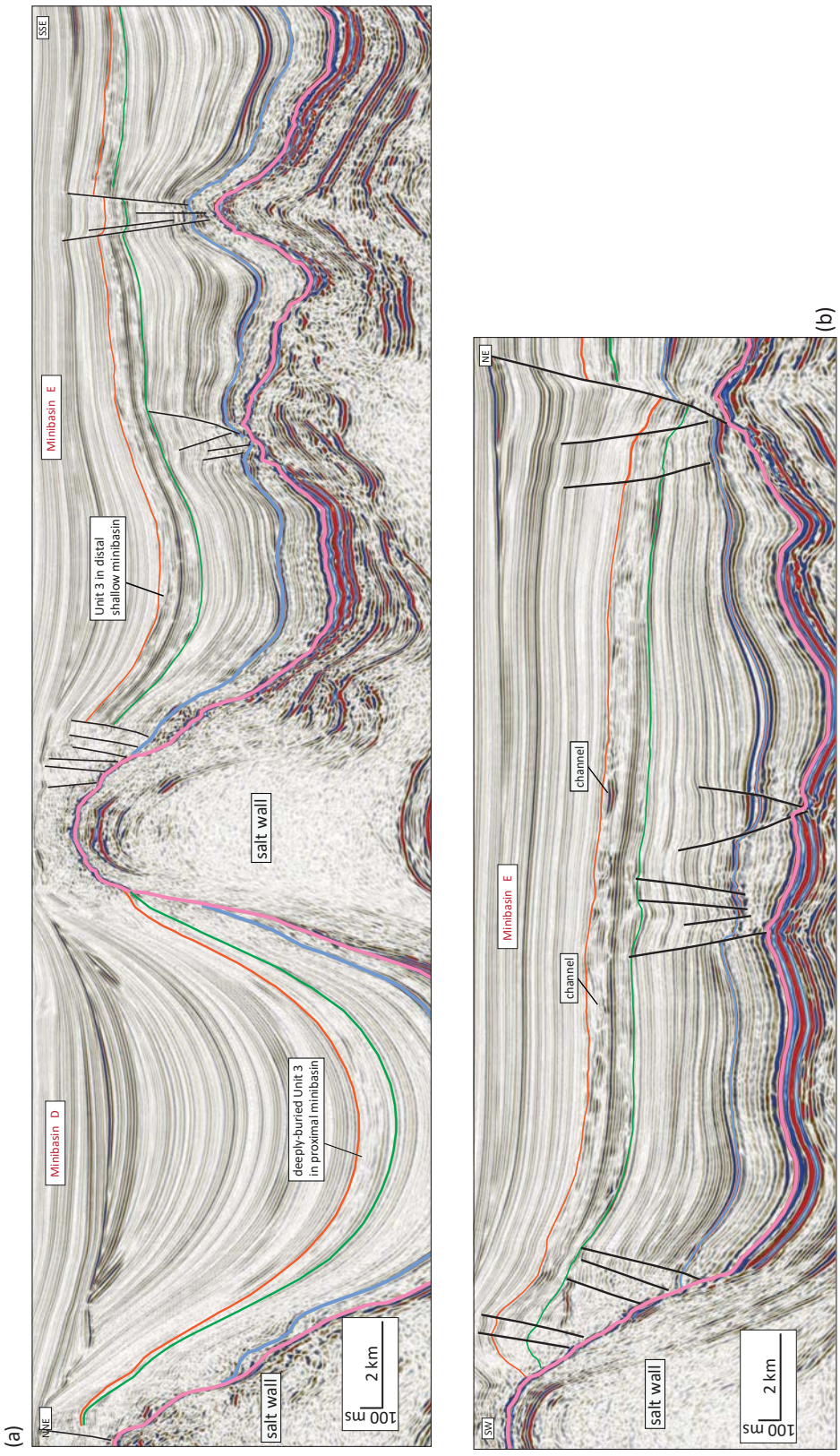


FIGURE 6.14. (a) Seismic sections across deep minibasins D and shallow minibasin E. (b) Seismic section across minibasin E. See locations on Figure 6.13

Based on similar trends and morphology, I suggest channels presently contained in minibasins D and E, and now separated by a large diapir, were previously part of a through-going, continuous system that extended across the diapir (Figs. 6.9b, 6.10a). Likewise, I suggest that at least the northern part of the salt wall currently dividing minibasins B and C did not represent a barrier to channels flowing between these depocenters, but that subsequent growth of the diapir initially underlying the channels, subsequently dissected these depositional systems (Fig.6. 12c). Furthermore, I interpret that channels flowing across the ISPFB and the distal minibasins probably spilled over from proximal minibasins west of minibasin A, which are not imaged in the seismic dataset. Towards the distal minibasins, structurally-induced changes in channel sinuosity occurred due to coeval salt-cored highs on the paleoseabed. LAPs are only developed when channels are unconfined or only weekly confined, recording lateral channel migration to towards the minibasin centres. In addition, levees and lobes are deposited confined within minibasins or in the intra-minibasin fold- and thrust-bounded synclines associated with shortening of salt and its overburden (Fig. 6.15).

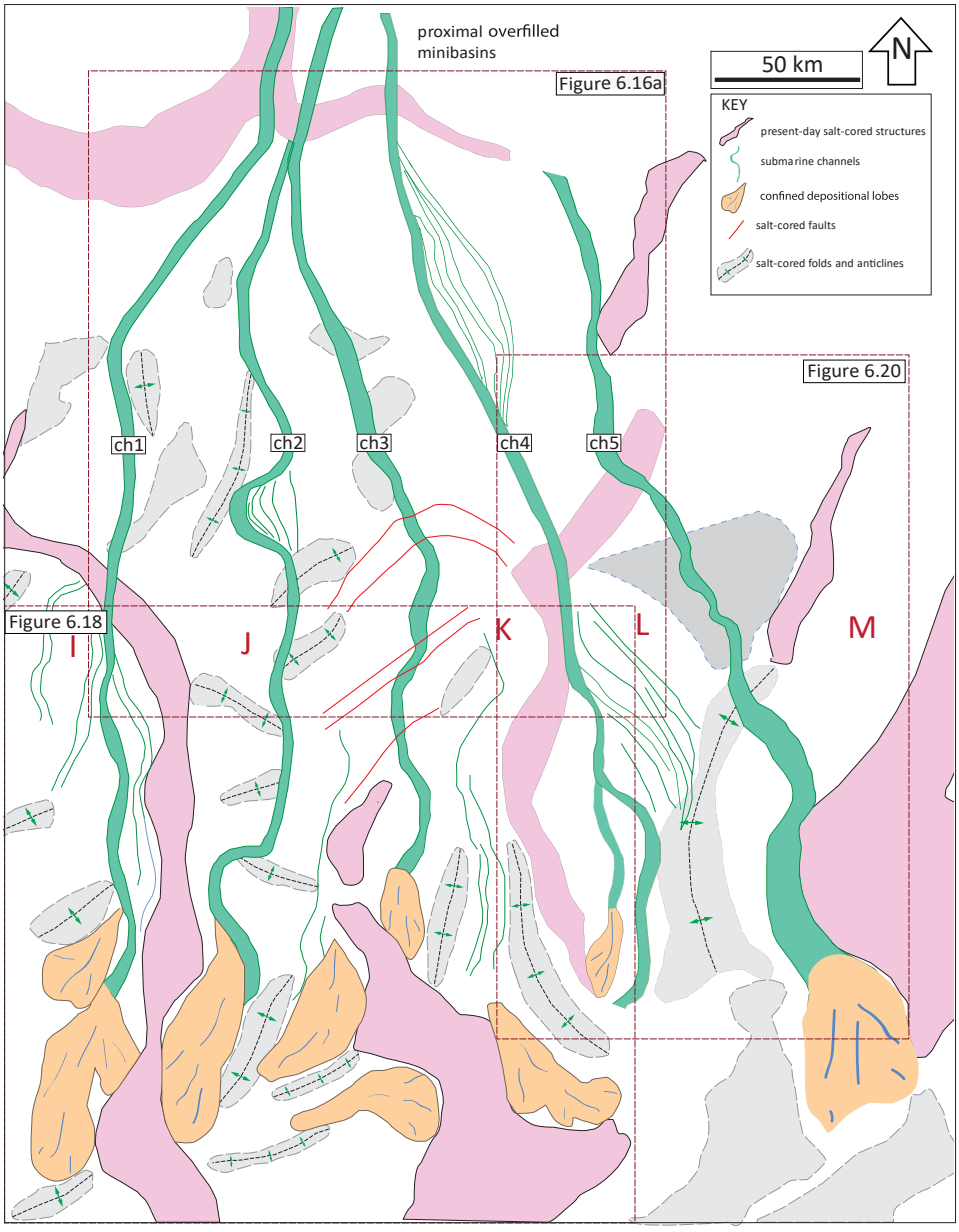


FIGURE 6.15: Unit 3 deep-water depositional systems across part of the Inner Sao Paulo Fold Belt and the distal minibasins on the Sao Paulo Plateau. Based on seismic attribute analysis and thickness maps. Detailed isochrons, attribute maps and seismic sections are shown on Figures 6.16-6.22

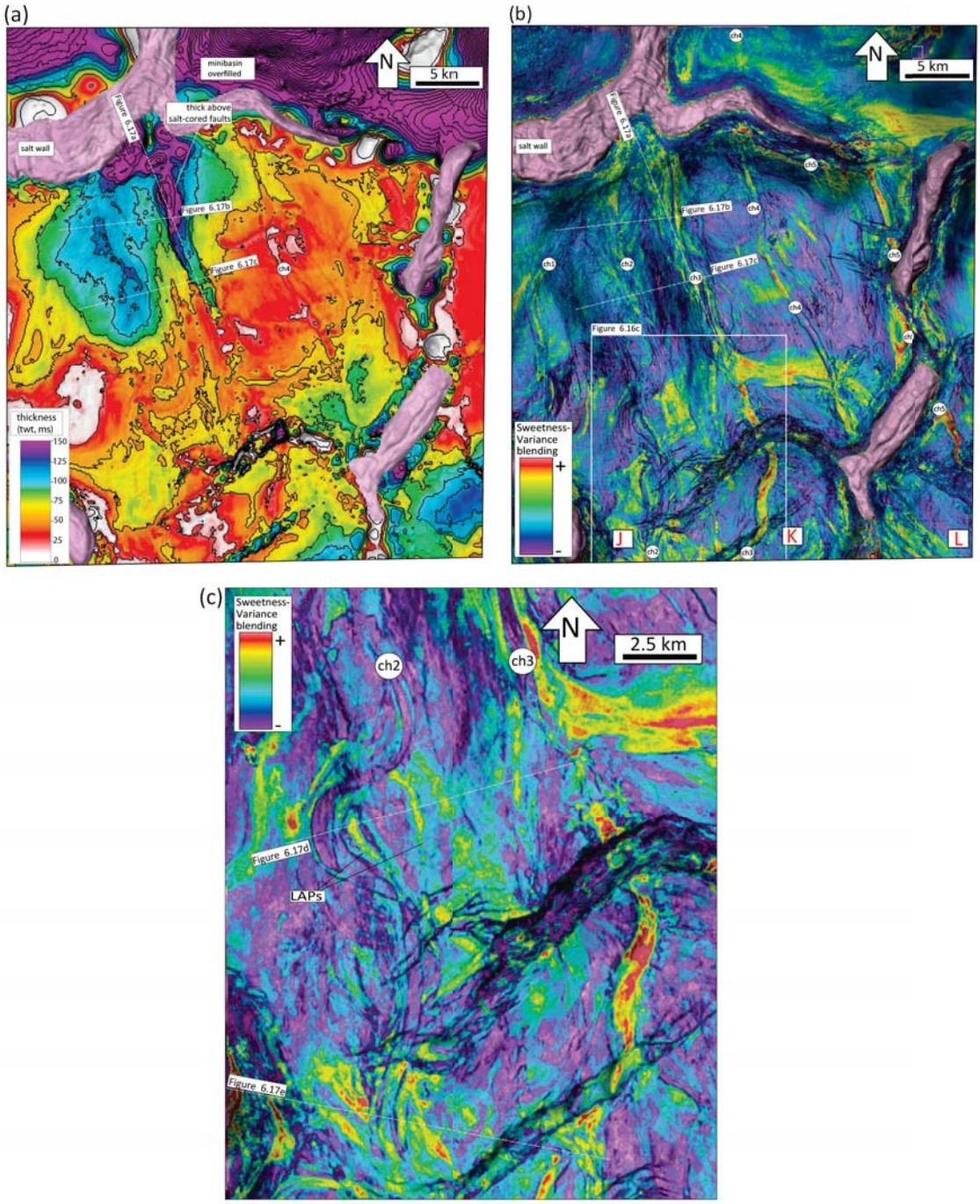


FIGURE 6.16: (a) Unit 3- Detailed isochron map highlighting increase in thickness above synclines and salt-cored faults. See location on Figure 6.15. (b) sweetness and variance visual blending illustrating the spill of channels from proximal overfilled minibasins towards distal minibasins. (c) channel deflection and development of lateral accretion packages. See location on 6.16 b and 6.15

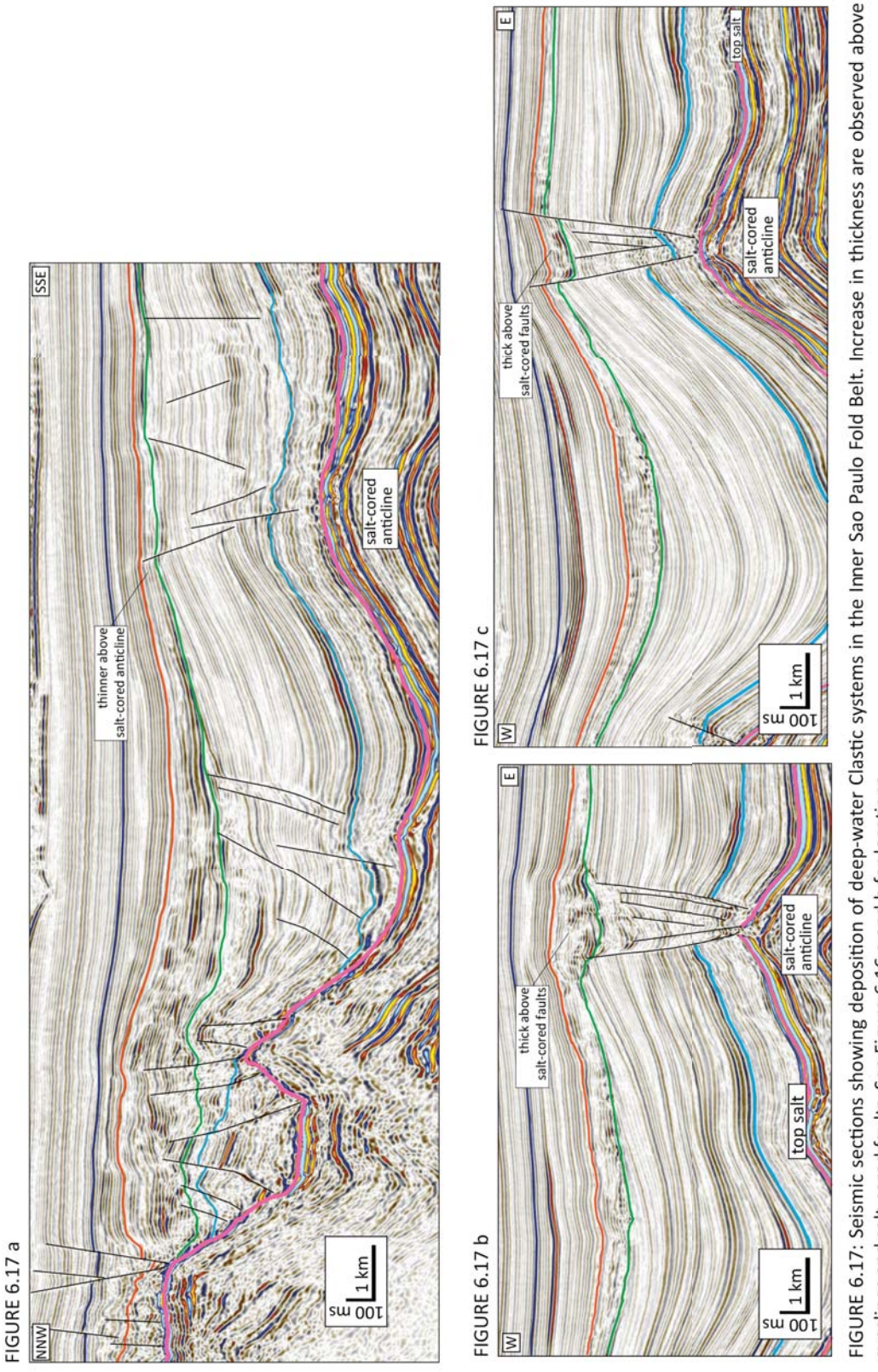


FIGURE 6.17: Seismic sections showing deposition of deep-water Clastic systems in the Inner Sao Paulo Fold Belt. Increase in thickness are observed above synclines and salt-cored faults. See Figure 6.16 a and b for locations.

FIGURE 6.17 d

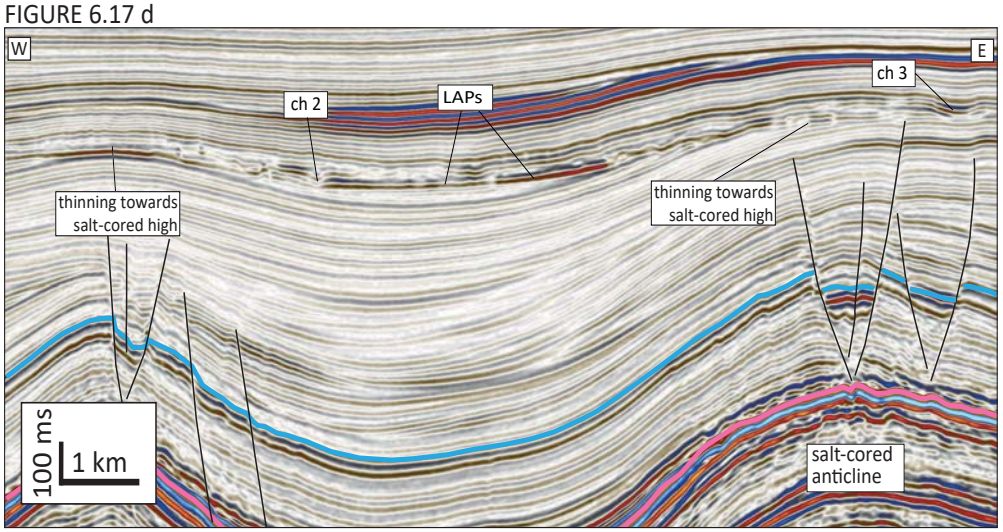


FIGURE 6.17 e

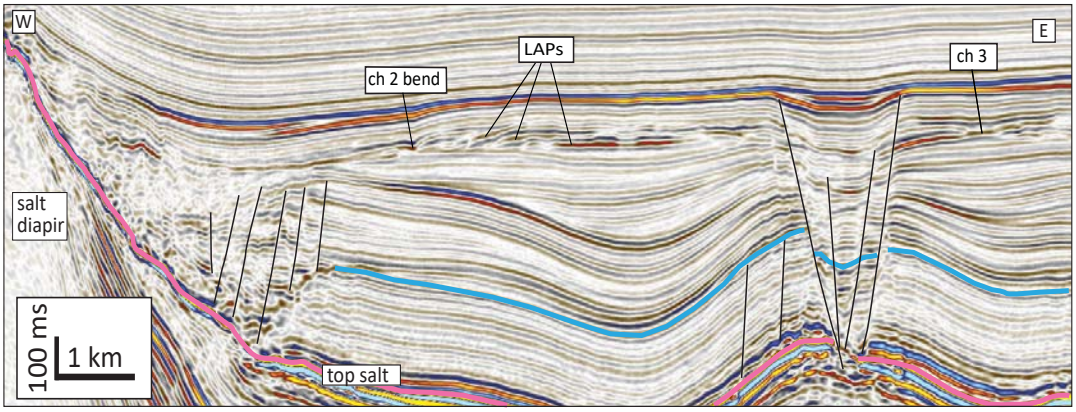


FIGURE 6.17: Seismic sections illustrating high-amplitude lateral accretion packages. See Figure 6.16 c for locations.

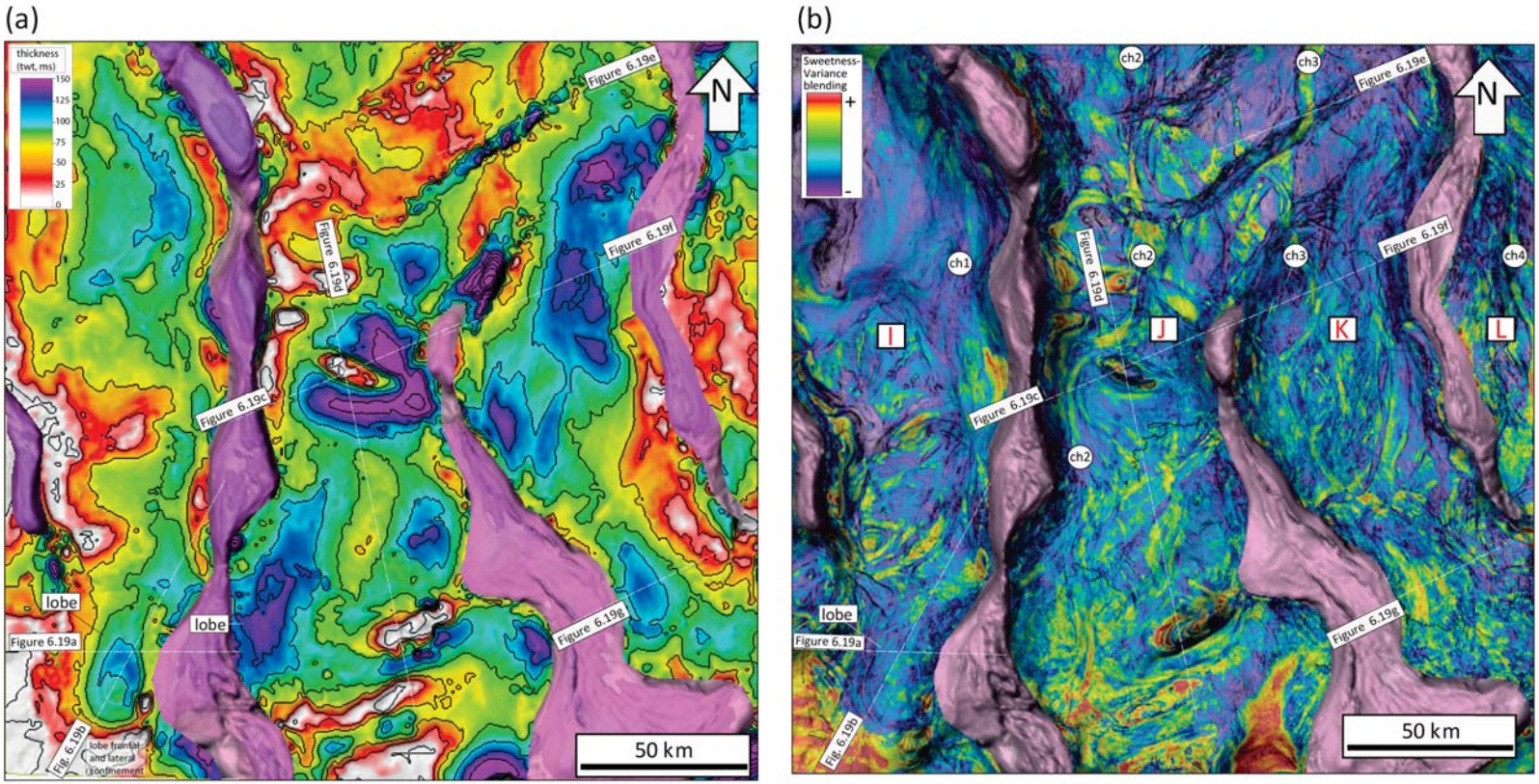


FIGURE 6.18. (a) Detailed isochron map for Unit 3 in minibasins I, J and K. Increase in thickness occurs around salt-cored folds and associated to lobes deposition where frontally confined. (b) Sweetness and variance blending illustrating deep-water clastic deposition within minibasins I, J and K. See interpretation and location in Figure 6.15. Channel deflection next to a salt cored fold can be observed within Minibasin K. See also Figure 6.19 c.

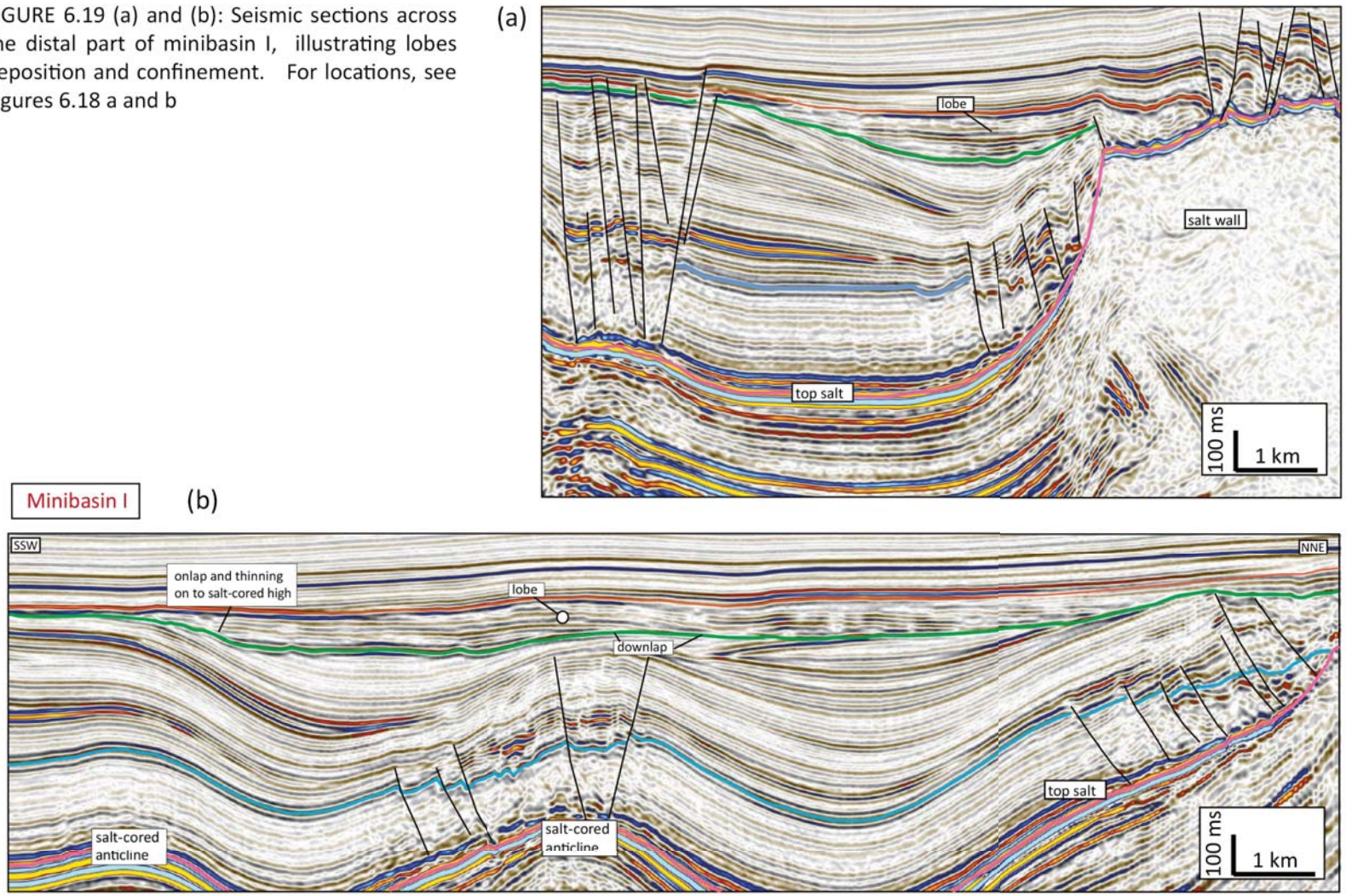


FIGURE 6.19 (a) and (b): Seismic sections across the distal part of minibasin I, illustrating lobes deposition and confinement. For locations, see Figures 6.18 a and b

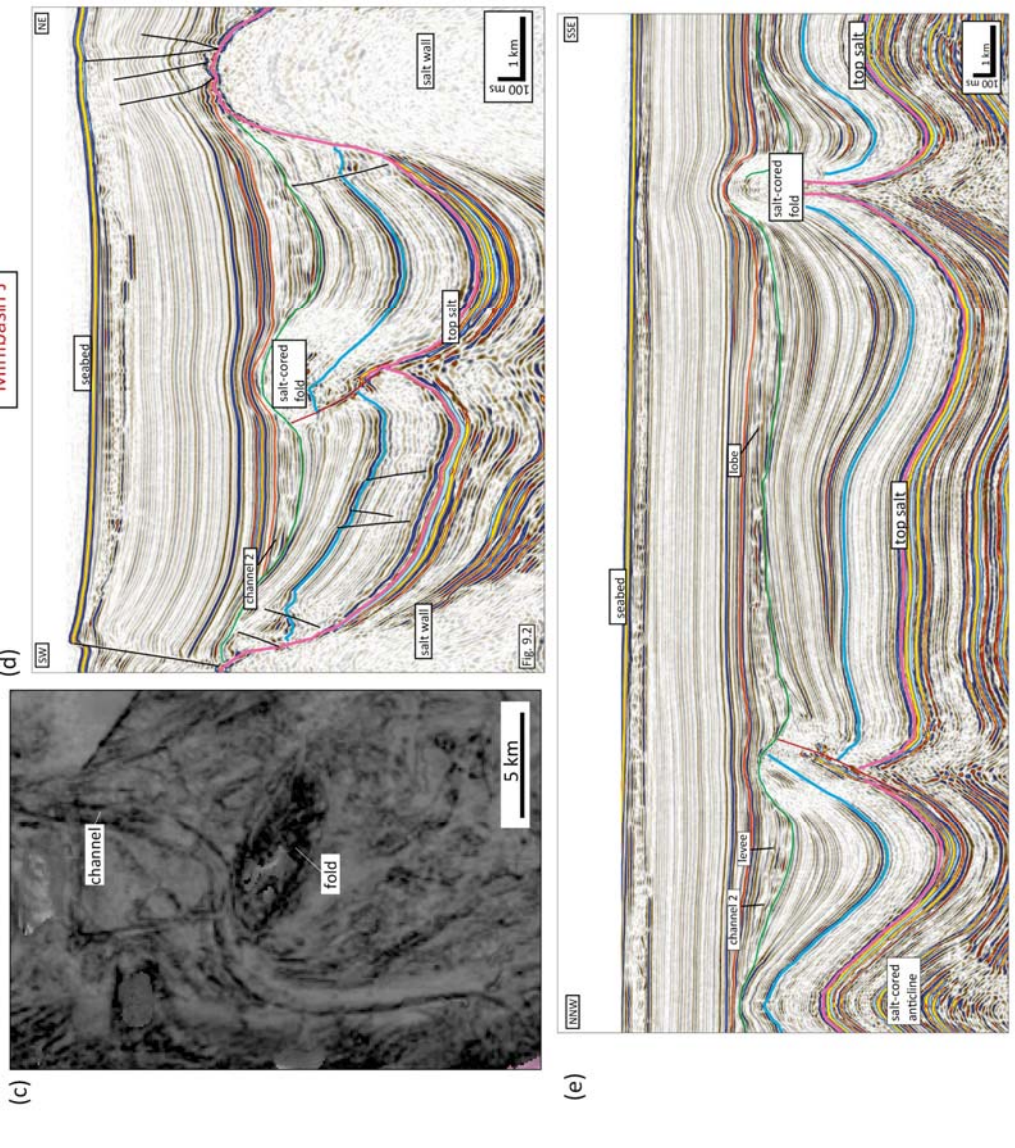


FIGURE 6.19 : (c) Amplitude contrast showing channel deflection around salt-cored fold. (d) and (e) Seismic sections across minibasin J. For locations, see Figures 6.18 a and b

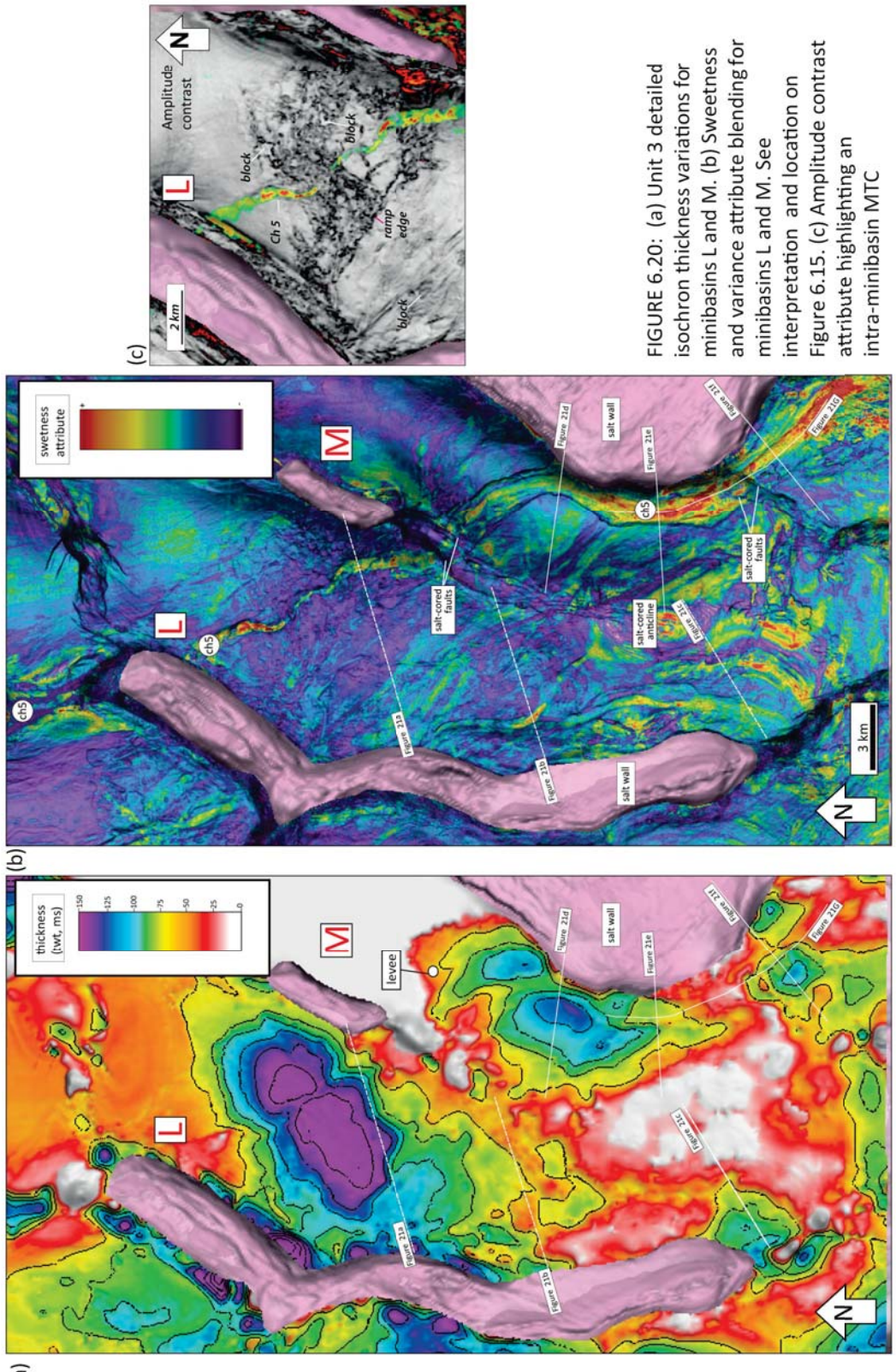


FIGURE 6.20: (a) Unit 3 detailed isochron thickness variations for minibasins L and M. (b) Sweetness and variance attribute blending for minibasins L and M. See interpretation and location on Figure 6.15. (c) Amplitude contrast attribute highlighting an intra-minibasin MTC

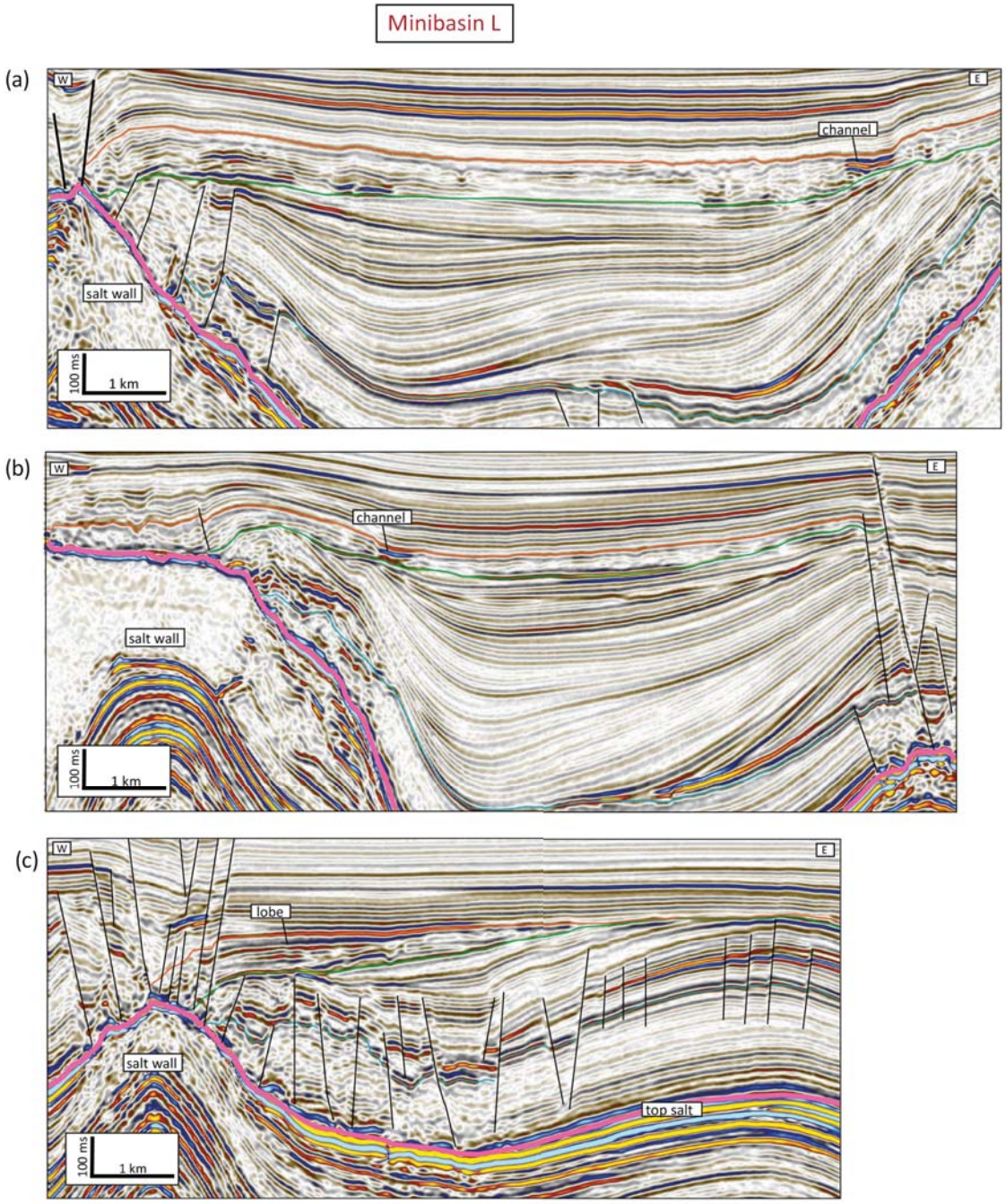
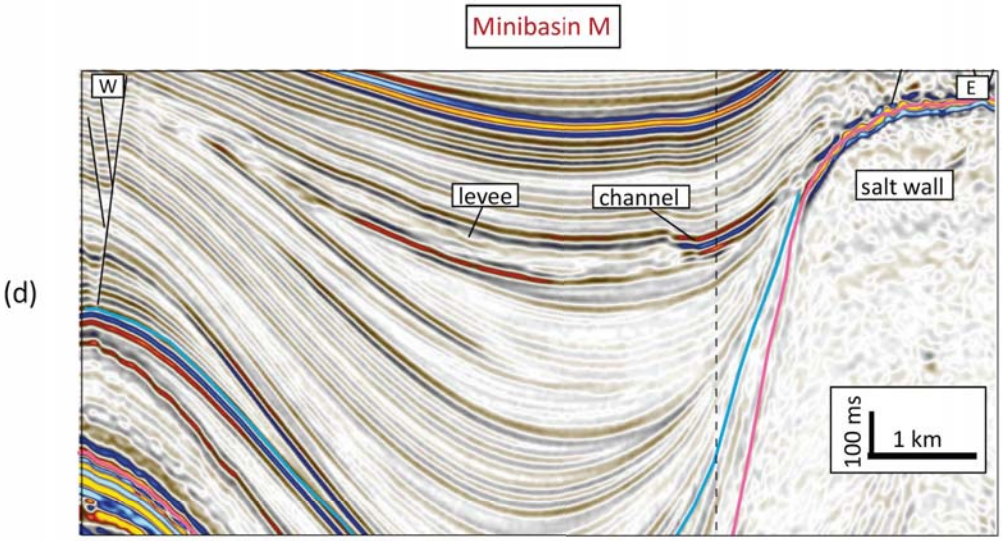
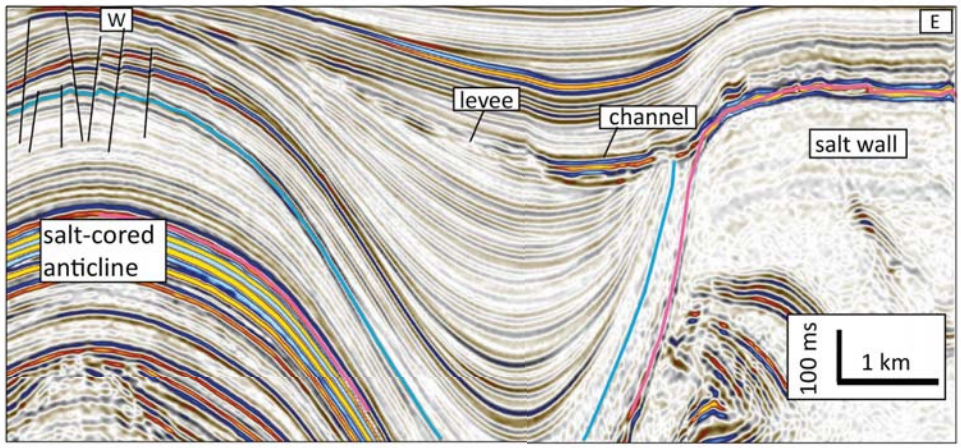


FIGURE 6.21 (a), (b) and (c): Seismic sections accross minibasin L. See locations on Figure 6.20.

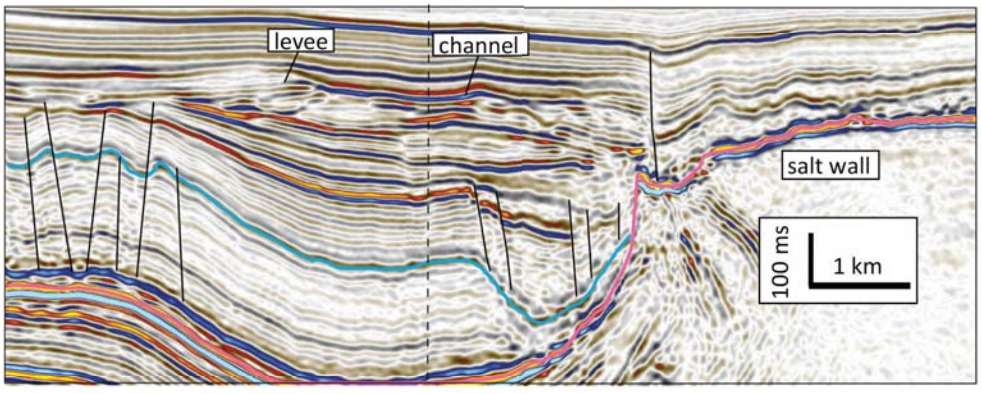


(d)

Figure 21



(e)



(f)

FIGURE 6.21 (d), (e) and (f): Seismic sections accross minibasin M. See locations on Figure 6.20.

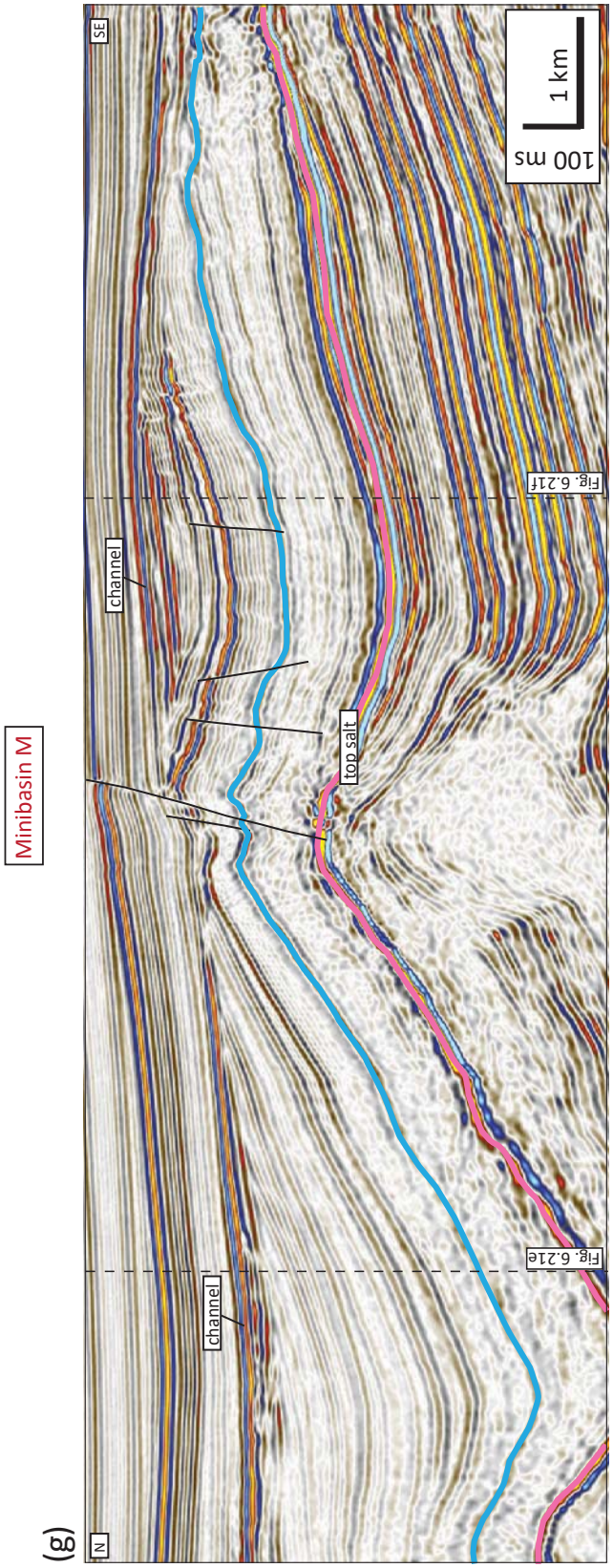


FIGURE 6.21 (g): Seismic sections along Channel 5 in minibasin M. See locations on Figure 6.20.

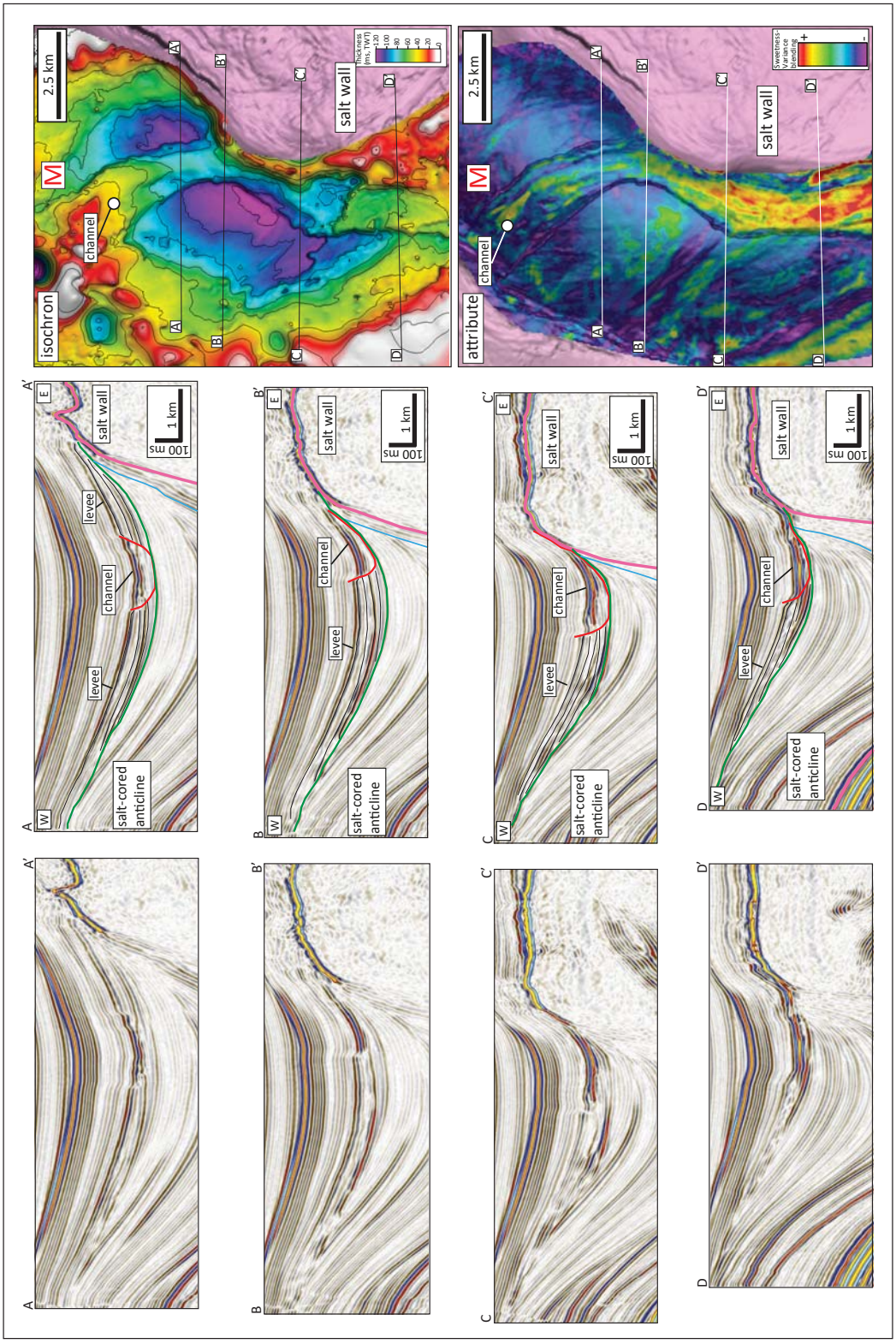


FIGURE 6. 22: Channel and Levee geometry, thickness and amplitudes variations in minibasin M. Rotation of intra-levee seismic reflections towards the channel axis indicate salt growth during deposition.

6.7.4 Unit 4: Palaeocene to Mid-Oligocene

Deposition within Unit 4 extends further east than in unit 3 (Fig. 6.9d). Thickness changes in Unit 4 indicate proximal thick minibasins were still activity subsiding, although deposition was now also occurring above bounding salt walls (e.g., minibasin D; Fig. 6.9d).

Rather than containing relatively abundant channel-levee systems and lobes like units 2 and 3, Unit 4, more specifically sub-intervals 4a and 4c within the proximal thick minibasins, are dominated by MTCs (Figs. 6.11, 6.23). The proximal parts of MTCs in unit 4a contain relatively angular megaclasts that are up to 5 km long and 1 km wide overlying sub-continuous to chaotic seismic facies and thrusts (Figs. 6.11b, 6.23). In contrast, MTC blocks within unit 4c are less angular and smaller (1 km long by 500 m wide; Figs. 6,11b, 6.23). In the Inner Fold Belt and within the distal elongated minibasins, at least 200 km long, N- and NW-trending linear, sub-parallel grooves are developed along a single seismic event at the base of unit 4 (Fig. 6.24). These grooves are overlain by blocks that are smaller (200 m long by 100 m wide) than those observed in the proximal thick minibasins (Fig. 6.24).

During deposition of Unit 4, some of the proximal and distal minibasins continue to actively subside into salt (Fig. 6.9d). However, unit 4 marks a significant change in the style of clastic sediment deposition within the basin. More specifically, I see a cessation of coarse-grained clastic deposition within channels and lobes, and the initiation of widespread MTC emplacement (Figs. 6.9d, 6.11, 6.23). It is not possible to constrain the source of MTCs contained within the proximal thick minibasins, and it is thus unknown if they were derived from collapse of the distal shelf-edge or slope, or if they were locally sourced from the uplifted and rotated minibasin margins flanking the bounding diapirs. However, thrusts within unit 4a within the proximal minibasins may indicate MTCs were sourced from the NNE (Figs. 6.11b, 6.23). In contrast, the regionally extensive grooves capping the distal minibasins and ISPFB suggest MTC emplacement from the NW (Fig. 6.24).

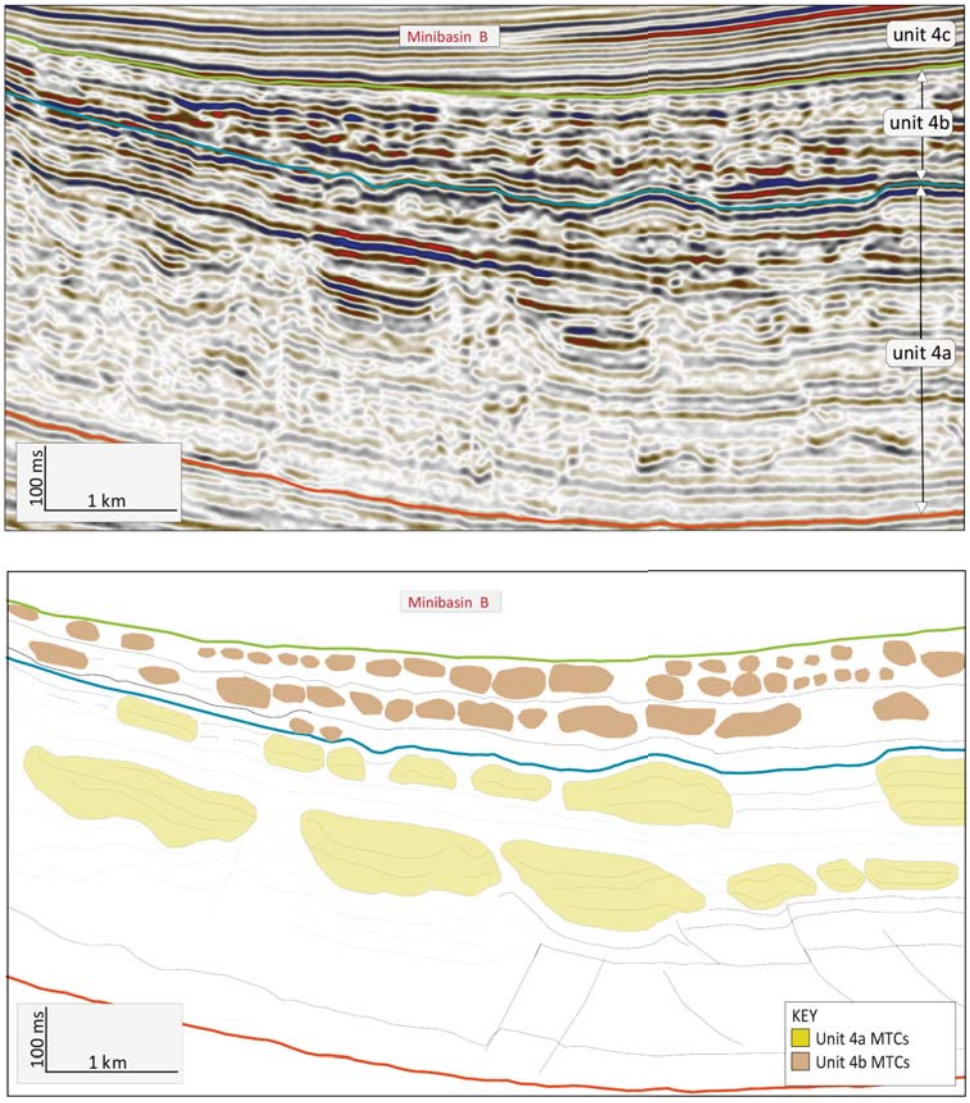


FIGURE 6.23: (a) Unit 4 seismic expression of mass transport complexes within minibasin B. See Figure 6.11 b and c for location. (b) Sweetness and variance attribute blending for Unit 4a. (c) Sweetness and variance attribute blending for Unit 4b.

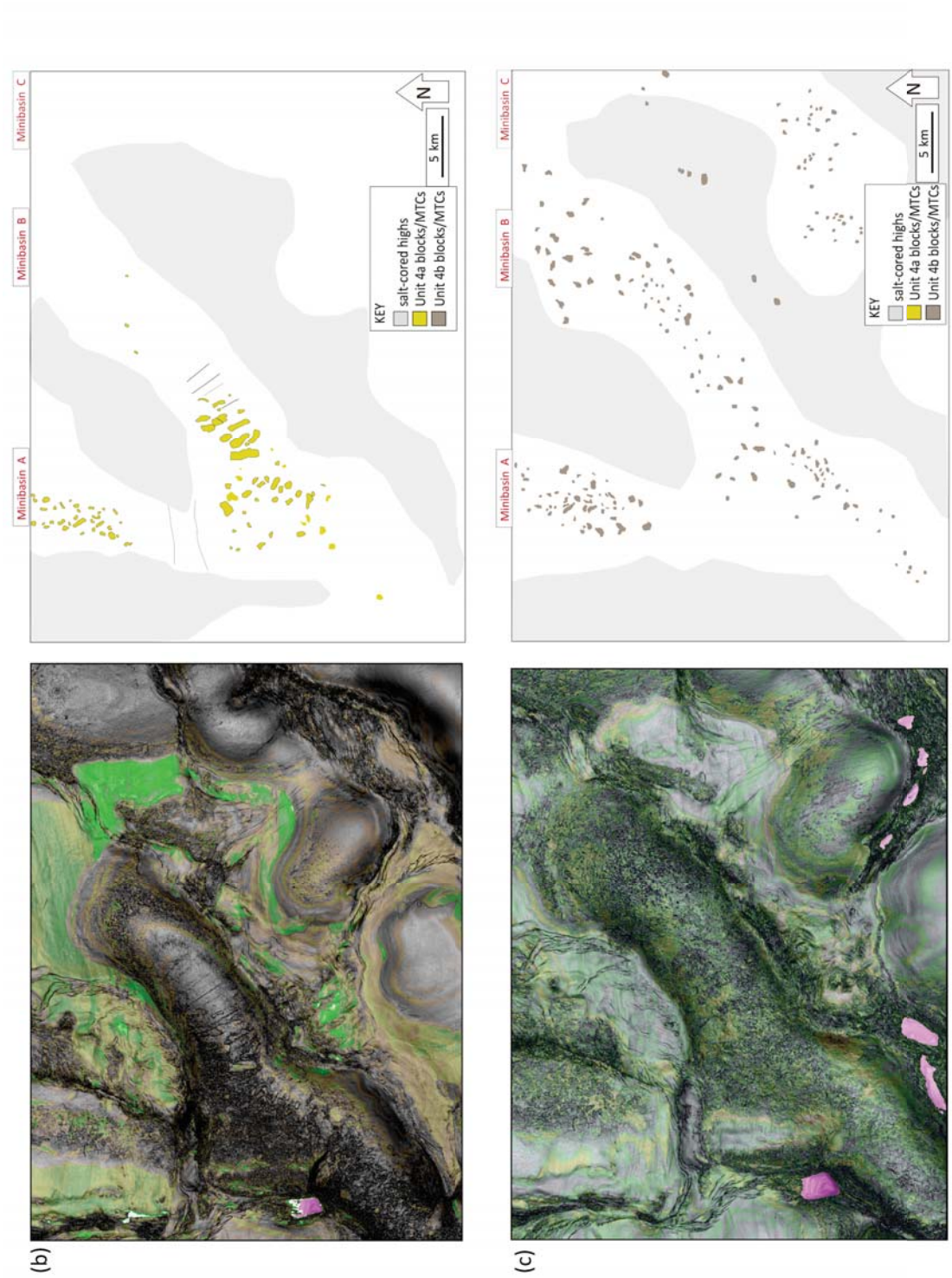

Minibasin A
Minibasin B
Minibasin C
KEY
salt-cored highs
Unit 4a blocks/MTCs
Unit 4b blocks/MTCs
5 km
N
(b)
(c)

FIGURE 6.23

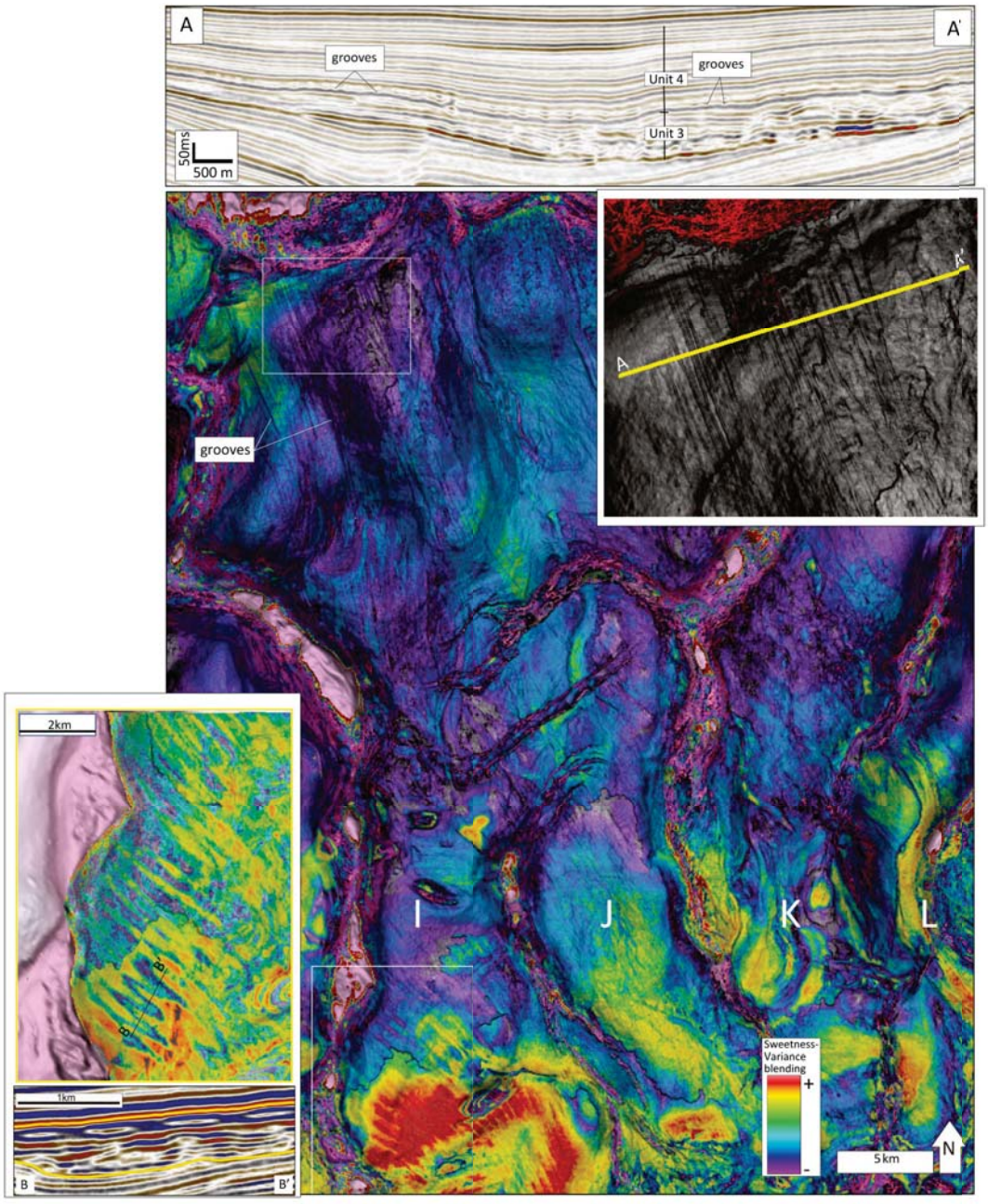


FIGURE 6.24: Seismic expression of regional-scale linear MTCs marking the end of deep-water deposition across the Inner Sao Paulo Fold Belt and the Sao Paulo plateau

6.8.1 Unit 5: Mid-Oligocene to Pleistocene

Unit 5 is more extensive than underlying units, with the main minibasin depocentres still occurring in the NW of the study area (e.g., minibasin D; Fig. 6.9e). I identify at least three MTC-bearing sub-intervals within Unit 5, all of which are contained within a single minibasin in the NW of the study area (Figs. 6.9e; 6.25). In contrast to the regionally developed, Palaeocene MTC identified within Unit 3, these younger MTCs are confined by salt-cored diapirs. The two lowermost MTCs are dominated by highly chaotic seismic facies and lack megaclasts, whereas the shallower MTC contains abundant megaclasts contained within a chaotic matrix (Fig. 6.25; see also Jackson et al., 2011).

Because these MTCs extend to the NW outside of the seismic dataset, their source is unknown. However, regional considerations suggest they were sourced from large shelf-edge and slope failures north or north-west of the study area (Contreras et al., 2010; Jackson, 2011). Therefore, Unit 5 records Neogene emplacement of several MTCs in response to repeated collapse of the north-western basin margin shelf-edge and/or slope.

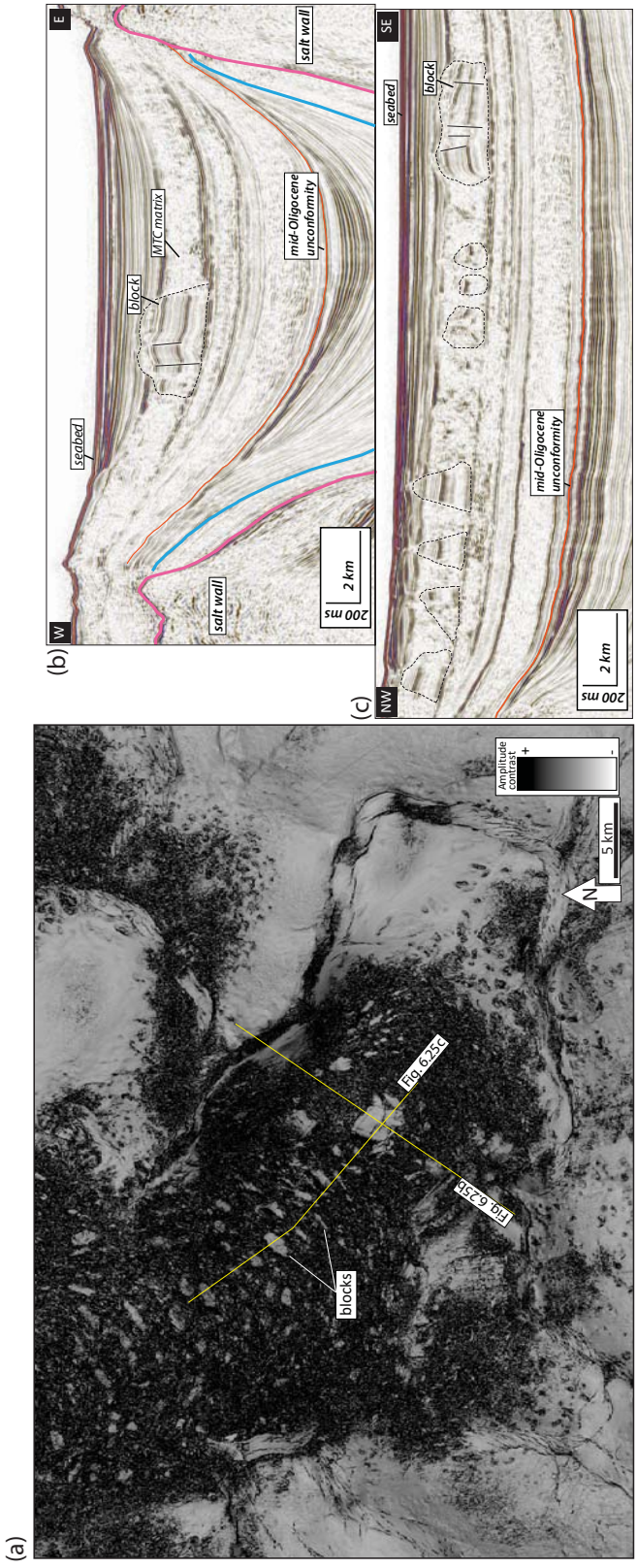


FIGURE 6.25: Seismic expression of MTCs within Unit 5. (a) Amplitude contrast attribute of intra-Unit 5 horizon highlighting blocks and chaotic matrix. (b) seismic secion across the minibasin; (c) seismic secion along the minibasin

6.8 Discussion

I used 3D seismic reflection and borehole data to illustrate the spatial and temporal variations in the size and type of deep-water depositional elements within the post-salt succession of the salt-influenced deep-water slope of the Santos Basin, offshore Brazil. I here discuss regional controls on minibasin development, and key local controls on paleo-seafloor relief and its effect on deep-water sediment architecture.

6.8.1 Regional controls on minibasin tectono-stratigraphic architecture

Previous regional studies in the Santos Basin offshore Brazil assume that most clastic sediment was trapped behind a large scale (4 km thick, 200 km long, 10 km wide), salt-controlled, intra-slope depocenter; i.e., the Albian Gap (e.g, Modica and Brush, 2004; Guerra and Underhill, 2012). As a result, the stratigraphic architecture of deep-water deposition and its interaction with salt has been overlooked basinward of this depocenter.

This study has improved our understanding of the tectono-stratigraphic setting and evolution of the post-salt sequence in central deep-water Santos Basin. More specifically, I have provided conclusive evidence for relatively coarse-grained deep-water depositional elements up to 200 km from the Late Cretaceous shelf margin, indicating that not all sediment was trapped landward of the Albian Gap (cf. Modica and Brush, 2004; Guerra and Underhill, 2012). Sediment dispersal basinward of the Albian Gap occurred in four key phases, which were directly related to temporal and spatial changes in the mechanisms controlling the development of this salt-influenced deep-water slope.

I show that the initial phase (Turonian to Mid Campanian; unit 2) of coarse clastic deposition on this salt-influenced slope was restricted to the north, with submarine channels and lobes confined within proximal minibasin depocenters (minibasins A and C, Fig. 6.10a, b, 6.12). Additional, intra-minibasin relief was generated by salt pillows and landward-dipping,

salt-detached listric faults (Fig. 6.10a; 6.12 a, b). The main phase of clastic deposition occurred during the Maastrichtian to Palaeocene (unit 3), during which time salt- and fault-related accommodation in the proximal minibasins was filled or 'healed', leading to deep-water sediment dispersal systems to extend further downslope (minibasins C, D and E; Figs. 6.10d, 11a, 13, 14). Furthermore, welding of proximal minibasins in response to continued sediment loading led to the formation of a turtle anticlines and lateral shifting of depocenters towards the immediately flanks of bounding diapirs (minibasin B, Fig. 6.10c, 612d). During the third and final phase (unit 4; Palaeocene to mid-Oligocene), deposition was dominated by the emplacement of MTCs sourced from either the flanks of intraslope minibasins, or the shelf-edge and/or slope; channel and lobe systems are rare in this stratigraphic interval, suggesting a regionally significant change in sediment supply occurred between the Palaeocene and Eocene (Figs. 6.10d, 6.11b, 6.23). This sudden change in deep-water deposition may have been driven by river capture and diversion of sediment supply towards the northern Santos and the Campos Basin, which have been attributed to the uplift of the onshore coastal mountain range (e.g. Cobbold et al. 2001). Localised salt movement and minibasin subsidence continued during a fifth and final phase (unit 5; mid-Oligocene to present-day). Deposition at this time was dominated by suspension settling of relatively fine-grained deposits, although locally developed MTCs provides evidence for continued failure of the shelf-edge and/or slope (Fig. 6.24).

The two initial phases of sediment deposition, first in proximal locations and then reaching further downslope along a healed slope, indicate progressive basinward filling or healing of this salt-influenced slope. The Santos Basin therefore displays many similar characteristics to the 'fill and spill' model initially developed to capture salt-sediment interaction in deep-water slopes of the Gulf of Mexico (e.g., Auger Basin, Booth, 2003; Hudec, 2009), but which has subsequently been applied to a range of other similar settings (e.g. Espirito Santo Basin, offshore Brazil; Albertao et al., 2011; North Sea; Jackson et al., 2010; Lower Congo Basin, offshore West Africa, Oluboyo et al., 2014). Spilling between minibasins tends to occur in

locations where salt-cored structures trend perpendicular to flow, with long-distance confinement characterising locations where salt walls are oriented parallel or at a low angle to sediment supply (e.g., Booth et al., 2003; Oluboyo et al., 2014). Similar to that documented in the Lower Congo Basin (Oluboyo et al., 2014), I observe that, in areas where the channels are continuous across adjacent minibasins, the bounding salt-cored highs are at a high angle to the systems (channel 5, minibasins L and M; Fig 6.20). In contrast, long distance confinement and hence no spilling occurs along the distal elongated minibasins (minibasins I-K; Fig. 6.18). More specifically, my analysis of intraslope minibasins in the Santos Basin illustrate local sediment spilling due to welding of the minibasin floor and associated formation of turtle anticlines, which cause the diversion of deep-water channels towards the downslope minibasin (e.g.; Fig 6.10c). My 3D seismic reflection and borehole-based analysis thus presents a record of salt-sediment interactions occurring over a considerably longer timescale (ca. 60 Myr) than typically presented in studies focused on shallowly buried systems (e.g.; Winker, 1996; Pirmez et al., 2000; Fonnesu, 2003; Gee and Gawthorpe, 2004, 2006; Cartwright, 2009; 2011). A key observation is that continued diapir growth can dissect previously through-going depositional systems (e.g., salt wall between D and E, Figs. 6.12-6.14). Moroever, this study illustrates that filling of intraslope minibasins can be locally controlled by intra-minibasin salt-cored faults and salt pillows (Fig. 6.10; 6.11).

6.8.2 Local controls on paleo-seafloor relief and sediment architecture

Having discussed the regional controls on basin-scale deep-water stratigraphic architecture, I here consider the more local controls on syn-depositional seafloor relief and sediment dispersal at the intra-minibasin scale. In addition, I discuss the implications of my findings on the overall evolution of the Santos Basin, offshore Brazil. In this context, I observe the following end-member styles of salt-sediment interaction: (i) local *diversion* of channels by pre-existing seafloor relief, which also results in a change in channel sinuosity (e.g., Figs. 6.12,

6.20); (ii) *deflection* of channels towards structural lows on the seafloor, leading to channel stacking and lateral migration away from to emerging salt-cored highs (e.g., Figs 6.16c, 6.17d-f); (iii) *confinement* of channels by adjacent salt-cored highs resulting in channel stacking, levee growth and lobes deposition, where frontally confined (e.g., Figs. 6.18, 6.19); (iv) *blocking* of channels by intra-minibasin salt pillows and salt-detached faults, preventing deposition downstream (e.g.; Figs. 6.10a, b, 6.11d) (cf. Clark and Cartwright 2009; 2011). However, two key questions I answer below are; (i) where the salt-cored highs were static or actively growing during the entire life-cycle of the depositional elements?; and (ii) did the structures continue to grow after the channels and lobes were deposited?

Local channel *deflection* is evident south of the study area, occurring next to emerging shortening-related salt-cored buckle folds and thrust-cored folds (Figs. 6.15; 6.16c; 6.18a, b). Likewise, channel *diversion* occurs to the south next to a salt wall (minibasin M, Fig. 6.20), as well as within the proximal minibasins (minibasins B, C, Figs. 6.12). The salt-cored highs next to which channel *deflection* and *diversion* are observed are oriented nearly-perpendicular to the depositional slope. The with channel structurally-induced sinuous geometry adjacent to the high clearly suggest that the salt-cored highs emerged before Late Maastrichtian/Palaeocene submarine channels flowed through the São Paulo Plateau. Furthermore, my detailed analysis of the geometry of the depositional elements suggests that these salt-core highs were, in fact, moving during deposition. Syn-depositional growth of salt-cored highs is supported by the following evidence: (i) onlap and thinning towards the coeval highs (Figs. 6.19, 6.21, 6.22); (ii) local stacking/ponding in the thrust-cored syncline (minibasin J; Fig. 6.19c); and (iii) uplift, tilting and rotation of intra-levee reflections towards the channel axis (sensu Clark and Cartwright, 2009; minibasin M; Fig. 6.22). Salt structure growth may have also continued after deposition, as suggested by the channel tilting and uplift (Fig. 6.21d). Despite, I observe, LAP's around salt-cored folds, whether deposition of this potentially reservoir-prone channel axis deposits is stratigraphically related or structurally induced is unclear (channel 2; north of minibasins J, Fig. 6.16c, 6.17).

My data provide evidence for channel *blocking* and *confinement* (e.g., within proximal minibasins B, Fig. 6.11 b,d). These controls suggest salt-cored highs causing either blocking or confinement evidently predate deposition, although I also see evidence for the transition from blocking to confinement. For example, channels and lobes initially ponded north of minibasin B (depocenters B1, B2) or diverted towards minibasin C, eventually flowed along minibasin B before ponding again against a salt wall at the minibasins southern end (depocenters B3; Fig. 6.12d). In addition, I suggest local increase in accommodation during minibasin confinement leads to: (i) an increase in seismic amplitude, width and thickness of the channel as it flows axially along the minibasins potentially associated to an increase in sandstone deposition (e.g., Fig. 6.22); (ii) preferential deposition of levees where accommodation locally increases (minibasins L, M, Fig. 6.20); (iii) preferential deposition of (confined) lobes in synclines between intra-minibasin salt-cored anticlines and eventual healing of paleoseafloor relief (Figs. 6.18, 6.19). I suggest earlier movement and syn-sedimentary growth of the complex salt-cored structures bounding the folded minibasins in the contractional domain provided confined accommodation, causing channels to aggrade within the basin and preferential deposition of levees and lobes.

These observations have implications for the salt-related structural evolution of the central deep-water Santos Basin. I propose that the seafloor salt-cored folds and anticlines were the expression of Late Cretaceous-to-Palaeocene, syn-sedimentary, thin-skinned shortening, resulting from downslope flow of salt and its overburden. The distribution and architecture of syn-kinematic channels and levees systems provide a stratigraphic record of this structural growth.

Similar observations of salt-sediment interaction comes from very shallow (i.e., at the seafloor or up to 500 m deep), undrilled, relatively young deep-water systems, which are then used as analogues to understand similar salt-sediment interactions in older, more deeply buried systems (e.g., Winker, 1996; Beaubouef and Friedmann, 2000; Pirmez et al., 2000; Fonnesu,

2003; Gee and Gawthorpe, 2004, 2006; Clark and Cartwright, 2009; 2011). Contrastingly, my results have revealed the influence of salt movement on deep, Late Cretaceous-Palaeocene- age coeval depositional systems. Furthermore, previous studies are focused on single minibasins or covering relatively small areas of c. 400 km^2 (e.g., Gulf of Mexico, Booth et al., 2000, 2003) or up to 1400 km^2 (e.g.; offshore Angola, Jones et al. 2012). Moreover, previous regional-scale (up to 10,000 km^2) studies have focused on the analysis of specific stratigraphic intervals recording relatively short time scales of ca. 15 Myrs (e.g.; Olobuyo et al., 2014). In contrast, my 3D seismic reflection and borehole-based analysis illustrates a long timescale (ca. 60 Myrs) record of salt-sediment interaction in more than ten minibasins covering an area of c. 20,122 km^2; thus, documents the post-salt tectonostratigraphic evolution of the central deep-water Santos Basin from the initial minibasin development in the Turonian up to present-day.

6.8.3 Exploration significance

I propose that the salt-related controls observed in central deepwater Santos Basin led to changes in the geometry, distribution and potential structural and stratigraphic trapping of reservoir-prone units. As such, this part of the Santos Basin may have exploration potential, with these previously unexplored post-salt sequences being prospective (see Fainstein et al., 2001). My findings have important implications for trap development and seal presence, in particular, I have illustrated the presence of: (i) fault-block traps (e.g., Figs. 6.11b, d); (ii) turtle anticlines (minibasin C, Fig. 6.11a); (iii) stratigraphic traps related to the pinch-out of channels and lobes towards salt-cored highs (e.g., Figs. 6.11b, e; 6.21). For the potential reservoir-prone units discussed in this paper (e.g. channels, lobes and, perhaps to a lesser extent, levees), 'background' deposits, such as slope mudstone, and salt represent the main seals (Table 6.2). Local, mud-rich MTCs may also form lateral and vertical seals (e.g., minibasin L, regional unconformity above the submarine channel systems, Fig. 6.22.).

The deep-water depositional systems I have identified in the Santos Basin could be distal analogues of the Turonian confined turbidites in the Merluza field, Santos Basin (e.g., Enciso and Tisi, 1998) and the Campanian to Maastrichtian deposits in the Roncador Field, Campos Basin (e.g., Bruhn et al., 2003). Moroever, the distal deepwater reservoirs in the Campos Basin occur in stratigraphic traps. Overall, there appears to be less confinement of depositional elements, hence traps and fields are larger. In contrast, distal deepwater depositional systems in the Santos Basin have been confined axially for more than 150 km. Because of this confinement, it is likely that any potential traps and fields would be smaller than observed in the Campos Basin (cf. Gulf of Mexico; e.g., Booth, 2003). For example, the seismic stratigraphy geometry and distribution of the more proximal reservoir-prone intervals of stacked submarine channels and fans or sheet-sand reservoirs illustrated in this study are strikingly similar to reservoir-prone units being currently produced in the Gulf of Mexico (i.e., Auger Basin, Booth et al., 2003; Jackson and Hudec, 2016; Fig. 6.11b-e). A key exploration risk for the Santos Basin is migration, principally due to the thick, likely very low-permeability salt between sub-salt source rocks and supra-salt reservoirs (Figs. 6.7b, c). This is a particular risk in distal areas, where thick allochthonous salt remains; in proximal areas, salt welds may facilitate the vertical migration of hydrocarbon, although the mudstone-dominated nature of many of the minibasin may still pose a migration risk. Moreover, migration could provide through rotated minibasins flanks that are underlying the depositional elements (e.g, Figs. 6.21 and 6.22). Likewise, the presence of salt-cored faults and turtle anticlines, due to minibasin welding, may promote the vertical hydrocarbon migration of hydrocarbons.

Risks could also be associated to the shallow units containing the MTCs, which may represent geohazards for the potential drilling of these deep-water plays. In addition, the MTCs near diapir seals and eroded by submarine channels (eg., minibasin K) could compromise the quality of the reservoir units. However, I suggest that for an analysis of these potential plays which is beyond the scope of this study, further detailed mapping, volume estimations and petroleum systems modelling are recommended.

6.8.3 Conclusions

Integration of 3D seismic and borehole data has revealed:

1. Overall, I recognise three minibasin types, from proximal to distal locations i.e. (i) thick minibasins, apparently welded, (ii) shallow minibasins, overlying thick salt and (iii) distal elongated minibasins deformed by intra-minibasin salt-cored folds.

2. Four main types of deep-water sediment depositional elements were deposited within the minibasins in central deep-water Santos Basin within the post-salt sequence: channels, levees, MTCs and background deposits.

3. Borehole information indicates that the Minibasin-confined leveed-channel belts are composed of interbedded sandstone, siltstone and mudstone. Whereas distal boreholes suggest siltstone rich channels and depositional lobes.

4. Sedimentation in central deep-water Santos Basin occurred during three main phases of minibasin subsidence:

- Phase I: Turonian to the Mid-Campanian: sand-rich channels and lobes, and MTCs of unconstrained composition were confined within proximal minibasins and to the hangingwalls of landward-dipping, salt-detached listric faults.

- Phase II-Mid-Campanian to the Paleocene: sand-rich channels and lobes eventually filled and bypassed proximal minibasins, with coarse clastic deposition then occurring further downslope in distal minibasins, >100 km from the coeval shelf margin.

- Phase III and IV: Paleocene-to-middle Oligocene: continued rise of proximal salt walls dissected previously deposited deep-water systems, with deposition from diapir- and shelf-edge sourced MTCs becoming increasingly important

5. Syn-depositional seabed deformation, driven by passive and active diapirism, and

salt-detached thrusting and folding, caused changes in the geometry, architecture and distribution of deep-water depositional systems:

i) channel deflection and diversion around salt-cored highs

ii) channel and levee uplift and rotation on the flanks of rising salt-cored anticlines and diapirs

iii) progressive lateral channel migration, expressed in the form of lateral accretion packages (LAPs)

iv) local ponding and long-distance confinement of channels, levees and lobes.

v) channel width and thickness increase due to intraminibasin increase in accommodation

6. The deep-water depositional elements identified have important implications for post-salt hydrocarbon prospectivity in the central, deepwater Santos Basin, with a range of reservoir types and trapping styles being developed in this previously underexplored interval

Chapter 7

Evidence for and significance of submarine salt dissolution

7.1. Abstract

Salt dissolution occurs when evaporite-dominated rocks come into contact with NaCl-undersaturated fluids. The effects of salt dissolution in sedimentary basins can have direct implications for hydrocarbon and mineral exploration, seismic imaging, drilling, and basin restorations. However, due to seismic imaging issues and a lack of borehole data, few studies have analysed salt dissolution-related morphologies (i.e., salt karst) and associated deformation within the post-salt sedimentary overburden. In this study, I integrate high quality 3D seismic reflection data, a regional 2D seismic reflection line and wellbore data from the Santos Basin, offshore Brazil to characterise salt dissolution-related features at the crest of buried salt diapirs. Salt karst features consist of (i) up to 100 m thick, sub-circular, residual mounds rising above the Top Salt; (ii) up to 100 m deep, oval-to-circular, dissolution sinkholes below the main level of the Top Salt; and (iii) up to 75 m tall breccia pipes capped by collapse sinkholes within the overburden. The results of this study also suggest a direct link between the intrasalt stratigraphic heterogeneity, and the style of salt karst and related deformation in post-salt sedimentary overburden. In addition, seismic-stratigraphic-relationships in post-salt strata suggest multiple mechanisms of salt dissolution. Furthermore, reverse-basin modellingv

suggests salt dissolution occurred in a fully submarine environment in water depths of 1900 m (± 100 m). These findings differ to most modern cases of salt dissolution which occur in a subaerial or near-surface setting. In this paper, I discuss the possible mechanisms leading to submarine salt dissolution at the crest of salt walls, in the Santos Basin, offshore Brazil and the significance and implications of this process.

7.2. Introduction

Salt is typically dissolved when it comes into contact with NaCl-undersaturated waters. In this study, I use the term 'salt' to refer to evaporite rocks in general, i.e. rocks comprised of soluble minerals that precipitate from the evaporation of brines. The most soluble and weaker evaporite minerals are the bittern salts (K and Mg salts, e.g., carnallite, tachyhydrite) followed by halite (NaCl), whereas the less soluble are anhydrite and gypsum (e.g.; Warren, 2006). Hence, when salt dissolution occurs, the more-soluble evaporites (bitterns and halite) are dissolved first, resulting in the enrichment of anhydrite and intrasalt insoluble residue. Prolonged contact with undersaturated fluids may lead to rehydration of the anhydrite and gypsum formation within the caprock (Jackson et al. 1990; Hovorka, 2000; Warren, 2006). In addition; anaerobic microbial activity within caprocks can also lead to the deposition of thick calcium-carbonate-dominated sequences and sulphite deposits (e.g.; Kyle and Posey, 1991; Jackson and Hudec, 2017).

Salt dissolution generally results in: (i) discordant geometrical relationships between the remaining salt and the overburden, (ii) the formation of a residual caprock or diapiric solution breccias, (iii) the development of salt karst features such as sinkholes, grooves, caves and residual mounds; and (iv) deformation of the overburden (e.g.; Jackson et al., 1990; Warren, 1997; Cartwright et al., 2001; Warren, 2006; Bruthans et al., 2009; Hudec et al., 2011; Jackson and Hudec, 2017). Present-day subaerial exposure of salt has been extensively studied; thus

providing the best documentation of morphology (salt karst) likely to result from salt dissolution (Fig. 7.1a; e.g., Bruthans et al., 2009; Frumkin, 2013; Gutiérrez and Lizaga, 2016). Salt karst in Iran resemble those related to subterranean karstic dissolution of calcium carbonate, which have been imaged by seismic data and studied due to the importance of carbonate rocks as hydrocarbon reservoirs (Fig. 7.1b; e.g. Evans et al., 1994; Vahrenkamp et al., 2004; Sullivan et al. 2006; Zeng et al., 2011; Burberry et al., 2016). Salt dissolution is not limited to that occurring near-surface or during subaerial exposure. Recent studies have described similar rugose morphologies and semicircular depressions related to salt dissolution in submarine settings (e.g., Bertoni and Cartwright, 2005; Talbot and Augustin, 2016). However, seismic-scale submarine salt karst studies are limited. For example, potentially dissolved flat-topped and rugose-topped salt walls have been imaged near or at the seabed in the Barents Sea (Fig. 7.1c; e.g. Koyi et al. 1995) and in the North Sea (Fig 1d; e.g, Duin, 2001), but there have been no attempts to document possible submarine salt dissolution at their crests. A spectacular example documented in the Orca Basin, Gulf of Mexico, reveals a rugose salt canopy exposed at the seabed, which is currently being dissolved by NaCl-undersaturated seawater producing brines that flow downslope into an enclosed submarine brine lake (Fig. 7.1e; Shokes et al., 1977; Tompkins and Shephard, 1979; Pilcher and Blumstein, 2007). However, previous studies in the Orca Basin are not conclusive about the presence or composition of caprock or salt karst morphology at the crest or if the canopy is covered by overburden; thus, it is not clear if the salt is directly in contact with seawater or if seawater penetrates a thin veneer to reach the salt.

Being able to identify the evidence for salt dissolution has a range of implications and applications. First, the less-soluble residual evaporite rocks at the crest of dissolved salt structures (i.e, caprock) are the source of economic minerals and have the potential to become reservoir rocks (e.g., Posey and Kyle, 1988; Kyle, 1999). Salt dissolution has been related to the creation of local depocenters and faulting within the overburden, potentially promoting reservoir deposition, trapping and compartmentalisation (e.g., Ge and Jackson, 1998;

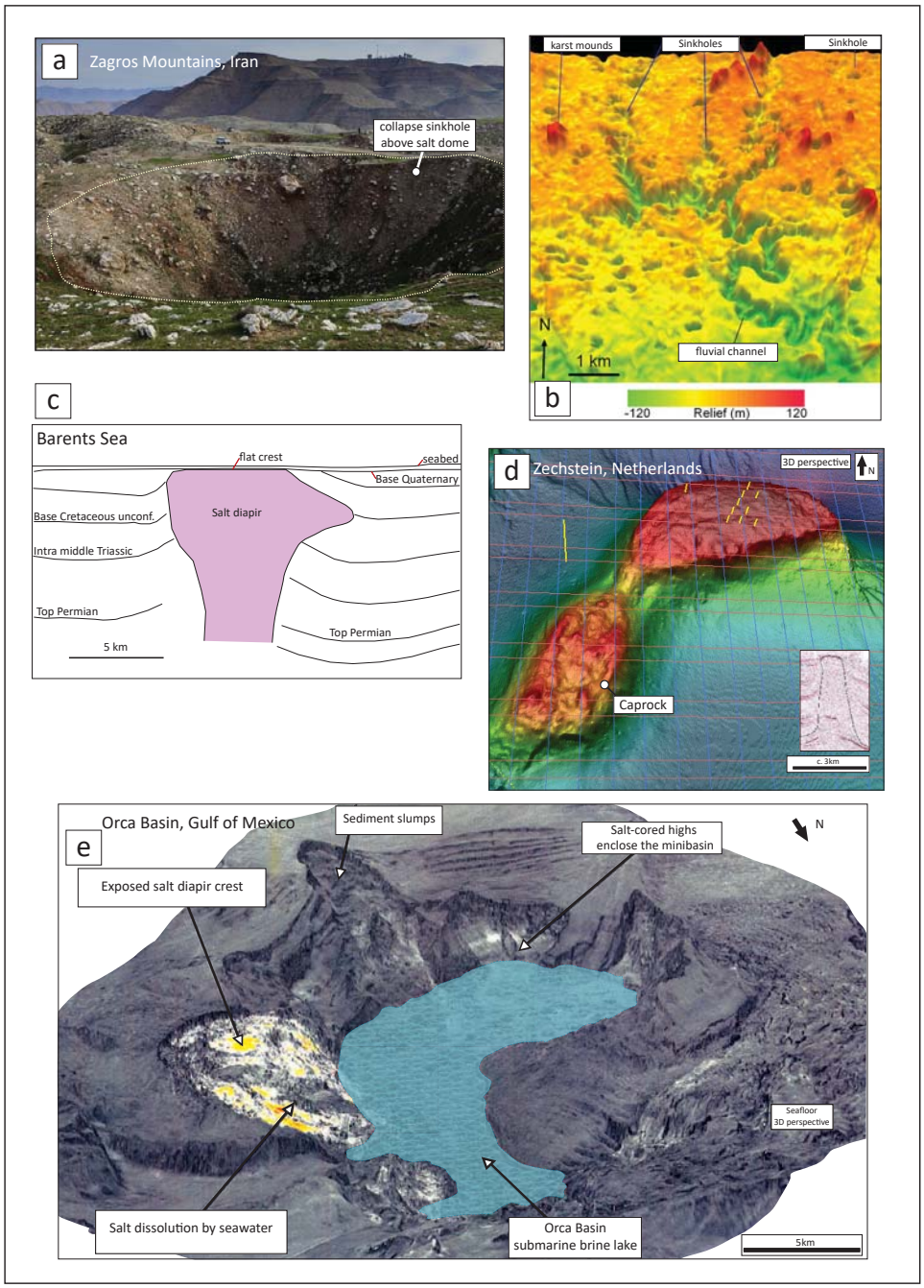


FIGURE 7.1: Worldwide evidence of dissolution: (a) Collapse sinkhole above a salt dome in the Zagros Mountains, Iran, after Gutierrez and Lizaga (2016); (b) Deeply-buried, Ordovician-age carbonate karst morphologies in the Tarim Basin, China, after Zeng et al. (2011); (c) near-seabed flat-topped salt diapir in the Barents Sea, after Koyi et al. (1995); (d) Salt wall caprock in Netherlands, after Duin (2001); (e) present-day submarine brine lake in the Gulf of Mexico, after Pilcher and Blumstein (2006).

Cartwright et al., 2001; Hudec and Jackson, 2011; Jackson et al., 2010). In addition, the collapse and deformation associated with karst can generate mega-pores or reduce the sealing properties of the salt and its overburden, hence its proper characterisation is relevant for evaluating reservoir and seal potential (e.g., Walles, 1993; Vahrenkamp, 2004). Accurate seismic imaging requires a proper understanding of the caprock stratigraphy and associated seismic velocities at the crest and lateral margins of salt structures (e.g., Jackson and Lewis, 2012; Jones and Davison, 2014). Furthermore, the amount of salt dissolved from the geological record is often unknown, limiting the accuracy in basin restorations and reconstructions (e.g, Koyi et al. 1995; Cartwright et al., 2001). Finally, salt dissolution pose challenges when drilling due to fractures, cavities and diagenetic alterations at the crest and lateral margins of salt structures (eg. Black, 1997; Willson and Fredrich, 2005; Jackson and Hudec, 2017).

However, regardless of its broad significance, surprisingly few studies have used seismic reflection data to investigate salt-related dissolution, characterise seismic-scale karst morphology, and to understand its impact on the overburden and remnant salt (e.g.; Bertoni and Cartwright, 2005; Jackson and Lewis, 2012; Burberry et al., 2016). Seismic-scale salt dissolution studies can be challenging due to seismic imaging issues and the lack of sufficient seismic resolution to precisely analyse salt karst morphologies and deformation within the caprock, overburden and intrasalt units. In addition, there is a limited amount of borehole data to correlate seismic expression to the lithology within caprock and its overburden. Nevertheless, 3D seismic reflection data provide a valuable tool to characterise the expression of salt dissolution compared to 1D- borehole and 2D-seismic reflection data and quasi–three-dimensional outcrops.

In this study I integrate high quality 3D seismic reflection, 2D seismic and borehole data from the Santos Basin, offshore Brazil, to; (i) identify and map seismic-scale salt dissolution, (ii) understand the mechanisms driving salt dissolution (iii) discuss the implications of salt dissolution in sedimentary basins in general, and, specifically, in the overall regional

geodynamic evolution of the central deepwater Santos Basin. To achieve this, I characterise the variations in the external geometry and seismic-scale style of salt dissolution in six salt diapirs. In addition, I assess the impact of dissolution on the intrasalt stratigraphy and the overburden. Lastly, I reconstruct the basin geometry to the time of salt dissolution. With this analysis, I will attempt to answer three key questions: (i) what is the role of the intrasalt stratigraphic heterogeneity in the resulting salt-dissolution-related morphology?; (ii) were the salt walls subaerially exposed or did salt dissolution occur in a submarine setting? and (iii) what is the likely origin of the dissolving fluids?

There are currently no published studies documenting any occurrence of salt dissolution in the deep-water Santos Basin despite the highly-reflective nature of the salt and its overburden (e.g. Jackson et al., 2014a, 2015b; Rodriguez et al., in press/Chapters 5 and 6). This makes it an ideal location to analyse the intra-salt stratigraphy and its relationship with the style of dissolution at the crest of salt walls. With this work, I contribute to the characterisation of submarine salt karst. My methods and results can be applied to other salt-dominated basins for the accurate prediction and understanding of salt-related karst and its impact in the overburden.

7.3 Geological setting

The Santos Basin is located in eastern offshore Brazil and originated as a result of the opening of the South Atlantic Ocean between east South America and West Africa (Fig. 7.2). During the initial stage of its evolution in Barremian times, non-marine to shallow marine sediments were deposited within fault-bounded half-graben basins (Fig. 7.3; e.g., Demercian, 1996; Meisling et al., 2001; Gomes et al., 2002; Moreira et al., 2007). An initially isolated and irregular rift-related valley accompanied by intermittent seawater incursions and subsequent dessication events, led to the deposition of a regionally extensive, up 2.5 km thick, interbedded evaporite

sequence or salt giant (i.e., Aptian-age Ariri Formation in the Santos Basin; e.g., Szatmari 2000; Dias 2004; Davison 2007; Karner and Gambôa, 2007; Davison et al., 2012; Rodriguez et al. in press/Chapter 5). The subsequent widening and deepening of the proto-south Atlantic Ocean promoted the deposition of a shallow-marine, carbonate platform and related distal marls in the Albian (Fig 7.3; Moreira et al., 2007). Normal marine conditions were reached in the Upper Cretaceous following the drowning of the Albian-age carbonate platform and accompanied by margin tilting and the development of a major clastic-dominated progradation (Fig. 7.3, e.g. Modica and Brush, 2004; Moreira et al., 2007).

From the Turonian and up to the paleocene, channel-levee complexes were deposited within a salt-controlled, intra-slope depocenter (i.e., Albian Gap) and within proximal salt-bounded minibasins eventually bypassing to deposit clastics confined along distal elongated minibasins (e.g. Rodriguez et al. in press/Chapter 6). During the Eocene, sediment supply into the Santos Basin was only dominated by shelf-sourced and salt-sourced mass transport complexes (MTCs) possibly due to onshore uplift and diversion of the Paraiba do Sul river drainage systems to the NE (e.g., Cobbold et al., 2001; Modica and Brush, 2004; Guerra and Underhill, 2012; Rodriguez et al. in press/Chapter 6). Except for locally confined shelf-sourced MTCs and local minibasin subsidence in proximal locations (eg., Jackson 2011; Rodriguez et al., in press/ Chapter 6), the Oligocene and up to the Pleistocene, the central deepwater Santos Basin is dominated by fine-grained sediment deposition due to a sea level hightstand and absence of onshore drainage systems supplying sediments into the basin (Fig. 7.3; Modica and Brush, 2004; Moreira et al., 2007; Guerra and Underhill, 2012).

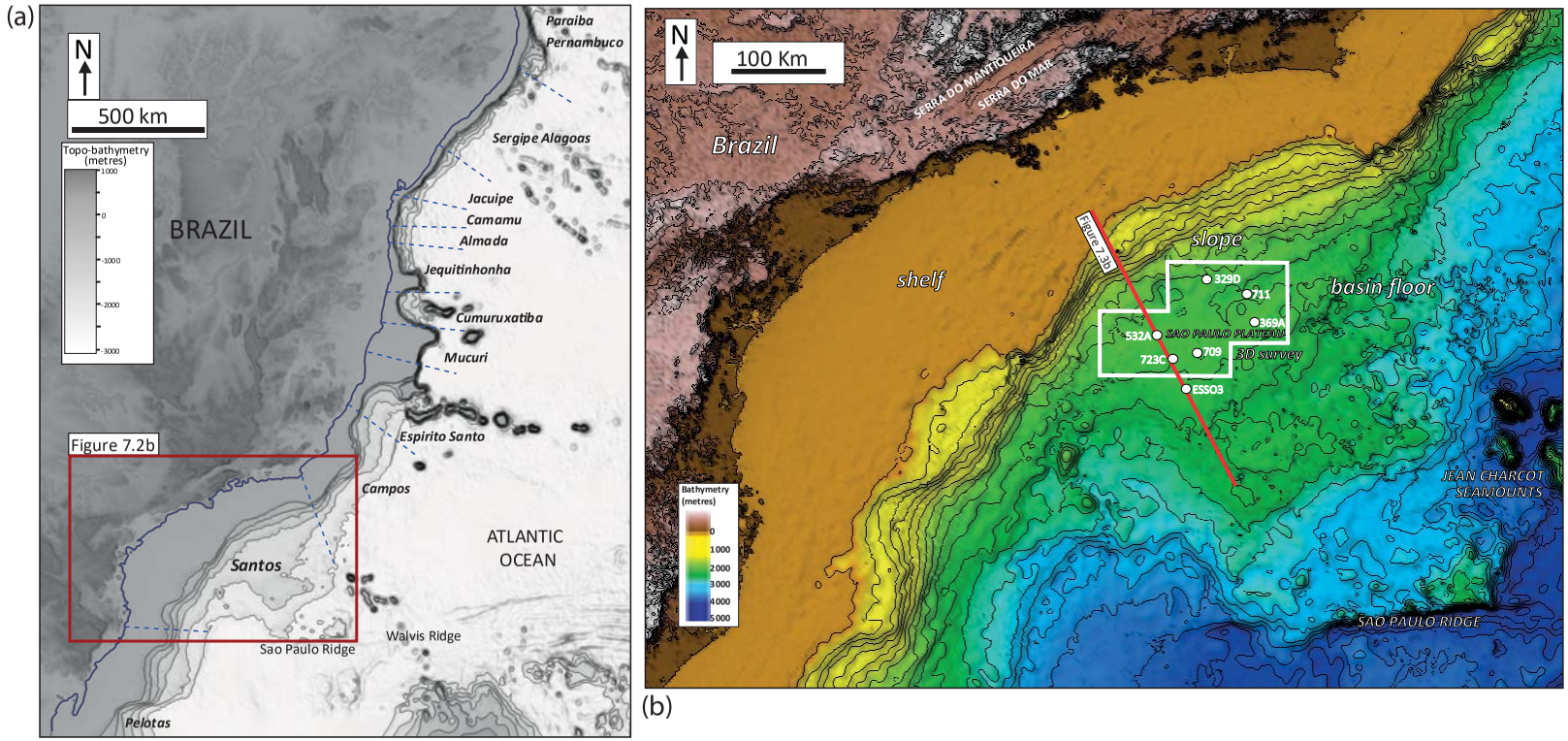


FIGURE 7.2: (a) Eastern Brazil salt-dominated sedimentary basins highlighting the location of the Santos Basin, offshore Brazil; (b) Study area in the central deep-water Santos Basin. Location of 2D seismic profile used for basin modelling and 3D seismic reflection and borehole data

(a)

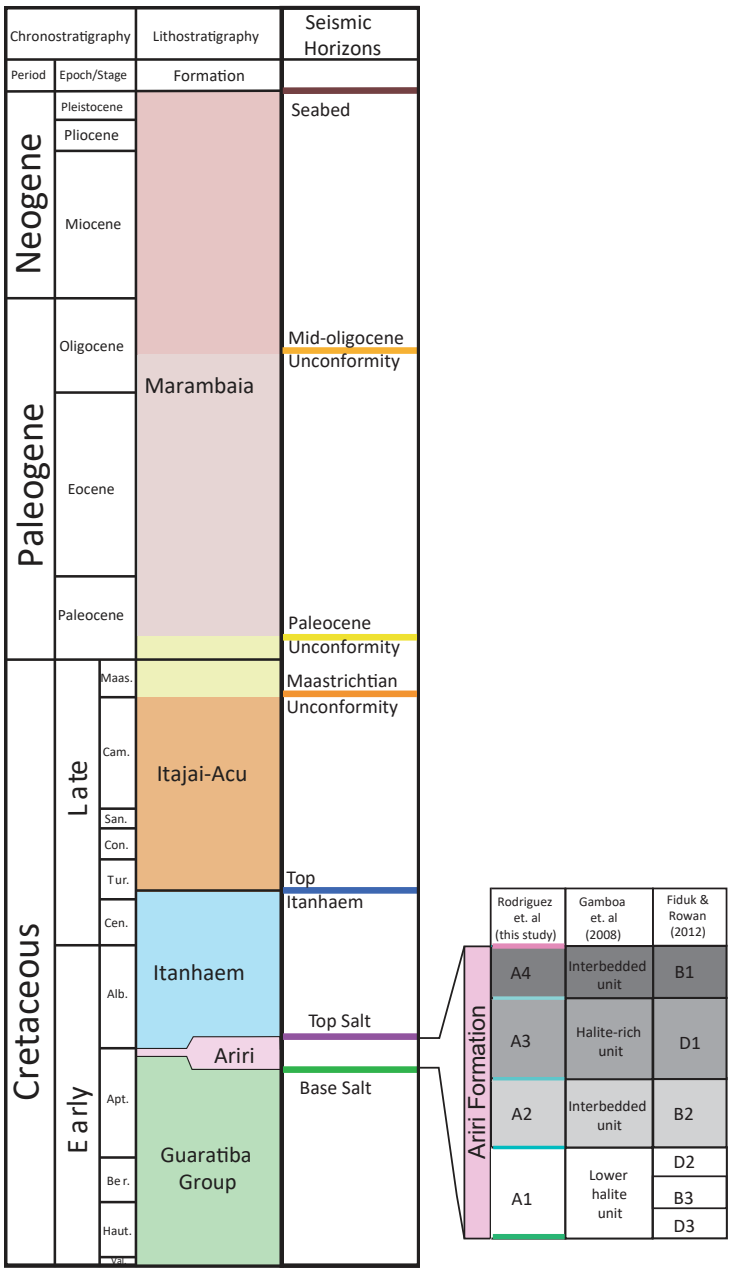
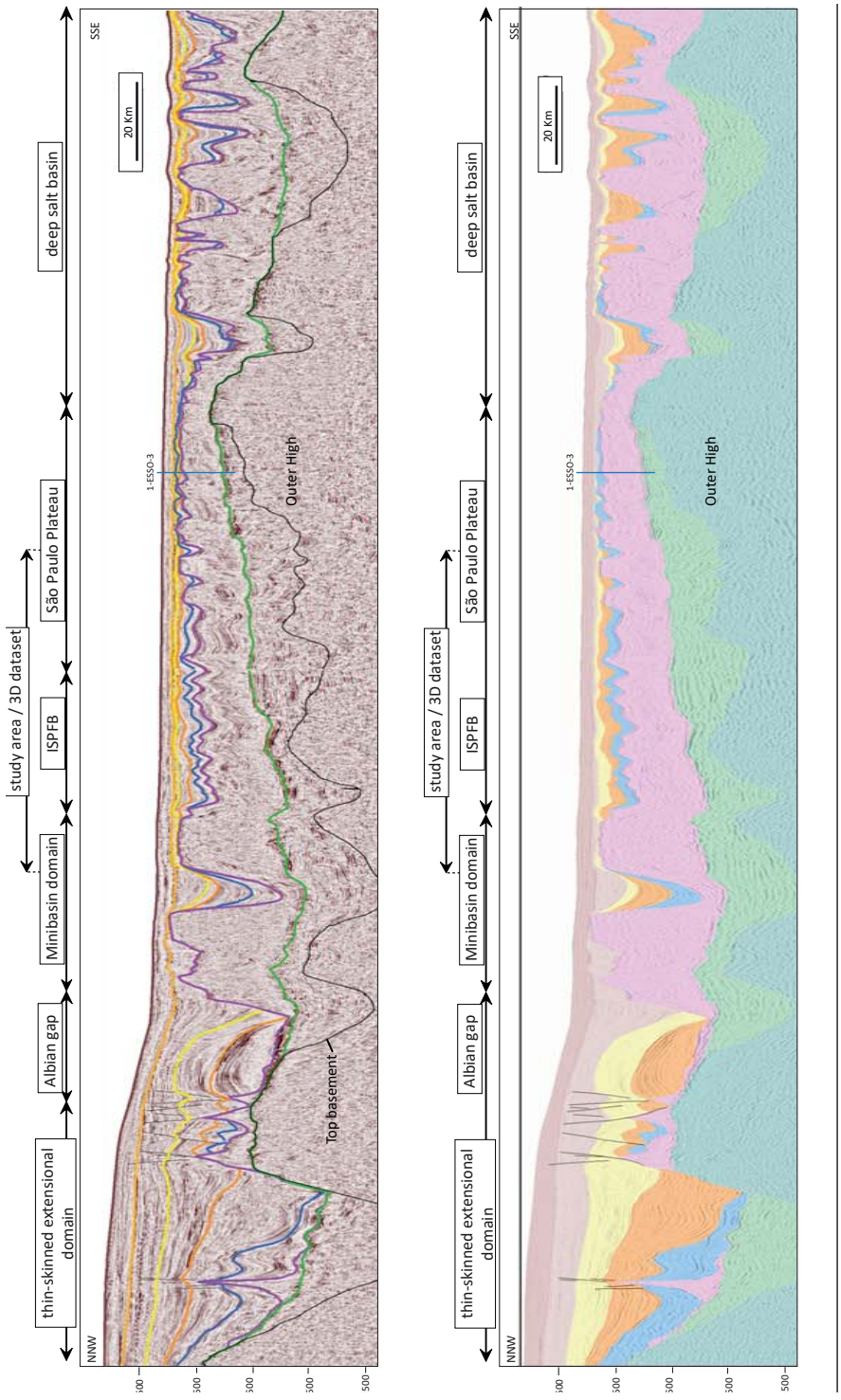


FIGURE 7.3: (a) Seismic stratigraphic framework; Intrasalt key stratigraphic intervals are specified for this and previous studies. B1, B2 and B3 refer to competent layers or 'beams' defined by high amplitude continuous reflections. D1, D2 and D3 refer to ductile detachment zones defined by acoustically transparent, poorly continous reflections (Fiduk and Rowan, 2012). (b) 2D depth seismic profile illustrating salt-related structural domains in the Santos Basin. (c) Geoseismic profile with units interpreted.


thin-skinned extensional domain
Albian gap
Minibasin domain
ISPFB
São Paulo Plateau
study area / 3D dataset
deep salt basin
NNW
SSE
20 Km
1-ESSO-3
Outer High
Top basement

7.4 Dataset

The data used in this study include a high-quality 3D time-migrated seismic reflection volume (provided by CGG), 2D post-stack depth-migrated seismic that intersects the 3D volume (provided by WesternGeco) and data from eight publicly available boreholes (Fig. 7.2b). Borehole data is sparse across the study area and contain lithology and formation markers for the presalt, the intrasalt and postsalt sequences. Two of the boreholes contain a comprehensive set of electrical logs (eg. GR, Neutron, Density and P-Sonic), and these have aided me to tie seismic and borehole data, and to assign lithology information to the mapped intervals (Figs. 7.5a and 7.6).

The 2D depth seismic profile is c. 350 km long and has a record length of 16 km providing a good quality regional image along the central deep-water Santos Basin (Fig. 7.3). The high-quality 3D seismic reflection volume covers an area of 20,122 km2 and contains trace data from the sea level down to 5.5 seconds two-way time (TWT). The 3D dataset has a vertical sample rate of 4 ms, inline spacing (east-west) of 18.75 m and crossline spacing (north-south) of 25 m. The stratigraphic units of interest (i.e.; unit 3, unit 4 and the intrasalt within the crests of salt walls; Fig. 7.5) lie between 3.2-3.6 s TWT interval of the 3D seismic data. The dominant frequency varies with depth but it is c. 40 Hz in unit 3 and unit 4 and c. 37 Hz in the intrasalt units near the crest of the salt walls. The vertical seismic resolution of these units is estimated to be 12 m and 30 m, using interval velocities of 1900 m s^{-1} for the overburden and 4500 m s^{-1} for the intrasalt. The interval velocities used for the stratigraphic units of interest are an average of interval velocity values derived from checkshot data in three boreholes; i.e.; 532A, 723C and 709 (Figs. 7.2a; 7.5). Regional seismic profiles (2D and 3D data) are displayed with SEGY normal polarity, where a downward increase in acoustic impedance is represented by a positive reflection event (black) and a downward decrease in acoustic impedance is represented by a negative reflection event (red). In seismic sections illustrating small-scale (<2 km wide; <200 ms tall) salt karst morphology a positive reflection event is red and a

negative reflection event is blue.

7.5 Methods

I mapped eight key regional horizons were interpreted in depth along the 2D seismic profile; seabed, mid-Oligocene unconformity, Palaeocene unconformity, Maastrichtian unconformity, top Itanhaem, Top Salt, Base Salt and basement (Fig. 7.3). These horizons (excluding Basement); in addition to three intrasalt horizons along salt diapir crests, were interpreted using the 3D seismic volume in TWT (top A1, top A2 and top A3; Figs. 7.5a; 7.6). For the intrasalt stratigraphy, a synthetic seismogram provides a tie between lithology and seismic expression (borehole 709; Fig. 7.4a, see also Rodriguez et al. in press/Chapter 5). For the post-salt stratigraphy, ages and lithology were assigned to seismic horizons based on regional studies (Modica and Brush, 2004; Contreras et al.; 2010; Guerra and Underhill, 2012), or because they correlate to major lithological breaks or unconformities identified in two boreholes nearby (532A, 723C, Fig. 7.2). For the detailed analysis at the crests of salt diapirs, high resolution (i.e.; seismic grid spacing of 18.75 m x 25 m) structural maps were generated for the Top Salt and overburden horizons.

I use a range of seismic attributes to aid in the analysis: (1) amplitude contrast, which involves the calculation of amplitude derivatives between neighbouring traces (Schlumberger, 2012), used here mainly in map-view in order to highlight the discontinuities along the top salt; (2) chaos, is a texture attribute used to map disorganized seismic traces within a 3D window (Randen and Sønneland, 2005), and is key in this study to investigate and map intra-salt facies variations subcropping the salt crests; and (3) sweetness, which relates the amplitude strength (envelope) and the instantaneous frequency (Hart, 2008), mainly used here to highlight lateral and vertical facies variations (in vertical section) along the crest of salt walls and between and within the key intrasalt intervals.

I reconstruct the basin geometry along a 2D regional seismic profile in order to estimate the paleo-water depths at which dissolution likely occurred. This reconstruction allows me to constrain if the crests of salt walls where dissolved in a submarine setting or if dissolution occurred while subaerially exposed, as it has been documented in other salt basins (e.g.; the Zechstein salt in the North Sea; Clark et al., 1998). To reconstruct the basin geometry at the time that I suspect salt dissolution occurred (i.e., ca. Palaeocene), I apply a reverse-basin modelling technique (or 'backstripping') using the workflow in FlexDecompaction, software developed by Badley Gecoscience Ltd (e.g., Roberts et al., 2009; Bell et al., 2014). I justify the application of this reverse-basin modelling technique for the following reasons: (i) salt movement was likely to be minimal in the study area at the time salt dissolution occurred (i.e., Palaeocene); hence, with this modelling, I am not attempting to reconstruct phases of salt-related deformation (i.e., Albian-Maastrichtian; Modica and Brush, 2004; e.g.; Rodriguez et al. in press/Chapter 6). By the Palaeocene salt had already moved into the diapirs I see today in the study area.; and (ii) thickness variations within the post-salt sedimentary overburden are relatively consistent above the crests of salt walls in the study area; thus, there are limited lateral variations in sediment thickness which justifies the 2D basin modelling technique used here (Fig. 7.3). Overall, the reverse reverse-basin modelling technique involves removing: (1) the effect of sediment load and (2) the effect of post-rift thermal subsidence of each of the sedimentary layers in the overburden until the horizon of interest is reached. The removal of each sedimentary layer results in the decompaction of the remaining layers allowing the basin geometry at the time at which the horizon of interest was deposited to be resolved.

A summary of the post-salt sediment key input parameters used for the reverse-basin modelling technique in the study area can be found in Table 7.1. The lithology information used for the sediment input parameters are based on the integration of post-salt interpretation (Rodriguez et al., in press/Chapter 6) and the final well reports available (Fig. 7.2; Table 7.1). A key crustal parameter in the basin reconstruction and estimation of paleo-bathymetry is the effective elastic thickness (T_e), which measures the strength of the lithosphere (Watts, 1992). In this

study, I use a T_e of 5 km, which is representative of the Santos Basin thinned and weak crust where loads are supported locally, over short wavelengths (i.e. Airy isostasy; e.g., Davison et al.; 2012). Another key crustal parameter for the reconstruction of the basin to the time of salt dissolution is the Beta stretching factor (β), for which I have considered minimum and maximum estimated profiles by Scotchman et al. (2006). The low-end profile estimated by Scotchman et al. (2006) assumes that the base salt subsidence from Aptian to present is due to both syn-rift and post-rift subsidence. Conversely, the high-end profile was estimated assuming that the base salt subsidence from Aptian to present is due to post-rift thermal subsidence only (Scotchman et al., 2006, 2010).

Table 7.1: Post-salt sediment key input parameters based on seismic interpretation and well reports available

Horizon age (Ma)	Horizon name	Unit name	Lithology	Near-surface porosity (%)	Decay constant (1/km)	Matrix density (g/cc)
0	Top Marambaia (Seabed)	Unit 5	90% shale 10%sand	61.6	0.49	2.71
~28	Mid Oligocene Unconformity	Unit 4	80% shale 20%sand	60.2	0.46	2.71
~60	Paleocene unconformity	Unit 3	40% shale 60%sand	54.6	0.37	2.68
~67	Maastrichtian unconformity	Unit 2	60% shale 40%sand	57.4	0.41	2.69
~95	Top Itanhaem	Unit 1	70% shale 30% limestone	65.1	0.57	2.72

7.6 Salt-related structural domains

Before I overview the dissolution-related morphologies at the crests of salt structures, here I describe the salt-related structural domains along the slope and the overall external shape of salt walls in the study area.

The 2D seismic profile I have interpreted illustrates how salt-related deformation in the Santos Basin varies from NW to SE. Overall, six structural domains are identified in this study (Fig. 7.3), i.e.; (i) an upslope thin-skinned extensional domain characterised by salt pillows and landward- and basinward- dipping listric faults; (ii) the Albian Gap, a large scale salt-controlled intraslope depocenter which trapped a large amount of Cretaceous-to-Eocene-age sediments in proximal locations (e.g., Jackson et al. 2015a); (iii) a minibasin domain: characterised by thick minibasins overlying thin or welded salt and bounded by up to 20 km-wide salt walls; (iv) the 'Inner São Paulo Fold Belt' (ISPFB; *sensu* Jackson et al. 2015b) characterised by folding of the salt layer and the development of buckle folds and intra-salt thrusts; (v) the São Paulo plateau (SPP), mainly characterised by a landward-dipping base salt due to the underlying 'Outer High' and the occurrence of a highly-reflective up to 2.5 km thick salt sequence and distal minibasins; and (vi) a deep and thick salt sub-basin basinward of the Outer High.

The Top Salt structural map generated from the 3D seismic interpretation illustrates the present-day salt-related deformation in the study area (Fig. 7.4a). This study focuses on salt diapirs in the minibasin domain, the ISPFB and the SPP. Overall, I identify two main types of salt diapirs in the study area. Salt diapirs in the minibasin domain and the ISPFB, are characterised by crests that are more rounded and highly irregular or rugose (*R-west*; *R-central* or Liam, *sensu Jackson et al. (2015 b)*; and *R-east*; Fig. 7.4). Contrastingly, salt diapirs in the more distal SPP are characterised by nearly-horizontal (<10◦ dip) tops or flat crests (*F-west, F-central*, and *F-east*; Figs. 7.4a, 7.4b and 7.4c). *F-central* and *F-east* correspond to *Jimmi* and *Freddy* in study by Jackson et al. (2015b).

The salt walls with rugose crests are broadly oriented E-W and N-S. Conversely, the flat-topped salt walls are broadly oriented N-S and NE-SW (Fig. 7.4a). The salt walls with rugose crests are broadly thinner (up 10 km wide) and taller (up to 4 km tall) than the flat-topped salt walls (up to 15 km wide and up to 2.5 km tall) (Figs. 7.4b and 7.4c).

Despite the relatively simple external morphology that characterise the salt diapirs in the study area, a great amount of intra-salt structural complexity has been previously documented (e.g., Davison et al., 2012; Fiduk and Rowan, 2012; Jackson et al., 2014a, 2015b). Of particular interest for this study, the upper parts of the flat-crested salt walls are all dominated by allochthonous, poorly-reflective intra-salt sheets (Fig. 7.4c, e.g., Jackson et al. 2014a, 2015b). Contrastingly, the internal structural complexity along the rugose-crested salt walls is more variable. Although intra-salt sheets are also locally emplaced (e.g. *R-east* in Fig. 7.4b), the rugose crests are also characterised by intrasalt reverse shear zones and upright symmetrical anticlines (*R-west* and *R-central* in Fig 7.4b, see also Jackson et al., 2015b). This variability is important when I later consider the style of salt dissolution along top salts and its relationship with the subcropping intrasalt stratigraphy.

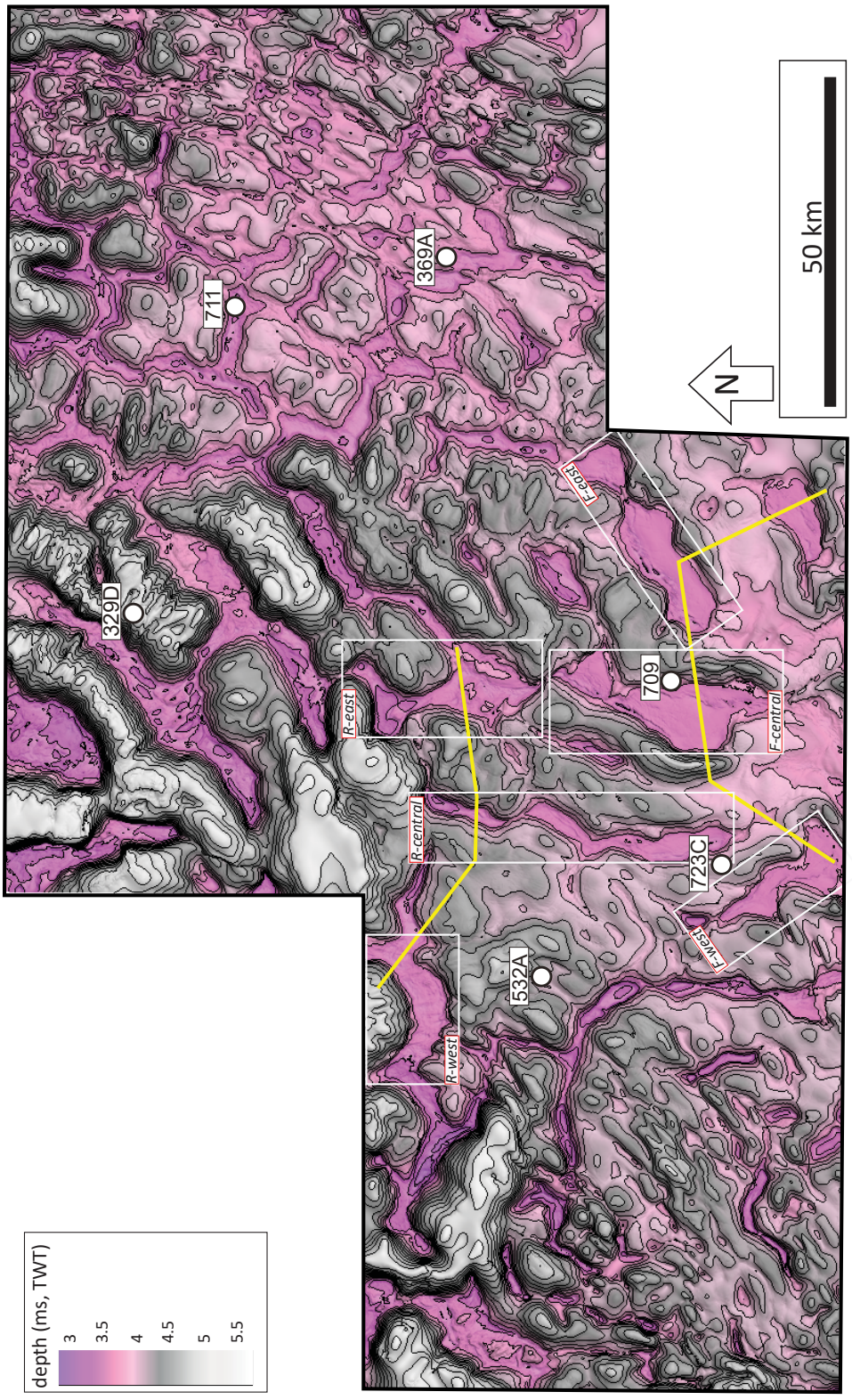


Figure 7.4a: Top salt structural map with locations of salt walls of interest

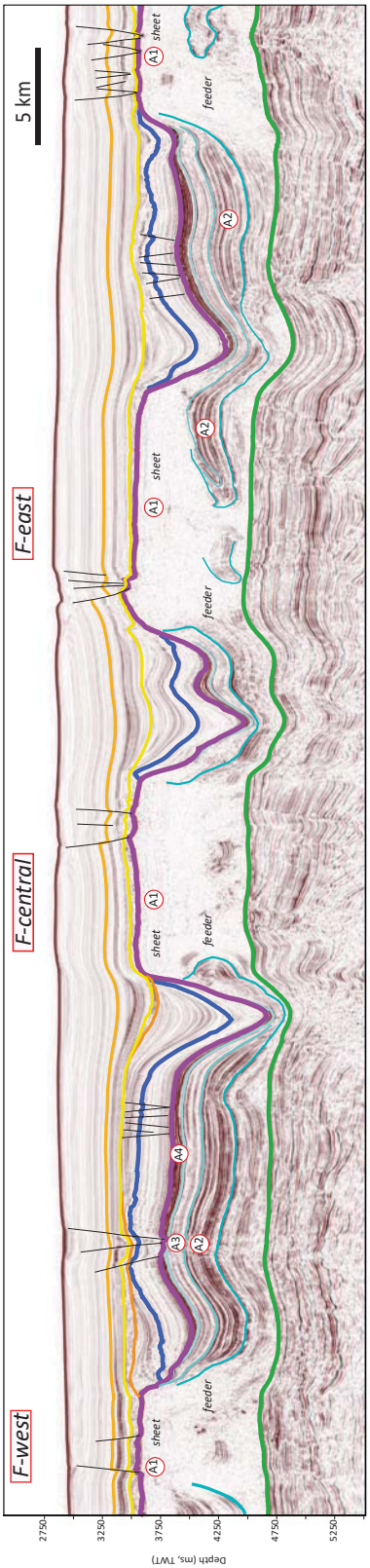


Figure 7.4b: Seismic section across salt diapirs with flat crests

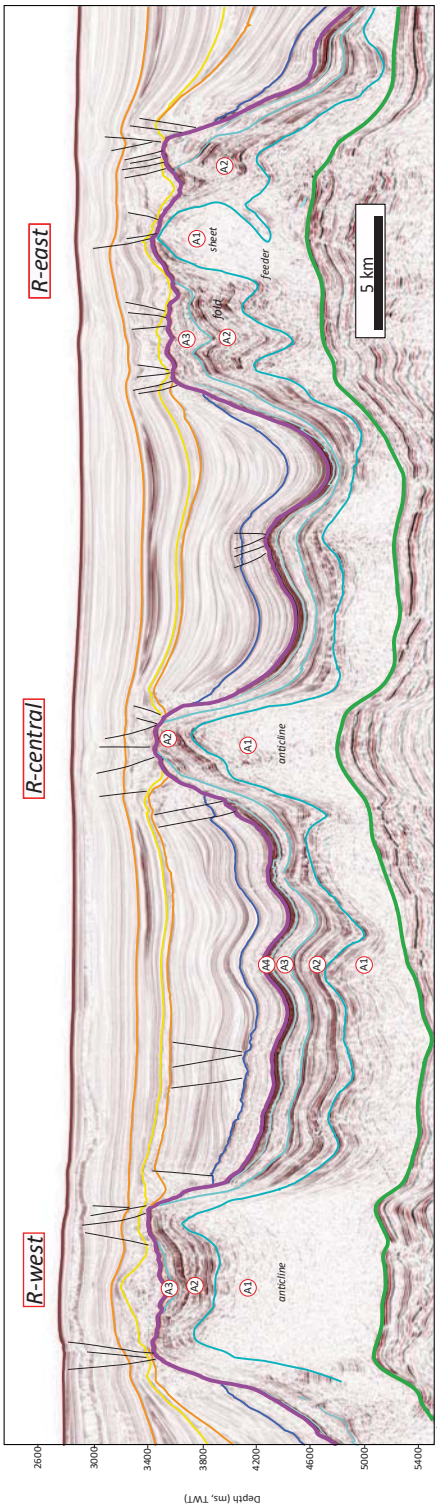


Figure 7.4c: Seismic section across salt diapirs with rounded and rugose crests

7.7 Top Salt and intrasalt stratigraphy

Seismic data show that the Top Salt is characterised by a high-amplitude and broadly continuous seismic event (Figs. 7.4 and 7.5). Along the flat crests, the Top Salt overlies poorly reflective, halite-rich, A1-allochtonous sheets (Table 7.2; Figs. 7.4a; see also Jackson et al.; 2015b). Conversely, along the rugose crests, the Top Salt exhibits mainly discordant geometrical relationships with highly reflective, interbedded A2 and low-to-moderate-amplitude halite-rich A3 (Table 7.3; Fig. 7.4b; Rodriguez et al. in press/Chapter 5). Boreholes penetrating the salt sequence indicate that the Top Salt correlates with an anhydrite layer varying in thickness from c. 12 metres and up to c. 56 metres (Fig. 7.5a).

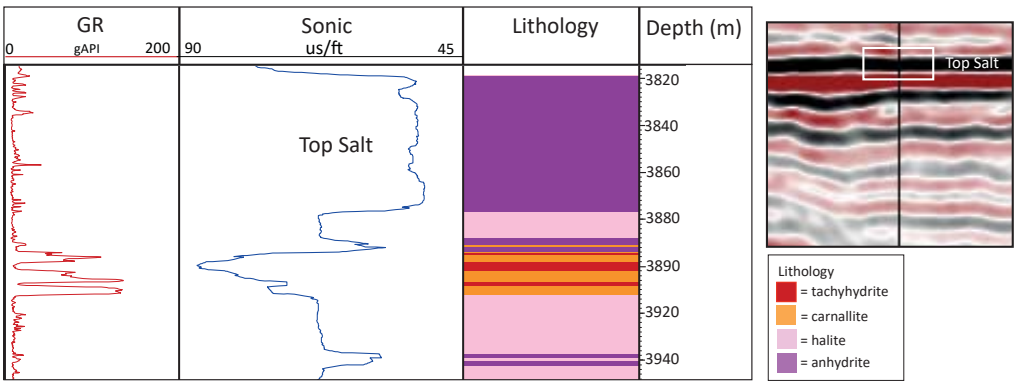


FIGURE 7.5 a: Top Salt lithology in a structurally-low and reltively undeformed area (borehole 532A)

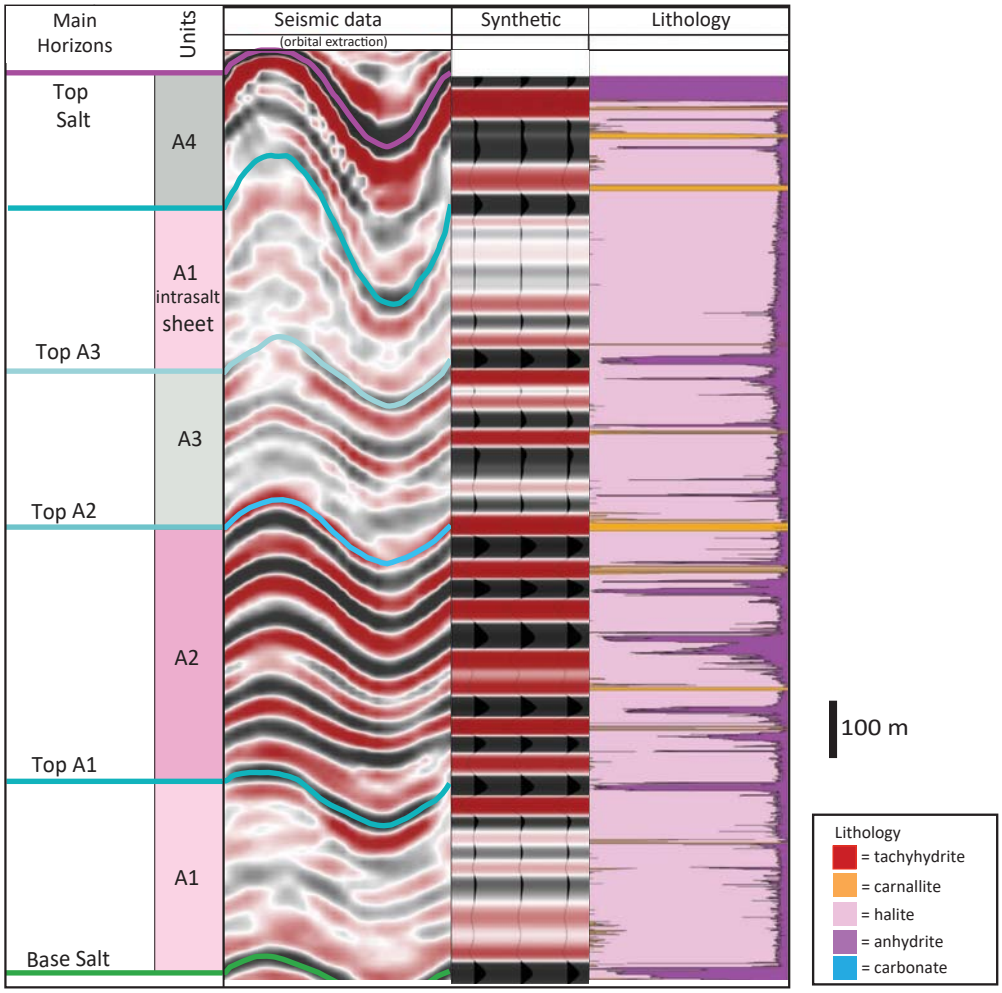


FIGURE 7.5 b: Intrasalt seismic expression and stratigraphy for borehole 709

7.8 Post-salt sedimentary overburden

Seismic data show the post-salt sequence in the distal ISPFB and SPP is characterised by low-to-moderate amplitude, continuous seismic reflections, except for Unit 3, which is defined by unconformity-bound wedges composed by moderate-to-high-amplitude, discontinuous to chaotic seismic facies (i.e., Maastrichtian-to-Palaeocene-age seismic unit on Fig. 7.6; see also Rodriguez et al. *in press*/ Chapter 6). Above the crests, Unit 3 is dominated by low-to-moderate amplitude reflections, although its seismic expression varies between salt diapirs; i.e., conformable continuous sheets, disrupted sheets with apparent downlap, mounded, rotated and chaotic (SF1-SF7; Table 7.2 and 7.3).

Rodriguez et al., *in press* (Chapter 6) shows that Unit 3 contains channel-levee and lobes complexes across the central deep-water Santos Basin. More specifically, Rodriguez et al., *in press* illustrate that submarine channels are present above *R-west* and above *R-central* and onlap and dip away from *F-west* and *F-central* (Figs. 6.15 and 6.22 in Chapter 6). In addition, seismic attributes at the top of Unit 3 indicate the occurrence of several SE-trending parallel and laterally extensive (c. 100 km long) linear features or grooves suggestive of a basin-scale event triggering the deposition of regional mass transport complexes, MTCs (Fig. 6.25, Rodriguez et al., in press, Chapter 6). These observations about the post-salt sedimentary overburden capping and flanking the salt diapirs is relevant when I later discuss the possible mechanisms of dissolution and the origin of the dissolving fluids (section 7.11.1).

Boreholes that penetrate the *ISPFB* and the *SPP* indicate that the post-salt succession is mostly dominated by fine-grained lithologies, predominantly mudstones and marls (boreholes 532A, 723C, 709, 594, Figs. 7.2, 7.6). However, a notable exception occurs on the eastern flank of a distal minibasin in the SPP, where Unit 1 and Unit 3 are characterised by interbedded siltstone, sandstone and mudstone (borehole 723C, Fig. 7.6). The salt diapir crests of interest are not penetrated by boreholes.

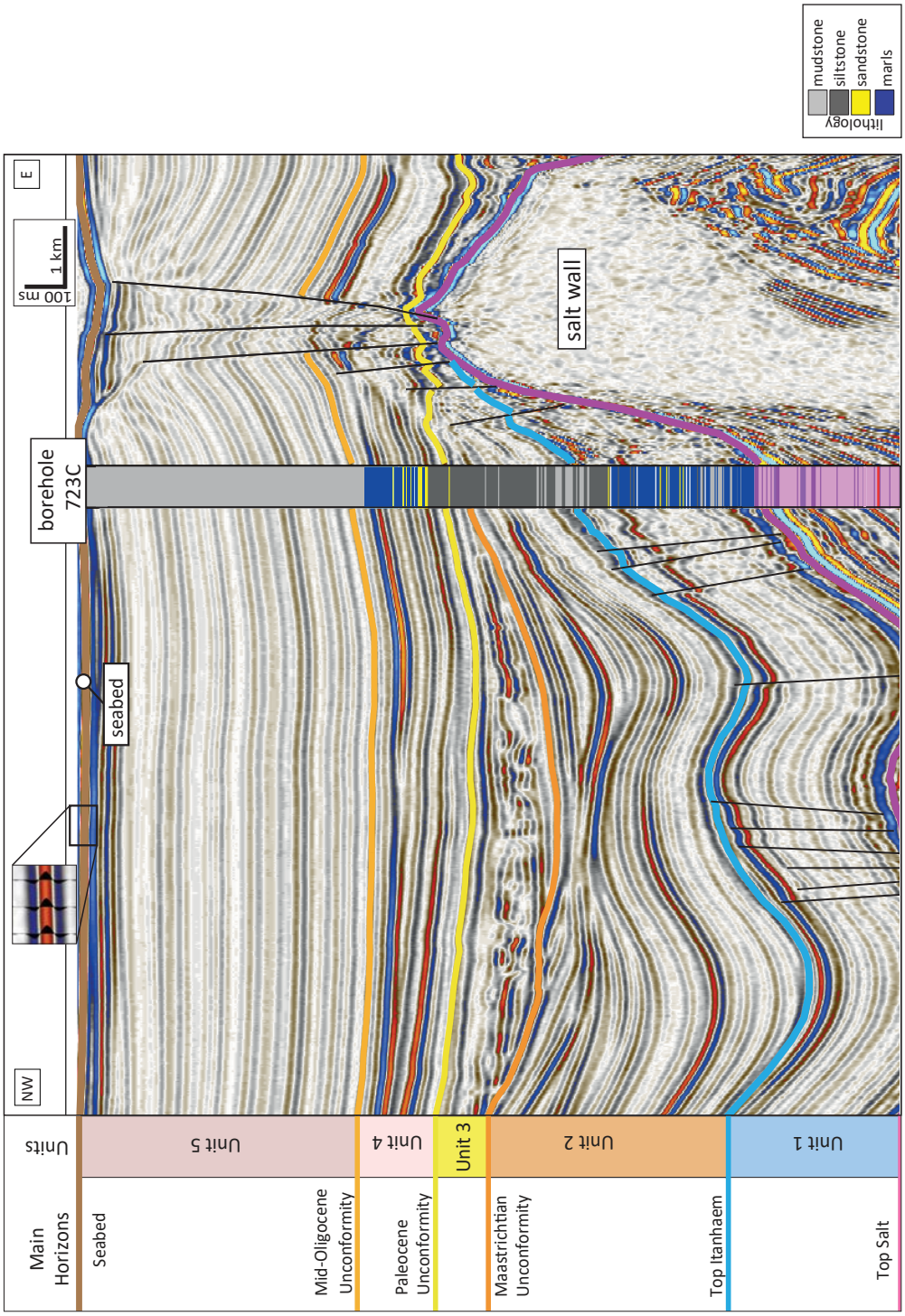


FIGURE 7.6: Overburden seismic expression and stratigraphy. Post-salt seismic-borehole tie

Table 7.2: Overburden seismic expression and thickness variations above dissolved flat crests.

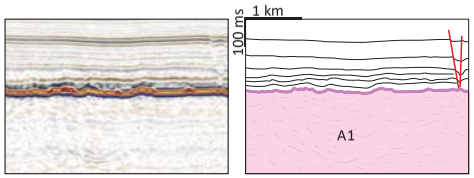
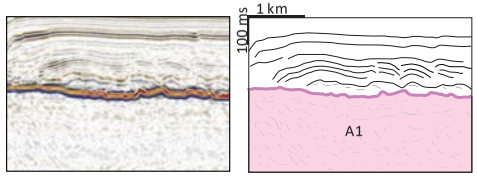
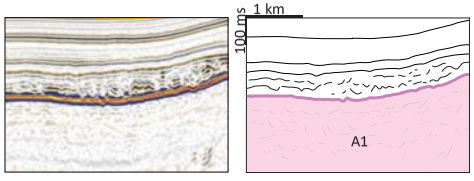
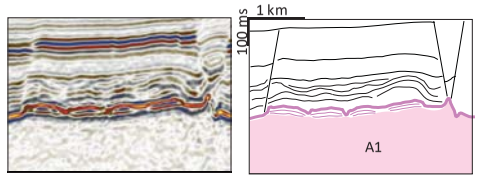
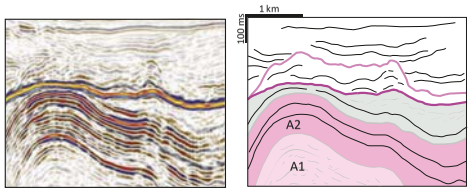
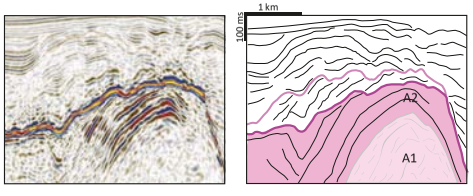
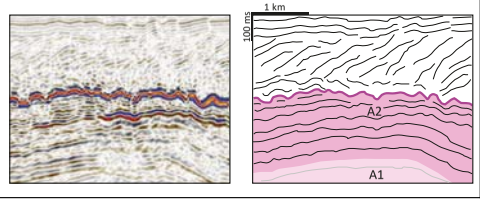
Seismic facies		External shape relationship to salt crests	Amplitude, continuity reflection configuration	Ocurrence	Thickness variations	Interpretation
SF1		sheet drape conformable to top salt	low-to-moderate amplitudes continuous parallel to sub-parallel	Flat crest - east Above A1-allocthonous intrasalt sheet	minor thickness variations c.± 50ms local depocenters up to c.80ms above lows on top salt	fine-grained lithology deposited on flat crest before dissolution post-depositional dissolution not too obvious at seismic scale
SF2		sheet to mound apparent downlap on top salt	low-to-moderate amplitudes semicontinuous to disrupted parallel to sub-parallel	Flat crest - central Above flat A1-allocthonous intrasalt sheet	minor thickness variations c.± 75 ms local depocenters up to c.125 ms above lows on top salt	fine-grained lithology deposited on salt crest before dissolution post-depositional dissolution led to local collapse and deformation within the overburden
SF3		sheet to wedge conformable & apparent downlaps on top salt	low-to-moderate amplitudes discontinuous wavy to chaotic	Flat crest - central Above lows on A1-allocthonous intrasalt sheet	minor thickness variations c.± 75 ms local depocenters up to c.125 ms above lows on top salt	fine-grained lithology deposited on salt crest before dissolution post-depositional dissolution led to local collapse and deformation within the overburden
SF4		sheet to mound conformable & apparent downlaps on top salt	moderate to high amplitudes semicontinuos subparallel to wavy	Flat crest - west Above discrete mounds on top salt	minor thickness variations c.± 100 ms local depocenters up to c.150 ms above lows on top salt	fine-grained lithology deposited on salt crest during dissolution syn-depositional dissolution led to local collapse and deformation within the overburden

Table 7.3: Overburden seismic expression and thickness variations above dissolved rugose crests.

Seismic facies	External shape relationship to salt crests	Amplitude, continuity reflection configuration	Ocurrence	Thickness variations	Interpretation
SF5 	mound sub-parallel to intrasalt stratigraphy onlapped by overburden	low-to-moderate amplitudes discontinous suparallel to wavy to chaotic	Rugose crest-central Above truncated A3 reflections	mounds are thicker where more evaporites depletion is evident	Interpretation1: residual solution breccia or caprock composed by less-soluble and insoluble intrasalt and overburden lithology (e.g, anhydrite carbonates, fine-grained sediments) Interpretation 2: Carbonate reef deposited after dissolution of the underlying crest
SF6 	mound sub-parallel and follow the dips of underlying intrasalt stratigraphy	low-to-moderate amplitudes discontinous suparallel to wavy	Rugose crest - east Above truncated and tilted A2 reflections	mounds are thicker where more evaporites depletion is evident	
SF7 	sheet downlapped by rotated overburden	low to moderate amplitudes chaotic subparallel to disrupted	Rugose crest - west Above truncated A2 reflections	overburden is thicker where more evaporites dissolution is evident	Dissolution at the crest led to rotation and collapse of the overbuden

7.9 Seismic expression of salt karst

Having described the broad external morphology of the crests of salt walls and the stratigraphy and seismic expression within the salt and the post-salt sedimentary overburden, I, here use high resolution (seismic grid spacing of 18.75 m x 25 m) top salt structural maps and seismic attributes to describe small-scale (<150 ms TWT tall; up to 2 km long) morphologies at the crests of salt walls and within the overburden. Furthermore, in this section I relate the observed local morphologies along the crests to the underlying variations in intra-salt lithology and overburden deformation patterns.

7.9.1 Salt dissolution-related sinkholes or dolines

In cross-section, the Top Salt is characterised by local depressions up to 50 ms, TWT deep (c. 100 metres deep) (Figs. 7.7 and 7.8). The depressions have steep or gentle sides and their bases are nearly flat (u-shaped) or concave-upward (v-shaped) (Figs. 7.7 c, d). I note that the bases of these depressions are characterised by lower sweetness attribute values along the Top Salt, suggesting variations in the composition (Figs. 7.7 d and 7.8 b). In contrast, although the chaos attribute has the lowest values (white colours) along the Top Salt, the seismic facies within the depressions are characterised by high chaos values similar to the post-salt sedimentary overburden (black) (Fig. 7.8 c).

In plan-form, these features define clustered or isolated, circular to oval-shaped depressions at the top of the salt diapirs, with diameters ranging from c. 50 to 500 m (Figs. 7.7 a, b). I note that these negative-relief features are easily recognised in plan-form by its characteristic high amplitude contrast attribute values (Fig. 7.7b). In terms of their spatial occurrence, these circular depressions (i) are best developed along diapirs characterised by rugose crests, (ii) underlie mounded-to-chaotic overburden (*SF6 and SF7*); and (iii) overlie A3 and truncated, dipping A4 (e.g., *R-west*, *R-central* and *R-east*; Table 7.3; Figs. 7.7, 7.8, 7.14a-c).

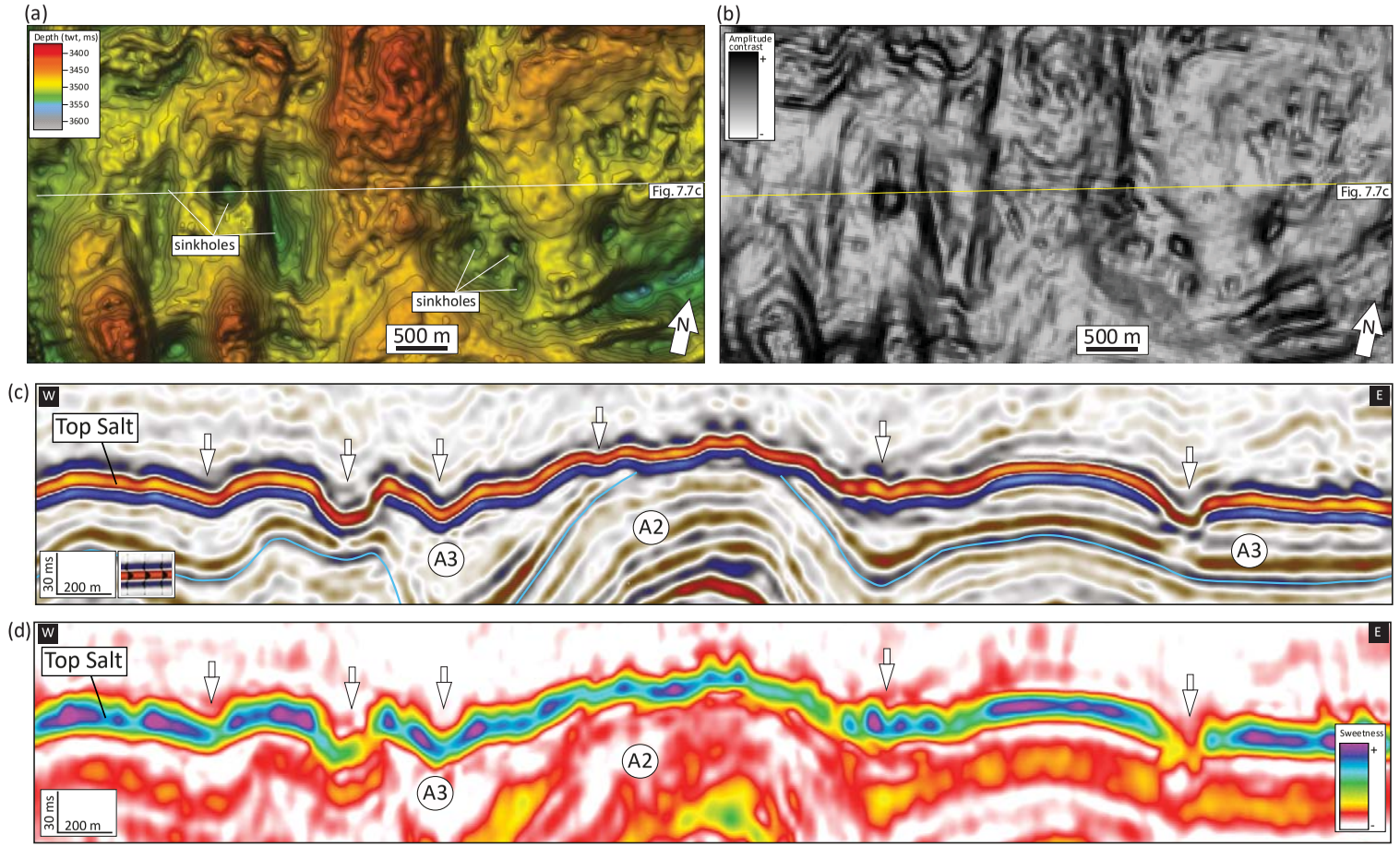


FIGURE 7.7: Seismic expression of sinkholes: (a) R-west top salt structural map. See Figure 7.14 a for location; (b) Amplitude contrast attribute map for R-west; (c) Seismic section along the crest of R-west illustrating the geometry of sinkholes (indicated by white arrows) and their relationship to A3 intrasalt stratigraphy. Location shown on Fig. 7.7 a and b; (d) Sweetness arrtibute of section on Figure 7.7c illustrating amplitude variaitons along the Top Salt.

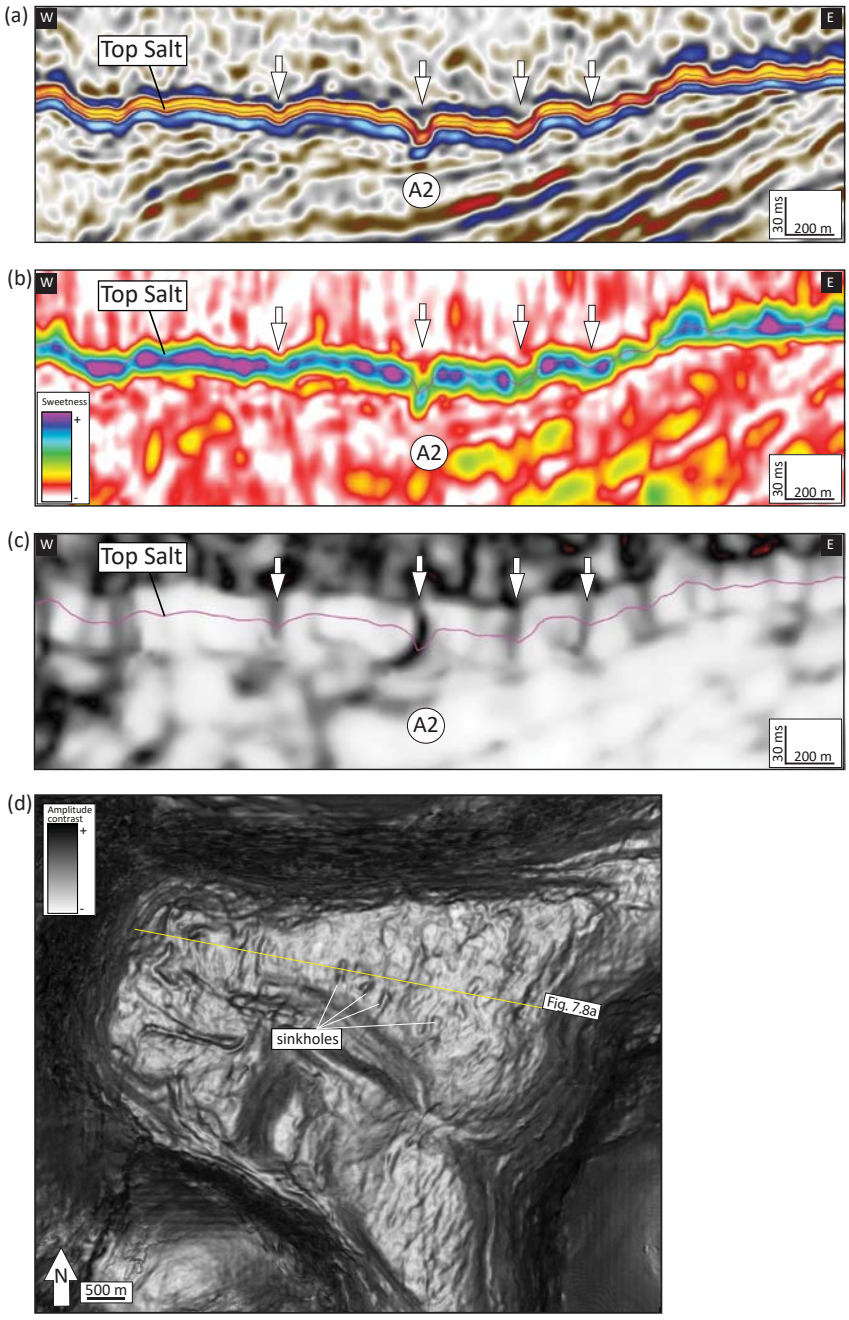


FIGURE 7.8: Seismic expression of sinkholes: (a) Seismic section along the crest of R-east illustrating the geometry of sinkholes (indicated by white arrows) and their relationship to dipping-A2 intrasalt stratigraphy. Location is shown on Fig. 7.8 d; (b) Sweetness arrtibute of section on Figure 7.8a illustrating amplitude variaitons along the Top Salt; (c) Chaos attribute of section on Figure 7.8a illustrating sinkholes along the Top Salt; (d) Amplitude contrast attribute map of R-east. See Figure 7. 14 c for location

Based on their seismic expression, geometry, scale and occurrence, I interpret these features as sinkholes or dolines that formed due to dissolution of the evaporite-dominated crests. My interpretation is also supported by comparison to notable examples from sedimentary basins in Spain and United States where surface and near-surface salt dissolution has also been documented (e.g., Elorza and Santolalla, 1998; Johnson, 2005, 2008; Gutiérrez et al., 2008; Galve et al., 2009). Furthermore, my analysis suggest that the intrasalt stratigraphic variability along the crests of the salt walls (*R-west, R-central* and *R-east*) led to the preferential dissolution and development of sinkholes mainly above the more soluble halite rich A3 interval and atop dipping, heterogeneous A2 (Figs. 7.7 c, 7.8 a and 7.14 a-c). I further infer that the dissolution sinkholes, atop dipping, heterogeneous A2, form due to the preferential dissolution of the more soluble halite and carnallite. In addition, I interpret that the development of sinkholes due to dissolution along the crests led to the collapse, rotation and foundering of the strata immediately above the Top salt (e.g., SF6 and SF7; Table 7.3).

7.9.2 Residual mounds

In cross-section, local positive-relief features are identified along the Top Salt (Figs. 7.9a, 7.10a and 7.11a). These features have a relief of up to 50 ms, TWT (c. 100 metres) and are defined by steeply-dipping to vertical walls and smooth or rugose tops (Figs. 7.9a, 7.10a and 7.11a). I note that, in contrast to the negative-relief sinkholes described above, these features are characterised by variable sweetness attribute values along the top salt (Figs. 7.9b and 7.10c). In addition, these mounds are bounded by high chaos attribute values, representing discontinuities along the top salt and in the overburden (Fig. 7.10b).

In plan-form these features define clustered or isolated, sub-circular, elongate or irregular mounds with dimensions ranging from 50 m to 500 m in diameter (Figs. 7.9 c; 7.10 d and 7.11 b). Similary to the sinkholes described above, these mounds are easily identified in plan-form by the high amplitude contrast attributes values that characterise them (Figs. 7.9 d and

7.11 c). These positive-relief features are most evident where they appear in clusters below semi-continuous to disrupted strata (*SF1, SF2* and *SF4*) and above poorly-reflective, A1-allocthonous-sheets (e.g., *F-west*, *F-central* and *F-east*; Table 7.3; Figs. 7.9-7.11, 7.14d-f). In addition, some isolated mounds are also found along the rugose crests, overlying poorly-reflective A3 and highly-reflective A2 and underlying mounded-to-chaotic overburden strata (e.g, *SF5*, *R-central*; Fig. 7.14b).

Based on their geometry, scale and occurrence, I interpret these positive-relief features as salt dissolution-related karst mounds or karst towers. I suggest that the clusters of salt karst mounds represent a local caprock formed by the enrichment of less-soluble and insoluble intrasalt residuals resulting from the dissolution of the halite-rich A1-allochthonous-sheets (Figs. 7.9-7.11; e.g., Posey and Kyle, 1988; Warren, 1997; Kyle and Posey, 1991; Hovorka, 2000; Jaworska and Novak, 2013; Jackson and Hudec, 2017). I suggest that the more isolated, salt karst mounds rising above the rugose crests represent the remains of the partial dissolution of A4 and A3 in the upper parts of intrasalt anticlines (Fig. 7.11). My interpretation is also supported by comparison to notable examples of gypsum- or carbonate-dominated residual karst hills or mounds from sedimentary basins where dissolution have also been documented (e.g., Stafford et al., 2008, Chiesi et al., 2010; Zeng et al.; 2011).

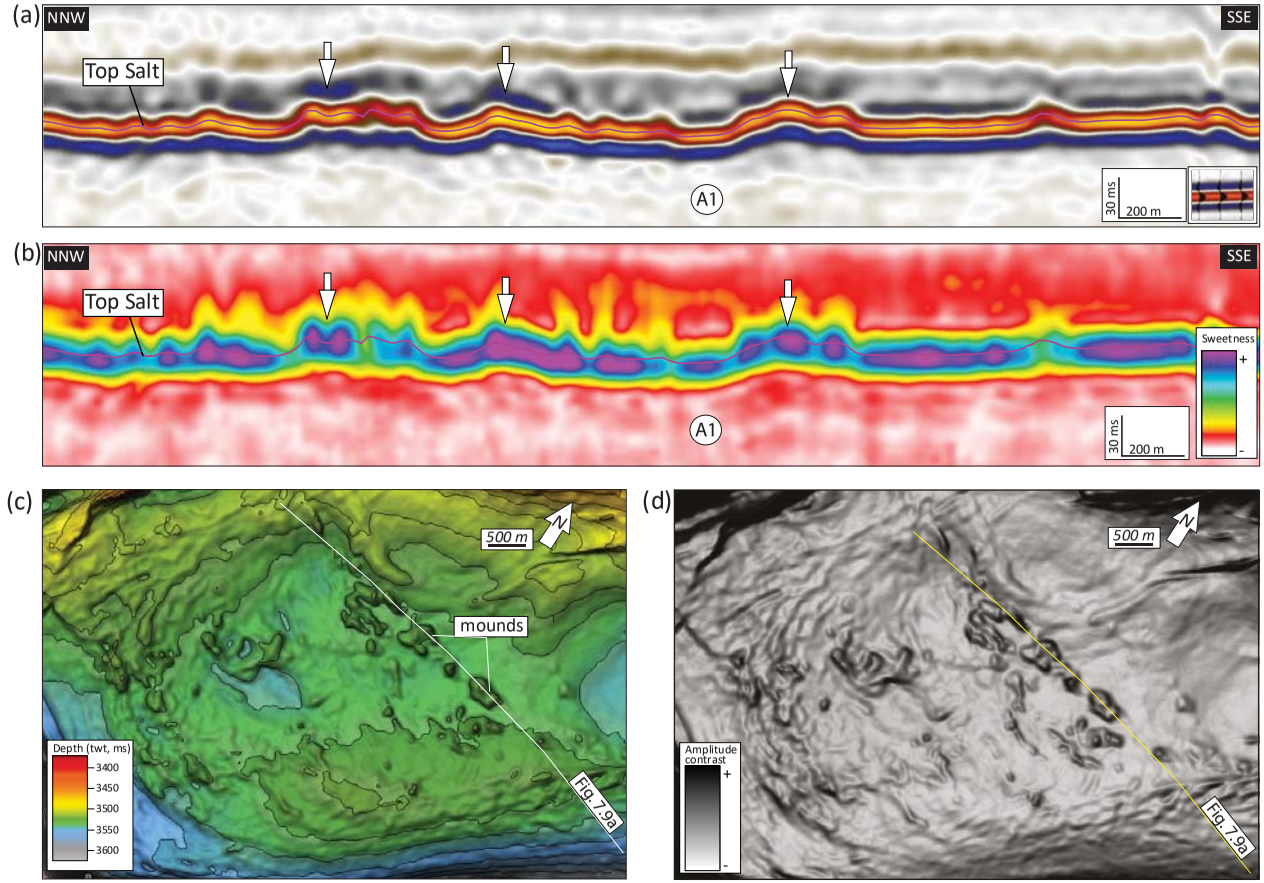


FIGURE 7.9. Seismic expression of residual mounds: (a) Seismic section along the crest of F-east illustrating residual mounds above the main top salt level (mounds are indicated by white arrows), See Figure 7.9 c and d for location; (b) Sweetness attribute for section on Figure 7.9 a illustrating facies variations along the Top Salt; (c) Top Salt structure map for F-east. See Figure 7.14 f for location; (d) Amplitude contrast attribute map for F-east Top Salt highlighting residual mounds above the nearly-horizontal Top Salt.

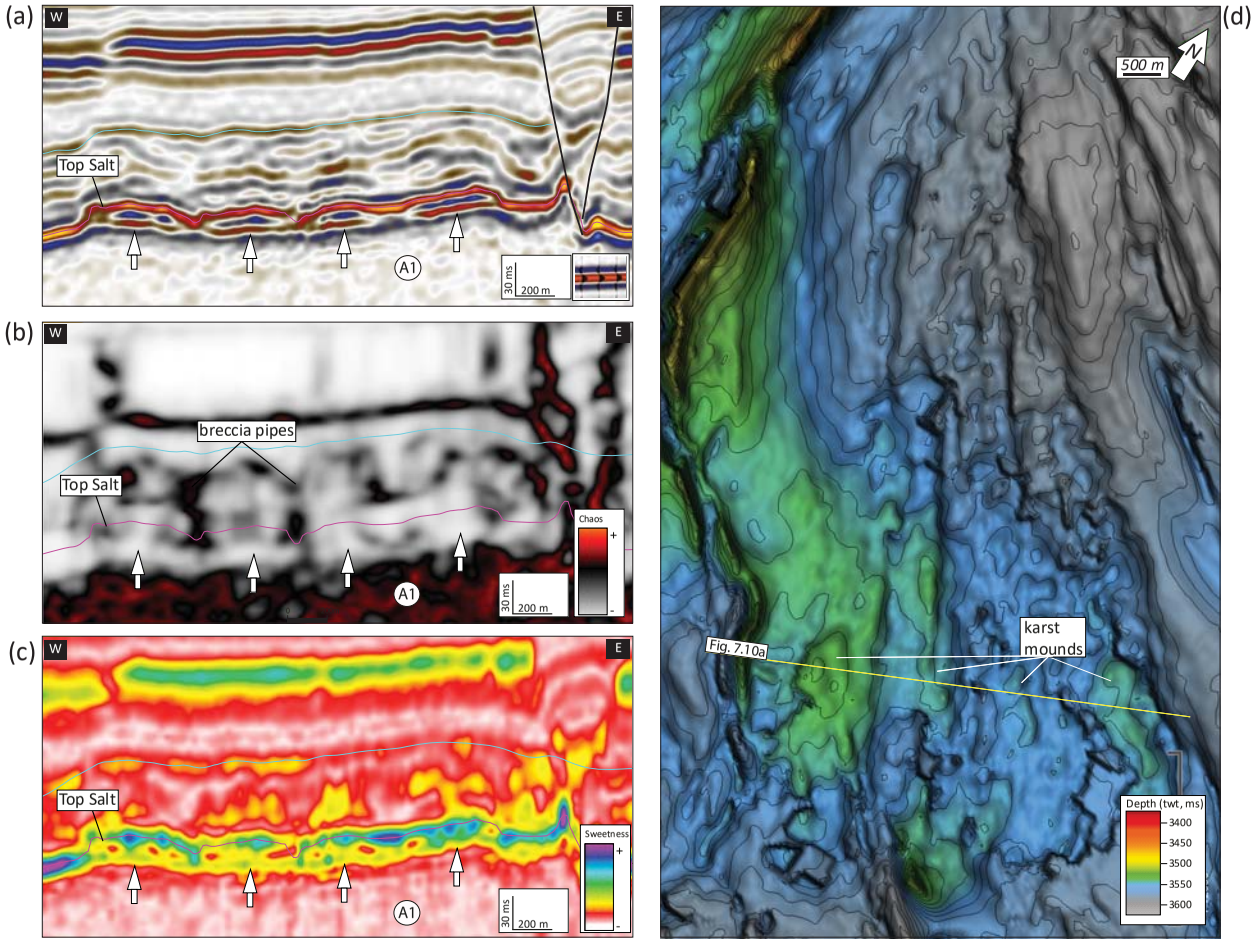


FIGURE 7.10. Seismic expression of residual salt karst-related mounds. (a) Seismic section along the crest of F-west illustrating residual mounds defined by highly-reflective packages along the Top Salt (mounds are indicated by white arrows). See location on (d); (b) Chaos attribute for seismic section on (a) highlighting the discontinuities along the Top Salt and within the overburden; (c) Sweetness attribute for section on (a) illustrating the facies variations within the mounds; (d) Top Salt structural map for F-west. See Fig. 14.d for Location

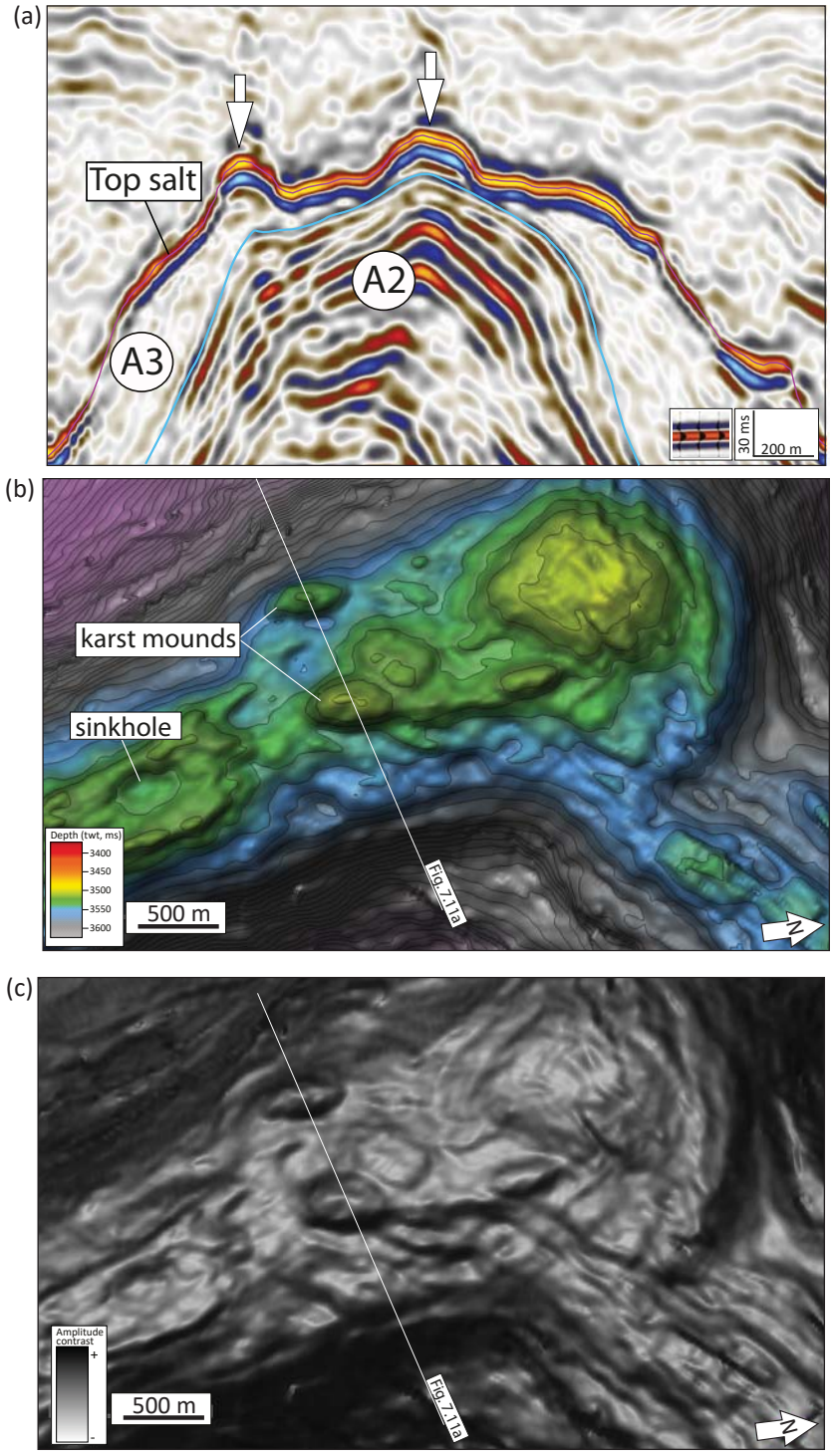


FIGURE 7.11. Seismic expression of residual salt karst-related mounds. (a) Seismic section across mounds on R-Central salt diapir illustrating remnant mounds after A3 dissolution. See (b) and (c) for location; (b) Top Salt structural map for R-Central. See Fig. 14b for location; (c). Amplitude contrast attribute map highlighting the location of residual mounds.

7.9.3 Breccia pipes or chimneys and associated sinkholes

In cross-section, the overburden is disrupted by multiple, parallel to sub-parallel pipes. These pipes are defined by downward-deflected v-shaped depressions up to c. 150 ms (TWT) tall (Fig. 7.12 a). These pipes cross-cut the overburden strata defining apparent downlaps on the Top Salt (SF2, Table 7.2). The vertical discontinuities within the overburden are defined by high chaos and relatively low sweetness attribute values (Figs. 7.12 b, c).

In plan-form these features define parallel to sub-parallel linear depressions containing multiple, aligned, sub-circular to oval-shaped discrete hollows (Figs 12d, e). The linear features are up c. 2 km long and up to c. 200 metres wide and the discrete depressions within are up to c. 200 metres long and c. 100 metres wide. The edges of the pipes are identified by a characteristic high variance attribute in plan-form (Fig. 7.12e). In terms of its occurrence, these pipes are more evident on *F-central* and in less extent on *F-east*, *F-west* and *R-west*. Overall, I note that the pipes within the overburden are aligned at depth with steps along the Top Salt (e.g., Figs.7.10b; 7.12a and 7.13 c, d).

Based on their geometry, scale and occurrence, I infer that these pipes are formed by local subsidence or collapse of the overburden above the dissolving salt crests. Hence, I interpret these features as dissolution-related breccia pipes or chimneys capped by subsidence sinkholes in the uppermost strata. I infer that these chimneys are likely to be filled with insoluble collapse breccia sediment, however, seismic resolution and lack of borehole data at this location does not allow me to confirm this. The downward flexure defining the pipes die-out upwards; thus, this allows me to estimate the approximate timing of collapse; i.e., Late-Maastrichtian-to-Paleocene-age (Figs 7.10b and 7.13 c, d). The approximate timing of dissolution-related collapse is also constrained by the horizon onlapping the uppermost subsidence sinkholes, which cap the breccia pipes (e.g. Fig. 13 c, d). Similar dissolution-related downward deflected disruptions have been previously illustrated on 2D and 3D seismic reflection data in carbonate- and evaporite-dominated basins (e.g. Hardage et al., 1996; Bertoni and Cartwright, 2005;

Burberry et al., 2016). These authors interpret that the disruptions are caused by karts pipes or chimneys. However, only Bertoni and Cartwright (2005) uses 3D seismic reflection data to clearly illustrate a direct link between the formation of collapse pipes and related sinkholes with the depletion of underlying salt-dominated stratigraphy.

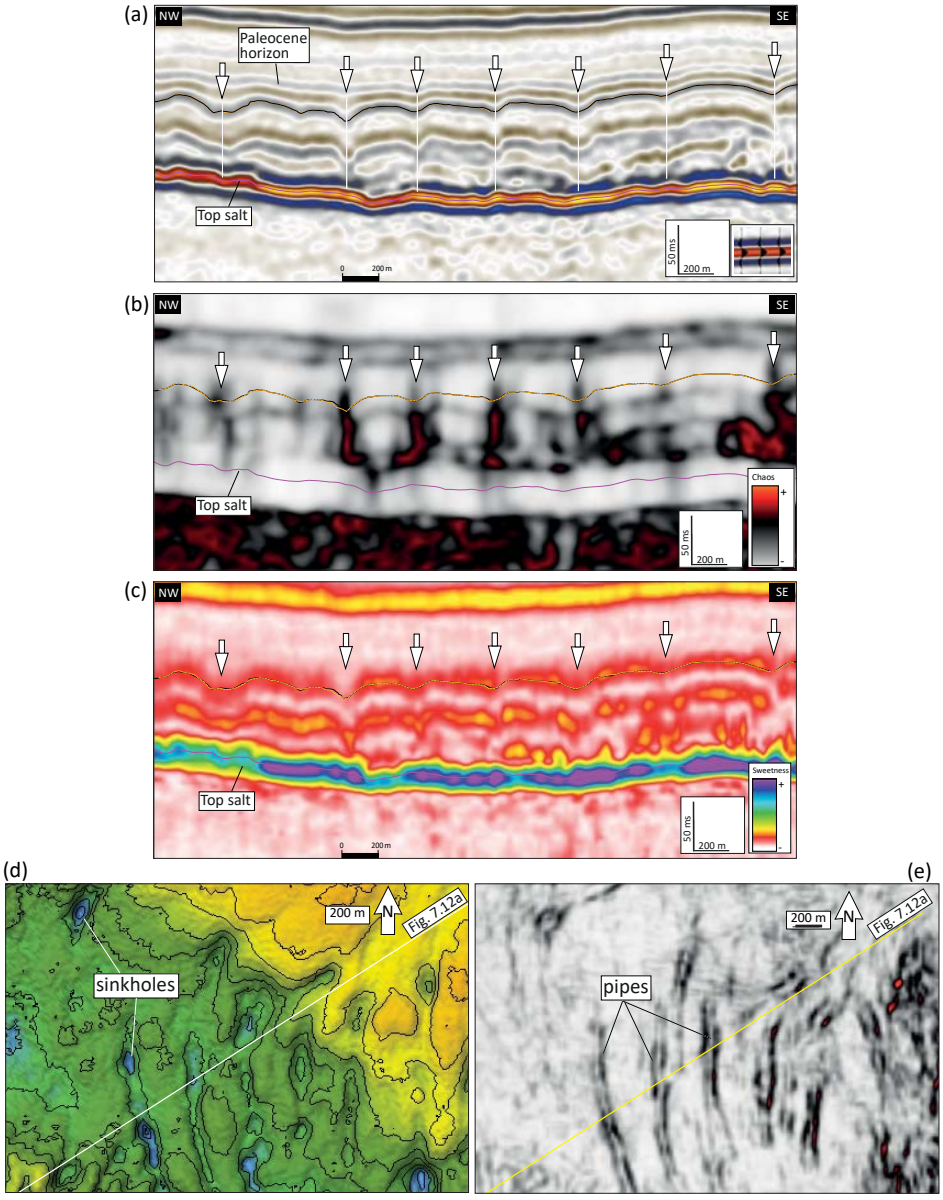


FIGURE 7.12: Seismic expression of collapse breccia pipes indicated by the white arrows. (a) Seismic seccion across F-central illustrating local collapse within the overburden. (b) Chaos attribute of seismic section on (a) highlighting breccia pipes (c) Sweetness attribute of seismic section on (a) highlighting discontinuities along the Top Salt/caprock. (d) Map of intra-Unit 3 horizon illustrating the pipes in plan-form. (e) Variance attribute map of intra-Unit 3 horizon on (d).

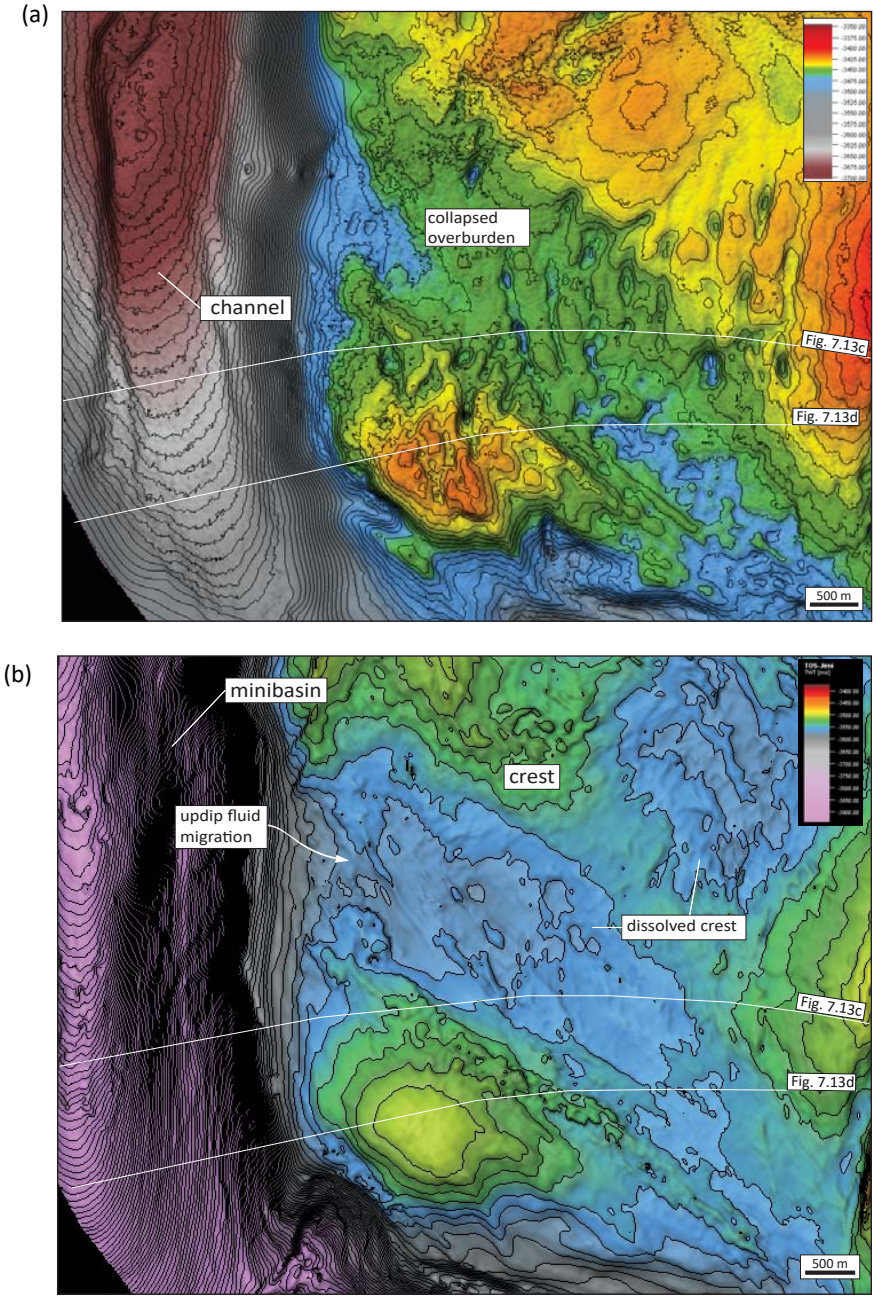


FIGURE 7.13: (a) Map of intra-Unit 3 horizon showing deformation within the overburden/roof above F-central. (b) Map of Top Salt for F-central illustrating dissolution of the crest

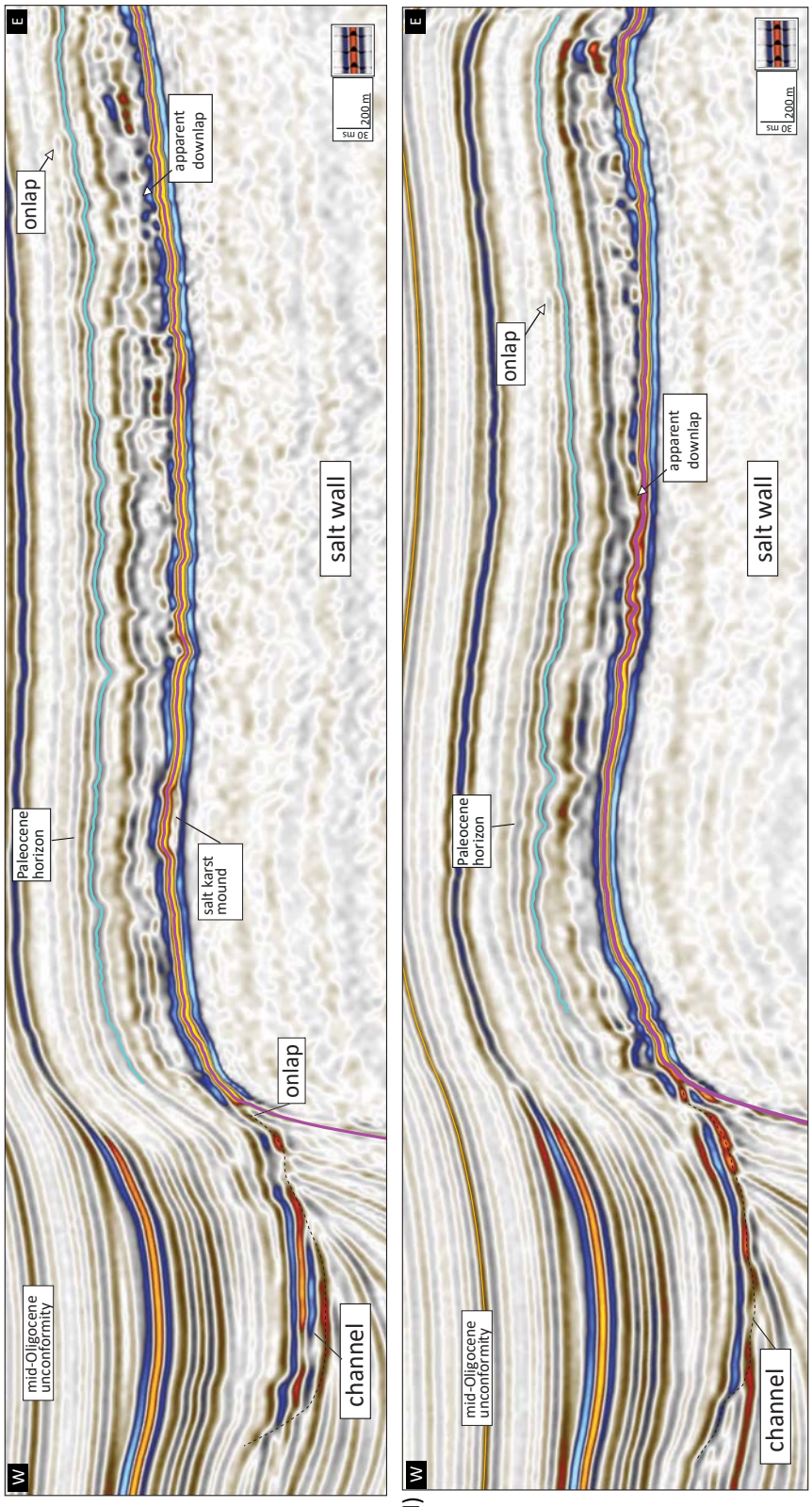


FIGURE 7.13. (c) and (d): Seismic sections across F-central showing flanking minibasin and channel.

Figure 14a
R-west Top Salt

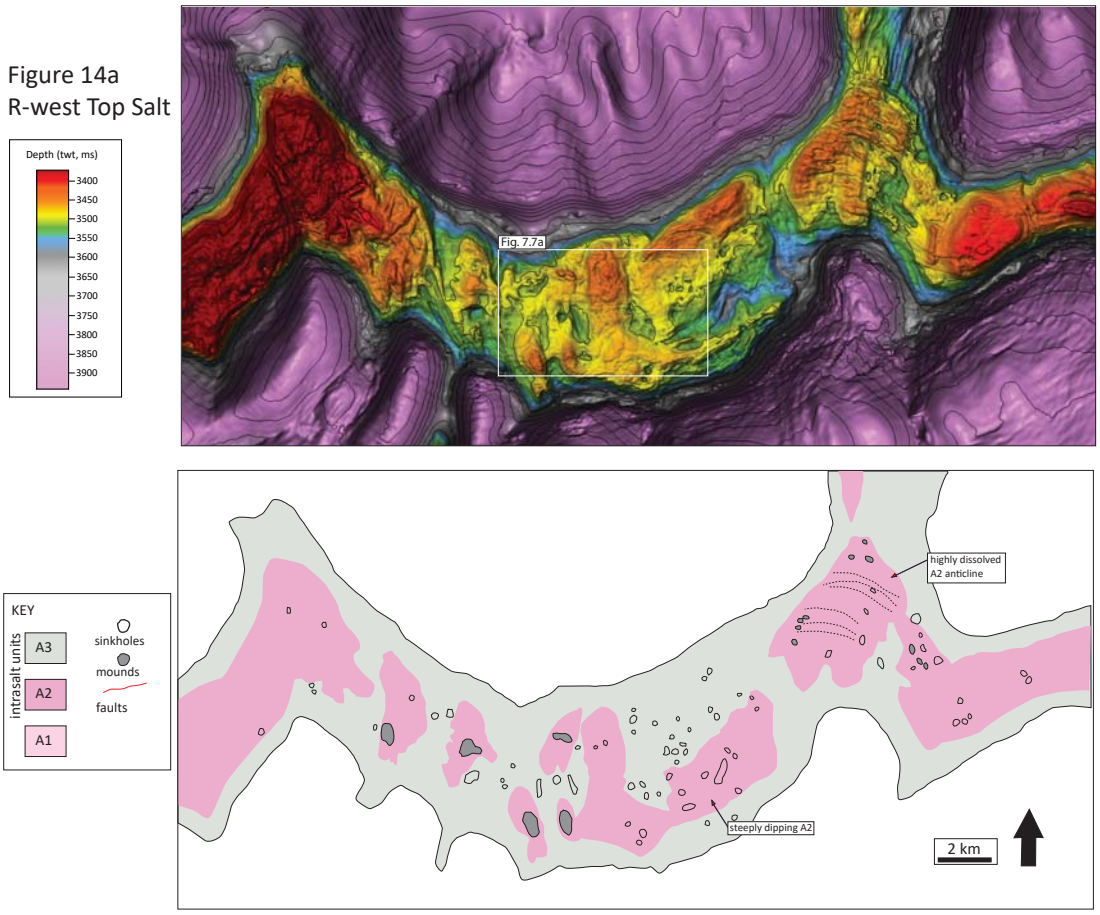


Figure 14b
R-central Top Salt

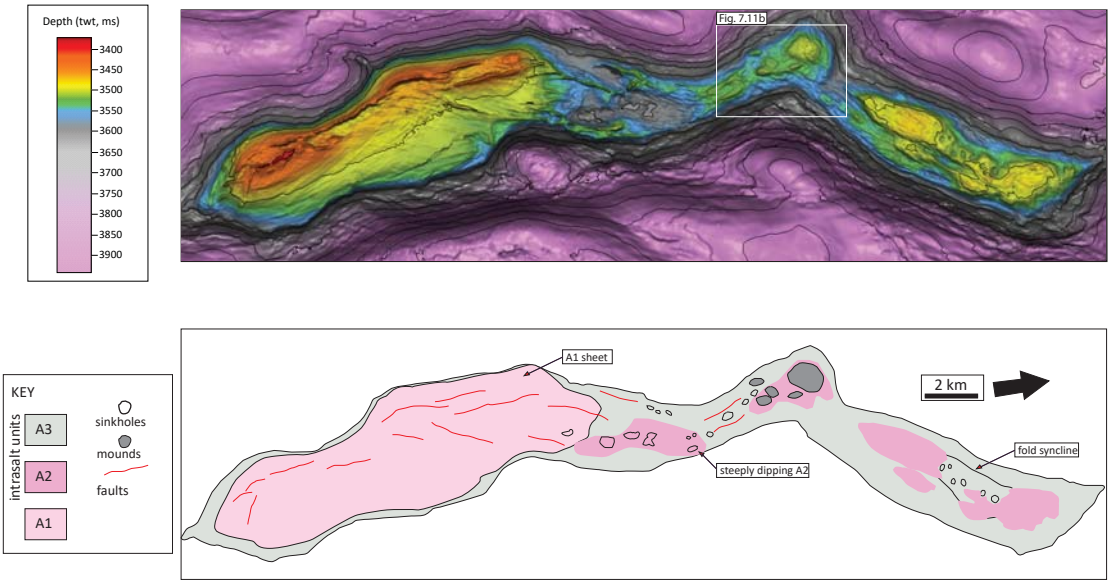


Figure 14c
R-east Top Salt

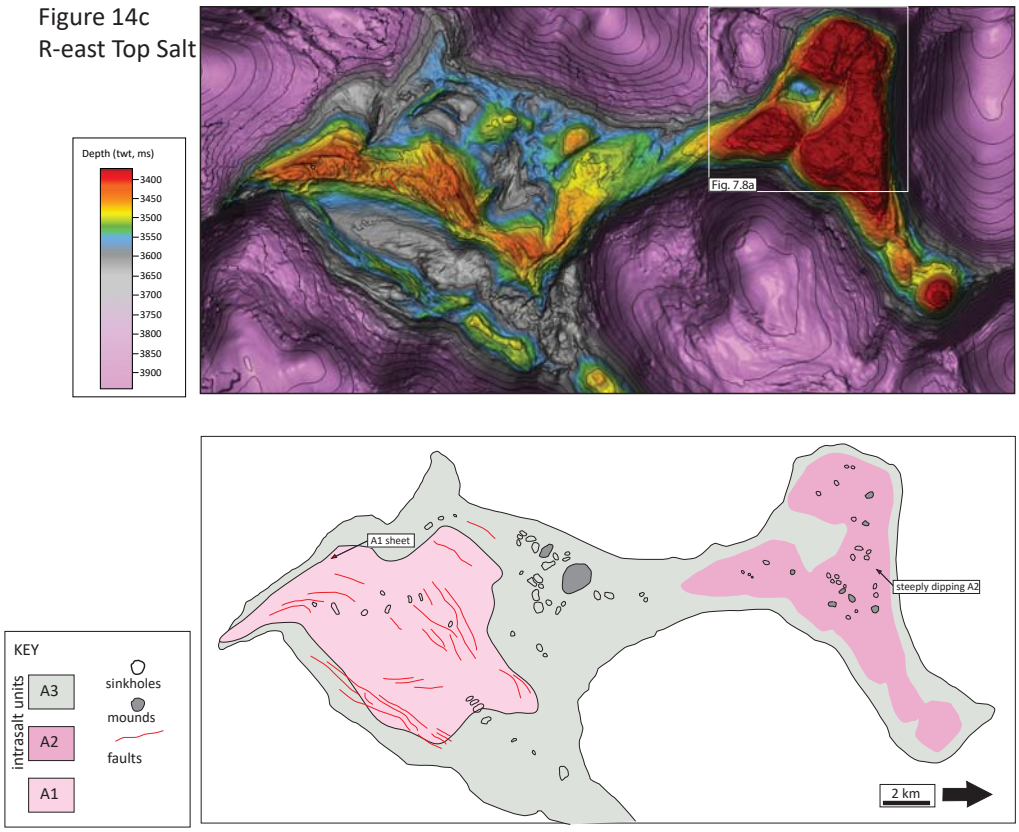


Figure 14d
F-west Top Salt

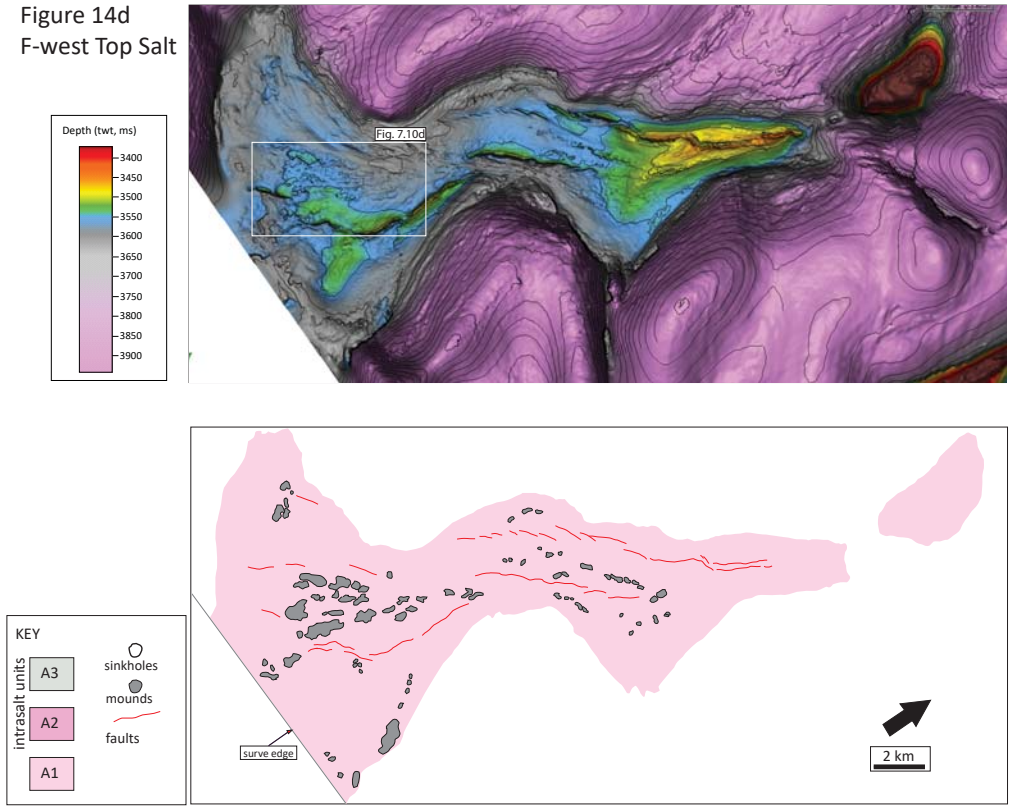


Figure 14e
F-central Top Salt

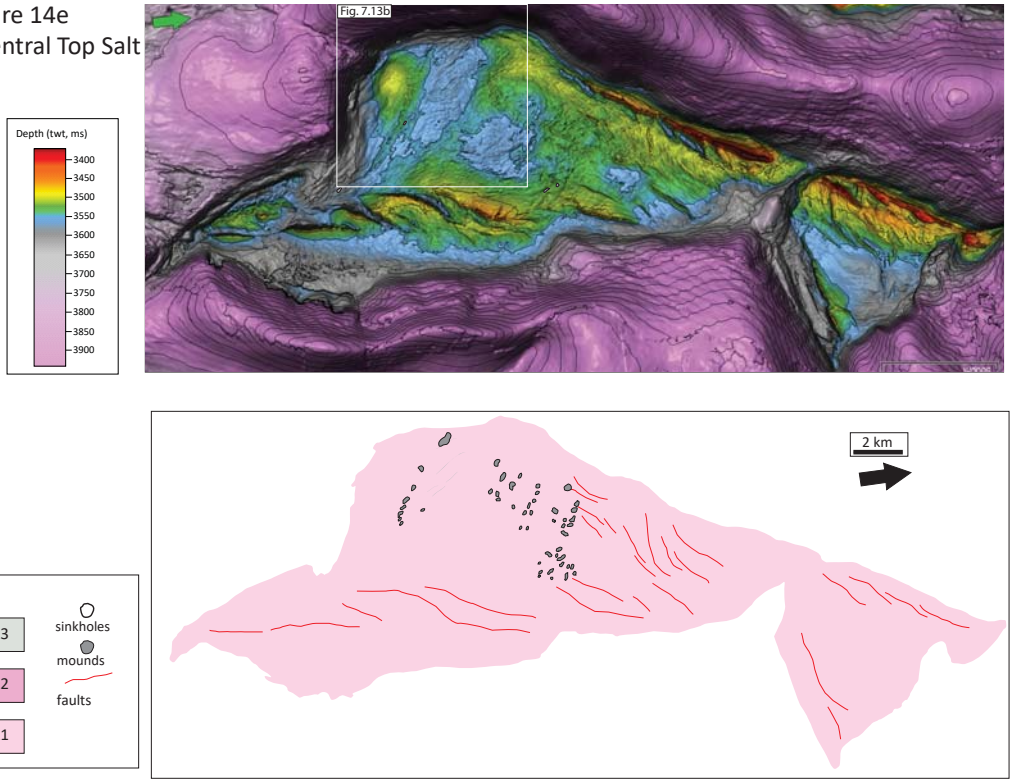
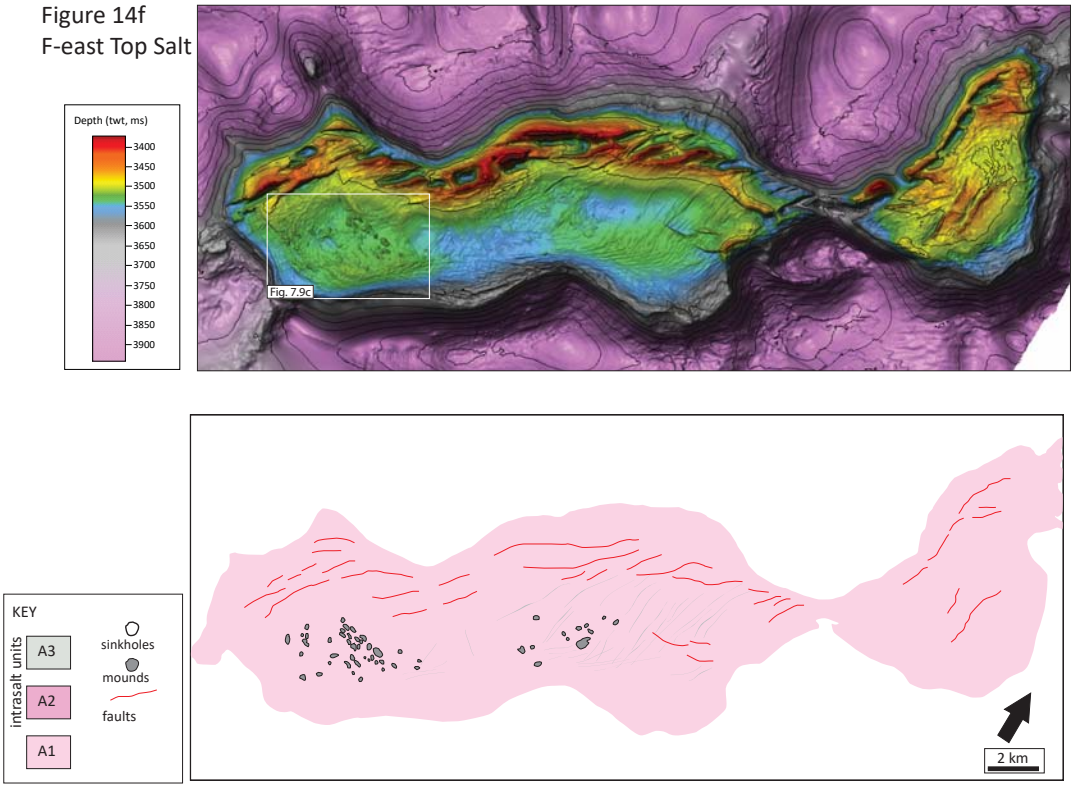


Figure 14f
F-east Top Salt



7.10 Subaerial or submarine salt dissolution?

I have illustrated some clear evidence of salt dissolution at the crest of salt diapirs in central deep-water Santos Basin. Furthermore, deformation within the overburden (Tables 7.2 and 7.3) and its relationship with salt karst (section 7.9) suggest that dissolution at the crests occurred in subterranean conditions, under a fine-grained roof up to c. 60 metres thick (e.g., Figs. 7.10, 7.12 and 7.13). However, it is still uncertain if the salt-cored highs were under subaerial, or submarine conditions when dissolution occurred. In this section, I constrain the likely paleowater depths at which dissolution occurred.

The following observations provide the associated key constrains on the basin restoration and estimations of paleowater depths. The approximate timing of collapse of the breccia pipes (section 7.9.3) is constrained by the uppermost downward flexure within the deformed overburden (Figs 7.10 and 7.13 c, d). Furthermore, the uppermost sinkholes capping the breccia pipes are onlapped by, I estimate, an intra-paleocene-age seismic horizon (e.g; Fig. 13 c, d). Therefore, based on seismic interpretation and borehole data available I infer that salt dissolution occurred in the Paleocene, just after deposition of Unit 3 (Fig. 7.6). In Chapter 6, I demonstrate that the Late Maastrichtian-to-Paleocene Unit 3 is dominated by submarine channels, levees and associated lobes which were deposited confined within distal minibasins in the Sao Paulo plateau (Fig. 6.15). Furthermore, my interpretation illustrates that the salt diapirs flanking (e.g., *F-west*, *F-central* and the southern part of *R-central*) formed highs at the seabed which deflected and confined deep-water depositional systems (minibasins K, M; Fig. 6.15; Chapter 6). Moreover, interpretation suggest that submarine channels flowed above R-west and the northern part of R-central salt walls spilling from proximal minibasins (Figs 6.15, Chapter 6).

Hence, based on the stratigraphic context illustrated in Chapter 6, and previous studies of the Santos Basin (e.g., Modica and Brush, 2004; Moreira et al., 2007; Guerra and Underhill, 2012),

I infer that the subaerial exposure of the salt-cored highs was unlikely in the study area. However, reconstruction of the basin to the Paleocene can provide further constrains about the paleowater depths at which salt dissolution occurred. The reconstruction is needed to rule-out the possibility of subaerial exposure, as it has been documented in other salt basins (e.g.; the Zechstein salt in the North Sea; Clark et al., 1998; Cartwright et al., 2001 and Texas salt diapirs; Jackson and Seni, 1984, Hudec and Jackson, 2011).

The basin reconstructions for the 2D seismic depth profile are shown on Figures 7.15 b-e. These restorations satisfy the crustal and sediment key input parameters for the central deep-water Santos Basin discussed in the Methods section and shown in Table 7.1. To estimate the paleowater depths at the top of Unit 3, the effect of sediment load and post-rift thermal subsidence during Unit4 and Unit 5 deposition are removed (Fig. 7.15). The removal of Unit 4 and Unit 5 results in the decompaction of the remaining layers and illustrates the basin geometry at the end of deposition of Unit 3 (Figs. 7.15 b-d). Here, I present two restorations based on the minimum and maximum β estimate profiles by Scotchman et al. (2006, 2010) (Figs. 7.15 f, g). The restoration to the top of Unit 3 predicts variable water depths for the crest of salt structures across salt-related structural domains (Figs. 7.15 d, e). However, regardless of the β factor, the salt-cored highs are always submarine. The predicted palaeowater depths at the salt-cored highs vary between 1800 and 2000 metres (*R-west* and *F-west*, Fig. 7.15 b). Thus, the basin reconstructions performed along the 2D seismic profile restore the crests of salt structures to palaeowater depths of 1900 m ± 100 m; hence suggesting that dissolution occurred in a fully submarine setting (Fig. 7.15).

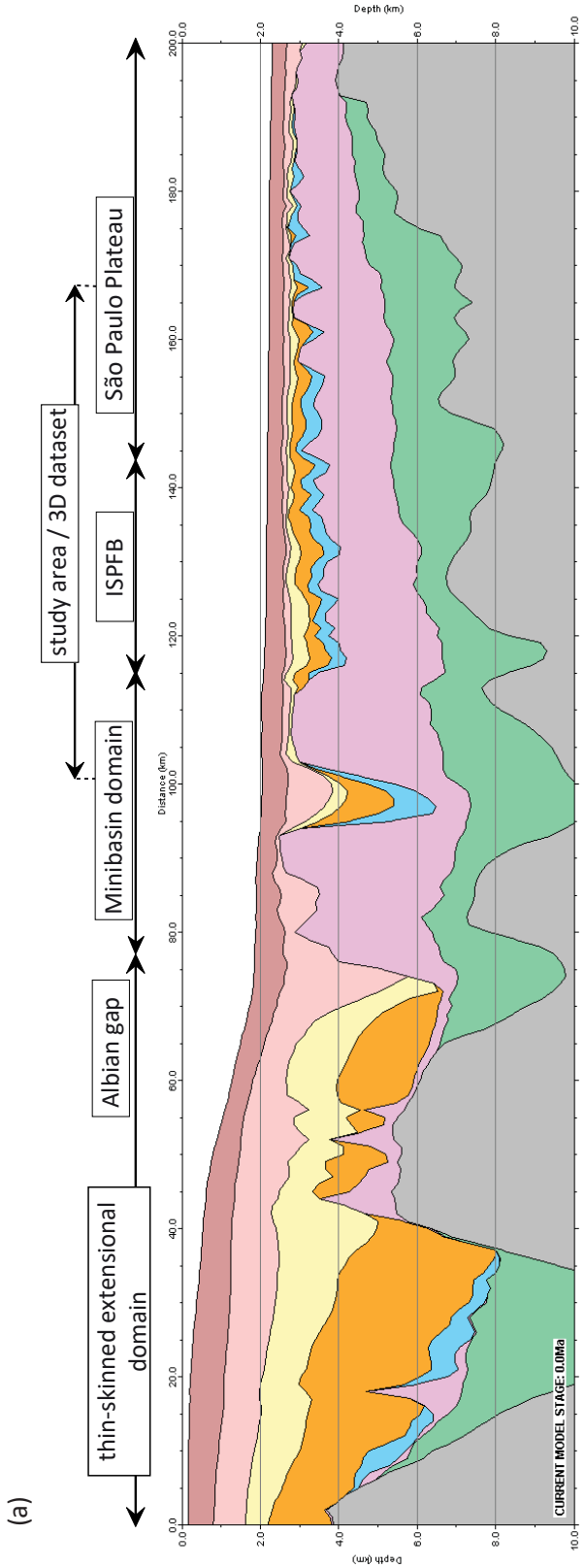


FIGURE 7.15: (a) Model used for basin restoration based on interpretation of 2D seismic profile. see Key on Figure 7.3

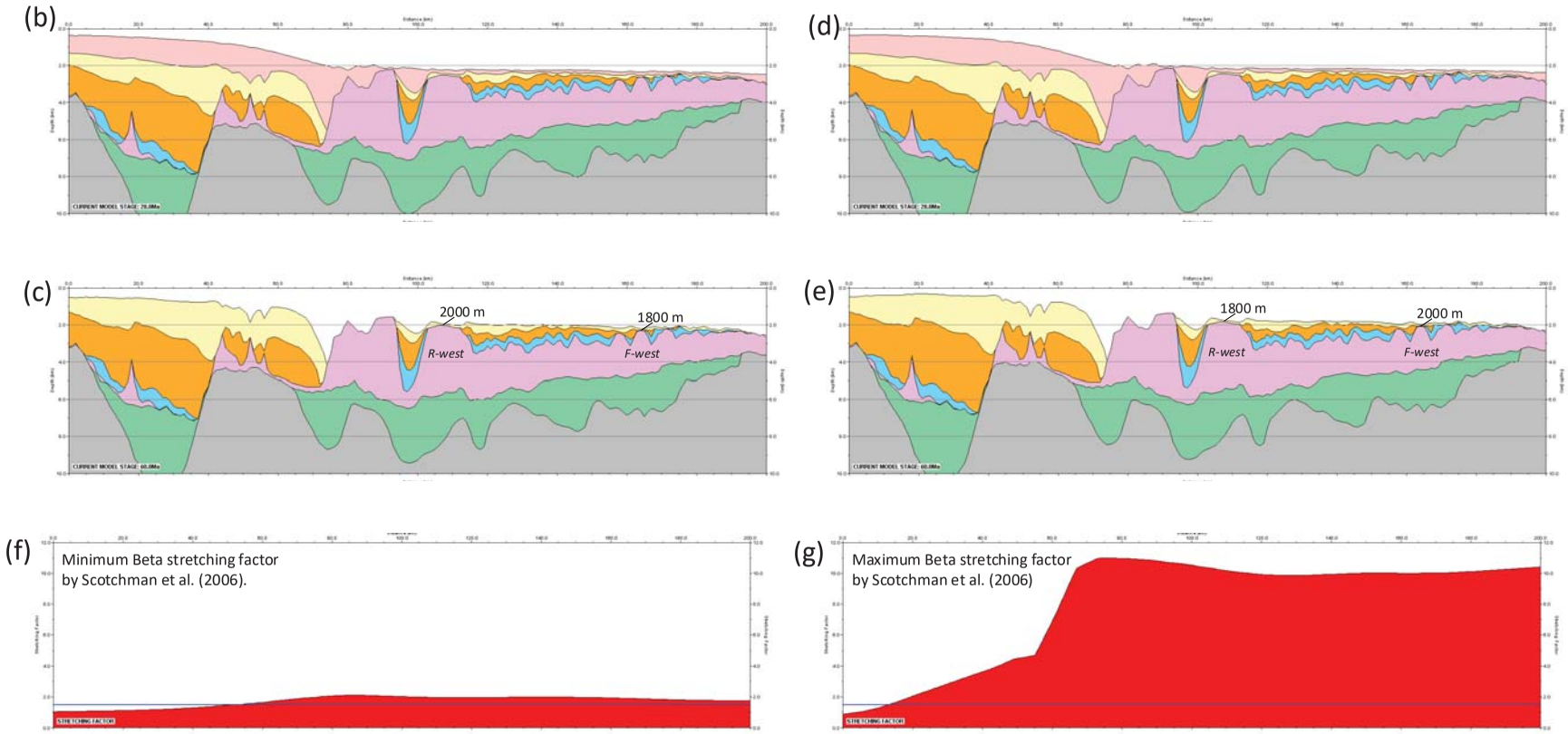


FIGURE 7.15: Basin restorations to Mid-Oligocene on (b) and (c): using minimum and maximum Beta stretching factor, respectively. Basin restorations to Paleocene on (c) and (e) using minimum and maximum Beta stretching factors, respectively

7.11 Discussion

In this study I have documented clear evidence of seismic-scale submarine salt dissolution at the crest of salt walls in central deep-water Santos Basin. Furthermore, my results illustrate a direct control between the intrasalt stratigraphic heterogeneity along the salt wall crests and the resulting regional and local dissolution-related morphologies formed at the crests and within the overburden (Fig. 7.14). I now discuss: (1) the mechanisms that may have triggered salt dissolution; and (2) the applied implications of these findings.

7.11.1 Mechanism of salt dissolution

Previous studies suggest that salt dissolution occurs by (i) descending NaCl-undersaturated fluids that come into contact with the salt (superjacent dissolution); (ii) along the lateral margins of basin flanks (lateral dissolution); or (iii) due to sub-salt deep-basin fluids that migrate upwards (subjacent dissolution) (e.g., Posey and Kyle, 1988; Warren, 1997; Loucks, 1999; Cartwright et al., 2001; Bertoni and Cartwright. 2005; Warren 2006; Hovorka, 2000; Jackson and Lewis, 2012; Machel et al., 2012; Burberry et al., 2016; Jackson and Hudec, 2017).

In this study I illustrate clear evidence of seismic-scale salt dissolution and local formation of caprock at the crests of salt structures. In addition, I demonstrate that salt dissolution at the crests of salt walls in the central deep-water Santos Basin occurred in a submarine setting; i.e. c. 1900 ± 100 m palaeowater depths. Furthermore, my interpretation suggests that dissolution likely occurred in the Paleocene, when the diapirs were exposed at the seabed under fine-grained-dominated overburden.

However, questions remain regarding the provenance of the NaCl-undersaturated fluids and the mechanisms that caused such dissolution: (i) were the crests of salt diapirs dissolved by superjacent NaCl-undersaturated seawater that penetrated the relatively thin (up to c. 60 metres) overburden?; (ii) were the crests of salt walls dissolved by subjacent NaCl-

undersaturated deep-basin fluids that migrated upwards or laterally from the minibasin flanks?.

Subjacent dissolution has been previously invoked for the localised depletion of relatively thin (up to 250 ms, TWT) evaporite-dominated units (e.g.; eastern Mediterranean; Bertoni and Cartwright; 2005). However, I suggest that subjacent dissolution or the upward migration of undersaturated fluids below the salt sequence is unlikely considering the thickness (> 1000 ms; TWT) of the salt walls and the largely impermeable nature of the intrasalt stratigraphy (Fig. 7.4 b, c). Although clastics and carbonates are present, it is only in small proportions and they are likely left in salt welds (e.g.; Jackson et al. 2014 b). Therefore, I infer that dissolution of the crests occurred either by superjacent NaCl undersaturated seawater or by fluids that migrated laterally upwards from the minibasin flanks.

I propose that superjacent dissolution is a feasible mechanism for Paleocene-age, widespread salt dissolution in the central deep-water Santos Basin. Similar to the submarine conditions in the Orca Basin (Fig 7.16; Fig. 7.1; Pilcher and Blumstein, 2007), NaCl-undersaturated seawater, could have penetrated the unlithified roof driving dissolution of the crests. I suggest that subsequent roof deformation, driven by underlying salt depletion, further facilitated penetration of seawater leading to more salt dissolution (Fig. 7.16 a). Furthermore, I infer that pore water within the roof stratigraphy could have also facilitated dissolution at the crests.

Nevertheless, considering the timing of salt dissolution and the stratigraphic context of the post-salt sedimentary overburden (section 7.10; Figs. 7.13; Chapter 6), I suggest that lateral dissolution, by the migration of fluids from the minibasin flank, is a plausible mechanism (Fig. 7.16 b). More specifically, I infer that formation fluids flowing through sandstone-rich deepwater turbidites migrated from the minibasin flanks towards the crests (Figs. 7.13). Furthermore, I propose that this mechanism likely promoted the dissolution of the F-central and F-west salt walls, which are both flanked by deep-water channels and lobes (Fig. 6.15; Chapter 6).

For example, I interpret that formation fluids within the sandstone-rich channels onlapping the crest of F-central became in contact with the A1-halite-rich crests and led to depletion, subsidence and the formation of salt karst atop the crest (e.g, Figs. 7.14 d, 7.16 b). I further propose three likely mechanisms that occur isolated or in conjunction, triggering the dewatering of the submarine channels and lobes and the migration of fluids towards the crest: i) initial compaction of the sand-rich submarine channels and lobes (cf. West Africa, Pilcher and Argent, 2007); (ii) coeval salt movement which caused rotation of the channels and levees during deposition (see Rodriguez et al. (b), in press/ Chapter 6); or (iii) a regional basin-scale event associated to the deposition of mass transport complexes (MTCs) in the Palaeocene and leading to the escape of overpressure fluids (Fig. 6.24, Chapter 6) .

This lateral dissolution mechanism could also explain the variations in the magnitude and style of dissolution between the crests of flat-topped salt walls (Fig. 7.14). For example, I observe that F-west seem to have dissolved more relative to F-east given the larger number of thicker and widespread karst mounds forming the highly-reflective caprock (compare Fig.7.9 with 7.10 and see also Fig. 7.14 d and f). Related to this, I note that submarine channels and lobes within Unit 3 occur on both sides of the highly-dissolved crest of F-west (salt wall flanking the western side of minibasin K; Figs. 6.15, 6.18b; Chapter 6). Moreover, F-central shows more depletion of the evaporite-dominate crest adjacent to the flanking submarine channel (Figs. 7.13, 7.14 e). Conversely, submarine channels are not observed at seismic scale next to F-east; suggesting that superjacent dissolution by NaCl-undersaturated seawater may have caused the relatively lower magnitude dissolution observed at its crest (Fig. 7.9, 7.14f).

In addition, my analysis suggests that local superjacent dissolution is also a likely mechanism mainly for R-west and R-central salt walls. In Rodriguez et al. (b), in press (Chapter 6) I demonstrate that the Maastrichtian-to-Palaeocene Unit 3 comprises sandstone-dominated turbidity channels, which entered the ISPFB and SPP from proximal overfilled minibasins North of R-west (Fig 6.15). Similarly; seismic attribute analysis by Rodriguez et al.; in press (b)

(Chapter 6) illustrate the spilling of submarine channels across the northern part of R-central (salt wall bounding minibasin L, Fig 6.15, Chapter 6). Therefore, I infer that submarine channels spilling from the north and northwest likely eroded and led to local dissolution of the upper crest of the R-west and R-central salt walls and deformation of its overburden (Table 7.3).

7.11.2 Salt dissolution implications

The findings I show in this study have major implications for hydrocarbon exploration considering the widely-held notion that salt structures bounding clastic-dominated minibasins are impermeable and this represent high-quality seals (e.g., Jackson and Hudec, 2017). Due to the generally poorly imaged salt-sediment interface and salt crests (e.g; Jackson and Lewis; 2012; Jones and Davison; 2014), the incorrect interpretation of a potential hydrocarbon trap, could lead to the drilling of dry wells. Hence, the precise assessment of the potential for dissolution at the flanks and the crests of salt structures is essential before placing exploration and production wells.

However, the assessment of seismic-scale salt dissolution evidence can be challenging using seismic imaging where the stratigraphic and structural complexity above and around salt diapirs has been oversimplified (e.g.; Jones and Davison; 2014). In this study I have illustrated a variety of reflection configurations within strata above dissolved salt walls, which are strongly dependent of the underlying intrasalt stratigraphy, the timing of deposition relative to dissolution and the magnitude of underlying salt-related dissolution (Tables 7.2 and 7.3). For example, I have demonstrated that the dissolution of evaporites-interbedded salt crests can result in the truncation of the intrasalt stratigraphy and the formation, above, of residual less-soluble caprock that can sometimes preserve the dipping of underlying intrasalt units (Table 7.3; Fig. 7.16). In addition to the complex reflection configurations; the composition of the overburden can also be highly variable comprising a combination of less-soluble residual evaporites combined with sediments collapse from the overburden during subterranean salt depletion.

Furthermore, as I have demonstrated in this study, salt dissolution can significantly influence the continuity within strata in the overburden (section 7.9.3). The resultant geometries and deformations documented here, can be considered when characterising reservoir compartment above salt. For example, carbonate karst collapse chimneys in the Boonsville gas field, Texas, has directly influenced reservoir compartmentalization in the overlying clastic dominated sequence (e.g.; Hardage et al., 1996).

The misinterpretation of the stratigraphy and structure within the overburden as an input for velocity models, ray tracing and seismic depth migration techniques have direct implications in the resulting seismic image surrounding the crests of diapirs. Nevertheless, as I have demonstrated, the assessment of local salt karst morphologies at the crest of salt walls and deformation in the overburden can be possible with conventional high-quality 3D seismic reflection data. This was possible in part due to the relatively thin and simple overburden that characterises the SPP in the central deep-water Santos Basin. Moreover, the precise high-resolution mapping, and the integration with seismic attributes and colour scales that highlight potential salt-related karsting can be beneficial during the analysis of these local salt dissolution-related features (see also Talbot and Augustin, 2016).

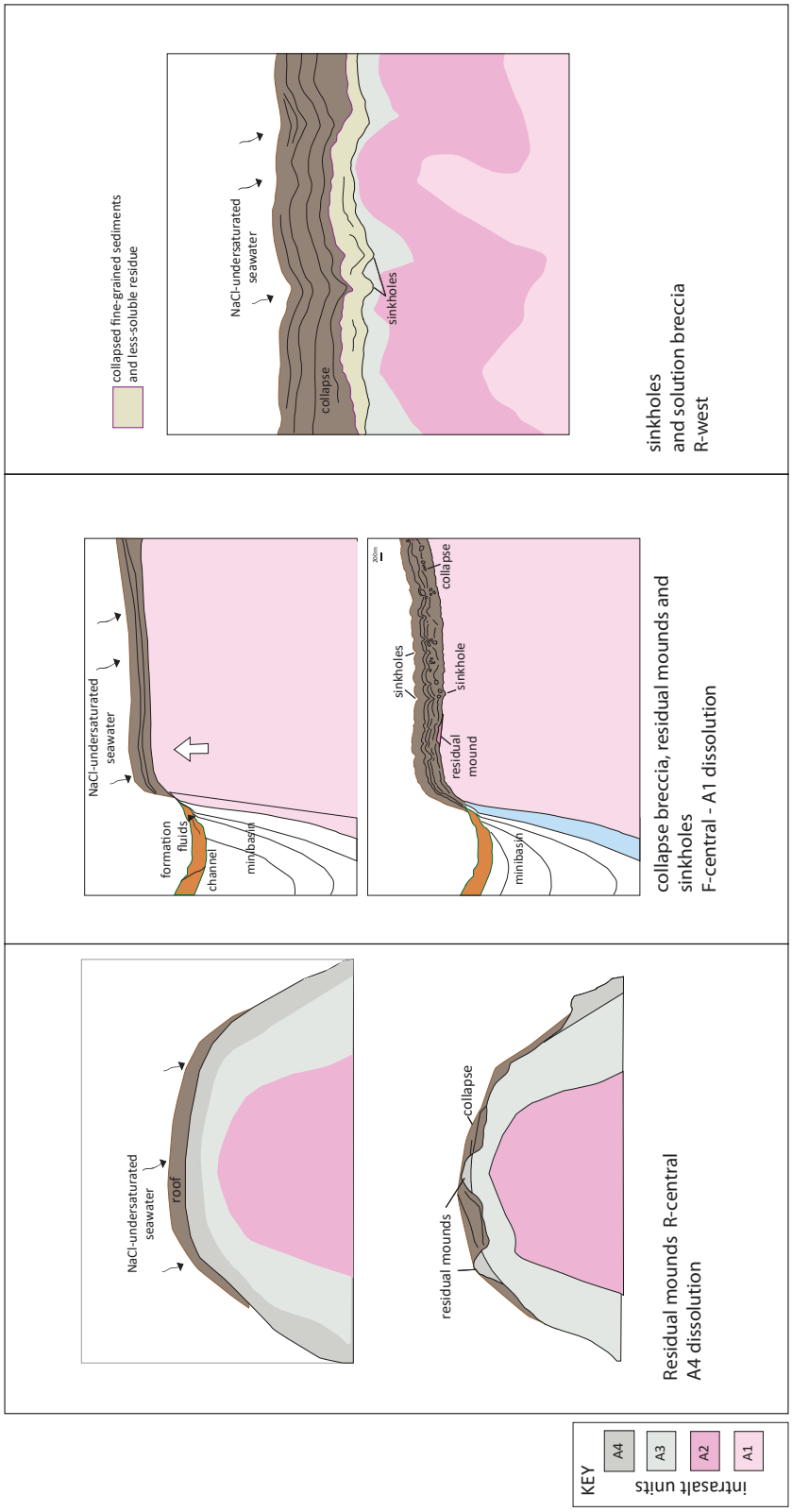


FIGURE 7.16 - Styles of dissolution

7.12 Conclusions

The integration of 2D and 3D seismic reflection and borehole data has revealed evidence of submarine salt dissolution in the Santos Basin, offshore Brazil:

1. Seismic stratigraphy and seismic attribute analysis illustrate salt karst features at the crests of salt diapirs consisting of: (i) up to 100 m thick, sub-circular, residual mounds rising above nearly horizontal (<10◦) Top Salt; (ii) up to 100 m deep, oval-to-circular, dissolution sinkholes below the main level of the Top Salt; and (iii) up to 60 m tall breccia pipes capped by collapse sinkholes within the overburden. Styles of dissolution identified suggest a direct link between the salt karst morphologies and the intrasalt stratigraphic heterogeneity along the top salt.

2. Seismic-stratigraphic-relationships in post-salt strata indicate several deformation patterns within the overburden; from local disruption of conformable sheets, rotation and apparent downlap, mounds and highly chaotic. The magnitude of deformation within the overburden is controlled by the magnitude of dissolution of the underlying evaporite-dominated crests; thus, indicating subterranean salt dissolution.

3. Reverse-basin modelling indicates that salt dissolution occurred in a fully submarine environment in water depths of 1900 m (± 100 m).

4. Dissolution was triggered by two feasible mechanisms that acted individually or in conjunction: (i) Superjacent dissolution by NaCl undersaturated seawater during partial salt diapir exposure (under an up 60 m thick, fine-grained dominated roof) at the seabed; and/or (ii) Lateral dissolution by formation fluids migrating from Late-Maastrichtian-to-Paleocene submarine channels and lobes directly onlapping the crests

5. Results presented in this study has direct implications for seismic imaging, reservoir characterisation and sealing capacity of the crests of salt diapirs and its overburden.

Chapter 8
Discussion and Conclusions

My work offers new insights into the scientific understanding of salt giants in terms of their deposition, composition and overall stratigraphic architecture. Furthermore, the results of my study contribute to a better understanding of salt deformation during passive margin evolution and its impact on sediment distribution and architecture along salt-influenced slopes. In addition, my thesis highlights the role of intrasalt stratigraphic heterogeneity in the eventual dissolution at the crests of salt diapirs as well as its impact in the overburden. In particular, the findings of my study challenge previous studies and improve the current knowledge about the tectonostratigraphic evolution of the Santos Basin, offshore eastern Brazil. In this chapter, the key conclusions of my thesis are outlined and their implications are discussed focused on addressing the research aims and the specific questions defined in Chapter 1.

8.1 How rapidly was the Santos Basin salt giant deposited and what are the implications of this rapid deposition?

In Chapter 5 I show that the evaporite-dominated Ariri Formation records at least 12 cycles of basin filling and near- or complete dessication in < 530 ka (Fig. 5.13). My estimation is based on the thickness (c. 100-250 metres) of the evaporite cycles interpreted in two boreholes and depositional rates in ancient salt giants (i.e.; Paradox Formation, 0.4 cm/a; Trudgill, 2010; Mediterranean salt, 0.66 cm/a; Clauzon et al., 1996) and a modern rift-related salt basin, Lake Assal (1 cm/a; Imbert & Yann, 2005). Furthermore, my analysis of the two boreholes suggest

that duration of deposition varied across the study area and was partly controlled by the syndepositional basin physiography (Fig. 5.13; Chapter 5; see also section 8.2).

My results illustrate, regular, high-frequency, short-term cycles (≤ 30 ka) within the heterogeneous A2 intrasalt interval (Fig. 5.13; Chapter 5). I infer that this depositional timescale may have been driven by low-amplitude, 4th-to-5th order sea level variations (, i.e. few meters to decimetres in c.10ka to c. 100ka) such as those characterising the greenhouse conditions and an arid paleoclimate. Such conditions have previously been proposed for the Late Aptian of the South Atlantic (e.g., Evans 1978; Taylor, 1998; Dias, 2004; Gambôa et al, 2008).

I suggest that a combination of an arid paleo-climate, low-amplitude sea-level changes, and relatively rapid deposition (< 530 ka) of a thick (1.2 km -. 2.5 km) salt sequence also prevented the deposition of non-evaporite lithologies in the central deepwater Santos Basin. Although broadly similar in terms of overall thickness, the depositional timescale and at least the sea-level controls I infer for salt deposition in the Santos Basin, is unlike that suggested for the Zechstein Supergroup, NW Europe (c. 1.5 km thick and deposited in in 5 Myr; e.g., Taylor, 1990; Tucker, 1991) and the Paradox Formation, North America (c. 2 km thick and deposited in 7 Myr; e.g.; Trudgill, 2011; Eoff et al., 2013). The presence of non-evaporite lithologies (e.g. sandstone, mudstone) within the Zechstein Supergroup and the Paradox Formation suggest that fully marine conditions periodically occurred in the basins and the salt sequences were deposited during less arid conditions, higher amplitude sea-level changes and relatively slower deposition (> 5 Myr).

In addition, rapid deposition (<530 ka) also implies that syn-depositional tectonics may have been insignificant during salt deposition, although salt loading may have been important for the creation of local accommodation in the basin (e.g.; Davison et al., 2012).

8.2 Can thickness and stratigraphic variability within a salt giant provide clues to temporal and spatial variations in syndepositional basin physiography?

My thesis reveals that rifting-inherited basin physiography controlled salt thickness and composition of the Ariri Formation leading to stratigraphic variations across structural domains in central deep-water Santos Basin (see Chapter 5). Findings I show in Chapter 5 suggest that during salt deposition, the Santos Basin was characterized by a series of sub-basins of varying water depth promoting vertical salinity variations. As a result, the thickness and composition of the salt giant vary laterally and are spatially related to structural domains (Figs. 5.10-5.12). My results indicate that thinner salt (c. 1.8 km) and higher anhydrite net thickness (c. 350 m) occur towards the structurally high Sugar Loaf domain, compared to flanking, structurally lower domains where the mean salt thickness is >2.2 km and anhydrite net thickness are less (c. 180 m) (Figs. 5.10 and 5.12).

I further infer that the thickness and stratigraphic variations I have found within the salt were also directly controlled by the depth of the basin during salt deposition (Chapter 5). Based on my interpretation, I propose that the halite-rich-A1 interval largely filled a pre-existing rift-related relief within which the Sugar Loaf sub-high represented an intra-basin structural high covered by relatively shallow water (Fig. 5.12). In addition, my results suggest that subsequent deposition of the heterogeneous, cyclic, A2 interval occurred in a basin with more subdued relief and reduced accommodation which promoted higher-frequency desiccation of the salt basin when compared with A1 deposition (Fig. 5.12). Moreover, the subdued thickness and compositional variability of A3 and A4, suggest that A1 and A2 had filled most of the pre-existing relief. I propose that during periods of relatively high sea-level, thinner salt and higher proportions of gypsum/anhydrite were deposited along the basin margins and on shallow, intra-basinal structural highs such as the Sugar Loaf domain (Figs. 5.7; 5.10). In contrast, during periods of relatively low sea-level, thicker salt and higher proportions of halite and bittern salts were deposited in the basin centre and deeper isolated sub-basins, such as those

now represented by the thick salt, minibasin and Tupi domains (Figs. 5.7; 5.10 and 5.11).

My observations imply that the Santos Basin Outer High (Sugar Loaf and Tupi sub-highs) has been a longstanding, positive structural element, at least since the onset of salt deposition in the Late Aptian (Fig. 5.2c). This finding challenge previous studies indicating the Outer High developed as a Late-Cretaceous flexural bulge by vertical loading and perhaps by horizontal compression (e.g., Cobbold et al. 2010). Moreover, my work support previous studies suggesting the Outer high was initially uplifted at the end of the early syn-rift phase and which may have been at least periodically emergent before and during salt deposition (Fig.5.2c; Gomes et al., 2002; Carminatti et al., 2009; Gomes et al., 2009; Scotchman et al., 2010).

Furthermore, considering the rapid deposition discussed above, I suggest that syn-salt subsidence and accommodation was only important locally and driven by salt loading (see also Davison et al., 2012). Post-rift thermal subsidence and/or fault-related subsidence was probably insignificant unlike suggested by previous regional studies discussed in Chapter 5 (e.g., Karner et al., 2003; Dias, 2004; Karner and Gambôa, 2007).

Other ancient salt giants evolved under the influence of similar controls to those inferred for the Ariri Formation. For example, previous studies in the North Sea suggest that pre-Zechstein faults, inherited from the earlier Permian rift phase or even formed syn-depositionally during Late Permian rifting, directly controlled thickness and lithology variations within the Zechstein Supergroup (Clark et al. 1998; Jackson and Lewis, 2013, 2016). During deposition of the Zechstein Supergroup, periodically submerged intra-basinal highs formed shallow areas where carbonate and anhydrites was deposited (e.g., Taylor, 1990). In addition, In deeper waters, an up to 1.5 km thick succession of basin centre facies, comprise mainly of halite, was deposited (e.g., Clark et al. 1998).

8.3 What can salt giants stratigraphic architecture tell us about syn-depositional basin hydrology?

Salinity variations during salt deposition may have also been controlled by the distance relative to the influx of seawater and the input of fresh continental water; thus, modifying the concentrations needed for a particular evaporite to precipitate (e.g.; Hsü, 1972; Fig. 2.3; Chapter 2). My findings indicate the influence of syn-depositional basin hydrology during salt deposition. In Chapter 5 I illustrate that thickness and stratigraphic variations occur across the Outer High, from the Sugar Loaf sub-high to the south, towards the Tupi sub-high to the north. Assuming that both, the Sugar Loaf and Tupi sub-highs were shallower than the surrounding domains at the onset of salt deposition, then, I suggest, that the main factor controlling salinity variations and thus lithologies found on the Outer High may be the position of this area with respect to the putative sill controlling seawater influx into the basin.

Therefore, I propose that during salt deposition, gypsum/anhydrite was precipitated in larger quantities, to the south, closer to the entry of seawater (i.e., the Sugar Loaf domain); whereas larger amounts of halite and bittern salts were deposited farther away from the sill, towards the north, in the deeper, more isolated domains (i.e.; the Tupi domain) (Fig. 5.11; Chapter 5). My observations are consistent with those of Demercian (1996), who suggested that gypsum/anhydrite deposition was controlled by the position and direction of the seawater inflow from the southern Florianopolis high (São Paulo Ridge), with concentrations increasing northwards. Nevertheless, my study provides, for the first time, a detailed intrasalt stratigraphic architecture across the Outer High, based on the analysis and integration of 3D seismic reflection and borehole data (Fig 5.11 in Chapter 5; see also Fig. 4. 4 and 4.6 in Chapter 4).

Similar salinity variations to these interpreted for the Outer High have been observed in Lake Asal, Djibouti, which represents a modern example of a marine-fed rift basin actively accumulating interbedded evaporites (e.g.; Jackson et al., 2000). Here, seawater incursions occur through a highly fractured, 10 km wide volcanic ridge that bounds the southeastern

margin of the lake. Close to the seeps that bring seawater to the surface, gypsum precipitation dominates, whereas stacked halite crusts characterise the opposite side of the lake where salinities are higher (e.g.; Warren, 2006).

Regarding the influx of freshwater from the continent, previous studies suggest that anhydrite is thicker and more voluminous in the west of the Santos Basin due to freshwater influx from the continent during the Aptian (De Freitas, 2006). Conversely, eastwards on the São Paulo Plateau, away from this freshwater source, salinities were higher and halite and bittern salts were thicker. Interestingly, my findings are opposite to those of De Freitas (2006) considering the presence of the Outer High promoted higher proportions of anhydrite precipitation in distal locations (Chapter 5). Nevertheless, the composition of the Ariri Formation in the salt weld located beneath a proximal thick minibasins (Chapter 5; see also Jackson et al. 2015a), indicates the presence of some sandstone within the Ariri Formation, which may support De Freitas (2006) observations. However, I argue that the impact of continental river discharge was likely to have a minor impact on basin salinity and thus salt composition, given that the study area is located a considerable distance (> c. 100 km) from the coeval coastline.

8.4 How does salt movement control instraslope deep-water sediment architecture along the Santos Basin slope?

Previous regional studies in the Santos Basin offshore Brazil assume that most clastic sediment was trapped behind a large scale (4 km thick, 200 km long, 10 km wide), salt-controlled, intra-slope depocenter; i.e., the Albian Gap (e.g, Modica and Brush, 2004; Guerra and Underhill, 2012). As a result, the stratigraphic architecture of deep-water deposition and its interaction with salt has been overlooked basinward of this depocenter.

In Chapter 6, I challenge this notion by analysing the distribution and architecture of deep-water depositional elements along the Santos Basin slope. By characterising the stratigraphy and geomorphology of deep-water depositional systems, I clearly demonstrate that deep-water clastics are found at least 100 km from the Albian Gap depocenter and record > 60 Myrs of salt and sediment interactions (e.g. Fig 6.20).

The results of my work, thus clearly highlight how gravity-driven downdip salt flow directly controlled the Santos Basin deep-water slope morphology and influenced sediment dispersal and architecture (Chapter 6):

During the first phase of deep-water sedimentation (Turonian-middle Campanian), sand-rich channels and lobes were confined within proximal minibasins and to the hangingwalls of landward-dipping, salt-detached listric faults.

During the middle Campanian-to-Paleocene phase, sand-rich channels and lobes eventually filled and bypassed proximal minibasins, with coarse clastic deposition then occurring further downslope. My results highlight that syn-depositional seabed deformation, driven by passive and active diapirism, and salt-detached thrusting and folding directly controlled sediment distribution and architecture within distal minibasins downslope (Chapter 6):

(i) channel deflection and diversion around salt-cored highs

(ii) channel and levee uplift and rotation on the flanks of rising salt-cored highs

(iii) progressive lateral channel migration, expressed in the form of lateral accretion packages (LAPs)

(iv) local ponding and long-distance lateral and frontal confinement of channels and lobes

During the Paleocene-to-middle Oligocene, continued rise of proximal salt walls dissected previously deposited deep-water systems, with deposition from diapir- and shelf-edge sourced MTCs becoming increasingly important

These results represent a significant advance in the understanding of the tectonostratigraphic evolution of the Santos Basin. However, due to the lack of seismic and borehole data landwards of the minibasin domain, it is still not clear how deep-water sediments were deposited basinwards of the intraslope depocenter; i.e.; the Albian Gap. Hence, further studies are needed to solve this controversy (see section 8.10).

8.5 Could previously underexplored post-salt intervals have hydrocarbon exploration significance?

Due to previous regional studies suggesting limited deep-water deposition in central deep-water Santos Basin (e.g.; Modica and Brush, 2004; Guerra and Underhill, 2012), the hydrocarbon potential within the post-salt sequence in the Santos Basin has been overlooked or misinterpreted by previous studies. However, in this thesis I demonstrate that sediments within the same stratigraphic interval of reservoirs currently producing upslope Santos Basin (Fig. 2.9b; Merluza field; e.g.; Mohriak, 2012) and in the Campos Basin (e.g., Roncador field; Bruhn et al., 2003) could also be prospective in central deep-water Santos Basin (Chapter 6).

The salt-related controls on the geometry and architecture of deep-water depositional elements illustrated in Chapter 6 have important implications for trap development and seal

presence. Based on the analysis I have presented in this thesis, I suggest that the previously unexplored post-salt sequence in the Santos Basin have exploration potential. In Chapter 6 I illustrate several salt-related trapping of reservoir-prone units within the post-salt of central deep-water Santos Basin: (i) fault-block traps; (ii) turtle anticlines; and (iii) stratigraphic traps related to the pinch-out of channels and lobes towards salt-cored highs.

For the potential reservoir-prone units I describe in Chapter 6 (e.g. channels, lobes and, perhaps to a lesser extent, levees), 'background' deposits, such as slope mudstone, and salt represent the main seals. In addition, local, mud-rich MTCs may also form lateral and vertical seals.

The deep-water depositional systems I have identified in the Santos Basin could be distal analogues of the Campanian to Maastrichtian deposits encountered further north in the Roncador field, Campos Basin (e.g., Bruhn et al., 2003). The distal deepwater reservoirs in the Campos Basin occur mostly in stratigraphic traps. Overall, there appears to be less confinement of depositional elements, hence traps and fields are larger. Because of the confinement I illustrate in proximal minibasins in the Santos Basin, it is likely that any potential traps and fields would be smaller than observed in the Campos Basin (cf. Gulf of Mexico; e.g., Booth, 2003). The seismic stratigraphy geometry and distribution of the more proximal reservoir-prone intervals of stacked submarine channels and fans or sheet-sand reservoirs illustrated in this study are strikingly similar to reservoir-prone units being currently produced in the Gulf of Mexico (i.e., Auger Basin, Booth et al., 2003; Jackson and Hudec, 2016). Despite the fact that some of the distal potential reservoir I illustrate in Chapter 6 are defined by a channel-levee system with a frontal lobe, these are axially confined in local fold-related synclines along elongated minibasins for more than 150 km.

Findings I present in Chapter 6, suggest that a key exploration risk for the Santos Basin is migration, principally due to the thick, likely very low-permeability salt between sub-salt source rocks and supra-salt reservoirs. This is a particular risk in distal areas, where thick

allochthonous salt remains; in proximal areas, salt welds may facilitate the vertical migration of hydrocarbon, although the mudstone-dominated nature of many of the minibasin may still pose a migration risk. Likewise, the presence of salt-cored faults and turtle anticlines, due to minibasin welding, may promote the vertical hydrocarbon migration of hydrocarbons (Chapter 6).

8.6 What are the implications of these findings for the overall understanding of salt and sediment interactions along salt-influenced slopes?

Seismic reflection-based studies of ancient intra-slope depositional systems that interact with salt are challenging due to the low seismic resolution of deeply-buried depositional elements which limits the level of detail that can be investigated and the poorly imaging of the dipping minibasin flanks which could also be misleading when examining the relative timing of paleoseafloor relief during sedimentation.

Previous seismic-scale studies of salt and sediment interactions have been largely constrained in the spatial extent and the geological time scales that are documented. Most of the current understanding of salt-sediment interactions comes from very shallow (i.e., at the seafloor or up to 500 m deep), undrilled, relatively young deep-water systems, which are then used as analogues to understand similar salt-sediment interactions in older, more deeply buried systems (e.g., Winker, 1996; Beaubouef and Friedmann, 2000; Pirmez et al., 2000; Fonnesu, 2003; Gee and Gawthorpe, 2004, 2006; Clark and Cartwright, 2009; 2011). In addition, previous studies are focused on single minibasins or covering relatively small areas of c. 400 km2 (e.g., Gulf of Mexico, Booth et al., 2000, 2003) or up to 1400 km2 (e.g.; offshore Angola, Jones et al. 2012). Moreover, previous regional-scale (up to 10,000 km2) studies have focused on the analysis of specific stratigraphic intervals recording relatively short time scales of ca. 15 Myrs (e.g.; Olobuyo et al., 2014). Contrastingly, my 3D seismic reflection and borehole-based analysis illustrates a longer timescale (ca. 60 Myrs) record of salt-sediment interaction in more than ten minibasins covering an area of c. 20,122 km2 (Chapter 6).

In particular, the analysis I present in Chapter 6 illustrate local sediment spilling due to welding of the minibasin floor and associated formation of turtle anticlines, which cause the diversion of deep-water channels towards the downslope minibasins.

Furthermore, a key result of my work, which has been overlooked in other salt-influenced sedimentary basins, is that continued diapir growth can dissect previously through-going depositional systems (e.g., Figs. 6.12-6.13; Chapter 6). Moreover, my study illustrates that filling of intraslope minibasins can be locally controlled by intra-minibasin salt-cored faults and salt pillows (e.g.; Fig. 6.10, 6.11 b; Chapter 6). This control, thus, can promote the filling of distal minibasins before deep-water sediments are deposited in more proximal minibasins, contrary to the classical 'fill and spill' model (e.g.; Gulf of Mexico; Auger Basin, Booth, 2003; Hudec, 2009; Espirito Santo Basin, offshore Brazil; Albertao et al., 2011; North Sea; Jackson et al., 2010; Lower Congo Basin, offshore West Africa, Oluboyo et al., 2014; Chapter 6). Hence, the regional-scale detailed 3D mapping and seismic attribute analysis of minibasin stratigraphy presented in Chapter 6 represents a significant advance over previous studies and in future can help understanding the complete post-salt tectonostratigraphic evolution in other salt-influenced sedimentary basins.

8.7 What is the role of the intrasalt stratigraphic heterogeneity on the development of local dissolution-related morphologies, and the overall external morphology of salt structures?

Prior to this study, it was still uncertain how dissolution was expressed at the crests of and within the strata above buried salt diapirs. Seismic resolution and seismic imaging has typically limited the level of detail that can be investigated along and above deformed and highly heterogeneous dissolved crests. Based on a detailed seismic-based analysis (mapping and attributes) with a conventional 3D seismic cube; I characterise seismic-scale salt karst morphology above six buried salt diapirs in the central deep-water Santos Basin and illustrate a direct link with the intrasalt stratigraphy described in Chapter 5. In addition, I discuss the feasible mechanisms promoting dissolution of the crests and illustrate how dissolution drives deformation within the overburden.

Previous studies suggest that the dissolution at the crest of halite-rich salt diapirs will result in the formation of residual, diagenetic, anhydrite-gypsum-carbonate-rich caprocks (e.g. Posey and Kyle, 1988; Warren, 1997). Caprock formation in well-documented salt-influenced sedimentary basins has been generally attributed to periods of sub-aerial exposure of the crest of salt structures (e.g., Warren 1997). For example, in Texas, flat dissolution crests with less than 30 m thin residual cap rocks formed at the top of halite-rich diapirs that were passively exposed at the surface (e.g., Jackson and Seni, 1984, Hudec and Jackson, 2011). However, caprocks has not been accurately imaged by seismic data and no previous studies exist that directly relates crestal caprocks to intrasalt structure or stratigraphy.

In Chapter 7, I characterise, for the first time, the styles of dissolution at the crests of two types of salt diapirs identified in the Santos Basin; salt diapirs with more rounded and rugose crests and salt diapirs with nearly-horizontal (<10◦ dip), flat crests.

My results illustrate that the flat crests are broadly subcropped by halite-rich A1-allochthonous-sheets (see also Jackson et al., 2015b) and the seismic-scale salt karst is mainly expressed by up -to- 50 ms, TWT thick, residual mounds along the Top Salt horizon. The residual mounds are defined by up-to-three, highly-reflective seismic reflection events below the Top Salt and underlying the transparent and chaotic halite-rich A1. Based on the seismic attribute analysis and observations presented in Chapter 7, I suggest that the remnant mounds along the top salt represent the localised formation of, less-soluble caprock due to the dissolution of the halite-dominated A1 (section 2.3; Chapter 2). I further suggest that the less-soluble residue is composed by anhydrite or carbonates within the A1 sheets. The formation of insoluble residue due to halite dissolution and subsidence has been previously documented in the Permian Basin in the United States (e.g.; Hovorka; 2000).

Contrastingly, I show that, the rugose crests are mainly subcropped by variable intrasalt stratigraphy, including: (i) truncated, steeply-dipping, highly reflective, heterogeneous-A2; (ii) highly-reflective A2-cored folds; (iii) thrust-related synclines with transparent, halite-rich A3 and (iv) transparent, halite-rich A1-alloctonous sheets (Chapter 7; see also Jackson et al., 2015 b). In contrast with the halite-dominated flat crests, seismic-scale salt karst is mainly expressed along the heterogenous, rugose crests, as circular, up-to-50 ms, TWT deep, depressions or sinkholes. However, residual mounds are also evident between the sinkholes. My findings suggest that the sinkholes along the rugose crests are mainly developed above halite rich A3 and the anhydrite-halite-bittern salts- interbedded, steeply dipping A2. Although I lack borehole data that penetrates the crests of the salt diapirs, I suggest that the sinkholes formed above the dipping A2 form by the preferential dissolution of the more soluble halite and bittern salts that are interbedded with the less soluble anhydrite.

The results found in this study can provide insights into the understanding of flat-topped salt diapirs in Texas(e.g. Jackson and Seni, 1984, Hudec and Jackson, 2011) and the Barents Sea (e.g.; Koyi, 1998).

8.8. What was the impact of salt dissolution in the post-salt sedimentary overburden?

Previous studies suggest that salt dissolution drives the creation of local depocenters and faulting within the overburden, potentially promoting reservoir deposition, trapping and compartmentalisation (e.g., Ge and Jackson, 1998; Cartwright et al., 2001; Hudec and Jackson, 2001; Jackson et al., 2010). In addition, the collapse and deformation associated with karst can generate mega-pores or reduce the sealing properties of the salt and its overburden, hence its proper characterisation is relevant for evaluating reservoir and seal potential (e.g., Walles, 1993; Vahrenkamp, 2004). The characterisation of deformed strata above buried and dissolved salt crests requires high-quality seismic imaging and high seismic resolution; however, these are, in most cases, simplified or limited.

In Chapter 7, I illustrate how subterranean dissolution at the crests of salt diapirs in the Santos Basin drove deformation within c. 60 metres of overburden. The overburden seismic expression varies between the salt diapirs studied. I have identified a range of deformation patterns within the overburden; from local disruption of conformable sheets, rotation and apparent downlap, mounds and highly chaotic. I suggest that the magnitude of deformation within the overburden is controlled by the magnitude of dissolution of the underlying evaporite-dominated crests; thus, indicating subterranean salt dissolution (Chapter 7). For example, I demonstrate that the local disruption, and apparent downlap within the overburden is related to the development of parallel, up-to-100 ms, TWT tall collapsed breccia pipes, which are capped by oval-shaped collapse sinkholes (Chapter 7). Similar breccia pipes associated with the underlying depletion of evaporite layers have been identified by previous studies in carbonate-dominated basins (e.g. the Dead Sea, Frumkin and Raz, 2001; the Persian Gulf, Burberry et al., 2016). My findings, however, go beyond previous studies by providing a better image of the pipes and demonstrating that these can develop in fine-grained-dominated overburden above the crests of salt diapirs.

In addition, my results illustrate that the collapse, rotation and foundering of overburden strata due to the formation of solution sinkholes occurs along the Top Salt. Furthermore, in Chapter 7, I highlight the presence of low-to-moderate amplitudes mounded 'overburden' above the Top Salt which broadly preserves the dipping of underlying heterogenous intrasalt stratigraphy (mainly A2). This mounded 'overburden' is onlapped and downlapped by overlying strata. I suggest that these are either solution breccias composed by less-soluble residues and insoluble fine-grained sediments (e.g.; Hovorka; 2000, Warren 2006), or carbonate reefs formed above the salt-cored highs.

The variety of reflection configurations within strata, I have illustrated in my study, are controlled by the underlying intrasalt stratigraphy, the timing of deposition relative to dissolution and the magnitude of underlying salt-related dissolution. For example, I have shown that the dissolution of heterogeneous evaporite-dominated salt crests can result in the truncation of the intrasalt stratigraphy and the formation, above, of residual less-soluble caprock that can sometimes preserve the dipping of underlying intrasalt units. In addition to the complex reflection configurations; the composition of the overburden can also be highly variable comprising a combination of less-soluble residual evaporites combined with sediments collapse from the overburden during subsequent phases of buried salt depletion.

I strongly suggest that these new findings (sections 8.7 and 8.8) are taking into account when interpreting the Top Salt and the overburden as an input for velocity models, ray tracing and seismic depth migration techniques. I believe, these can have direct implications in the resulting seismic image at and surrounding the crests of salt diapirs.

8.9. What was the mechanism leading to salt dissolution?

Previous studies suggest that salt dissolution occurs by (i) descending NaCl-undersaturated fluids that come into contact with the salt (superjacent dissolution); (ii) along the lateral margins of basin flanks (lateral dissolution); or (iii)due to sub-salt deep-basin fluids that migrate upwards (subjacent dissolution) (Section 2.3; Chapter 2; e.g., Posey and Kyle, 1988; Warren, 1997; Loucks, 1999; Cartwright et al., 2001; Bertoni and Cartwright. 2005; Warren 2006; Hovorka, 2010; Jackson and Lewis, 2012; Machel et al., 2012; Burberry et al., 2016; Jackson and Hudec, 2017).

Subjacent dissolution has commonly been documented in salt-dominated sedimentary basins due to salt exposure under subaerial and near-surface conditions (e.g.; Jackson and Seni, 1984; Cartwright et al., 2001; Bruthans et al., 2009; Hudec and Jackson, 2011; Frumkin, 2013; Gutiérrez and Lizaga, 2016). Despite, subjacent salt dissolution is also known to have occurred under submarine conditions, by NaCl-undersaturated seawater; only few previous studies exist providing some evidence (e.g.; Pilcher and Blumstein, 2007; Talbot and Augustin, 2016). Moreover, evidence of salt dissolution under submarine conditions is limited and unconclusive. For example, it is still unclear how is the salt-related karst expressed along the salt canopy in the Orca Basin (Pilcher and Blumstein, 2007). In addition, salt dissolution under submarine conditions has most commonly been documented occurring in buried evaporite-dominated successions and due to deep-basin fluids promoting subjacent dissolution (e.g.; Bertoni and Cartwright. 2005; Burberry et al., 2016).

In Chapter 7, I demonstrate that dissolution at the crests of salt diapirs in the Santos Basin, offshore Brazil, occurred under fully submarine conditions, in water depths c. 1900 m (±100 m). In addition, my analysis of the overburden, also suggest that dissolution at the crests occurred in the Late-Maastrichtian-to-Paleocene under buried conditions; below a up to 60 m thick roof dominated by fine-grained sediments. 8. These findings differ to most modern cases of salt dissolution which occur in a subaerial or near-surface setting.

Based on the Late-Maastrichtian-to-Paleocene stratigraphic context of the post-salt sedimentary overburden in central deep-water Santos Basin (fully described in Chapter 6), I further propose that dissolution was triggered by two feasible mechanisms that acted individually or in conjunction (Chapter 7): (i) Superjacent dissolution by NaCl undersaturated seawater during partial salt diapir exposure (under a fine-grained dominated roof) at the seabed (Chapter 6); and/or (ii) Lateral dissolution by formation fluids migrating from Late-Maastrichtian-to-Paleocene submarine channels and lobes directly onlapping the crests (Chapter 6 and 7).

I propose that superjacent dissolution by NaCl-undersaturated seawater could have penetrated the unlithified roof driving dissolution of the underlying evaporite-dominated crests. The subsequent collapse and the development of breccia pipes within the overburden further facilitated penetration of seawater and more dissolution (Chapter 7). In addition, pore water in the roof could have also facilitated dissolution.

Nevertheless, lateral dissolution could have occurred due to dewatering of the recently-deposited submarine channels along the flanking minibasins (Chapter 6). I further propose three likely mechanisms that occur isolated or in conjunction, triggering the dewatering of the submarine channels and lobes and the migration of fluids towards the crest: i) initial compaction of the sand-rich submarine channels and lobes; (ii) coeval salt movement which caused rotation of the channels and levees during deposition (Chapter 6); or (iii) a regional basin-scale event associated to the deposition of mass transport complexes (MTCs) in the Palaeocene-to-Eocene and leading to the scape of overpressure fluids (e.g., West Africa, Pilcher and Argent, 2007) .

8.10. Future work

My thesis provides key insights into the tectonostratigraphic evolution of the Santos Basin salt giant; however, there are several key questions that remain unanswered that I suggest being further addressed:

Intrasalt thickness variations

Seismic data indicate that structurally-induced thickness variations exist within the A1-to-A4 intrasalt intervals (e.g. Dooley et al., 2008; Cartwright et al., 2012; Jackson et al., 2014a). However, during my analysis of the intrasalt stratigraphy, I identified areas that suggested syndepositional thickness variation within A1 and A2, similar to findings by Stewart and Clark (1999), in the North Sea. Previous studies in the Santos Basin suggest 'early' salt deformation due to reactivation of pre-existing extensional faults, supported by the observed syn-depositional thickness variations within the evaporites with the initial deposition of halite creating accommodation for subsequent layers of anhydrites before the whole salt layer flowed downslope in response to thermal subsidence (Gambôa et al., 2008; Davison et al., 2012). However, Fiduk and Rowan (2012) and Jackson et al. (2015b) argue that the majority of salt flow is 'late' as opposed to Aptian syn-depositional deformation. However, I suggest that a more detailed analysis is needed across the Santos Basin to assess the effect of the potential lateral stratigraphic heterogeneity described in Chapter 5. I suggest that the stratigraphic heterogeneity within the salt could have promoted spontaneous subsidence during salt deposition in some locations. This spontaneous subsidence model has been applied in the North Sea to explain early minibasin subsidence of denser carbonate and evaporite rocks into halite while evaporites were still precipitating (Stewart and Clark, 1999).

Halokinetic sequence stratigraphy

I suggest the application of halokinetic sequence stratigraphy in the Santos Basin as an alternative approach to analyse minibasin development and salt growth (Giles and Lawton,

2002; Giles and Rowan, 2012). The analysis will require the identification of halokinetic sequences at flanks of the minibasins (i.e. angular unconformities separating genetically related packages of halokinetic growth strata). This can be achieved by the high-quality 3D seismic reflection data available in the study area.

Albian Gap and deep-water sediment dispersal

The results presented in Chapter 6 represent a significant advance in the understanding of the tectonostratigraphic evolution and Upper Cretaceous to present-day paleogeography of the deep-water Santos Basin. However, due to the lack of seismic and borehole data landwards of the minibasin domain, it is still not clear how deep-water sediments were deposited basinwards of the Albian Gap intraslope depocenter (e.g.; Jackson et al., 2015a). Therefore additional seismic and borehole data are required to analyse minibasin evolution and reservoir deposition in more proximal locations.

Salt dissolution volume estimations

Further work on the characterisation and estimations of submarine salt dissolution are suggested. The additional analysis at the crests of salt diapirs can complement the findings presented in Chapter 7.

Seismic-well tie and calibrations

The limited number of available boreholes and logs recorded for the post-salt has added uncertainty to the age assignment considering the only borehole containing ages information penetrates a completely enclosed minibasin. In addition, the lack of density logs resulted in the approximate seismic-well tie for the post-salt (Chapter 6). Additional boreholes with a complete set of logs will allow to corroborate the ages assigned in Chapter 6 and can be used to further calibrate lithologies with seismic facies and attributes response.

Bibliography

Abreu, V., M. Sullivan, C. Pirmez, and D. Mohrig, 2003, Lateral accretion packages (LAPs): an important reservoir element in deep water sinuous channels: Marine and Petroleum Geology, v. 20, pp. 631-648.

Adam, J., Z. Ge, and M. Sanchez, 2012, Salt-structural styles and kinematic evolution of the Jequitinhonha deepwater fold belt, central Brazil passive margin. Marine *and Petroleum Geology*, *37*(1), pp. 101-120.

Albertão, G.A.T. Mulder, and R. Eschard, 2011, Impact of salt-related palaeotopography on the distribution of turbidite reservoirs: Evidence from well-seismic analyses and structural restorations in the Brazilian offshore: Marine and Petroleum Geology, v. 28, pp. 1023-1046.

Alves, T.M., J. Cartwright, and R.J. Davies, 2009, Faulting of salt-withdrawal basins during early halokinesis: Effects on the Paleogene Rio Doce Canyon system (Espírito Santo Basin, Brazil): AAPG Bulletin, v. 93, pp. 617-652.

Anderson, J.E., J. Cartwright, S.J. Drysdall, and N. Vivian, 2000, Controls on turbidite sand deposition during gravity-driven extension of a passive margin: examples from Miocene sediments in Block 4, Angola: Marine and Petroleum Geology, v. 17, pp. 1165-1203.

Arai, M., 2014, Aptian/Albian (Early Cretaceous) paleogeography of the South Atlantic: a paleontological perspective: Brazilian Journal of Geology, v. 44, pp. 339-350.

Archer, S.G., G.I. Alsop, A.J. Hartley, N.T. Grant, and R. Hodgkinson, 2012. Salt tectonics, sediments and prospectivity: an introduction. Geological Society, London, Special Publications, 363(1), pp. 1-6.

Argent, J.D., S.A. Stewart, and J.R. Underhill, 2000, Controls on the Lower Cretaceous Punt Sandstone Member, a massive deep-water clastic deposystem, Inner Moray Firth, UK North Sea. Petroleum Geoscience, 6(3), pp. 275-285.

Aslanian, D., M. Moulin, J.-L. Olivet, P. Unternehr, L. Matias, F. Bache, M. Rabineau, H. Nouzé, F. Klingelheofer, and I. Contrucci, 2009, Brazilian and African passive margins of the Central Segment of the South Atlantic Ocean: Kinematic constraints: Tectonophysics, v. 468, pp. 98-112.

Baar, C.A. ed., 2013, Applied salt-rock mechanics 1: the in-situ behavior of salt rocks (Vol. 16). Elsevier.

Babel, M. and B.C. Schreiber, 2014, 9.17-Geochemistry of evaporites and evolution of seawater. Treatise on geochemistry, pp. 483-560.

Bacoccoli, G., R.G. Morales, and O.A. Campos, 1980, The Namorado oil field: A major oil discovery in the Campos basin, Brazil.

Bacoccoli, G., R.G. Morales, and P.J.M. De Castro, 1979, Oil Exploration in Campos Basin, Brazil; Model for Exploration in Atlantic-Type Basins: ABSTRACT, pp: 412-412

Badalini, G., B. Kneller, and C.D Winker, 2000, Architecture and processes in the late Pleistocene Brazos-Trinity turbidite system, Gulf of Mexico continental slope. In Deep-Water Reservoirs of the World: SEPM, Gulf Coast Section, 20th Annual Research Conference, pp. 16-34.

Barbeau, D.L., 2003. A flexural model for the Paradox Basin: implications for the tectonics of the Ancestral Rocky Mountains. Basin Research, 15(1), pp. 97-115.

Bate, R.H., 1999, Non-marine ostracod assemblages of the Pre-Salt rift basins of West Africa and their role in sequence stratigraphy: Geological Society, London, Special Publications, v. 153, pp. 283-292.

Beaubouef, R.T. and S.J. Friedmann, 2000, December. High resolution seismic/sequence stratigraphic framework for the evolution of Pleistocene intra slope basins, western

Gulf of Mexico: depositional models and reservoir analogs. In Deep-water reservoirs of the world: Gulf Coast Section SEPM 20th Annual Research Conference (pp. 40-60).

Bell, R.E., C. Jackson, G.M. Elliott, R.L. Gawthorpe, I.R. Sharp, and L., Michelsen, 2014, Insights into the development of major rift-related unconformities from geologically constrained subsidence modelling: Halten Terrace, offshore mid Norway. Basin Research, 26(1), pp. 203-224.

Bertoni, C. and J.A. Cartwright, 2005, 3D seismic analysis of circular evaporite dissolution structures, Eastern Mediterranean. Journal of the Geological Society, 162(6), pp. 909-926.

Bird, D.E., K. Burke, S.A Hall, and J.F Casey, 2005, Gulf of Mexico tectonic history: Hotspot tracks, crustal boundaries, and early salt distribution. AAPG bulletin, 89(3), pp. 311-328.

Black, T.J., 1997, Evaporite karst of northern lower Michigan. Carbonates and Evaporites, 12(1), p. 81.

Booth, J.R., M.C. Dean, A.E. DuVernay, and M.J. Styzen, 2003, Paleo-bathymetric controls on the stratigraphic architecture and reservoir development of confined fans in the Auger Basin: central Gulf of Mexico slope: Marine and Petroleum Geology, v. 20, pp. 563-586.

Braitsch, O., 2012, Salt deposits their origin and composition (Vol. 4). Springer Science & Business Media.

Broucke, O., F. Temple, D. Rouby, C. Robin, S. Calassou, T. Nalpas, and F. Guillocheau, 2004, The role of deformation processes on the geometry of mud-dominated turbiditic systems, Oligocene and Lower–Middle Miocene of the Lower Congo basin (West African Margin): Marine and Petroleum Geology, v. 21, pp. 327-348.

Bruhn, C.H., J.A.T. Gomes, C. Del Lucchese Jr, and P.R. Johann, (2003, January). Campos basin: reservoir characterization and management-Historical overview and future challenges: Offshore Technology Conference.

Bruhn, C.H., and R.G. Walker, 1995, High-resolution stratigraphy and sedimentary evolution of coarse-grained canyon-filling turbidites from the Upper Cretaceous transgressive megasequence, Campos Basin, offshore Brazil: Journal of Sedimentary Research, v. 65 (4).

Brun, J.P., and X. Fort, 2004, Compressional salt tectonics (Angolan margin): Tectonophysics, v. 382, pp. 129-150.

Brun, J.P. and X. Fort, 2011, Salt tectonics at passive margins: Geology versus models. Marine and Petroleum Geology, 28(6), pp. 1123-1145.

Bruthans, J., M. Filippi, N. Asadi, M. Zare, S. Šlechta, and Z. Churáčková, 2009, Surficial deposits on salt diapirs (Zagros Mountains and Persian Gulf Platform, Iran): Characterization, evolution, erosion and the influence on landscape morphology. Geomorphology, 107(3), pp: 195-209.

Burberry, C.M., C.A.L. Jackson, and S.R. Chandler, 2016, Seismic reflection imaging of karst in the Persian Gulf: Implications for the characterization of carbonate reservoirs. AAPG Bulletin, 100(10), pp. 1561-1584.

Burke, K., D.S. MacGregor, and N.R. Cameron, 2003, Africa's petroleum systems: four tectonic 'Aces' in the past 600 million years: Geological Society, London, Special Publications, v. 207, pp. 21-60.

Candido, A., and C.A. Cora, 1992, The Marlim and Albacora Giant Fields, Campos Basin, Offshore Brazil: Chapter 8.

Carminatti, M., B. Wolff, and L. Gamboa, 2008, New Exploratory Frontiers In Brazil, One Petro.19th World Petroleum Congress, June 29 - July 3, 2008 , Madrid, Spain.

Cartwright, J., 2007. The impact of 3D seismic data on the understanding of compaction, fluid flow and diagenesis in sedimentary basins. Journal of the Geological Society, 164(5), pp. 881-893.

Cartwright, J., M. Jackson, T. Dooley, and S. Higgins, 2012, Strain partitioning in gravity-driven shortening of a thick, multilayered evaporite sequence: Geological Society, London, Special Publications, v. 363, pp. 449-470.

Cartwright, J., S. Stewart, and J. Clark, 2001, Salt dissolution and salt-related deformation of the Forth Approaches Basin, UK North Sea. Marine and Petroleum Geology, 18(6), pp. 757-778.

Chang, H.K., R.O. Kowsmann, A.M.F. Figueiredo, and A. Bender, 1992, Tectonics and stratigraphy of the East Brazil Rift system: an overview: Tectonophysics, v. 213, pp. 97-138.

Charts Halliburton Log Interpretaton, 1994, Halliburton Energy Services. Houston, Texas, USA.

Chiesi, M., J. De Waele, and P. Forti, 2010, Origin and evolution of a salty gypsum/anhydrite karst spring: the case of Poiano (Northern Apennines, Italy). Hydrogeology Journal, 18(5), pp. 1111-1124.

Chopra, S., J. Castagna, and O. Portniaguine, 2006. Seismic resolution and thin-bed reflectivity inversion. CSEG recorder, 31(1), pp. 19-25.

Clark, I.R. and J.A. Cartwright, 2009, Interactions between submarine channel systems and deformation in deepwater fold belts: Examples from the Levant Basin, Eastern Mediterranean sea: Marine and Petroleum Geology, v. 26, pp. 1465-1482.

Clark, I.R. and J.A. Cartwright, 2011, Key controls on submarine channel development in structurally active settings: Marine and Petroleum Geology, v. 28, pp. 1333-1349.

Clark, J., S. Stewart, and J.A. Cartwright, 1998, Evolution of the NW margin of the North Permian Basin, UK North Sea: Journal of the Geological Society, v. 155, pp. 663-676.

Clarke, F., 1924, The Data of Geochemistry: US Geological Survey Bull, v. 770, p. 841.

Clauzon, G., J.-P. Suc, F. Gautier, A. Berger, and M.-F, Loutre, 1996, Alternate interpretation of the Messinian salinity crisis: controversy resolved? Geology, 24, pp. 364–366.

Cobbold, P.R., K.E. Meisling, and V.S. Mount, 2001, Reactivation of an Obliquely Rifted Margin, Campos and Santos Basins, Southeastern Brazil: AAPG Bulletin, v. 85, pp. 1925-1944.

Cobbold, P.R., D. Chiossi, P.F. Green, P. Jaspen, and J. Bonow, 2010, "Compressional reactivation of the Atlantic Margin of Brazil: Structural styles and consequences for hydrocarbon exploration." Search Discovery 30114 (2010).

Cobbold, P.R. and P. Szatmari, 1991, Radial gravitational gliding on passive margins: Tectonophysics, v. 188, pp. 249-289.

Cobbold, P.R., P. Szatmari, L.S. Demercian, D. Coelho, and E.A. Rossello, 1995, Seismic and experimental evidence for thin-skinned horizontal shortening by convergent radial gliding on evaporites, deep-water Santos Basin, Brazil.

Cooper, A.H., 1986, Subsidence and foundering of strata caused by the dissolution of Permian gypsum in the Ripon and Bedale areas, North Yorkshire. Geological Society, London, Special Publications, 22(1), pp. 127-139.

Contreras, J., R. Zühlke, S. Bowman, and T. Bechstädt, 2010, Seismic stratigraphy and subsidence analysis of the southern Brazilian margin (Campos, Santos and Pelotas basins): Marine and Petroleum Geology, v. 27, pp. 1952-1980.

Davison, I., 1999, Tectonics and hydrocarbon distribution along the Brazilian South Atlantic margin: Geological Society, London, Special Publications, v. 153, pp. 133-151.

Davison, I., 2007, Geology and tectonics of the South Atlantic Brazilian salt basins: Geological Society, London, Special Publications, v. 272, pp. 345-359.

Davison, I., L. Anderson, and P. Nuttall, 2012, Salt deposition, loading and gravity drainage in the Campos and Santos salt basins: Geological Society, London, Special Publications, v. 363, pp. 159-174.

Davison, I. and R. Bate, 2004, Early opening of the South Atlantic: Berriasian rifting to Aptian salt deposition: PESGB/HGS 3rd International Joint Meeting—Africa: the Continent of Challenge and Opportunity, London, pp. 7-8.

De Freitas, J.T.R. 2006, Ciclos deposicionais evaporiticos da Bacia de Santos: una análise cicloestratigráfica a partir de dados de 2 poços e de tracos de sismica., Universidade Federal do Rio Grande do Sul, Brazil, p. 168.

De Gasperi, A. and O. Catuneanu, 2014, Sequence stratigraphy of the Eocene turbidite reservoirs in Albacora field, Campos Basin, offshore Brazil: AAPG bulletin, v. 98, pp. 279-313.

Demercian, L.S., 1996, A halocinese na evolução do Sul da Bacia de Santos do Aptiano ao Cretáceo Superior, MS thesis. , p. 201.

Demercian, S., P. Szatmari, and P.R. Cobbold, 1993, Style and pattern of salt diapirs due to thin-skinned gravitational gliding, Campos and Santos basins, offshore Brazil: Tectonophysics, v. 228, pp. 393-433.

De Waele, J., L. Plan, and P. Audra, 2009, Recent developments in surface and subsurface karst geomorphology: an introduction.

Dias, J.L. 2004, Tectônica, estratigrafia e sedimentação no Andar Aptiano da margem leste brasileira: Boletim de Geociências da PETROBRAS, v. 13, pp. 7-25.

Dingle, R. 1999, Walvis Ridge barrier: its influence on palaeoenvironments and source rock generation deduced from ostracod distributions in the early South Atlantic Ocean: Geological Society, London, Special Publications, v. 153, pp. 293-302.

Dooley, T.P., M.P Jackson, C.A.L. Jackson, M.R. Hudec, and C.R. Rodriguez, 2015, Enigmatic structures within salt walls of the Santos Basin—Part 2: Mechanical explanation from physical modelling. Journal of Structural Geology, 75, pp. 163-187.

Duarte, C.S. and A.R. Viana, 2007, Santos Drift System: stratigraphic organization and implications for late Cenozoicpalaeocirculation in the Santos Basin, SW Atlantic Ocean. Geological Society, London, Special Publications, 276(1), pp. 171-198.

Duin, E. 2001, A detailed 3D seismic interpretation of a salt dome and its caprock, a case study in the northeastern Netherlands. In SEG Technical Program Expanded Abstracts 2001 (pp. 670-673) Society of Exploration Geophysicists.

Elorza, M.G. and F.G. Santolalla, 1998, Geomorphology of the Tertiary gypsum formations in the Ebro Depression (Spain). Geoderma, 87(1), pp. 1-29.

Enciso, G. and A.L. Tisi, 1998. Santos basin–Merluza field turbidite model revisited. American Association of Petroleum Geologists Search and Discovery Article, 90933.

Eoff, J., K. Whidden, R. Dubiel, S. Hawkins, K. Marra, O. Pearson, and A.J. Pitman, 2013, Expression of Low- to Intermediate-Frequency Cyclicity in Siliciclastic Intervals of the Paradox Formation, Paradox Basin, Utah: Search and Discovery Article #50777. AAPG Rocky Mountain Section meeting.

Evans, R. 1978, Origin and significance of evaporites in basins around Atlantic margin: AAPG Bulletin, v. 62, pp. 223-234.

Evans, M.W., S.W. Snyder, and A.C. Hine, 1994, High-resolution seismic expression of karst evolution within the upper Floridan Aquifer system: Crooked Lake, Polk County, Florida. Journal of Sedimentary Research, 64(2).

Fainstein, R., G. Jamieson, A. Hannan, N. Biles, A. Krueger, and D. Shelander, 2001, October. Offshore Brazil Santos Basin exploration potential from recently acquired seismic data. In 7th International Congress of the Brazilian Geophysical Society.

Fiduk, J.C., and M.G. Rowan, 2012, Analysis of folding and deformation within layered evaporites in Blocks BM-S-8 & -9, Santos Basin, Brazil: Geological Society, London, Special Publications, v. 363, pp. 471-487.

Figueiredo, A., M. Pereira, W. Mohriak, P. Gaglianone, and L. Trinidade, 1985, Salt Tectonics and Oil Accumulation in Campos Basin, Offshore Brazil: ABSTRACT: AAPG Bulletin, v. 69, pp. 255-255.

Fonnesu, F., 2003, 3D seismic images of a low-sinuosity slope channel and related depositional lobe (West Africa deep-offshore): Marine and Petroleum Geology, v. 20, pp. 615-629.

Fort, X., J.-P. Brun, and F. Chauvel, 2004, Salt tectonics on the Angolan margin, synsedimentary deformation processes: AAPG Bulletin, v. 88, pp. 1523-1544.

Friedman, G.M., 1997, Dissolution-collapse breccias and paleokarst resulting from dissolution of evaporite rocks, especially sulfates. Carbonates and Evaporites, 12(1), pp. 53-63.

Frumkin, A., 1994, Hydrology and denudation rates of halite karst. Journal of Hydrology, 162(1-2), pp. 171-189.

Frumkin, A., 2013, Salt karst. Treatise on geomorphology, 6, pp. 407-424.

Frumkin, A. and E. Raz, 2001, Collapse and subsidence associated with salt karstification along the Dead Sea. Carbonates and Evaporites, 16(2), pp. 117-130.

Galve, J. P., F. Gutiérrez, J. Remondo, J. Bonachea, P. Lucha, and A. Cendrero, 2009, Evaluating and comparing methods of sinkhole susceptibility mapping in the Ebro Valley evaporite karst (NE Spain). Geomorphology, 111(3), pp: 160-172.

Gamboa, D., T. Alves, J. Cartwright, and P. Terrinha, 2010, MTD distribution on a 'passive'continental margin: the Espírito Santo Basin (SE Brazil) during the Palaeogene: Marine and Petroleum Geology, v. 27, pp. 1311-1324.

Gambôa, L.A. P., M.A.P. Machado, D.P. Silveira, J.T.R. De Freitas, and S.R.P. Da Silva, 2008, Evaporitos estratificados no Atlantico Sul: Interpretacao sismica e controle tectono-estratigrafino na Bacia de Santos.: In Mohriak, W., Szatmari, P. & Anjos, S.M.C. Sal: Geologia e Tectonica, Exemplos nas Basicas Brasileiras., v. Beca Edicoes Ltda, São Paulo, Brasil, pp. 340-359.

Ge, H. and M.P. Jackson, 1998, Physical modeling of structures formed by salt withdrawal: Implications for deformation caused by salt dissolution. AAPG bulletin, 82(2), pp. 228-250.

Ge, H., M.P.A. Jackson, and B.C. Vendeville, 1997, Kinematics and dynamics of salt tectonics driven by progradation: AAPG Bulletin, v. 81, pp. 398-423.

Gee, M., and R. Gawthorpe, 2006, Submarine channels controlled by salt tectonics: Examples from 3D seismic data offshore Angola: Marine and Petroleum Geology, v. 23, pp. 443-458.

Gee, M., and R. Gawthorpe, 2007, Early evolution of submarine channels offshore Angola revealed by three-dimensional seismic data: Geological Society, London, Special Publications, v. 277, pp. 223-235.

Gee, M., R. Gawthorpe, and S. Friedmann, 2006, Triggering and evolution of a giant submarine landslide, offshore Angola, revealed by 3D seismic stratigraphy and geomorphology: Journal of Sedimentary Research, v. 76, pp. 9-19.

George, M., O.K. Olakunle, J.S. Emil, and P. Abrahamson, 2017, Seismic interpretation and characterization of anhydrite caprocks in the Tromsø Basin, SW Barents Sea. Marine Geology, 390, pp. 36-50.

Giles, K.A., T.F. Lawton, A. Shock, R.A. Kernen, T.E. Hearon, and M.G. Rowan, 2012. A halokinetic drape-fold Model for Caprock in diapir-flanking and subsalt positions. In AAPG 2012 Annual Convention Abstracts Volume, Long Beach, Calif.

Giles, K.A., and M.G. Rowan, 2012, Concepts in halokinetic-sequence deformation and stratigraphy: Geological Society, London, Special Publications, v. 363, pp. 7-31.

Gladczenko, T., K. Hinz, O. Eldholm, H. Meyer, S. Neben, and J. Skogseid, 1997, South Atlantic volcanic margins: Journal of the Geological Society, v. 154, pp. 465-470.

Glennie, K.W., J. Higham, and L. Stemmerik, 2003, The Permian of the Northern North Sea. In Millennium Atlas: Petroleum Geology of the Central and Northern North Sea (pp. 91-103). Geological Society of London.

Gomes, P.O., B. Kilsdonk, J. Minken, T. Grow, and R. Barragan, 2009, The outer high of the Santos Basin, Southern São Paulo Plateau, Brazil: pre-salt exploration outbreak, paleogeographic setting, and evolution of the syn-rift structures: American Association of Petroleum Geologists Search and Discovery Article, v. 10193.

Gomes, P.O., J. Parry, and W. Martins, 2002, The outer high of the Santos Basin, southern São Paulo Plateau, Brazil: tectonic setting, relation to volcanic events and some comments on hydrocarbon potential: AAPG Hedberg Conference,'Hydrocarbon Habitat of Volcanic Rifted Passive Margins, pp. 8-11.

Goteti, R., S.J. Ings, and C. Beaumont, 2012, Development of salt minibasins initiated by sedimentary topographic relief: Earth and Planetary Science Letters, v. 339, pp. 103-116.

Guardado, L.R., L.A. Gamboa, and C.F. Lucchesi, 1989, Petroleum Geology of the Campos Basin, Brazil, a Model for a producing atlantic type basin: part 1. Guardado, L., A. Spadini, J. Brandão, and M. Mello, 2000, AAPG Memoir 73, Chapter 22: Petroleum System of the Campos Basin, Brazil.

Guerra, M.C.M., and J.R. Underhill, 2012, Role of halokinesis in controlling structural styles and sediment dispersal in the Santos Basin, offshore Brazil: Geological Society, London, Special Publications, v. 363, pp. 175-206.

Gutiérrez, F., J. Guerrero, and P. Lucha, 2008, A genetic classification of sinkholes illustrated from evaporite paleokarst exposures in Spain. Environmental Geology, 53(5), pp. 993-1006.

Gutiérrez, F., and I. Lizaga, 2016, Sinkholes, collapse structures and large landslides in an active salt dome submerged by a reservoir: The unique case of the Ambal ridge in the Karun River, Zagros Mountains, Iran. Geomorphology, 254, pp. 88-103.

Gutiérrez, F., M. Parise, J. De Waele, and H. Jourde, 2014, A review on natural and human-induced geohazards and impacts in karst. Earth-Science Reviews, 138, pp. 61-88.

Hadler-Jacobsen, F., M.H. Gardner, and J.M. Borer, 2007, Seismic stratigraphic and geomorphic analysis of deep-marine deposition along the West African continental margin: Geological Society, London, Special Publications, v. 277, pp. 47-84.

Hallager, W.S., Ulrich, M.R., Kyle, J.R., Price, P.E. and Gose, W.A., 1990. Evidence for episodic basin dewatering in salt-dome cap rocks. Geology, 18(8), pp.716-719.

Hardage, B.A., D.L. Carr, D.E. Lancaster, J.L. Simmons Jr, R.Y. Elphick, V.M. Pendleton, and R.A. Johns, 1996, 3-D seismic evidence of the effects of carbonate karst collapse on overlying clastic stratigraphy and reservoir compartmentalization. Geophysics, 61(5), pp. 1336-1350.

Hart, B., 2008, Stratigraphically significant attributes: The Leading Edge, v. 27, pp. 320-324.

Hearon IV, T.E., M.G. Rowan, K.A. Giles, and W.H. Hart, 2014, Halokinetic deformation adjacent to the deepwater Auger diapir, Garden Banks 470, northern Gulf of Mexico: Testing the applicability of an outcrop-based model using subsurface data: Interpretation, v. 2, pp. SM57-SM76.

Helle, H.B., A. Bhatt, and B. Ursin, 2001, Porosity and permeability prediction from wireline logs using artificial neural networks: a North Sea case study. Geophysical Prospecting, 49(4), pp. 431-444.

Horschutz, P.M.C., L. Freitas, C.V. Stank, A.D.S. Barroso, W. Cruz, and M. Halbouty, 1978, The Linguado, Carapeba, Vermelho and Marimbá Giant Fields, Campos Basin, Offshore Brazil: Giant oil and gas fields of the decade, v. 1988, pp. 137-153.

Hovorka, S.D., 2000, Understanding the Process of Salt Dissolution and Subsidence. Solution Mining Research Institute Proceedings.

Hsü, K.J., 1972, Origin of saline giants: a critical review after the discovery of the Mediterranean evaporite: Earth-Science Reviews, 8(4), pp. 371-396.

Hsü, K.J., W.B.F. Ryan, and M.B. Cita, 1973, Late Miocene desiccation of the Mediterranean. Nature, 242(5395), pp. 240-244.

Hübscher, C., J. Cartwright, H. Cypionka, G. J. De Lange, A. Robertson, J.-P. Suc, and J. L. Urai, 2007, Global Look at Salt Giants: E.O.S., v. 88, pp. 177-182.

Hudec, M.R., and M.P.A. Jackson, 2007, Terra infirma: Understanding salt tectonics: Earth-Science Reviews, v. 82, pp. 1-28.

Hudec, M.R., M.P. Jackson, and D.D. Schultz-Ela, 2005, A Compressional Origin for Minibasins near the Sigsbee Scarp, Gulf of Mexico.

Hudec, M.R., M.P.A. Jackson, and D.D. Schultz-Ela, 2009, The paradox of minibasin subsidence into salt: Clues to the evolution of crustal basins: Geological Society of America Bulletin, v. 121, pp. 201-221.

Hudec, M.R., M.P. Jackson, B.C. Vendeville, D.D. Schultz-Ela, and T.P. Dooley, 2011, The salt mine: A digital atlas of salt tectonics.

Imbert, P., and Y. Philippe (2005, December), The Mesozoic opening of the Gulf Coast of Mexico: Part 2: Integrating seismic and magnetic data into a general opening model. In Petroleum systems of divergent continental margin basins: 25th Annual Gulf Coast Section SEPM Foundation Bob F. Perkins Research Conference, Houston, Texas, pp. 1151–1189.

Jackson, C.A.L., 2011, Three-dimensional seismic analysis of megaclast deformation within a mass transport deposit; implications for debris flow kinematics. Geology, 39(3), pp. 203-206.

Jackson, C.A.L., 2012, The initiation of submarine slope failure and the emplacement of mass transport complexes in salt-related minibasins: A three-dimensional seismic-reflection case study from the Santos Basin, offshore Brazil: Geological Society of America Bulletin, v. 124, pp. 746-761.

Jackson, M.P.A., R.R. Cornelius, C.H. Craig, A. Gansser, J. Stöcklin, and C.J. Talbot, 1990, Salt diapirs of the Great Kavir, central Iran. Geological Society of America Memoirs, 177, pp. 1-150.

Jackson, M.P.A., C. Cramez, and J.-M. Fonck, 2000, Role of subaerial volcanic rocks and mantle plumes in creation of South Atlantic margins: implications for salt tectonics and source rocks: Marine and Petroleum Geology, v. 17, pp. 477-498.

Jackson, M.P. and M.R. Hudec, 2017. Salt Tectonics: Principles and Practice. Cambridge University Press. pp. 424-428 .

Jackson, C.A.L., M.P. Jackson, and M.R., Hudec, 2015a, Understanding the kinematics of salt-bearing passive margins: A critical test of competing hypotheses for the origin of the Albian Gap, Santos Basin, offshore Brazil. Geological Society of America Bulletin, v. 127(11-12), pp. 1730-1751.

Jackson, C. A.L., M.P. Jackson, M.R. Hudec, and C.R. Rodriguez, 2014a, Internal structure, kinematics, and growth of a salt wall: Insights from 3-D seismic data: Geology, v. 42, pp. 307-310.

Jackson, C.A.L., M.P.A. Jackson, M.R. Hudec, and C.R. Rodriguez, 2015b, Enigmatic structures within salt walls of the Santos Basin—Part 1: Geometry and kinematics from 3D seismic reflection and well data: Journal of Structural Geology, v. 75, pp. 135-162.

Jackson, C.A., K.E. Kane, and E. Larsen, 2010, Structural evolution of minibasins on the Utsira High, northern North Sea; implications for Jurassic sediment dispersal and reservoir distribution. Petroleum Geoscience, 16(2), pp. 105-120.

Jackson, C.A.L. and M.M Lewis, 2012, Origin of an anhydrite sheath encircling a salt diapir and implications for the seismic imaging of steep-sided salt structures, Egersund Basin, Northern North Sea. Journal of the Geological Society, 169(5), pp. 593-599.

Jackson, C.A.L. and M.M. Lewis, 2013, Physiography of the NE margin of the Permian Salt Basin: new insights from 3D seismic reflection data: Journal of the Geological Society, v. 170, pp. 857-860.

Jackson, C.A.L. and M.M. Lewis, 2016, Structural style and evolution of a salt-influenced rift basin margin; the impact of variations in salt composition and the role of polyphase extension. Basin Research 28(1): 81-102.

Jackson, C.A.L., M.M. Lewis, and A.S. Mannie, 2013. Characterization and origin of anhydrite-rich 'lateral caprock'adjacent to halite-cored salt diapirs; implications for prospectivity in salt basins. In AAPG 2013 Annual Convention and Exhibition, Pittsburgh, Pennsylvania, May 19–22, 2013.

Jackson, C.A.L., C.R. Rodriguez, A. Rotevatn, and R.E. Bell, 2014b, Geological and geophysical expression of a primary salt weld: An example from the Santos Basin, Brazil: Interpretation, v. 2, pp. SM77-SM89.

Jackson, M.P.A. and S.J. Seni, 1984, The domes of East Texas, pp. 163-179.

Jackson, M. and C.J. Talbot, 1991, A glossary of salt tectonics, Bureau of Economic Geology, University of Texas at Austin.

Janocko, M., W. Nemec, S. Henriksen, and M. Warchoł, 2013, The diversity of deep-water sinuous channel belts and slope valley-fill complexes: Marine and Petroleum Geology, v. 41, pp. 7-34.

Jaworska, J. and M. Nowak, 2013, Anhydrites from gypsum cap-rock of Zechstein salt diapirs. Geology, Geophysics and Environment, 39(3), pp. 233-250.

Johnson, K.S., 2005. Subsidence hazards due to evaporite dissolution in the United States. Environ Geol, 48 (3), pp. 395-409.

Johnson, K.S., 2008. Evaporite-karst problems and studies in the USA. Environmental Geology, 53(5), pp. 937-943.

Jones, I.F. and I. Davison, 2014, Seismic imaging in and around salt bodies. Interpretation, 2(4), pp. SL1-SL20.

Jones, G., M. Mayall, and L. Lonergan, 2012, Contrasting depositional styles on a slope system and their control by salt tectonics: through-going channels, ponded fans, and mass transport complexes: Rosen, NC, Weimer, P., Coutes dos Anjos SM, Henrickson, S., Marques, E., Mayall, M., Fillon, pp. 40-60.

Karner, G. D., N.W. Driscoll, and D. H. N. Barker, 2003, Syn-rift regional subsidence across the West African continental margin: the role of lower plate ductile extension: Geological Society, London, Special Publications, v. 207, pp. 105-129.

Karner, G.D. and L.A.P. Gambôa, 2007, Timing and origin of the South Atlantic pre-salt sag basins and their capping evaporites: Geological Society, London, Special Publications, v. 285, pp. 15-35.

Kendall, A.C., 1978, Facies models 12. Subaqueous evaporites. Geoscience Canada, 5(3).

Kolla, V., and J. Urruty, 2000, Ph. Bourges 'Evolution of a deep-water Tertiary sinuous channel offshore Angola (Africa) and implications to reservoir architecture': AAPG Bulletin, p. 1373.

Koyi, H., 1998, The shaping of salt diapirs. Journal of Structural Geology, 20(4), pp. 321-338.

Koyi, H., C.J. Talbot and B.O. Torudbakken, 1995, Analogue models of salt diapirs and seismic interpretation in the Nordkapp Basin, Norway. Petroleum geoscience, 1(2), pp. 185-192.

Krijgsman, W., F.J. Hilgen, I. Raffi, F.J. Sierro, and D.S. Wilson, 1999, Chronology, causes and progression of the Messinian salinity crisis: Nature, v. 400, pp. 652-655.

Kupfer, D.H., 1968, Relationship of internal to external structure of salt domes. American Association of Petroleum Geologists. Memoir 8. 79-80.

Kyle, J.R., 1999, Industrial-Mineral Resources Associated with Salt Domes, Gulf of Mexico Basin, USA. In Proceedings of the 34th Forum on the Geology of Industrial Minerals: Oklahoma Geological Survey, Circular (Vol. 102, pp. 161-178).

Kyle, J.R. and H.H. Posey, 1991, Halokinesis, cap rock development, and salt dome mineral resources. Developments in sedimentology, 50, pp. 413-474.

Land, L.S., J.A. Kupecz, and L.E. Mack, 1988. Louann salt geochemistry (Gulf of Mexico sedimentary basin, USA): a preliminary synthesis. Chemical Geology, 74(1-2), pp. 25-35.

Laznicka, P., 1988, Breccias and coarse fragmentites: petrology, environments, associations, ores (Vol. 25). Amsterdam; New York: Elsevier.

Lentini, M.R., S. I. Fraser, H.S. Sumner, and R.J. Davies, 2010, Geodynamics of the central South Atlantic conjugate margins: implications for hydrocarbon potential: Petroleum Geoscience, v. 16, pp. 217-229.

Liu, Z. and J. Li, 2011. Control of salt structures on hydrocarbons in the passive continental margin of West Africa. Petroleum Exploration and Development, 38(2), pp. 196-202.

Loncke, L., V. Gaullier, J. Mascle, B. Vendeville, and L. Camera, 2006, The Nile deep-sea fan: an example of interacting sedimentation, salt tectonics, and inherited subsalt paleotopographic features: Marine and Petroleum Geology, v. 23, pp. 297-315.

Lopes, M.R.F., C.H.L. Bruhn, R.A. Santos, C.A.G. Corá, M.R. Becker, R.R.P. Alves, and D.J. Sarzenski, 1999, Architecture of Sand-Rich, Turbidite Reservoirs from Deep Water Campos Basin, Brazil: 1999 AAPG Conference & Exhibition, San Antonio, Texas.

Loucks, R.G., 1999, Paleocave carbonate reservoirs: origins, burial-depth modifications, spatial complexity, and reservoir implications. AAPG bulletin, 83(11), pp. 1795-1834.

Lugli, S., V. Manzi, and M. Roveri, 2008, New facies interpretation of the Messinian evaporites in the Mediterranean. In CIESM Workshop Monogr (Vol. 33, pp. 67-72).

Macedo, J., L.A.P. Gamboa, J.A. Ricci, L.F.G. Caddah, and W. Winter, 1998, Stratigraphic comparisons between the post-rift section of the Campos and Santos Basins, Southeast Brazilian margin: Extended Abstracts, AAPG: ABGP/AAPG International Conference and Exhibition, Rio de Janeiro.

Machado, L.C.R., R.O. Kowsmann, W. Almeida-Jr, C.Y. Murakami, S. Schreiner, D.J. Miller, and P. Piauilino, 2004, Geometria da porção proximal do sistema deposicional turbidítico moderno da Formação Carapebus, Bacia de Campos: modelo para heterogeneidades de reservatório: Boletim de Geociências da Petrobras, v. 12, pp. 287-315.

Machel, H.G., M.L. Borrero, E. Dembicki, H. Huebscher, L. Ping, and Y. Zhao, 2012, The Grosmont: the world's largest unconventional oil reservoir hosted in carbonate rocks. Geological Society, London, Special Publications, 370(1), pp. 49-81.

Manzi, V., R. Gennari, S. Lugli, M. Roveri, N. Scafetta, and B.C. Schreiber, 2012, High-frequency cyclicity in the Mediterranean Messinian evaporites: evidence for solar–lunar climate forcing: Journal of Sedimentary Research, v. 82, pp. 991-1005.

Marton, L., G.C. Tari, and C.T. Lehmann, 2000, Evolution of the Angolan Passive Margin, West Africa, With Emphasis on Post-Salt Structural Styles: Atlantic rifts and continental margins, pp. 129-149.

Massoth, T.W. and B.T. Tripp, 2011, Well Database of Salt Cycles of the Paradox Basin, Utah, Utah Geological Survey.

Mayall, M., L. Lonergan, A. Bowman, S. James, K. Mills, T. Primmer, D. Pope, L. Rogers, and R. Skeene, 2010, The response of turbidite slope channels to growth-induced seabed topography: AAPG bulletin, v. 94, pp. 1011-1030.

Mayall, M. and C. O'Byrne, 2012, January. Reservoir prediction and development challenges in turbidite slope channels. In Offshore Technology Conference. Offshore Technology Conference.

Mayall, M. and I. Stewart, 2000, The architecture of turbidite slope channels: Deep-Water Reservoirs of the World: SEPM, Gulf Coast Section, 20th Annual Research Conference, p. 586.

Meisling, K.E., P.R. Cobbold, and V.S. Mount, 2001, Segmentation of an Obliquely Rifted Margin, Campos and Santos Basins, Southeastern Brazil: AAPG Bulletin, v. 85, pp. 1903-1924.

Modica, C.J. and E.R. Brush, 2004, Postrift sequence stratigraphy, paleogeography, and fill history of the deep-water Santos Basin, offshore southeast Brazil: AAPG Bulletin, v. 88, pp. 923-945.

Mohriak, W.U., J. Lira Rabelo, R.D. De Matos, and M.C. De Barros, 1995, Deep seismic reflection profiling of sedimentary basins offshore Brazil: Geological objectives and preliminary results in the Sergipe Basin: Journal of Geodynamics, v. 20, pp. 515-539.

Mohriak, W., M. Mello, J. Dewey, and J. Maxwell, 1990, Petroleum geology of the Campos Basin, offshore Brazil: Geological Society, London, Special Publications, v. 50, pp. 119-141.

Mohriak, W. and P. Szatmari, 2008, Introdução às propriedades químicas e físicas dos evaporitos. Webster Mohriak, Peter Szatmari & Sylvia Couto Anjos, Sal: Geologia e Tectônica: Exemplos das Bacias Brasileiras. Rio de Janeiro: Beca, p. 19.

Mohriak, W., P. Szatmari, and S. Anjos, 2009, Sal Geologia e Tectônica. Terrae Didatica, 4, pp. 90-91.

Mohriak, W., P. Szatmari, and S. Anjos, 2012, Salt: geology and tectonics of selected Brazilian basins in their global context: Geological Society, London, Special Publications, v. 363(1), pp. 131-158.

Montaron, B. and P. Tapponier, 2010, A quantitative model for salt deposition in actively spreading basins, American Association of Petroleum Geologists, Search and Discovery. Article 30117.

Moraes, M.A., 1989, Diagenetic evolution of Cretaceous-Tertiary turbidite reservoirs, Campos Basin, Brazil: AAPG Bulletin, v. 73, pp. 598-612.

Moraes, M.A., P.R. Blaskovski, and P. Joseph, 2004, The Grèsd'Annot as an analogue for Brazilian Cretaceous sandstone reservoirs: comparing convergent to passive-margin confined turbidites: Geological Society, London, Special Publications, v. 221, pp. 419-437.

Moreira, J.L.P., C. Madeira, J.A. Gil, and M.A.P. Machado, 2007, Bacia de Santos: BulletinGeociencias Petrobras, v. 15, pp. 531-549.

Nunn, J.A. and N.B. Harris, 2007, Subsurface seepage of seawater across a barrier: A source of water and salt to peripheral salt basins: Geological Society of America Bulletin, v. 119, pp. 1201-1217.

Oard, M.J., 2005. The Messinian salinity crisis questioned. Journal of Creation, 19(1), pp. 11-13.

Oluboyo, A., R. Gawthorpe, K. Bakke, and F. Hadler-Jacobsen, 2014, Salt tectonic controls on deep-water turbidite depositional systems: Miocene, southwestern Lower Congo Basin, offshore Angola: Basin Research, v. 26, pp. 597-620.

Palagi, P., 2008, Evaporitos no Brasil e na América do Sul: Sal: Geologia e Tectônica. Editora Beca, São Paulo, pp. 188-207.

Pessoa, J., C.C. Martins, J. Heinerici, R.J. Jahnert, A.B. França, L. Trindade, and C. Francisco, 1999, Petroleum System And Seismic Expression In The Campos Basin: 6th International Congress of the Brazilian Geophysical Society.

Pettingill, H.S. and P. Weimer, 2002, Worlwide deepwater exploration and production: Past, present, and future. The Leading Edge, 21(4), pp. 371-376.

Pilcher, R. and J. Argent, 2007, Mega-pockmarks and linear pockmark trains on the West African continental margin. Marine Geology, 244(1), pp. 15-32.

Pilcher, R.S. and R.D. Blumstein, 2007, Brine volume and salt dissolution rates in Orca Basin, northeast Gulf of Mexico. AAPG bulletin, 91(6), pp. 823-833.

Pilcher, R.S., B. Kilsdonk, and J. Trude, 2011, Primary basins and their boundaries in the deep-water northern Gulf of Mexico: Origin, trap types, and petroleum system implications. AAPG bulletin, 95(2), pp. 219-240.

Poiate Jr, E., A. Maia, and J.L. Falcao, 2006, Well Design for Drilling Through Thick Evaporite Layers: IADC/SPE Drilling Conference. Society of Petroleum Engineers.

Posamentier, H.W. and V. Kolla, 2003, Seismic geomorphology and stratigraphy of depositional elements in deep-water settings: Journal of Sedimentary Research, v. 73, pp. 367-388.

Posey, H.H. and J.R., Kyle, 1988, Fluid-rock interactions in the salt dome environment: an introduction and review. Chemical Geology, 74(1-2), pp. 1-24.

Prather, B.E., J.R. Booth, G.S. Steffens, and P.A. Craig, 1998, Classification, lithologic calibration, stratigraphic succession of seismic facies of intraslope basins, deep-water Gulf of Mexico. AAPG bulletin, 82(5), pp. 701-728.

Pratson, L.F. and W.B. Ryan, 1994. Pliocene to recent infilling and subsidence of intraslope basins offshore Louisiana. AAPG bulletin, 78(10), pp. 1483-1506.

Prothero, D.R. and F. Schwab, 2004, Sedimentary geology. Macmillan.

Randen, T. and L. Sønneland, 2005, Atlas of 3D seismic attributes. In Mathematical Methods and Modelling in Hydrocarbon Exploration and Production (pp. 23-46). Springer Berlin Heidelberg.

Reston, T. J., 2010, The opening of the central segment of the South Atlantic: symmetry and the extension discrepancy: Petroleum Geoscience, v. 16, pp. 199-206.

Reuning, L., J. Schoenherr, A. Heimann, J.L. Urai, R. Littke, P.A. Kukla, and, Z. Rawahi, 2009, "Constraints on the diagenesis, stratigraphy and internal dynamics of the surface-piercing salt domes in the Ghaba Salt Basin (Oman): A comparison to the Ara Group in the South Oman Salt Basin." GeoArabia 14(3), pp. 83-120.

Richter-Bernburg, G., 1973, Paleogeographical Pre-conditions for the Genesis of Evaporites. In Congresso Brasileiro de Geologia, Vol. 27, pp. 163-169.

Riddle, T.W., D.K. Purcell, J.E. Kruger, and Y. Shoham, 1995, August, Seismic Modelling and Amplitude Analysis for Reservoir Prediction--Merluza Gas Development, Offshore Brazil. In 4th International Congress of the Brazilian Geophysical Society.

Roberts, A.M., R.I. Corfield, N.J. Kusznir, S.J., Matthews, E.K. Hansen, and R.J. Hooper, 2009. Mapping palaeostructure and palaeobathymetry along the Norwegian Atlantic continental margin: Møre and Vøring basins. Petroleum Geoscience, 15(1), pp. 27-43.

Rodriguez, C.R., C.A.L. Jackson, R.E. Bell, A. Rotevatn, and M. Francis, In press (b). Minibasin development and reservoir deposition on a salt-influenced deep-water slope: Santos Basin, offshore Brazil. To be submmited to the AAPG Bulletin.

Rodriguez, C.R., C.A.L. Jackson, A. Rotevatn, R.E. Bell, and M. Francis, In press (a). Stratigraphy of salt giants: new insights from the Santos Basin, offshore Brazil. Submitted to Geosphere.

Roveri, M., S. Lugli, V. Manzi, and B.C. Schreiber, 2008, The shallow-to deep-water record of the Messinian salinity crisis: new insights from Sicily, Calabria and Apennine basins. In CIESM Workshop Monographs (Vol. 33, pp. 73-82).

Rowan, M.G., F.J. Peel, and B.C. Vendeville, 2004, Gravity-driven fold belts on passive margins, in K.R. McClay, ed., Thrust tectonics and hydrocarbon systems: AAPG Memoir 82, pp. 157-182.

Rowan, M.G. and B.C. Vendeville, 2006, Foldbelts with early salt withdrawal and diapirism: Physical model and examples from the northern Gulf of Mexico and the Flinders Ranges, Australia. Marine and Petroleum Geology, 23(9), pp. 871-891.

Rowan, M.G. and P. Weimer, 1998, Salt-sediment interaction, northern Green Canyon and Ewing bank (offshore Louisiana), northern Gulf of Mexico. AAPG bulletin, 82(5), pp. 1055-1082.

Samuel, A., B. Kneller, S. Raslan, A. Sharp, and C. Parsons, 2003, Prolific deep-marine slope channels of the Nile Delta, Egypt. AAPG Bulletin, 87(4), pp. 541-560.

Savic, M., 2006, Sonic-density relationship for Southern North Sea evaporites. In SEG Technical Program Expanded Abstracts 2006 (pp. 2082-2086). Society of Exploration Geophysicists.

Schenk, P.E., P.H. von Bitter, and R. Matsumoto, 1994, Deep-basin/deep-water carbonate-evaporite deposition of a saline giant: Loch Macumber (Visean), Atlantic Canada. Carbonates and Evaporites, 9(2), pp. 187-210.

Schlumberger, 2012, Interpreter's guide to seismic attribuite, 4th edition, pp. 112-114.

Schlumberger Limited, 1991, Log Interpretation Principles/Applications. Schlumberger Educational Services.

Schmalz, R.F., 1969, Deep-water evaporite deposition: a genetic model. AAPG Bulletin, 53(4), pp. 798-823.

Schoenherr, J., R. Littke, J.L. Urai, P.A. Kukla, and Z. Rawahi, 2007, "Polyphase thermal evolution in the Infra-Cambrian Ara Group (South Oman Salt Basin) as deduced by maturity of solid reservoir bitumen." Organic Geochemistry 38(8), pp. 1293-1318.

Schreiber, B.C. and M.E. Tabakh, 2000, Deposition and early alteration of evaporites. Sedimentology, 47(s1), pp. 215-238.

Scotchman, I.C, G. Gilchrist, N. Kusznir, A. Roberts, and R. Fletcher, 2010, January, The breakup of the South Atlantic Ocean: formation of failed spreading axes and blocks of thinned continental crust in the Santos Basin, Brazil and its consequences for

petroleum system development: Geological Society, London, Petroleum Geology Conference series (Vol. 7, No. 1, pp. 855-866).

Scotchman, I.C., G. Marais-Gilchrist, F.G.D. Souza, F.F. Chaves, L.A. Atterton, A.M. Roberts, and N. J. Kusznir, 2006, A failed sea-floor-spreading centre, Santos Basin, Brazil: Rio Oil & Gas Expo and Conference, Rio de Janeiro.

Scott, E., F. Peel, C. Taylor, W. Bryant, and D. Bean, 2001, January. Deep water Gulf of Mexico sea floor features revealed through 3D seismic. In Offshore Technology Conference. Offshore Technology Conference.

Shokes, R.F., P.K., Trabant, B.J. Presley, and D.F. Reid, 1977, Anoxic, hypersaline basin in the northern Gulf of Mexico. Science, 196(4297), pp. 1443-1446.

Sinclair, H.D. and M. Tomasso, 2002, Depositional evolution of confined turbidite basins. Journal of Sedimentary Research, 72(4), pp. 451-456.

Smith, R.U., 2004. Silled sub-basins to connected tortuous corridors: sediment distribution systems on topographically complex sub-aqueous slopes. Geological Society, London, Special Publications, 222(1), pp. 23-43.

Stafford, K.W., R. Nance, L. Rosales-Lagarde, and P.J. Boston, 2008, Epigene and hypogene karst manifestations of the Castile Formation: Eddy County, New Mexico and Culberson County, Texas, USA.

Stefano, L., M. Vinicio, R. Marco, and S.B. Charlotte, 2010, The Primary Lower Gypsum in the Mediterranean: a new facies interpretation for the first stage of the Messinian salinity crisis: Palaeogeography, Palaeoclimatology, Palaeoecology, v. 297, pp. 83-99.

Stewart, S.A., 2007, Salt tectonics in the North Sea Basin: a structural style template for seismic interpreters: Geological Society, London, Special Publications, v. 272, pp. 361-396.

Stewart, S. A. and J.A. Clark, 1999, Impact of salt on the structure of the Central North Sea hydrocarbon fairways: Geological Society, London, Petroleum Geology Conference series, v. 5, pp. 179-200.

Strakhov, N.M., J.P. Fitzsimmons, and R.C. Murray, 1972, Principles of Lithogenesis. Soil Science, 114(5), p. 408.

Strozyk, F., H. Van Gent, J. Urai, and P. Kukla, 2012, 3D seismic study of complex intra-salt deformation: An example from the Upper Permian Zechstein 3 stringer, western Dutch offshore: Geological Society, London, Special Publications, v. 363, pp. 489-501.

Suarez, Y., K.F., Marfurt,and M. Falk, 2008, Seismic attribute-assisted interpretation of channel geometries and infill lithology: A case study of Anadarko basin Red Fork channels. In SEG Technical Program Expanded Abstracts 2008 (pp. 963-967). Society of Exploration Geophysicists.

Sullivan, E.C., K.J., Marfurt, A., Lacazette, and M., Ammerman, 2006, Application of new seismic attributes to collapse chimneys in the Fort Worth Basin. Geophysics, 71(4), pp. B111-B119.

Szatmari, P., 2000, AAPG Memoir 73, Chapter 6: Habitat of Petroleum Along the South Atlantic Margins, pp. 69-75.

Szatmari, P., R. Carvalho, and I. Simoes, 1979, A comparison of evaporite facies in the late Paleozoic Amazon and the Middle Cretaceous South Atlantic salt basins: Economic Geology, v. 74, pp. 432-447.

Szatmari, P., R.D. Carvalho, I.A. Simoes, P. Tibana, and D.C. Leite, 1974, Evaporitos de Sergipe. Geologia e geoquımica. Petrobras Projeto Evaporitos, 1, p. 159.

Szatmari, P., M.C.M. Guerra, and M. A. Pequeno, 1996, Genesis of large counter-regional normal fault by flow of Cretaceous salt in the South Atlantic Santos Basin, Brazil: Geological Society, London, Special Publications, v. 100, pp. 259-264.

Talbot, C. and N. Augustin, 2016, Submarine Salt Karst Terrains. AIMS Geosciences, 2(2), pp. 182-200.

Taylor, J.C.M., 1985, The role of evaporites in hydrocarbon exploration. Joint Association of Petroleum Explorationists (UK). Course notes, (39).

Taylor, J., 1990, Upper Permian—Zechstein: Petroleum Geology of the North Sea: Basic Concepts and Recent Advances, Fourth Edition, pp. 174-211.

Tompkins, R.E. and L.E., Shephard, 1979, Orca Basin: Depositional processes, geotechnical properties and clay mineralogy of Holocene sediments within an anoxic hypersaline basin, northwest Gulf of Mexico. Marine Geology, 33(3-4), pp. 221-238.

Torsvik, T.H., S. Rousse, C. Labails, and M.A. Smethurst, 2009, A new scheme for the opening of the South Atlantic Ocean and the dissection of an Aptian salt basin: Geophysical Journal International, v. 177, pp. 1315-1333.

Trudgill, B., 2011, Evolution of salt structures in the northern Paradox Basin: controls on evaporite deposition, salt wall growth and supra-salt stratigraphic architecture: Basin Research, v. 23, pp. 208-238.

Tucker, R.M. and J.R. Cann, 1986, A model to estimate the depositional brine depths of ancient halite rocks: implications for ancient subaqueous evaporite depositional environments. Sedimentology, 33(3), pp. 401-412.

Tucker, M.E., 1991, Sequence stratigraphy of carbonate-evaporite basins: models and application to the Upper Permian (Zechstein) of northeast England and adjoining North Sea: Journal of the Geological Society, v. 148, pp. 1019-1036.

Usiglio, J., 1849, Analyse de l'eau de la Mediterranee sur les cotes de France. Annalen der Chemie, v. 27, pp. 92-107, 172-191: Ann. Chem. Phys., 3rd. Ser., 28.

Vahrenkamp, V.C., F. David, P. Duijndam, M. Newall, and P. Crevello, 2004, Growth architecture, faulting, and karstification of a middle Miocene carbonate platform, Luconia Province, offshore Sarawak, Malaysia, in Seismic imaging of carbonate reservoirs and systems: AAPG Memoir 81, pp. 329-350.

Valyashko, M.G., 1956, Geochemistry of bromine in the processes of salt deposition and the use of the bromine content as a genetic and prospecting criterion. Geochemistry, 6, pp. 570-589.

Van Gent, H., J.L. Urai, and M. de Keijzer, 2011, The internal geometry of salt structures – A first look using 3D seismic data from the Zechstein of the Netherlands: Journal of Structural Geology, v. 33, pp. 292-311.

Veeken, P.C.H. and M. Da Silva, 2004, Seismic inversion methods and some of their constraints. First break, 22(6), pp. 47-70.

Waisman, G., 2008, Tectonica de sal da Bacia de Campos: Sal: Geologia e Tectônica. Editora Beca, Sao Paulo. Editora Beca, Sao Paulo, pp. 314-339.

Walles, F.E., 1993, Tectonic and diagenetically induced seal failure within the south-western Great Bahamas Bank. Marine and petroleum geology, 10(1), pp. 14-28.

Warren, J.K., 1997, Evaporites, brines and base metals: Fluids, flow and 'the evaporite that was'. AustralianJournal of Earth Sciences, 44(2), pp. 149-183.

Warren, J.K., 2006, Evaporites: Sediments, Resources and Hydrocarbons. Springer Science & Business Media.

Warren, J.K., 2010, Evaporites through time: Tectonic, climatic and eustatic controls in marine and nonmarine deposits: Earth-Science Reviews, v. 98, pp. 217-268.

Watts, A.B., 1992, The effective elastic thickness of the lithosphere and the evolution of foreland basins. Basin Research, 4(3-4), pp. 169-178.

Weimer, P. and H.S. Pettingill, 2007, Global overview of deep-water exploration and production. Atlas of deepwater outcrops, AAPG Studies in Geology, 56, pp. 7-11.

Wescott, W.A. and W.C. Hood, 1994. Hydrocarbon generation and migration routes in the East Texas Basin. AAPG bulletin, 78(2), pp. 287-306.

Willson, S.M. and J.T. Fredrich, 2005, January. Geomechanics considerations for through-and near-salt well design. In SPE Annual Technical Conference and Exhibition. Society of Petroleum Engineers.pp 1-17

Winker, C.D., 1996, January. High-resolution seismic stratigraphy of a late Pleistocene submarine fan ponded by salt-withdrawal mini-basins on the Gulf of Mexico

continental slope. In Offshore Technology Conference. Offshore Technology Conference.

Winter, W., R. Jahnert, and A. França, 2007, Bacia de Campos: Boletim de Geociências da PETROBRAS, v. 15, pp. 511-529.

Zalán, P.V., M.D.C.G., Severino, C.A., Rigoti, L.P.,Magnavita, J.A.B. De Oliveira, and A.R., Vianna, 2011, An entirely new 3D-view of the crustal and mantle structure of a South Atlantic passive margin–Santos, Campos and Espírito Santo Basins, Brazil. In AAPG Annual Conference and Exhibition, pp. 10-13.

Zarei, M., E. Raeisi, and C.J. Talbot, 2012, Karst development on a mobile substrate: Konarsiah salt extrusion, Iran. Geological Magazine, 149(03), pp. 412-422.

Zeng, H., G. Wang, X. Janson, R. Loucks, Y. Xia, L. Xu, and B. Yuan, 2011, Characterizing seismic bright spots in deeply buried, Ordovician paleokarst strata, Central Tabei uplift, Tarim Basin, Western China. Geophysics, 76(4), pp. B127-B137.